NUMERICAL SIMULATIONS OF PARTICLE ACCELERATION DURING SOLAR FLARES

by

XIAOCAN LI

A DISSERTATION

**Submitted in partial fulfillment of the requirements
for the degree of Doctor of Philosophy
in
The Department of Space Science
to
The School of Graduate Studies
of
The University of Alabama in Huntsville**

HUNTSVILLE, ALABAMA

2016

In presenting this dissertation in partial fulfillment of the requirements for a doctoral degree from The University of Alabama in Huntsville, I agree that the Library of this University shall make it freely available for inspection. I further agree that permission for extensive copying for scholarly purposes may be granted by my advisor or, in his/her absence, by the Chair of the Department or the Dean of the School of Graduate Studies. It is also understood that due recognition shall be given to me and to The University of Alabama in Huntsville in any scholarly use which may be made of any material in this dissertation.

Xiaocan Li   05/20/2016
(date)

DISSERTATION APPROVAL FORM

Submitted by Xiaocan Li in partial fulfillment of the requirements for the degree of Doctor of Philosophy in Space Science and accepted on behalf of the Faculty of the School of Graduate Studies by the dissertation committee.

We, the undersigned members of the Graduate Faculty of The University of Alabama in Huntsville, certify that we have advised and/or supervised the candidate of the work described in this dissertation. We further certify that we have reviewed the dissertation manuscript and approve it in partial fulfillment of the requirements for the degree of Doctor of Philosophy in Space Science.

Dr. Gang Li	05-17-2016 (Date)	Committee Chair
Dr. Gary P. Zank	5/16/16 (Date)	
Dr. Vladimir Florinski	5/16/2016 (Date)	
Dr. S.T. Wu	5/17/2016 (Date)	
G. M. Webb *Dr. Gary Webb*	5/16/2016 (Date)	
Dr. Gary P. Zank	5/16/16 (Date)	Department Chair
Sundar A. C. *Dr. Sundar Christopher*	5/26/2016 (Date)	College Dean
Dr. David Berkowitz	6/13/16 (Date)	Graduate Dean

ABSTRACT

School of Graduate Studies
The University of Alabama in Huntsville

Degree Doctor of Philosophy College/Dept. Science/Space Science

Name of Candidate Xiaocan Li

Title Numerical Simulations of Particle Acceleration during Solar Flares

Particle acceleration is a central topic of solar flare research. In this thesis, I study two topics concerning particle acceleration during solar flares.

The first topic is on the acceleration of charged particles by a time-dependent chaotic magnetic filed. We developed one model based on the solar observations of complex electric current system in solar corona and solar active regions. In this model, self-consistent chaotic magnetic field and electric field are generated by a time-dependent electric current system. Through test-particle simulations, we show that the low energy particles can be efficiently accelerated to nonthermal energies in this system. The results provide a possible mechanism for the efficient particle acceleration during solar flares as well as a pre-acceleration mechanisms for the diffusive shock acceleration by the CME-driven shocks.

The second topic is on particle acceleration by magnetic reconnection. We have carried out kinetic simulations of magnetic reconnection with and without a guide field. The results show that, in the low-β regime, both electrons and ions are efficiently accelerated to nonthermal energies. These nonthermal particles contain more than half of the total electrons, and their distribution resembles a power-law energy distribution with spectral index $p \sim 1$ in a closed boundary simulation. This is in contrast to the high-β cases, where no obvious power-law spectrum is obtained. By ensemble averaging the particle guiding center drift motions, we reveal the main acceleration mechanism as a *Fermi*-type acceleration accomplished by the particle curvature drift along the electric field induced by the reconnection outflows. We then performed a series of simulations with different guide field. The results show that the energy conversion becomes less efficient as the guide field increases. An interesting finding is that reconnection with no guide field preferentially accelerate ions, but reconnection with a strong guide field preferentially accelerate electrons. Both electrons and ions develop power-law energy distributions, which become steeper as the guide field gets stronger. Perpendicular acceleration is dominant for electrons in the cases with a weak guide field, and the parallel acceleration gets more important as the guide field increases. However, the perpendicular acceleration is always dominant for ions. The drift-current analysis shows that the dominant acceleration mechanism for ions is the polarization drift along the motional electric field.

Abstract Approval: Committee Chair ______________________
Dr. Gang Li

Department Chair ______________________
Dr. Gary P. Zank

Graduate Dean ______________________
Dr. David Berkowitz

ACKNOWLEDGMENTS

I am grateful to my advisor, Dr. Gang Li, for guiding me through my graduate study. He is very friendly and patient to me. He always encourages me to explore new research topics and helps me develop a strong background in my research. His way to explain and address problems is intuitive, which I learned a lot from him. I would also like to thank Dr. Hui Li and Dr. Fan Guo for providing me the opportunities to visit Los Alamos National Laboratory (LANL) and get access to the supercomputing resources. It is an inspiring experience to discuss with them on particle energization in all sorts of astrophysical problems. I appreciate Dr. Fan Guo for encouraging me to improve my writing. Thanks also go to Dr. Gary Zank, Dr. S.T. Wu, Dr. Vladimir Florinski and Dr. Gary Webb for agreeing to sit on my committee.

I would like to thank my colleagues and friends at CSPAR for making a great research environment. In particular, I am thankful to Laxman Adhikari, Aaron Arthur, Junxiang Hu, Tae Kim, Scott Ripperda, Udara Senanayake, Junye Ye, and Eric Zirnstein for the insightful discussion. We had so much fun together, making my PhD life more enjoyable. I'm also thankful to Wei Deng and Haocheng Zhang at LANL for our discussions to clarify fundamental ideas.

I would also like to thank my family for their love and support. They always remind me to balance my life and work, eat and sleep well. It wouldn't be possible for me to finish my research without their support.

Finally, I would like to acknowledge the financial support from a NASA Earth and Space Science Fellowship in Heliophysics, NNX13AM30H, which has supported my work since 2013. I gratefully thank William Daughton for providing access to the VPIC code and LANL Institutional Computing for providing the computational resources.

TABLE OF CONTENTS

List of Figures **xii**

List of Tables **xxii**

List of Symbols **xxiii**

Chapter

1 Introduction **1**

1.1 Multi-wavelength observations of solar flares 2

1.2 Particle acceleration during solar flares 5

1.3 Particle acceleration mechanisms 7

1.4 Particle properties during solar flares 12

1.5 Coronal magnetic field and electric currents 15

1.6 Problems to be addressed 16

2 Magnetic reconnection **21**

2.1 Magnetic reconnection theory 22

2.1.1 Sweet-Parker model 23

2.1.2 Petschek's fast reconnection model 25

2.1.3 Collisionless reconnection–Hall physics 26

2.1.4 The plasmoid instability 28

2.2 Particle acceleration during reconnection 35

2.2.1 Parallel acceleration 36

2.2.2 Perpendicular acceleration associated with magnetic islands . 37

2.2.3 Problems to be solved 38

3 Particle acceleration in a wire-loop-current-system 41

3.1 The wire-loop-current-system (WLCS) 42

3.1.1 A single WLCS 42

3.1.2 An ensemble of WLCSs 46

3.2 Particle motion and transport in a time-independent field 47

3.2.1 Particle trajectories 48

3.2.2 Particle spatial diffusion coefficient 49

3.3 Particle energization in a time-dependent field 52

3.4 Discussion and conclusion 55

4 Nonthermal electron acceleration during magnetic reconnection in a Low-beta plasma 59

4.1 Introduction 59

4.2 Numerical simulations 62

4.3 Simulation results 65

4.3.1 General energy evolution 65

4.3.2 Particle energization 68

4.3.3 Drift-current analysis of the energy conversion 69

4.4 Discussion and conclusion 78

5 Parametric study of particle acceleration during magnetic reconnection without a guide field **81**

5.1 Introduction . . . 81

5.2 Numerical simulations . . . 82

5.3 Results . . . 83

5.3.1 Evolution of magnetic field and plasma . . . 83

5.3.2 Energy evolution . . . 87

5.3.3 Particle acceleration . . . 90

5.3.4 Energy conversion in different regions . . . 97

5.4 Discussion and Conclusion . . . 108

6 Particle acceleration during magnetic reconnection with a guide field **112**

6.1 Introduction . . . 112

6.2 Numerical simulations . . . 114

6.3 Simulation results . . . 115

6.4 Conclusion . . . 122

7 Conclusion **124**

APPENDIX A: Solar corona plasma parameters **130**

APPENDIX B: Electromagnetic field in a wire-loop-current-system **133**

B.1 Electromagnetic field of a straight wire current . . . 133

B.2 Magnetic field of a loop current . . . 135

APPENDIX C: Generation of pressure anisotropy 139

APPENDIX D: Compressional effect in reconnection 144

APPENDIX E: Particle-in-cell method 146

E.1 Units and normalization 148

E.2 Time and space discretization (grids) 149

E.3 Field solver 150

E.4 Divergence clean for electric field 155

E.5 Particle advance 156

E.6 Particle sorting 158

E.7 Charge conservation current deposition 159

E.8 Diagnostics 162

REFERENCES 166

LIST OF FIGURES

FIGURE PAGE

1.1 Multi-wavelength observations of solar flares. (a) The great 'Seahorse Flare' of August 7th, 1972. This image in the blue wing of Hα shows the two-ribbon structure late in the event, with bright Hα loops connecting the ribbons. Image credit: Big Bear Solar Observatory (BBSO). (b) A radio source (blue; at 1.2 GHz) is observed at the top of hot flaring loops ($\sim$ 10 MK), which is nearly cospatial with a nonthermal hard X-ray (HXR) source (white contours; at 15 to 25 keV) seen by *RHESSI*. From Chen et al. (2015). Reprinted with permission from AAAS. (c) The "S" shaped sigmoid structures in soft X-ray. Reproduced from McKenzie and Canfield (2008). (d) The thermal emissions in the 6–8 keV range (green contours) show the location of the main flare loops also seen in the 193 Å SDO/AIA image. The non-thermal HXR emissions come from the footpoints of the thermal flare loops (blue contours), but also from above the main flare loop as outlined by the 30–80 keV contours. Reproduced from Krucker and Battaglia (2014) with permission of AAS. 4

1.2 A unified model of flares. Reproduced from Shibata et al. (1995) with permission of AAS. 6

1.3 Centroids of emission at different energies showing the energy loss with distance away from the acceleration point during a flare on 2002 April 15. The loop-top source is below these sources. Reproduced from Raymond et al. (2012) with permission of Springer. 7

1.4 Illustration of the interaction of collapsing magnetic traps. FOCS indicates a fast oblique collisionless shock. HTTCS indicates a high-temperature turbulent current sheet. Reproduced from Somov and Kosugi (1997) with permission of AAS. 11

1.5 (a) A schematic representation of the reconnecting field forming closed loops and coronal open field lines. The red dots indicate the plasma turbulence. Reproduced from Petrosian (2012) with permission of Springer. (b) Turbulent current layer from a 3D kinetic simulation of magnetic reconnection. Reproduced from Daughton et al. (2011) with permission of Nature Publishing Group. (c) Volume rendering of current densities in a 3D simulation of kinetic turbulence, showing the formation of current sheets. Reproduced from Roytershteyn et al. (2015) with permission of the Royal Society. 12

1.6 Electron energy flux spectrum $nVf(E)$ versus electron energy E for the X4.8 solar flare at 2002 July 23. The energy spectrum $f(E) = dN(E)/dE \sim E^{-2}$ and $\sim E^{-2.95}$ for the double power-law spectrum. Reproduced from Piana et al. (2003) with permission of AAS. 13

1.7 NLFFF extrapolation and current densities for AR 11158 on 2011 February 14. Left: selected field lines from the NLFFF extrapolation plotted over a cutout from the vertical field map. The lines are color-coded by the vertical current density at their footpoints (see the color bar); red field lines correspond to strong current density. Top right: vertical current density J_z derived from the vector magnetogram. Bottom right: the horizontal current density J_h distribution on a vertical cross section as derived from NLFFF extrapolation. Reproduced from Sun et al. (2012) with permission of AAS. 17

2.1 Sweet-Parker magnetic reconnection model. The blue region is the reconnection current sheet with a length $2L_{CS}$ and a thickness 2δ. $v_{\rm in}$ is the inflow speed. v_A is the Alfvén speed. The inflow magnetic field is $B_x = \pm B_0$. 23

2.2 Petschek's magnetic reconnection model. The blue region is the reconnection layer with a length $2l$ and a thickness 2δ. The dashed lines are standing slow-mode shocks. L is the system size. $l \ll L$ in this model. 25

2.3 Schematic of the structure of the dissipation region. The gray shaded region is the ion diffusion region with a thickness $\sim d_i = c/\omega_{pi}$. The white box is the electron diffusion region with a thickness $\sim d_e = c/\omega_{pe}$. The red dashed line is the electron flow. The blue dashed line is the ion flow. The $\odot$ and $\otimes$ symbols are the out-of-plane magnetic field direction. The dash-dotted line is the reconnection separatrix. 27

2.4 Schematic view of fractal reconnection. Reprinted from Shibata and Tanuma (2001) with permission of Springer. 34

2.5 Schematic illustration of different phase of magnetic island. The lines with directions are the magnetic field lines. The arrows are indicate the flow direction. The thin cross marks are the X-points of the primary reconnection sites. The thick cross mark indicates the anti-reconnection X-point at the magnetic island coalescence site. (a) Three primary reconnection sites forms two magnetic islands. (b) The two islands are contracting due to magnetic tension force. (c) The two islands coalesce and generate an anti-reconnection site. Reprinted from Oka et al. (2010) with permission of AAS. 38

2.6 Diagram showing volume filling magnetic islands at a reconnection site. Reprinted from Drake et al. (2006) with permission of Nature Publishing Group. 38

3.1 Illustration of the wire-loop-current-system (WLCS). The blue circle on the $x-y$ plane is the loop current with the origin point as its center. The red line is the wire current, which has an arbitrary inclination angle θ_0. Its cross point on the $x-y$ plane has a distance Δr to the origin. 42

3.2 Poincaré map the magnetic field lines. The field lines all start from $x_0 = 0$, $z_0 = 0$, and $y_0 = 0.2$ or 0.3. (a) Symmetric system. (b) Asymmetric system with $\Delta y = 0.01$. $\theta_0 = 0$. (b) Asymmetric system with $\Delta y = 0$. $\theta_0 = 1^\circ$. 43

3.3 Electromagnetic fields of an infinite straight wire along the z-direction with a time-varying current at $\omega t = 0$ and $\pi/2$. 44

3.4 Magnetic field of a loop current in a cylindrical coordinate system. a is the radius of the loop in cm. I_0 is the normalized current in Ampere. 45

3.5 An ensemble of WLCSs, which are placed at the eight corners of the inner cube (black dashed line). The radius of the loops is L_0. The length of the inner box is $2.5L_0$. The orientation of the wire current and the normal directions of the loop current are arbitrary. The outer box (black dash-dotted line) is the simulation domain with side length $7.5L_0$. 47

3.6 Particle trajectories in different system. (a) A single wire current along the z-direction. (b) A single loop current on the $x-y$ plane. (c) A symmetric WLCS. (d) An asymmetric WLCS with $\delta r = 0.1a$. (e) 8 WLCSs. 50

3.7 Particle running diffusion coefficient $D_{rr}(t)$ for (a) a single WLCS with different Δr and (b) 8 WLCSs. (c) $D_{rr}t$ for the same configurations. 51

3.8 Time evolution of proton energy spectra for system with $\omega = 0.001$ Hz for all runs. (a) $I_0 = 10^8$ A and $t_{\max} = 4$ sec, (b) $I_0 = 10^9$ A and $t_{\max} = 0.4$ sec, (c) $I_0 = 10^{10}$ A and $t_{\max} = 0.04$ sec, (d) $I_0 = 10^{11}$ A and $t_{\max} = 0.004$ sec. The black thick solid line is the accumulated spectrum for escaped particles. The black dashed line the fitted power-law spectrum. The fraction of particles remaining in the simulations $F_{\rm in}$ is shown in top right corner of each plot. 54

3.9 Time evolution of electron energy spectra for system with $\omega = 0.001$ Hz for all runs. (a) $I_0 = 10^8$ A and $t_{\max} = 0.1$ sec, (b) $I_0 = 10^9$ A and $t_{\max} = 0.01$ sec, (c) $I_0 = 10^{10}$ A and $t_{\max} = 10^{-3}$ sec, (d) $I_0 = 10^{11}$ A and $t_{\max} = 10^{-4}$ sec. The black thick solid line is the accumulated spectrum for escaped particles. The black dashed line the fitted power-law spectrum. The fraction of particles remaining in the simulations $F_{\rm in}$ is shown in top right corner of each plot. 55

3.10 Proton energy spectrum for different ω. $I_0 = 10^8$ A for all runs. (a) $\omega = 0.01$ Hz and $t_{\max} = 0.4$ sec, (b) $\omega = 0.1$ Hz and $t_{\max} = 0.04$ sec, The black thick solid line is the accumulated spectrum for escaped particles. The black dashed line the fitted power-law spectrum. The fraction of particles remaining in the simulations $F_{\rm in}$ is shown in top right corner of each plot. 56

4.1 Magnetic field profile of a force-free current sheet. $\lambda = d_i$ in this plot. B_x and B_y are normalized by B_0. 63

4.2 Out-of-plane current density for the case with $\beta_e = 0.02$ at (a) $t\Omega_{ci} = 0$, (b) $t\Omega_{ci} = 40$. The dashed lines indicate a cut along the z-direction. (c) j_y along the cut. 66

4.3 Out-of-plane current density j_y for the case with $\beta_e = 0.02$ at (a) $t\Omega_{ci} = 62.5$, (b) $t\Omega_{ci} = 400$. 67

4.4 (a) The energy evolution for $\beta_e = 0.02$ case. $\varepsilon_{bx}(t)$ is the magnetic energy of the reconnecting component. ε_e is the electric energy. K_i and K_e are ion and electron kinetic energies respectively. They are normalized by $\varepsilon_{bx}(0)$. (b) The ratio of electron energy gain ΔK_e to the initial K_e for different initial β_e. 67

4.5 (a) Electron energy spectra $f(E)$ at $t\Omega_{ci} = 800$ for different β_e. The electron energy E is normalized to the initial thermal energy E_{th}. The black dashed line is the initial thermal distribution. (b) Time evolution of the fraction of nonthermal electrons for different initial β_e. n_{nth} is the number of nonthermal electrons, obtained by subtracting the fitted thermal population from whole particle distribution. The fraction of electrons with energies larger than 3 times of the initial thermal energy at (c) $t\Omega_{ci} = 125$, (d) $t\Omega_{ci} = 400$. 70

4.6 Verification of the guiding-center drift approximation for the case with $\beta_e = 0.02$. (a) Energy conversion rate $d\varepsilon_c/dt$ (integrated over the simulation domain)i for electrons in the parallel and perpendicular directions with respect to local magnetic fields, compared with the energy change rate of electrons dK_e/dt. They are normalized by $m_e c^2 \omega_{pe}$. (b) Electron pressure agyrotropy $A\O_e$ at $t\Omega_{ci} = 400$. See Equation 4.12 for the definition of $A\O_e$. The momentum space distributions in the three blue boxes ($x = 53$, 61 and $71d_i$) are shown in Figure 4.7. Boxes 1 and 2 are close to the reconnection X-point. Box 3 is in the reconnection outflow. 71

4.7 Electron momentum distributions in the 3 boxes shown in Figure 4.6 (b). $\boldsymbol{u} = \gamma \boldsymbol{v}/c$, and γ is the Lorentz factor. 75

4.8 Various energization of electrons using a drift description for the case with $\beta_e = 0.02$. (a) the energy conversion rate due to different type of current terms, compared with the electron energy change rate dK_e/dt. $\boldsymbol{j}_c \cdot \boldsymbol{E}$, $\boldsymbol{j}_g \cdot \boldsymbol{E}$, and $\boldsymbol{j}_m \cdot \boldsymbol{E}$ represent energy conversion due to curvature drift, ∇B drift, and magnetization, respectively. (b) The converted magnetic energy due to various terms in (a), normalized to the initial magnetic energy of the reconnecting component $\varepsilon_{bx}(0)$. (c) Color-coded contours of energy conversion rate due to curvature drift at $t = 400\Omega_{ci}^{-1}$. $\boldsymbol{\kappa}$ and $\boldsymbol{u}$ indicate the directions of the magnetic field curvature and the bulk flow velocity. (d) Color-coded contours of energy conversion rate due to ∇B drift at $t = 400\Omega_{ci}^{-1}$. $\boldsymbol{B}$ and ∇B indicate the directions of the magnetic field and the gradient of $|\boldsymbol{B}|$. Both $\boldsymbol{j}_c \cdot \boldsymbol{E}$ and $\boldsymbol{j}_g \cdot \boldsymbol{E}$ are normalized to the $0.002 n_0 m_e c^2 \omega_{pe}$. (e) $\int_0^x \int_0^{L_z} \boldsymbol{j}_i \cdot \boldsymbol{E} dx' dz$ for $\boldsymbol{j}_i = \boldsymbol{j}_c$ and $\boldsymbol{j}_i = \boldsymbol{j}_g$. The black line is the sum of these two. 77

5.1 (a) Out-of-plane magnetic field B_y for run R1 at $t\Omega_{ci} = 60$, 152.5 and 800. The arrow in the middle panel indicates one island merging region. We study the energy conversion in the box in Figure 5.14. (b) The bulk flow velocity $v_x = \sum_s n_s m_s v_{sx} / \sum_s n_s m_s$ for run R1 at $t\Omega_{ci} = 60$ and 152.5. The dashed line in the upper two panels are a horizontal cut along $z = 0$. Plotted in (c) is v_x along the cut. The red line is the cut at $t\Omega_{ci} = 60$. The blue line is the cut at $t\Omega_{ci} = 152.5$. v_x is normalized to the reconnection inflow Alfvén speed v_A. The overplotted arrow indicates a reconnection X-point. The square indicates a contracting magnetic island with two smaller merging islands. 85

5.2 Parallel electric field $E_\parallel$ and out-of-plane electric field E_y for run R1 at (a) $t\Omega_{ci} = 60$ and (b) $t\Omega_{ci} = 152.5$. The parallel direction is respect to the local magnetic field direction. We normalize the electric field to $0.5 v_A B_0$. Note that the color scales are different for $E_\parallel$ and E_y. . . . 86

5.3 Reconnection rate for different runs. (a) 3 runs with the same $\beta_e =$ 0.02. R1 and R3 have $m_i/m_e = 25$ but different plasma temperature. R5 has a mass ratio $m_i/m_e = 100$. (b) 2 runs with the same plasma temperature but different magnetic field strength. The corresponding β_e is 0.007 for R6 and 0.2 for R8. 88

5.4 The out-of-plane current density j_y for (a) run R8, (b) run R7 (c) run R6 at $t\Omega_{ci} = 27.5$. 88

5.5 Time evolution of particle energy spectra for run R1 and R8. The lines with different colors are particle spectra at different times. Curves are evenly spaced in time interval of $\Delta t\Omega_{ci} = 25$ for R1 and $t\Omega_{ci} = 50$ for R8. The dashed line is the initial thermal distribution. The embedded plots give the time evolution of the maximum energy $\varepsilon_{\max}$ normalized to the initial thermal energy $\varepsilon_{\mathrm{th}}$. (a) Electron energy spectra for run R1. (b) Ion energy spectra for run R1. (c) Electron energy spectra for run R8. (d) Ion energy spectra for run R8. 91

5.6 Particle energy spectra for different simulations. $f(\varepsilon) \equiv dN/d\varepsilon$. We normalize the kinetic energy ε to the initial thermal energy $\varepsilon_{\rm th}$, which is same for both electrons and ions in our simulations. (a) Electron spectra for 4 runs with different plasma β. R8 has a $\beta_e = 0.2$. R7 has $\beta_e = 0.07$. R1 has $\beta_e = 0.02$. R6 has the lowest $\beta_e = 0.007$. (b) Electron spectra for 4 runs with the same β, but different plasma temperature. Among them, R5 has a different mass ratio $m_i/m_e = 100$. (c) Ion spectra for the 4 runs with different plasma β. (d) Ion spectra for the 4 runs with the same plasma β but different plasma temperature. All the dashed lines are power-law spectrum through fitting. For electrons, we fit the power-law spectrum over the whole distribution. For ions, we subtract the lower-energy thermal core to get the nonthermal component (thin solid lines in (c) and (d)). We then fit the power-law spectrum over the nonthermal component. . . 93

5.7 Three typical electron trajectories in run R1. The top panels of (a)–(c) show the trajectories in the simulation $x - z$ plane. The background is the out-of-plane electric field E_y. We plot E_y at three time frames, labeled at the top in (a)–(c). The green crosses are the particle position at that time step. The middle panels of (a)–(c) show the electron energy evolution with its x position. The bottom panels show the electron's y position versus its x position. We calculate the y position by integrating v_y over time. The green crosses correspond to 3 time frames indicated in the top panels. Note that the x can be larger than $200d_i$ in these two plots. As particles can cross the right boundary and come back from the left boundary due to the periodic boundary condition, we shift the leftmost trajectory points to the right. (d) The time evolution of the electron kinetic energies for the three electrons plotted in (a)-(c). Again, the green crosses corresponds to the three time steps for each electron. 96

5.8 Typical ion trajectories in run R1. The plots are similar to electrons in Figure 5.7. (a) One ion has three phases of acceleration. The plot in (b) and (c) is similar except that we plot one frame of E_y. (d) Time evolution of ion energy $\gamma - 1$ for the three ions. 98

5.9 Energy conversion rate $\dot{\varepsilon}_c$ through parallel current $\boldsymbol{j}_\parallel \cdot \boldsymbol{E}$, perpendicular current $\boldsymbol{j}_\perp \cdot \boldsymbol{E}$ and total current $(\boldsymbol{j}_\parallel + \boldsymbol{j}_\perp) \cdot \boldsymbol{E}$ for electrons (top) and ions (bottom). The electric field $\boldsymbol{E}$ is from the PIC simulation. It includes both ideal and non-ideal electric fields. $\dot{K}_e$ and $\dot{K}_i$ are the energy change rate for electrons and ions. They are all normalized to $m_e c^2 \omega_{pe}$. The energy conversion for the other runs are summarized in Table 5.3 and Table 5.4. 100

5.10 Energy conversion due to different drift currents for electrons (top) and ions (bottom) for run R1. $\boldsymbol{j}_c$ is due to particle curvature drift. $\boldsymbol{j}_g$ is due to particle ∇B drift. $\boldsymbol{j}_m$ is due to magnetization. $\boldsymbol{j}''_\perp \equiv \boldsymbol{j}_c + \boldsymbol{j}_g + \boldsymbol{j}_m$, which does not include the current densities due to particle polarization drift and agyrotropic pressure tensor. $\dot{K}_e$ and $\dot{K}_i$ are the energy change rate for electrons and ions, respectively. They are all normalized to $m_e c^2 \omega_{pe}$. 102

5.11 Energy conversion rate through perpendicular current densities for electrons (top) and ions (bottom) for run R1. $\boldsymbol{j}_\perp = nq\boldsymbol{u}_\perp$, and $\boldsymbol{j}''_\perp$ is the summation of the current densities due to particle curvature drift, ∇B drift and magnetization. $\boldsymbol{j}_p$ is due to particle polarization drift. $\boldsymbol{j}_a$ is due agyrotropic pressure tensor. The plotted quantities are normalized to $m_e c^2 \omega_{pe}$. 103

5.12 Energy conversion in the reconnection exhaust for run R1 at $t\Omega_{ci} = 137.5$ for (a) electrons, (b) ions. The top two rows plot the 2D contour of different terms. They are normalized to $0.1en_0 v_A^2 B_0$, where v_A is the Alfvén speed. The bottom panels are the accumulation of the top panels along the x-direction, e.g., $\int_{x_0}^{x}\int_{z_{\min}}^{z_{\max}} \boldsymbol{j}_c \cdot \boldsymbol{E} dxdz$. Overplotted are the directions of magnetic curvature $\boldsymbol{\kappa}$, bulk flow velocity $\boldsymbol{u}$, ∇B, the magnetic field $\boldsymbol{B}$, the acceleration of the ion bulk flow velocity $\dot{\boldsymbol{u}}_i = d\boldsymbol{u}_i/dt$ and the gradient of the perpendicular pressure $\nabla p_\perp$. . . 106

5.13 (a) Electric field and mangetic field at $t\Omega_{ci} = 137.5$, corresponding to Figure 5.12. (b) Electric field, magnetic field and flow velocity at $t\Omega_{ci} = 152.5$, corresponding to Figure 5.14. The magnetic field is normalized to B_0. The electric field is normalized to $v_A B_0$. The velocity is normalized to $v_A/2$. 106

5.14 Energy conversion in an island merging region for run R1 at $t\Omega_{ci} = 152.5$ for (a) electrons and (b) ions. Overplotted arrows are the direction of magnetic field curvature $\boldsymbol{\kappa}$, the bulk flow $\boldsymbol{u}$, the gradient of magnetic field ∇B and the acceleration of the ion flow. 108

6.1 In-plane electric field E_z and out-of-plane current density j_y at $t\Omega_{ci} = 100$ except that the case with $B_g = 4.0$ is at $t\Omega_{ci} = 150$. E_z is normalized by cB_0. j_y is normalized by $n_0 ce$. 117

6.2 Time evolution of particle energy spectra for cases which have different guide field. The lines with different colors are particle spectra at different times. Curves are evenly spaced in a time interval of $t\Omega_{ci} = 50$. The dashed line is the initial thermal distribution. The embedded plots give the time evolution of the maximum energy $\varepsilon_{\max}$ normalized by the initial thermal energy $\varepsilon_{\mathrm{th}}$. 119

6.3 Similar as Figure 6.2 but for ions. 120

6.4 Final energy spectra for cases with different B_g for (a) electrons, and (b) ions. $\varepsilon_{\mathrm{th}}$ is the initial particle thermal energy. The thick solid lines are the energy spectra. We shift it along the y-axis to clearly separate different cases. The thin solid lines are the nonthermal part of the spectra by subtracting a low-energy Maxwellian distribution. The dashed lines are the power-law fitting. 120

B.1 Illustration of a loop current with a radius a located in the $x-y$ plane. $\boldsymbol{J}$ is the current density. 135

E.1 Left: one cell in PIC simulation. λ_D is the Debye length. Electric and magnetic fields are sampled on the grids (black lines). The red and blue dots are computational particles. Right: one computing time step of PIC simulation. 147

E.2 2D Yee lattice for PIC simulation. 150

E.3 Leapfrog integration for the E/M field. 151

E.4 Vacuum dispersion solution of Maxwell's equations for finite Δx, Δt. In one dimension, no dispersion error occurs for $C = 1.0$, which is marginally stable. 154

E.5 Illustration of Borris rotation. 157

E.6 Common particle shapes. H is the cell width. $W(x)$ is the assignment function. For NGP, $W(x) = 1$, when $|x| < H/2$ or $x = H/2$. For CIC, $W(x) = 1 - |x|/H$, when $|x| \leq H$. For TSC, $W(x) = 3/4 - (x/H)^2$, when $|x| \leq \frac{H}{2}$; $W(x) = (3/2 - |x|/H)^2/2$, when $H/2 \leq |x| \leq 3H/2$. . 160

E.7 Yee lattice. $i \in [1, n_x]$, $j \in [1, n_y]$, $k \in [1, n_z]$. The fields indices are in $[0, n_x + 1]$, $[0, n_y + 1]$, $[0, n_z + 1]$. 163

E.8 Trilinear interpolation. $\Delta x, \Delta y, \Delta z \in [0,1]$. Q can be any component of $\boldsymbol{E}$, $\boldsymbol{B}$ and their derivatives. $V_1 \cdots V_8$ are the weights for the trilinear interpolation. $V_1 = (1-\Delta x)(1-\Delta y)(1-\Delta z)$, $V_2 = \Delta x(1-\Delta y)(1-\Delta z)$, $V_3 = (1-\Delta x)\Delta y(1-\Delta z)$, $V_4 = \Delta x \Delta y(1-\Delta z)$, $V_5 = (1-\Delta x)(1-\Delta y)\Delta z$, $V_6 = \Delta x(1-\Delta y)\Delta z$, $V_7 = (1-\Delta x)\Delta y \Delta z$, $V_8 = \Delta x \Delta y \Delta z$. . 164

LIST OF TABLES

TABLE PAGE

5.1 List of simulation runs 83

5.2 Energy conversion for different runs 84

5.3 Energy conversion ε_c due to different currents for electrons. The results are the ratios of different terms to ΔK_e, e.g., $\int \boldsymbol{j}_c \cdot \boldsymbol{E} d\boldsymbol{x} dt/\Delta K_e$ . . . 100

5.4 Energy conversion ε_c due to different currents for ions. The results are the ratios of different terms to ΔK_i, e.g., $\int \boldsymbol{j}_c \cdot \boldsymbol{E} d\boldsymbol{x} dt/\Delta K_i$ 101

6.1 Energy conversion for different runs 118

6.2 Energy conversion ε_c due to different currents for electrons. The results are the ratios of different terms to ΔK_e, e.g., $\int \boldsymbol{j}_c \cdot \boldsymbol{E} d\boldsymbol{x} dt/\Delta K_e$ . . . 121

6.3 Energy conversion ε_c due to different currents for ions. The results are the ratios of different terms to ΔK_i, e.g., $\int \boldsymbol{j}_c \cdot \boldsymbol{E} d\boldsymbol{x} dt/\Delta K_i$ 122

LIST OF SYMBOLS

SYMBOL	DEFINITION
$A\O_e$	Electron pressure agyrotropy
B	Magnetic field strength
B_0	Unit magnetic field strength
B_g	Guide field component of the magnetic field in reconnection
$\boldsymbol{B}$	Vector magnetic field
c	Light speed
c_s	Ion sound speed
d_e	Electron inertial length
d_i	Ion inertial length
D_{rr}	Running diffusion coefficient
e	Elementary charge
E	Electric field strength
$\boldsymbol{E}$	Vector electric field
E_D	Dreicer field
E_R	Reconnection rate
$E_\parallel$	Parallel electric field

$E_\perp$	Perpendicular electric field
$f(E), f(\varepsilon)$	Particle energy spectrum
I	Magnitude of electric current
I	Unit dyadic
j	Magnitude of the current density
$\boldsymbol{j}$	Current density
j_y	Out-of-plane electric current density
$\boldsymbol{j}_\parallel, \boldsymbol{j}_\perp$	Parallel and perpendicular current density
$\boldsymbol{j}_a$	Current density due to non-gyrotropic pressure tensor
$\boldsymbol{j}_c$	Current density due to curvature drift
$\boldsymbol{j}_g$	Current density due to gradient drift
$\boldsymbol{j}_m$	Current density due to perpendicular magnetization
$\boldsymbol{j}_{\boldsymbol{E}\times\boldsymbol{B}}$	Current density due to $\boldsymbol{E} \times \boldsymbol{B}$ drift
$\boldsymbol{j}_p$	Current density due to polarization drift
K_e	Electron kinetic energy
K_i	Ion kinetic energy
L, L_{CS}	Half-length of the reconnection current layer
L_x, L_z	Simulation domain sizes
m	Particle mass

m_e	Electron mass
m_i	Ion mass
n	Particle number density
n_{nth}	Nonthermal particle number
N_x, N_z	Simulation grid sizes
p	Scalar pressure
$p_{\parallel}$	Parallel pressure
$p_{\perp}$	Perpendicular pressure
P_e	Electron pressure tensor
S	Lundquist number
S_c	Critical Lundquist number
t	Time
T	Temperature
T_e, T_i	Electron and ion temperature
$\boldsymbol{u}$	Bulk velocity
v	One-dimensional particle velocity
$\boldsymbol{v}$	Vector velocity
v_A	Alfvèn speed
$\boldsymbol{v}_c$	Particle curvature drift velocity

v_e	Electron speed
v_i	Ion speed
v_{in}	Reconnection inflow velocity
v_{out}	Reconnection outflow velocity
v_{th}	Particle thermal speed
β	Plasma beta
β_e	Electron plasma beta
β_i	Ion plasma beta
δ	Half-thickness of the reconnection current layer
$\delta\boldsymbol{B}$	Perturbation to the magnetic field
δ_{SP}	Half-thickness of the reconnection current layer in the Sweet-Parker model
Δr	Displacement of the wire current on the loop plane to the center of the loop
η	Resistivity
ε	Energy
ε_c	Energy conversion
$\dot{\varepsilon}_c$	Energy conversion rate
$\varepsilon_{\mathrm{max}}$	Maximum particle energy
$\varepsilon_{\mathrm{th}}$	Initial particle thermal energy in reconnection

γ	Lorentz factor
Γ_0	Inverse of the Alfvènic time scale
θ_0	Inclination angle of the wire current to the norm direction of the loop plane
$\boldsymbol{\kappa}$	Curvature of a magnetic field
λ_D	Debye length
ν_e	Electron Coulomb collision frequency with ambient plasma
ϕ	Stream function
ψ	Magnetic flux function
ρ	Density
ρ_s	Ion sound radius
σ	Magnetization parameter
τ	Particle gyroperiod
τ_A	Alfvèn time
τ_{acc}	Characteristic acceleration time scale
τ_{diff}	Global Ohmic diffusion time
τ_{inj}	Injection time scale
τ_{rec}	Reconnection time scale
Ω_{ce}	Electron gyrofrequency

Ω_{ci}	Ion gyrofrequency
ω	Plasma vorticity
ω_{pe}	Electron plasma frequency
ω_{pi}	Ion plasma frequency

To my family

I know that I know nothing

—Socrates

CHAPTER 1

INTRODUCTION

If I have seen further it is by standing on the shoulders of Giants.

—Isaac Newton

Solar flares are the most explosive energy release in the solar system and the main driver of space weather. They accelerate electrons to tens of MeVs and ions to GeVs. Electromagnetic emission encompass a broad frequency band from radio emissions at the longest wavelength, through optical emission to X-rays and gamma rays at the shortest wavelength (e.g. Lin (2011)). One major unsolved problem in solar flare research is the acceleration of nonthermal particles, though several mechanisms have been proposed. Additionally, solar flares are usually accompanied by coronal mass ejections (CMEs), which drive shocks to accelerate energetic particles to even higher energies through the diffusive shock acceleration (DSA) mechanism[1]. The diffusive shock acceleration mechanism requires a "seed" particle population, which is most likely originated at the solar active region before the eruption of CMEs. The pre-acceleration mechanism of this "seed" population has not been well addressed. In this chapter, I will briefly review the solar flare observations relevant to this thesis

[1]Particles are scattered back and forth across a shock and get energized in a way similar to multiple reflections between two converging walls. The number of times that a particle cross a shock is random because the scattering by turbulence or plasma waves is a diffusive process (Zank, 2014).

research and then introduce the particle acceleration mechanisms. I will conclude by pointing out some of the key problems addressed in this thesis research.

1.1 Multi-wavelength observations of solar flares

Historically, solar flares were discovered in white light in 1859 (Carrington, 1859; Hodgson, 1859). In 1924, George Hale developed the spectrohelioscope, which can make narrow-band monochromatic images of the entire Sun for any chosen wavelength in the visible solar spectrum (Stenflo, 2015). When used with a Hα ($\lambda = 656.28$ nm) filter, the image from the spectrohelioscope often shows two beautiful ribbons as shown in Figure 1.1 (a). Interestingly, the distance between these two ribbons increases with time, which was recognized later as an evidence of magnetic reconnection in solar flares (Kopp and Pneuman, 1976). In 1908, George Hale used the spectrohelioscope to find the famous Zeeman splitting in sunspots, which established that sunspots are magnetic structures (Hale, 1908). This profound discovery led to extensive research of the role of magnetic field in solar energetic processes. The *Skylab* mission in early 1970s observed coronal soft X-ray loops above two-ribbon flares where magnetic field is strong. *Solar Maximum Mission* (*SMM*) in early 1980s obtained X-ray images of solar flares and showed that large-scale coronal structures with temperatures up to 10^7 Kelvin are associated with solar flares. *Yohkoh* and its follow-up *Hinode* made several key findings to support the magnetic reconnection process during solar flares, i.e., cusp-shaped soft X-ray arcades in long-duration flares (Shibata et al., 1995), above-the-loop-top hard X-ray sources in impulsive flares (Masuda et al., 1994) and soft X-ray sigmoid structures as signatures of the onset of flares and CMEs (Figure 1.1 (b)). *Transition Region and Coronal Explorer* (*TRACE*) and *Solar Dynamics Observatory* (*SDO*) have produced amazing images in the extreme ultraviolet (EUV) band. The background of Figure 1.1 (b) shows different bands of the *SDO*/AIA observations of the flare loops, overplotted are the contours of the hard X-ray (HXR) observations from *Reuven Ramaty High Energy Solar Spectroscopic Imager* (*RHESSI*) and the radio observations from the Very Large Array (VLA) (Chen et al., 2015). γ-ray emission has also been observed by *RHESSI* (Vilmer et al., 2011) and recently by the *Fermi* gamma-ray space telescope (Ajello et al., 2014; Ackermann et al., 2014).

All these emissions are produced by heated plasma or accelerated nonthermal particles. The microwave and high frequency radio (> 5 GHz) are by gyrosynchrotron emission[2], while lower-frequency radio (< 2 GHz) is due to plasma emission (White et al., 2011). Soft X-ray emission is due to bremsstrahlung between thermal electrons and ambient ions. Hard X-ray emission (> 10 keV) is due to bremsstrahlung between nonthermal electrons and ambient ions. Narrow and broad γ-ray emission is through nuclear interaction of energetic ions with ambient protons and heavy nuclei. To interpret the multiple-wavelength observations, we need to understand how plasma is heated from ~ 1 MK to 10s of MK and how particles are accelerated from a thermal population to nonthermal energies.

[2]The terminology gyrosynchrotron emission refers to the emission due to mildly relativistic electrons, in comparison to synchrotron radiation which is due to highly relativistic electrons (Lorentz factor $\gg 1$).

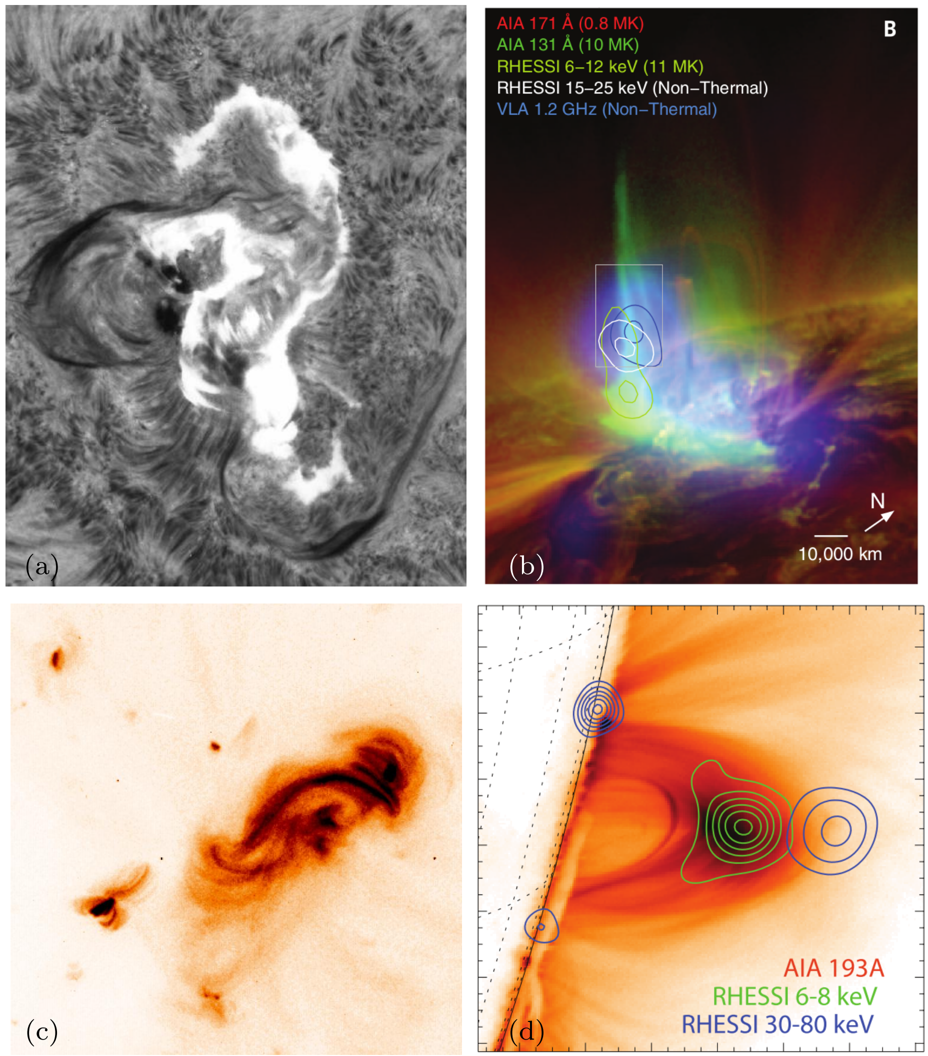

Figure 1.1 Multi-wavelength observations of solar flares. (a) The great 'Seahorse Flare' of August 7th, 1972. This image in the blue wing of Hα shows the two-ribbon structure late in the event, with bright Hα loops connecting the ribbons. Image credit: Big Bear Solar Observatory (BBSO). (b) A radio source (blue; at 1.2 GHz) is observed at the top of hot flaring loops ($\sim$ 10 MK), which is nearly cospatial with a nonthermal hard X-ray (HXR) source (white contours; at 15 to 25 keV) seen by *RHESSI*. From Chen et al. (2015). Reprinted with permission from AAAS. (c) The "S" shaped sigmoid structures in soft X-ray. Reproduced from McKenzie and Canfield (2008). (d) The thermal emissions in the 6–8 keV range (green contours) show the location of the main flare loops also seen in the 193 Å SDO/AIA image. The non-thermal HXR emissions come from the footpoints of the thermal flare loops (blue contours), but also from above the main flare loop as outlined by the 30–80 keV contours. Reproduced from Krucker and Battaglia (2014) with permission of AAS.

1.2 Particle acceleration during solar flares

With the discovery of strong magnetic field ($\sim 10^3$ Gauss) in sunspots (Hale, 1908), it is conceivable that magnetic field energy is the main energy source of solar flares. In 1947, Ronald Giovanelli proposed that magnetic energy can be dissipated through a current sheet containing a magnetic neutral point (Giovanelli, 1947). The standard solar flare model (CSHKP) including the magnetic reconnection process has evolved since then (Carmichael, 1964; Sturrock, 1966; Hirayama, 1974; Kopp and Pneuman, 1976). A unified model is shown in Figure 1.2. Magnetic energy is built up by flux emergence below the photosphere or shearing motions. The energy is stored in highly sheared magnetic structures called current sheets, in which magnetic energy is dissipated and magnetic field lines reconnect on a time scale of ~ 0.1 s. The newly reconnected field lines are strongly bent, and their tension force will drive bi-directional Alfvénic outflows. Preexisting flux ropes[3] will be released to the interplanetary space as well as newly formed plasmoids (flux ropes in 3D), leading to the eruption of CMEs, which drive shocks accelerating particles through the diffusive shock acceleration (DSA) (e.g., Drury, 1983). Using imaging and Doppler observations, reconnection inflows (e.g., Yokoyama et al., 2001) and outflows (e.g., Innes et al., 2003), as well as downward plamoid ejections (Takasao et al., 2012) have been observed. Particles are efficiently accelerated during this process. The energetic particles will precipitate along the magnetic loops to the chromosphere footpoint and generate Hα, HXR and even γ-ray emissions. The HXR emission can heat the chro-

[3] A flux rope is a twisted magnetic flux tube, which is the volume enclosed by a set of magnetic field lines that intersect a simple closed curve (Schrijver and Siscoe, 2009).

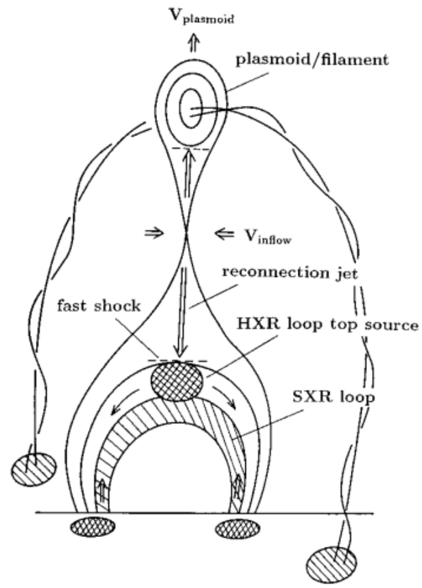

Figure 1.2 A unified model of flares. Reproduced from Shibata et al. (1995) with permission of AAS.

mospheric plasma so it will evaporate into the corona along the flare loops, producing soft X-ray emission in the flare loops (see Shibata and Magara (2011) for an extensive review).

Most of the HXR emission comes from the footpoint regions, where the plasma density is much higher than that in the corona. But coronal HXR sources have been observed in some solar flares. One of the best cases is the "Masuda flare" (Masuda et al., 1994), which reveals a coronal HXR source above the soft X-ray flare loops. One similar event studied by Krucker and Battaglia (2014) is shown in Figure 1.1 (d), where the coronal HXR source (blue contours) is clearly separated from the soft X-ray flare loop source (green contours). This suggests that the electron acceleration is above the flare loops and most likely associated with the reconnection processes. Another kind of coronal HXR source is the double coronal sources (Sui and Holman, 2003) shown in Figure 1.3. HXR sources appear to be located below and above

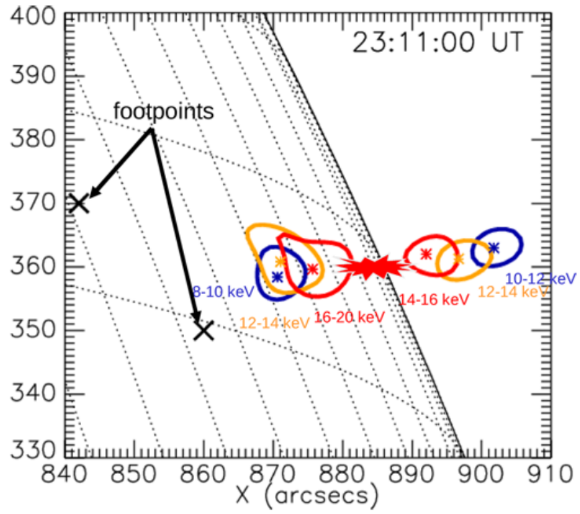

Figure 1.3 Centroids of emission at different energies showing the energy loss with distance away from the acceleration point during a flare on 2002 April 15. The loop-top source is below these sources. Reproduced from Raymond et al. (2012) with permission of Springer.

one reconnection X-line, and the spectrum becomes softer away from the central point, suggesting energy loss away from the energy release and particle acceleration region (Sui and Holman, 2003; Liu et al., 2008; Chen and Petrosian, 2012; Liu et al., 2013b). The highest temperature is above the loop-top X-ray source and well below the reconnection site, suggesting that primary plasma heating and particle acceleration occur in the reconnection outflow region (Liu et al., 2013b). While it is now widely acknowledged that the particle acceleration process is associated with magnetic reconnection, there is no agreement on the dominant acceleration mechanism (Miller et al., 1997; Zharkova et al., 2011).

1.3 Particle acceleration mechanisms

Below is a short review of available acceleration mechanisms, including sub-Dreicer and super-Dreicer electric field, collapsing magnetic trap, termination shocks driven by the reconnection outflow, MHD turbulence generated by fast reconnection outflows. Magnetic reconnection will be introduced in the next chapter.

The Dreicer field model considers electron acceleration under a large-scale electric field $\boldsymbol{E}$ (Zharkova et al., 2011). In one dimension, the equation of motion for a single particle is

$$\frac{dv}{dt} = \frac{eE}{m} - \nu_e v, \tag{1.1}$$

where $\nu_e \sim T_e^{-2/3} \sim v^{-3}$ is the Coulomb collision frequency with ambient plasma (see Appendix A). Then the equation can be rewritten as

$$m\frac{dv}{dt} = e\left(E - E_D\left[\frac{v_{\mathrm{th}}}{v}\right]^2\right), \tag{1.2}$$

where v_{th} is the electron thermal speed, and the Dreicer field is

$$E_D = m_e\nu_e(v_{\mathrm{th}})v_{\mathrm{th}}/e \approx 10^{-8}n(\mathrm{cm}^{-3})/T(K)\ \mathrm{V\ cm}^{-1}. \tag{1.3}$$

For coronal density $n \sim 10^9$ cm^{-3} and temperature $T = 10^6$ K, $E_D \sim 10^{-5}$ V cm^{-1}. If $E < E_D$ (sub-Dreiser), only high energy particles ($v > v_{\mathrm{c}} = v_{\mathrm{th}}\sqrt{E_D/E}$) can be accelerated, which will reduce the drag force due to collisions, yielding stronger acceleration and eventually runaway acceleration. Particles with $v < v_c$ are decelerated and remain collisionally redistributed maintaining Maxwellian distribution (Zharkova et al., 2011). The sub-Dreicer model was invoked to explain the thermal+nonthermal electron distributions (Benka and Holman, 1994), where the electric field is due to fragmented current/return current pairs and finite resistivity in solar corona. If $E > E_D$

(super-Dreicer), all particles with $v > v_{\rm th}$ are accelerated, leading to efficient acceleration of all electrons. This model has been invoked in single reconnection X-line acceleration, where reconnection electric field ~ 2 V cm^{-1} (Zharkova et al., 2011), much larger than the Dreicer field. The problem with this scenario is that this region is much smaller than the whole flare region, so it will not be able to accelerate a large portion of electrons in the flare region. As shown in a series of papers, a considerable portion ($> 10\%$) of electrons are accelerated in the solar flare regions (Krucker et al., 2010; Krucker and Battaglia, 2014; Oka et al., 2015). Besides, reconnection in solar flares should involve a large number of X-lines and magnetic island structures. This is discussed in the next chapter.

The standard flare model (e.g. Shibata et al., 1995) suggests that a termination shock (TS) can form when the reconnection outflow moves toward the dense and closed magnetic loops. Figure 1.4 illustrates the structure of a TS in solar flares. A TS accelerates particles through the diffusive shock acceleration (DSA) mechanism (see an extensive review by Drury (1983)). The TS acceleration has been invoked to explain the ≥ 300 keV spectral hardening in solar flares (Li et al., 2013) and the shock-induced type-II radio bursts (Kong et al., 2015). Chen et al. (2015) made significant progress by using high cadence radio observations from the Very Large Array (VLA) to identify a solar flare termination shock. The authors found that the formation and destruction of the TS are correlated with the HXR flux, suggesting that the TS is efficient at accelerating electrons to nonthermal energies.

Additionally, particles are trapped by the collapsing magnetic field lines from the reconnection region. The collapsing magnetic traps can accelerate particles through both *Fermi* acceleration and betatron acceleration. This can be seen from considering the conservation of magnetic moment and the longitudinal invariant of a charged particle moving in a B field. Assuming a charged particle moving in a smooth B field, then the parallel and perpendicular component of the particle momentum vary as

$$p_{1\perp} = p_{0\perp}\sqrt{B/B_0}, \quad p_{1\|} = p_{0\|}(L_1/L_0)^{-1}, \tag{1.4}$$

where $p_{0\|}$ are $p_{0\perp}$ are the particle's initial momenta, $p_{1\|}$ are $p_{1\perp}$ are the particle's momenta at a later time, L_0 is the initial length of a field line, L_1 is the length of the field line at a later time, B_0 is the initial magnetic field strength, B is the magnetic field strength at a later time. As the field lines shorten, $p_{1\|}$ increases, which is a *Fermi*-type mechanism (Fermi, 1949). At the same time, the field lines collapse to the flare loops where magnetic field becomes stronger, therefore $p_{1\perp}$ increases, which is the betatron acceleration.

Turbulence acceleration/stochastic acceleration has been proposed to explain the above-the-loop-top HXR sources. Turbulence or plasma waves generated by the Alfvènic reconnection outflows will cascade to smaller scales, during which turbulence can heat the plasma and accelerate particles (Hamilton and Petrosian, 1992; Miller et al., 1996; Chandran, 2003; Petrosian and Liu, 2004; Petrosian et al., 2006). Figure 1.5 (a) shows a schematic representation of turbulence acceleration model. Most acceleration occurs at the reconnection outflow region, which appears to be consistent with the observations (Liu et al., 2013b). This model requires an *ad hoc* injection of

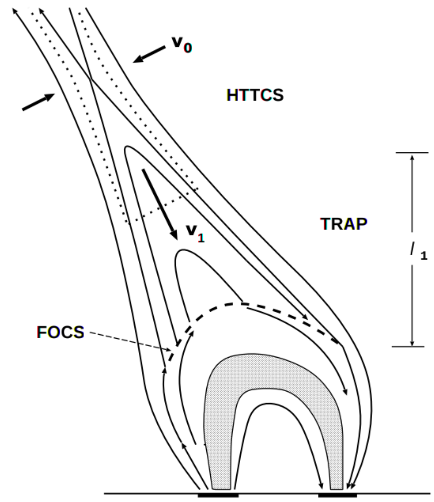

Figure 1.4 Illustration of the interaction of collapsing magnetic traps. FOCS indicates a fast oblique collisionless shock. HTTCS indicates a high-temperature turbulent current sheet. Reproduced from Somov and Kosugi (1997) with permission of AAS.

plasma waves (Zharkova et al., 2011), which is not well-justified. Both MHD (Huang and Bhattacharjee, 2016) and kinetic simulations (Daughton et al., 2011) do show self-generated plasma turbulence in 3D reconnection layer (Figure 1.5 (b)), which generates multiple secondary current sheets. This poses the question of whether the energy dissipation and particle acceleration occur dominantly through the current sheet or wave-particle interaction in a plasma turbulence. Recent 3D kinetic simulations of collisionless turbulence show that a large number of current sheets form in the simulation (Figure 1.5 (c)) (Roytershteyn et al., 2015), and the current sheets dissipate $\sim 50\%$ of the total energy conversion (Wan et al., 2015). Very likely current sheets and turbulence are tightly related to each other and studying the role of reconnection in turbulence energy dissipation and the role of turbulence on the reconnection processes may provide us a unified picture in the future.

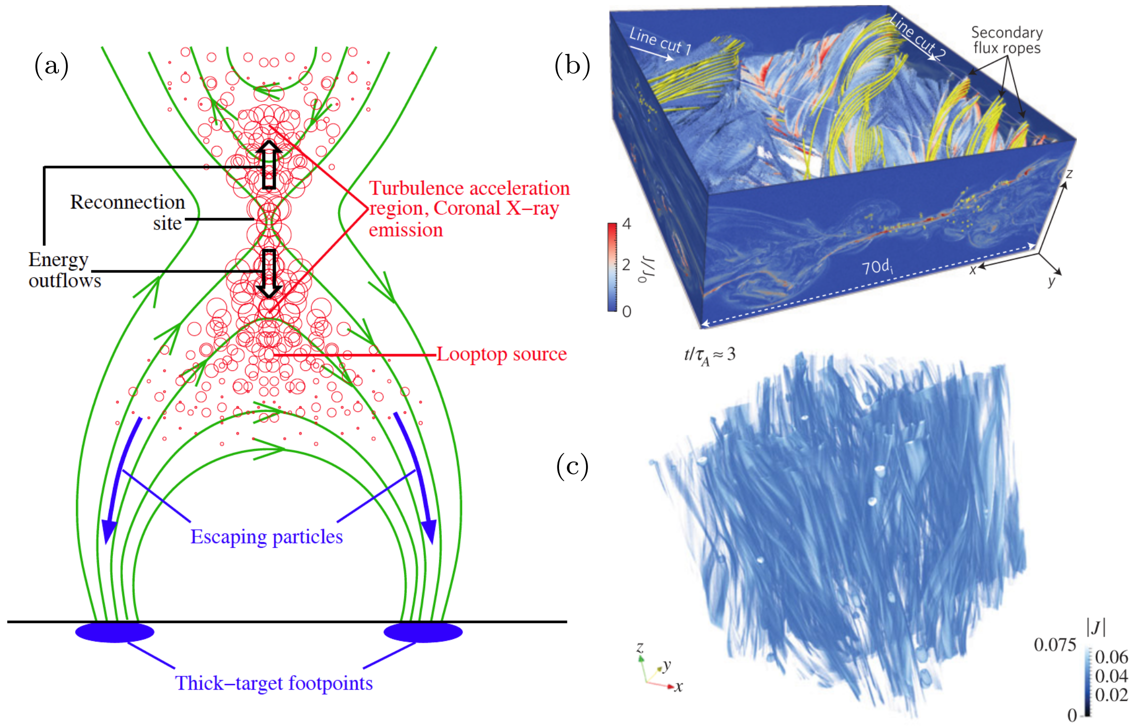

Figure 1.5 (a) A schematic representation of the reconnecting field forming closed loops and coronal open field lines. The red dots indicate the plasma turbulence. Reproduced from Petrosian (2012) with permission of Springer. (b) Turbulent current layer from a 3D kinetic simulation of magnetic reconnection. Reproduced from Daughton et al. (2011) with permission of Nature Publishing Group. (c) Volume rendering of current densities in a 3D simulation of kinetic turbulence, showing the formation of current sheets. Reproduced from Roytershteyn et al. (2015) with permission of the Royal Society.

1.4 Particle properties during solar flares

Observations not only can associate the acceleration processes with magnetic reconnection but also place several quantitative constraints on the accelerated particle properties, including particle energy spectrum, nonthermal population, energy partition between electrons and ions, ion composition, etc.

The electron energy spectrum inferred from the HXR observations is usually power-law $f(E) \sim E^{-p}$ or double power-law (Figure 1.6). The power-law index

$p > 2$. One of the key problem is to decide the low-energy cutoff E_c of the power-law

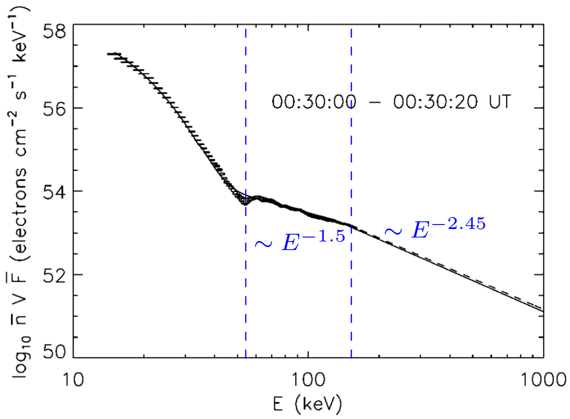

Figure 1.6 Electron energy flux spectrum $nVf(E)$ versus electron energy E for the X4.8 solar flare at 2002 July 23. The energy spectrum $f(E) = dN(E)/dE \sim E^{-2}$ and $\sim E^{-2.95}$ for the double power-law spectrum. Reproduced from Piana et al. (2003) with permission of AAS.

spectrum, so that we can better estimate how many particles and how much energy are contained in the power-law part (Kontar et al., 2011). E_c is typically ≤ 20 keV and sometimes as low as ~ 12 keV (Kontar et al., 2008). For some of the above-the-loop-top HXR source regions, the estimated nonthermal electron density is comparable with ambient thermal proton density, suggesting that the entire electron population within the above-the-loop-top source can be energized (Krucker and Battaglia, 2014). This highly efficient acceleration challenges the shock acceleration scenario, because we only expect $< 10\%$ of nonthermal particles in shock acceleration (Neergaard Parker and Zank, 2012). In large flares, the electron acceleration rate can reach $\sim 10^{36}$ s^{-1}, which generates a large current $\sim 10^{17}$ A and a current density $j = I/S \approx 0.3$ A cm^{-2} (Zharkova et al., 2011). Observations do show electric currents in the flare region but with a weaker current density ≤ 0.05 A cm^{-2} (see the next section).

There are fewer constraints on the ion energy spectrum than that on electrons, as only a handful of γ-ray lines with sufficient statistics exist (Lin, 2011). The derived ion spectra using these γ-ray line observations are unbroken power laws down to $\sim$1 MeV. The power-law index is about -4 (Lin et al., 2003). The estimated total energy contained in the energetic ions is comparable to the energy contained in energetic electrons > 20 keV (Lin et al., 2003). Thus, energetic ions also contain a substantial fraction of the total energy released in the flare (Ramaty et al., 1995; Lin et al., 2003). Shih et al. (2009) showed that the fluence of the 2.223 MeV γ-ray lines (by ≥ 30 MeV ions) is correlated to the > 0.3 MeV HXR fluence (by ≥ 0.3 MeV electrons), suggesting that the same mechanism accelerates ≥ 30 MeV ions and ≥ 0.3 MeV electrons.

The abundances of heavy ions put crucial constraints on acceleration mechanisms. α-particles, ^{3}He, Ne, Mg and Fe are over-abundant compared with normal coronal compositions (Vilmer et al., 2011), suggesting that the acceleration mechanism preferentially accelerates these particles. For a long time, wave-particle resonance in turbulence acceleration appeared to be the only plausible explanation for this observation (Miller et al., 1997). Recent simulations involving reconnection show heavy ions gain more energy when they are "picked-up" by the reconnection outflow (Drake et al., 2009a,b; Drake and Swisdak, 2014; Knizhnik et al., 2011), suggesting reconnection may be an alternative explanation of the heavy ion abundance.

1.5 Coronal magnetic field and electric currents

The coronal magnetic field is essential for understanding the magnetic energy storage, release and transport in solar active regions. The coronal magnetic field, to a very good approximation, is a force-free field (Wiegelmann and Sakurai, 2012). We start from the momentum of equation of the ideal MHD equations

$$\rho\left(\frac{\partial \boldsymbol{v}}{\partial t}+\boldsymbol{v}\cdot\nabla\boldsymbol{v}\right)=-\nabla p+\frac{\boldsymbol{j}\times\boldsymbol{B}}{c}, \tag{1.5}$$

which can be normalized as

$$\tilde{\rho}\left(\frac{v_0}{v_A}\frac{\partial\tilde{\boldsymbol{v}}}{\partial\tilde{t}}+\frac{v_0^2}{v_A^2}\tilde{\boldsymbol{v}}\cdot\tilde{\nabla}\tilde{\boldsymbol{v}}\right)=-\frac{\beta}{2}\tilde{\nabla}\tilde{p}+\tilde{\boldsymbol{j}}\times\tilde{\boldsymbol{B}}, \tag{1.6}$$

where the length is normalized to l_0, the magnetic field B is normalized to B_0, the density ρ is normalized to ρ_0, the time scale is normalized to l_0/v_A, $v_A = B_0/\sqrt{4\pi\rho_0}$ is the Alfvèn speed, the scalar pressure p is normalized to p_0, $\boldsymbol{j}$ is normalized to $j_0 = cB_0/4\pi l_0$, the plasma-beta $\beta = 8\pi p_0/B_0^2$. In the solar corona, the flow is sub-Alfvènic except in the reconnection outflow region, so $v_0/v_A \ll 1$. The plasma $\beta \ll 1$ in the lower region of the solar corona (Gary, 2001). Then, $\boldsymbol{j}\times\boldsymbol{B} = 0$, i.e. the force-free approximation is valid, resulting in the force-free equation (Wiegelmann et al., 2015).

$$\nabla\times\boldsymbol{B} = \alpha(\boldsymbol{x})\boldsymbol{B}, \tag{1.7}$$

where the spatial-dependent $\alpha(\boldsymbol{x})$ scales as $1/l$. It may be interpreted as the magnetic twist per unit length. The force-free equation indicates

$$\boldsymbol{B} \cdot \nabla \alpha = 0, \tag{1.8}$$

so α is constant along field lines. If α is globally constant, i.e. $\boldsymbol{x}$-independent, we call the force-free field model the linear force-free field (LFFF). If α varies with $\boldsymbol{x}$, we call it nonlinear force-free field (NLFFF). Equation 1.7 and Equation 1.8 can be solved numerically using the measured vector magnetic field at the photosphere as boundary conditions. The left panel of Figure 1.7 shows the selected field lines extrapolated from the NLFFF magnetic field (Sun et al., 2012). Knowing $\boldsymbol{B}$, the current density can be easily calculated by $\nabla \times \boldsymbol{B}$. The right panels of Figure 1.7 show the vertical and horizontal current densities. The vertical current switch directions across the polarity inversion line (PIL), and the horizontal current density peaks in the flux ropes, suggesting the current is along the magnetic loops. The current density shows complex patch structures and is very dynamic (Sun et al., 2012). The time-varying electric current can induce time-dependent magnetic field and hence electric field, which accelerates charged particles.

1.6 Problems to be addressed

In this thesis, I address two major topics on particle acceleration during solar flares. The first topic is particle acceleration by the electric field generated by large scale time-dependent electric currents in solar flare regions. Our model provides a new

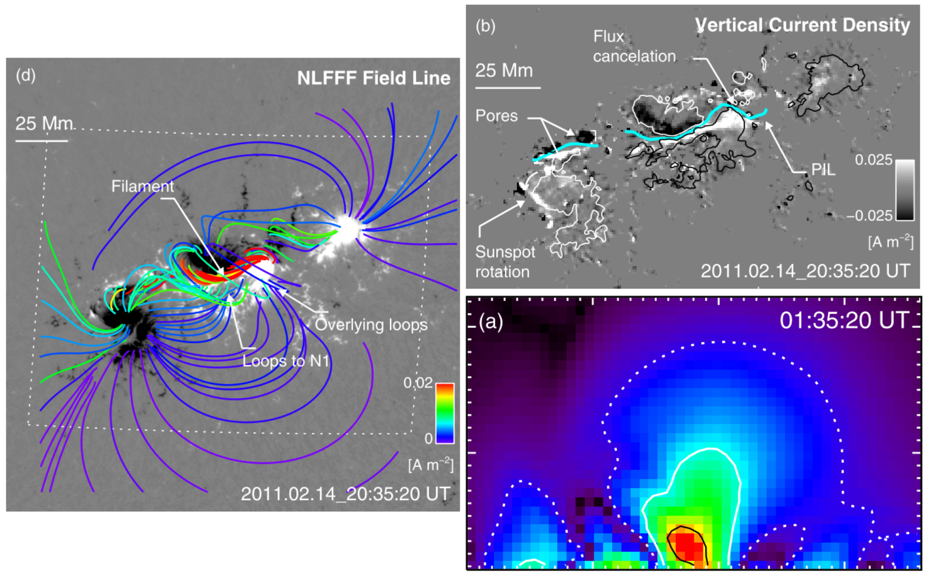

Figure 1.7 NLFFF extrapolation and current densities for AR 11158 on 2011 February 14. Left: selected field lines from the NLFFF extrapolation plotted over a cutout from the vertical field map. The lines are color-coded by the vertical current density at their footpoints (see the color bar); red field lines correspond to strong current density. Top right: vertical current density J_z derived from the vector magnetogram. Bottom right: the horizontal current density J_h distribution on a vertical cross section as derived from NLFFF extrapolation. Reproduced from Sun et al. (2012) with permission of AAS.

mechanism for particle energization during solar flares. The energized particles could provide a "seed" population for diffusive shock acceleration by CME-driven shocks. The second topic is to examine particle acceleration by magnetic reconnection. Our results show power-law formation in kinetic simulations of magnetic reconnection in nonrelativistic plasma for the first time. This could explain the highly efficient electron and ion acceleration during solar flares.

In Chapter 2, I will briefly introduce the reconnection theory, including the Sweet-Parker model, Petscheks fast reconnection model and the Hall reconnection model. I will emphasize the plasmoid instability that breaks an elongated current sheet into multiple magnetic islands, which are efficient in accelerating particles to nonthermal energies (e.g. Drake et al., 2006). I will discuss particle acceleration mechanisms in magnetic reconnection and point out unsolved problems in the research on particle acceleration during magnetic reconnection.

In Chapter 3 and Li et al. (2014), we investigate charged particle behavior in a chaotic magnetic field, which is generated from one or multiple asymmetric wire-loop-current-systems (WLCSs). We find that particle transport in one WLCS is a sub-diffusion process due to the trapping of the magnetic field. In contrast, particle transport in 8 WLCSs is a diffusion process as particles are not trapped by one WLCS but jump between different WLCSs. When including time-dependent electric currents, both electrons and protons are accelerated to develop power-law energy distribution with power-law index < 1, which is consistent with the model of particle acceleration by multiple reconnection current sheet (Dauphin et al., 2007). The spectra get harder with stronger electric current and faster varying electric current. The maximum energy reaches to $1 - 10$ MeV for both electrons and protons, which can provide a seed population for the CME-driven shock acceleration.

In Chapter 4 and Li et al. (2015), we carried out kinetic simulations in a non-relativistic plasma with low plasma β. The initial current sheet breaks into a chain of magnetic islands, which interact and merge with each other. Magnetic energy is converted into plasma kinetic energy during this process. The results show that accelerated nonthermal electrons contain more than half of the total electrons, and their distribution resembles a power-law energy distribution $f(E) \sim E^{-1}$ when particle loss is absent. By ensemble averaging the electron guiding center drift motions, we reveal the main acceleration mechanism as a *Fermi*-type acceleration accomplished by the particle curvature drift along the electric field induced by the reconnection outflows. This is in contrast to the high-β simulations, where no obvious power-law spectrum is obtained (e.g. Drake et al., 2010).

In Chapter 5 and Li et al. (2016), we perform 2D kinetic simulations of magnetic reconnection in a nonrelativistic proton-electron plasma with a range of plasma $\beta_e = \beta_i = 0.007 - 0.2$. This work is an extension of the earlier work of Li et al. (2015). We achieve lower plasma β condition by either increasing the magnetic field strength (or equivalently decreasing the particle density), or by decreasing the plasma temperature. We compare the energy conversion and particle acceleration for simulations with different plasma β. We find that both nonthermal electrons and ions develop power-law energy distributions with power-law index $p \sim 1$ in the low-β regime ($\beta_e \leq 0.02$). Through tracking a large number of particles we find that both electrons and ions get efficiently accelerated when they are drifting along the electric field induced by the bulk flow in the X-type region, anti-reconnection region where two islands are merging, and contracting magnetic islands. Furthermore, ions gain energy when they are "picked-up" by the reconnection outflow. This initial fast energy gain makes ions more energetic than electrons, so they can be accelerated more efficiently through the *Fermi* mechanism later in the simulation. This provides a good explanation on why ions gain more energy than electron in our simulations. By studying $\boldsymbol{j} \cdot \boldsymbol{E}$, we identify the major acceleration mechanism is through particle curvature drift along the motional electric field. Particle ∇B drift, polarization drift, parallel electric field and non-gyrotropic pressure tensor all play important role in different acceleration regions at different times.

In Chapter 6, we perform a series of kinetic simulations with different guide-field strength. We find that the energy conversion becomes less efficient as the guide field increases. This is due to the fact that the plasma becomes less compressible when there is a guide field. Reconnection with no guide field preferentially accelerate ions, and reconnection with a strong guide field preferentially accelerate electrons. Both electrons and ions develop into power-law energy distributions, which become steeper as the guide field gets stronger. Perpendicular acceleration is dominant for electrons in the cases with a weak guide field, and the parallel acceleration gets more important as the guide field increases. However, the perpendicular acceleration is always dominant for ions. The drift-current analysis shows that the dominant acceleration mechanism for ions is the polarization drift along the motional electric field.

CHAPTER 2

MAGNETIC RECONNECTION

Magnetic reconnection is a fundamental plasma process that rearranges the magnetic field topology, accompanied by the release of magnetic energy and particle energization (Priest and Forbes, 2000; Zweibel and Yamada, 2009; Yamada et al., 2010). It occurs ubiquitously in laboratory, space and astrophysical magnetized plasmas. An important unsolved problem is the acceleration of nonthermal particles in the reconnection region. Magnetic reconnection has been suggested as a primary mechanism for accelerating nonthermal particles in solar flares (Masuda et al., 1994; Krucker et al., 2010; Lin, 2011), Earth's magnetosphere (Øieroset et al., 2002; Fu et al., 2011; Huang et al., 2012), sawtooth crash of tokamaks (Savrukhin, 2001), and high-energy astrophysical systems (Colgate et al., 2001; Zhang and Yan, 2011; Arons, 2012). In this chapter, I will introduce the reconnection theories starting from the Sweet-Parker model, and proceed with Petschek's fast reconnection model and Hall reconnection model. Then, I will show that the plasmoid instability will lead to the formation of a large number of magnetic islands in high-Lundquist-number plasma such as solar corona, driving current sheets to kinetic scales. I will review current understandings of particle acceleration during reconnection and conclude by pointing out the problems to be solved.

2.1 Magnetic reconnection theory

If a plasma is perfectly conducting (conductivity $\sigma \to \infty$), it obeys the ideal Ohm's law $\boldsymbol{E} = -(\boldsymbol{v} \times \boldsymbol{B})/c$. The magnetic flux through any surface bounded by contour $\mathcal{C}$ moving with the fluid is conversed, and the magnetic field lines are frozen into the plasma (Alfvén, 1942; Zank, 2014). No reconnection of magnetic field lines can occur. If we introduce non-ideal effect $\boldsymbol{R}$ to the Ohm's law,

$$\boldsymbol{E} + (\boldsymbol{v} \times \boldsymbol{B})/c = \boldsymbol{R}, \quad \nabla \times \boldsymbol{R} \neq 0, \tag{2.1}$$

the frozen-in condition will be broken. The generalized Ohm's law includes several non-ideal terms.

$$\frac{m_e}{ne^2}\left[\frac{\partial \boldsymbol{j}}{\partial t} + \nabla \cdot \left(\boldsymbol{j}\boldsymbol{v} + \boldsymbol{v}\boldsymbol{j} - \frac{\boldsymbol{j}\boldsymbol{j}}{ne}\right)\right] = \boldsymbol{E} + \frac{\boldsymbol{v} \times \boldsymbol{B}}{c} - \frac{\boldsymbol{j} \times \boldsymbol{B}}{nec} + \frac{1}{ne}\nabla \cdot \mathbf{P}_e - \eta \boldsymbol{j}, \tag{2.2}$$

where $\mathbf{P}_e$ is the electron pressure tensor, η is the plasma resistivity. The term on the left is due to the electron inertia; the third term on the right is the Hall term; the fourth term on the right is the pressure term, and the last term is the resistive term, which is included in the Sweet-Parker reconnection model. The other terms become important when kinetic effects cannot be neglected in kinetic scales[1].

[1] These scales includes: the ion inertial length d_i, the electron inertial length d_e, the Debye length λ_D, the ion gyroradius r_i and the electron gyroradius r_e. See Appendix A for their definitions and their values in solar corona plasma.

2.1.1 Sweet-Parker model

The first reconnection quantitative model is from Sweet (1958) and Parker (1957b), well-known as the Sweet-Parker (SP) model. This model focuses on two-dimensional steady-state reconnection in an incompressible plasma (Birn and Priest, 2007). In this model, the antiparallel magnetic fields are carried toward each other

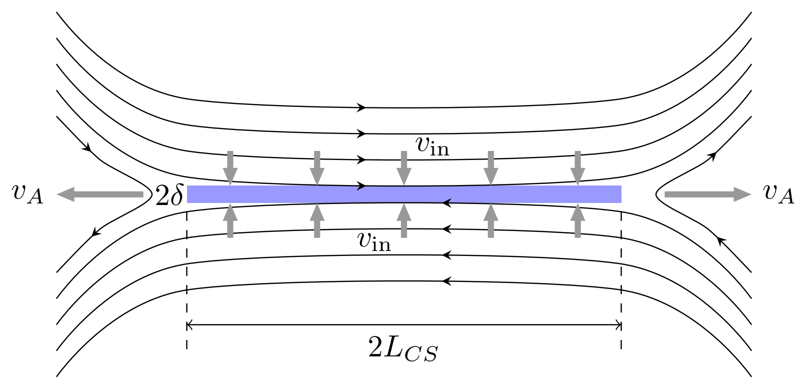

Figure 2.1 Sweet-Parker magnetic reconnection model. The blue region is the reconnection current sheet with a length $2L_{CS}$ and a thickness 2δ. $v_{\rm in}$ is the inflow speed. v_A is the Alfvén speed. The inflow magnetic field is $B_x = \pm B_0$.

with speed $v_{\rm in}$. The magnetic field lines reconnect in a current sheet with a length $2L_{CS}$ and a thickness 2δ. This drives bi-directional reconnection outflows $v_{\rm out}$. Considering the assumption of steady-state and impressibility, the continuity equation $d\rho/dt + \rho\nabla \cdot \boldsymbol{v} = 0$ yields $\nabla \cdot \boldsymbol{v} = 0$. Then,

$$\frac{v_{\rm in}}{v_{\rm out}} = \frac{\delta}{L_{CS}}. \tag{2.3}$$

Including finite resistivity in the Ohm's law, $\boldsymbol{E} = -(\boldsymbol{v} \times \boldsymbol{B})/c + \eta \boldsymbol{j}$, where η is the resistivity. Substituting $\boldsymbol{j}$ to the Faraday's law, we get the resistive induction equation

$$\frac{\partial \boldsymbol{B}}{\partial t} = \nabla \times (\boldsymbol{v} \times \boldsymbol{B}) + \frac{\eta c^2}{4\pi} \nabla^2 \boldsymbol{B}. \tag{2.4}$$

In a steady state, the left term is 0, the right terms should balance each other, leading to

$$v_{\rm in} \sim \eta c^2/(4\pi\delta). \tag{2.5}$$

The pressure balance of the inflow magnetic pressure and the outflow dynamic pressure yields $B_0^2/8\pi = n m_i v_{\rm out}^2/2$, which leads to

$$v_{\rm out} = \frac{B_0}{\sqrt{4\pi n m_i}} = v_A, \tag{2.6}$$

where v_A is the Alfvén speed of the inflow plasma. Using Equation 2.3, Equation 2.5 and Equation 2.6, the reconnection rate E_R becomes

$$E_R \equiv \frac{v_{\rm in}}{v_A} = \frac{\delta}{L_{CS}} = S^{-1/2}, \tag{2.7}$$

where $S = 4\pi L_{CS} v_A/(\eta c^2)$ is the Lundquist number, which is the ratio of the global Ohmic diffusion time $\tau_{\rm diff} = 4\pi L_{CS}^2/(\eta c^2)$ to the Alfvén time $\tau_A = L_{CS}/v_A$ (Zweibel and Yamada, 2009). The reconnection time scale is a geometric mean of these two time scales,

$$\tau_{\rm rec} = \tau_{\rm diff}^{1/2} \tau_A^{1/2} = S^{1/2} \tau_A. \tag{2.8}$$

Most astrophysical plasmas have very large S. For example, in solar corona, $S \sim 10^{12}$ and $\tau_A \sim 1$ s. Then, $\tau_{\text{rec}} \sim 10^6$ s, much larger than the typical solar flare time scales 10^{2-3} s (Lin, 2011). So the reconnection rate of the Sweet-Parker model is too small to explain the solar flare observations.

2.1.2 Petschek's fast reconnection model

The Sweet-Parker model is slow because of the large aspect ratio of the current sheet $L_{CS}/\delta \gg 1$. Petschek (1964) developed a model with a much shorter current sheet shown in Figure 2.2. The expense is to introduce four standing slow-mode shocks bounding the reconnection exhausts. Instead of passing through the resistive current layer, most plasma pass through the shocks and get heated at the shocks. This model yields a maximum reconnection rate $\pi/(8\ln S)$. For solar corona plasma condition, it yields a reconnection time scale $\tau_{\text{rec}} \sim 100$ s, consistent with observations.

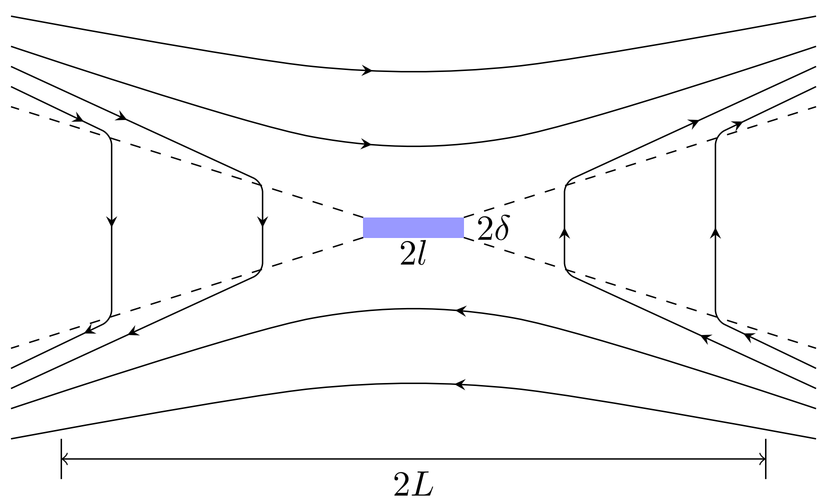

Figure 2.2 Petschek's magnetic reconnection model. The blue region is the reconnection layer with a length $2l$ and a thickness 2δ. The dashed lines are standing slow-mode shocks. L is the system size. $l \ll L$ in this model.

However, numerical simulations have failed to validate Petschek's model (Biskamp, 1986; Uzdensky and Kulsrud, 2000; Malyshkin et al., 2005), unless there is strongly enhanced resistivity at the reconnection X-point (Sato and Hayashi, 1979; Ugai, 1995; Scholer, 1989; Erkaev et al., 2000; Biskamp and Schwarz, 2001; Malyshkin et al., 2005). Without the enhanced local resistivity, the current sheet will evolve like the Sweet-Parker current layer. Kinetic-scale instabilities may give anomalously enhanced resistivity in the current sheet by driving micro-turbulence (Büchner and Elkina, 2005, 2006). This requires large 3D kinetic simulations that links the kinetic-scale instabilities and the MHD-scale dynamics (Loureiro and Uzdensky, 2016).

2.1.3 Collisionless reconnection–Hall physics

In high-S plasma, the thickness of the current sheet δ can be smaller than the ion inertial length $d_i = c/\omega_{pi} = c\sqrt{m_i}/\sqrt{4\pi ne^2}$, according to Equation 2.7. The Hall term in Equation 2.2 will be larger than the ideal term $\boldsymbol{v} \times \boldsymbol{B}/c$.

$$\frac{|\boldsymbol{v} \times \boldsymbol{B}|}{|\boldsymbol{j} \times \boldsymbol{B}|/ne} \sim \frac{v_A B}{cB^2/4\pi ne\delta} = \frac{\delta}{d_i} < 1. \tag{2.9}$$

In this region, $j/ne \sim v_e$ exceeds $v \sim v_i$ so that v_e exceeds v_i, which implies that the electron motion and ion motion decouple. Figure 2.3 shows the schematic of the structure of this region. Approaching this region, ions are diverted into the outflow direction, forming the ion diffusion region with a thickness d_i. The electrons are still frozen-in to the magnetic field and continue move to smaller scales. The electrons eventually decouple from magnetic field when they approach the d_e scale, where they are diverted to the outflow direction. The different motions of electrons and ions generate in-plane current loops, yielding a quadruple structure of the out-of-plane magnetic field B_y. Within the electron diffusion region, the outflow flux is (Dahlin,

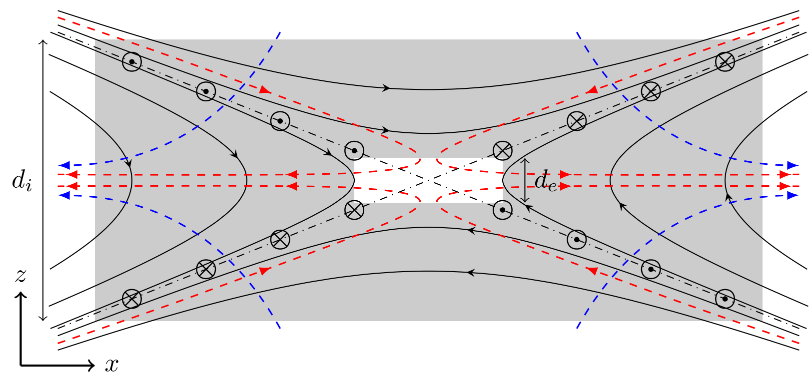

Figure 2.3 Schematic of the structure of the dissipation region. The gray shaded region is the ion diffusion region with a thickness $\sim d_i = c/\omega_{pi}$. The white box is the electron diffusion region with a thickness $\sim d_e = c/\omega_{pe}$. The red dashed line is the electron flow. The blue dashed line is the ion flow. The $\odot$ and $\otimes$ symbols are the out-of-plane magnetic field direction. The dash-dotted line is the reconnection separatrix.

2015)

$$\delta v_{\text{out}} \sim \delta \left(\frac{j}{ne} \right) \sim \delta \left(\frac{cB_0}{4\pi\delta} \right) \frac{1}{ne} \sim v_A d_i. \tag{2.10}$$

So the outflow flux is independent of the current sheet thickness, which effectively opens up the outflow region and enhances the reconnection rate of the Sweet-Parker model. Note that the Hall term itself cannot break the magnetic field line because it does not give energy dissipation. The other non-ideal terms in the generalized Ohm's law are required to break the field line, leading to dissipation.

2.1.4 The plasmoid instability

The Sweet-Parker model assumes that the current sheet is stable, but early simulations show that the SP-like current sheet is unstable to the plasmoid (magnetic island) formation (Biskamp, 1986; Lee and Fu, 1986; Yan et al., 1992). Bulanov et al. (1979); Biskamp (1986) argued that the large-aspect-ratio ($L_{CS}/\delta > 100$, $S \sim 10^4$) current sheets was unstable to a tearing mode instability (Furth et al., 1963; Coppi et al., 1976), leading to plasmoid formation. It is until recently that a linear theory of plasmoid instability in SP-like current sheet is developed by Loureiro et al. (2007). Below is a summary of this theory with reference to Loureiro et al. (2007); Baalrud et al. (2012); Comisso and Grasso (2016).

The two-dimensional ($\partial_z = 0$) reduced MHD equation in an incompressible plasma is

$$\partial_t \psi + \boldsymbol{v} \cdot \nabla \psi = \eta j + E_0, \tag{2.11}$$

$$\partial_t \omega + \boldsymbol{v} \cdot \nabla \omega = \boldsymbol{B} \cdot \nabla j, \tag{2.12}$$

where $\psi(x, y, t)$ is the magnetic flux function, ω is the z-component plasma vorticity, $\boldsymbol{B}$ is the magnetic field, $\boldsymbol{v}$ is the velocity field, j is z-component of the electric current density, and E_0 is the equilibrium electric field.

$$\boldsymbol{B} = \nabla \psi \times \hat{\boldsymbol{e}}_z, \quad \boldsymbol{v} = \hat{\boldsymbol{e}}_z \times \nabla \phi; \tag{2.13}$$

$$j = \nabla^2 \psi, \quad \omega = \nabla^2 \phi, \tag{2.14}$$

where $\phi(x, y, t)$ is the stream function. The current sheet is along the y-direction with an equilibrium flow profile

$$\boldsymbol{v}_0 = \begin{cases} (-\Gamma_0 x, \Gamma_0 y) & |x| \leq x_0 \text{ (inside the current sheet);} \\ (-\Gamma_0 x_0, 0) & x \geq x_0; \\ (\Gamma_0 x_0, 0) & x \leq -x_0, \end{cases} \tag{2.15}$$

where $\Gamma_0 = v_A/L_{CS}$, and L_{CS} is the half-length of the current sheet. So that outflow is Alfvènic. The stream function is then

$$\phi_0(x, y) = \begin{cases} \Gamma_0 xy & |x| \leq x_0; \\ \Gamma_0 x_0 y & x \geq x_0; \\ -\Gamma_0 x_0 y & x \leq -x_0, \end{cases} \tag{2.16}$$

The equilibrium magnetic field is assumed to be $(0, B_{0y}(x))$. When $|x| \leq x_0$, B_{0y} satisfies

$$\delta^2 \frac{dB_{0y}}{dx} + xB_{0y} = \frac{E_0}{\Gamma_0}. \tag{2.17}$$

One solution of B_{0y} that switches direction at $x = 0$ is

$$B_{0y}(\xi) = \alpha e^{-\xi^2/2} \int_0^\xi e^{z^2/2} dz, \tag{2.18}$$

according to Equation 2.11, where $\xi = x/\delta$, $\alpha = E_0/\Gamma_0\delta$. To match with the B_{0y} outside of the region $|x| \leq x_0$, a natural condition is that B_{0y} has its maximum or minimum at $\pm x_0$, so that

$$\partial_x B_{0y}|_{\pm x_0} = 0 \Rightarrow \xi_0 = 1.307. \tag{2.19}$$

When $x \geq x_0$ or $x \leq -x_0$, $B_{0y} = \pm E_0/\Gamma_0 x_0$, yielding $\alpha = 1.307$. Considering small perturbation to the system,

$$\psi(x, y, t) = \psi(x) + \psi_1(x, t)e^{ik(t)y}; \tag{2.20}$$

$$\phi(x, y, t) = \phi(x, y) + \phi_1(x, t)e^{ik(t)y}, \tag{2.21}$$

where $k(t) = k_0 \exp(-\Gamma_0 t)$, then

$$\partial_t \psi_1 + ikB_{0y}\phi_1 - \Gamma_0 x \partial_x \psi_1 = \eta(\partial_x^2 - k^2)\psi_1; \tag{2.22}$$

$$(\partial_x^2 - k^2)\partial_t \phi_1 + 2\Gamma_0 k^2 \phi_1 - \Gamma_0 x \partial_x (\partial_x^2 - k^2)\phi_1 = ik \left[\frac{d^2 B_{0y}}{dx^2} - B_{0y}(\partial^2 - k^2) \right] \psi_1, \tag{2.23}$$

We seek solutions of exponential growing modes.

$$\psi_1(x, t) = -i\Psi(x) \exp(\gamma t), \quad \phi_1(x, t) = \Phi(x) \exp(\gamma t), \tag{2.24}$$

with the growth rate $\gamma \gg \Gamma_0 = v_A/L_{CS}$. In this limit, $k(t) \approx k_0$, and the terms proportional to Γ_0 can be neglected. Then,

$$\lambda\Psi + B_{0y}\Phi = \frac{1}{\kappa}(\Psi'' - \kappa^2\epsilon^2\Psi); \tag{2.25}$$

$$\lambda(\Phi'' - \kappa^2\epsilon^2\Phi) = B_{0y}(\Psi'' - \kappa^2\epsilon^2\Psi) - B''_{0y}\Psi, \tag{2.26}$$

where the derivatives are with respect to ξ, and

$$\lambda \equiv \frac{\gamma}{k_0 v_A}, \quad \epsilon \equiv \frac{\delta}{L_{CS}}, \quad \kappa \equiv k_0 L_{CS}. \tag{2.27}$$

For elongated current sheet, $\epsilon \ll 1$. We also assume $\lambda \ll 1$, $\kappa \gg 1$, $\kappa\epsilon \ll 1$ and $\lambda\kappa \gg 1$. As in the standard tearing mode theory (Coppi et al., 1976), the spatial domain is separated into the outer region ($\xi \sim 1$) and the inner region ($\xi \ll 1$).

In the outer region, the system is "ideal". Equation 2.25 and Equation 2.26 reduce to

$$\Phi = \frac{\lambda}{B_{0y}}\Psi; \tag{2.28}$$

$$\frac{d^2\Psi}{d\xi^2} = \left(\frac{B''_{0y}}{B_{0y}} + \kappa^2\epsilon^2\right)\Psi. \tag{2.29}$$

Considering $\kappa^2\epsilon^2 \ll 1$, Equation 2.29 is solved perturbatively (Loureiro et al., 2007).

$$\Psi^{\pm}(\xi) = \begin{cases} \pm\frac{\alpha\Psi(0)}{\kappa\epsilon}B_{0y}(\xi) - \alpha\Psi(0)B_{0y}\int_{\pm\xi_0}^{\xi}\frac{dz}{B_{0y}^2(z)} & |\xi| \le \xi_0; \\ \frac{\alpha\Psi(0)}{\kappa\epsilon}\exp[\kappa\epsilon(\xi_0 \mp \xi)] & |\xi| \ge \xi_0, \end{cases} \tag{2.30}$$

where $\pm$ indicating solution for $\xi > 0$ or $\xi < 0$. The solution has a discontinuous derivative at $\xi = 0$. The jump of this derivative gives the tearing stability parameter (Furth et al., 1963; Loureiro et al., 2007).

$$\Delta' = \frac{1}{\Psi(0)}\left[\Psi'(+0) - \Psi'(-0)\right] \approx \frac{2\alpha^2}{\kappa\epsilon}. \tag{2.31}$$

In the inner region, where $|\xi| \ll 1$, we can assume $B_{0y} \approx \alpha\xi$ and $\partial_\xi \gg 1$. Equation 2.25 and Equation 2.26 reduce

$$\lambda\Psi + \alpha\xi\Phi = \frac{1}{\kappa}\Psi''; \tag{2.32}$$

$$\lambda\Phi'' = \alpha\xi\Psi''. \tag{2.33}$$

The resulted dispersion relation is (Coppi et al., 1976; Loureiro and Uzdensky, 2016; Comisso and Grasso, 2016)

$$\Lambda^{5/4}\frac{\Gamma\left[(\Lambda^{3/2}-1)/4\right]}{\Gamma\left[(\Lambda^{3/2}+5)/4\right]} = -\frac{8}{\pi}(\kappa\alpha)^{-1/3}\Delta'; \tag{2.34}$$

where Γ is the gamma function and $\Lambda = \lambda\alpha^{-2/3}\kappa^{1/3}$. Combining with Equation 2.31,

$$\Lambda^{5/4}\frac{\Gamma\left[(\Lambda^{3/2}-1)/4\right]}{\Gamma\left[(\Lambda^{3/2}+5)/4\right]} = -\frac{8}{\pi}(\kappa\alpha)^{-1/3}\frac{2\alpha^2}{\kappa\epsilon}. \tag{2.35}$$

Two limits of this equation are

$$\frac{\gamma}{\Gamma_0} \approx \left(-\frac{16\Gamma(5/4)}{\pi\Gamma(-1/4)}\right)^{4/5} \alpha^2\kappa^{-2/5}\epsilon^{-4/5} \approx 1.63\kappa^{-2/5}\epsilon^{-4/5}, \quad \text{when } \Lambda \ll 1; \tag{2.36}$$

$$\frac{\gamma}{\Gamma_0} \approx (\alpha\kappa)^{2/3} - \frac{\sqrt{\pi}}{3\alpha}\kappa^2\epsilon, \quad \text{when } \Lambda \to 1^-. \tag{2.37}$$

The maximum growth rate lies between the two limits. γ in Equation 2.37 peaks at $\kappa_{\max} \sim \epsilon^{-3/4} \gg 1$. Recall that $\epsilon = \delta/L_{CS} = S^{-1/2}$ for a SP-current sheet,

$$k_{\max}L_{CS} \sim S^{-3/8}; \tag{2.38}$$

$$\frac{\gamma_{\max}}{\Gamma_0} \sim \epsilon^{-1/2} \sim S^{1/4}. \tag{2.39}$$

For a high-S plasma, the instability grows extremely violent compared with the Alfvénic time scale $\tau_A = L_{CS}/v_A = \Gamma_0^{-1}$. The scaling of the wavenumber and growth rate has been validated by numerical simulations (Samtaney et al., 2009; Ni et al., 2010; Loureiro et al., 2013). Equation 2.38 predicts the number of plasmoid scales as $N \sim S^{3/8}$ at the linear stage. Numerical simulations have shown that $N \sim S$ in the nonlinear regime (Cassak et al., 2009; Huang and Bhattacharjee, 2010). In the nonlinear regime, plasmoids coalesce with each other and are ejected and convected with the reconnection outflow. Meanwhile, secondary current sheets are expected to form between the plasmoids, and new plasmoids are generated constantly in the reconnection layer (Huang and Bhattacharjee, 2010; Loureiro and Uzdensky, 2016). This gives rise to a hierarchical, fractal-like plasmoid structure (Shibata and Tanuma, 2001; Daughton et al., 2009b), which ends when the local current sheet is marginally stable (the growth rate of the plasmoid instability is comparable to the reciprocal Alfvènic time scale) and that their length yields a critical Lundquist number $S_c = 4\pi L_c v_A/\eta c^2$. The number of plasmoid then scales like $L/L_c \sim S/S_c$. The thickness of the local

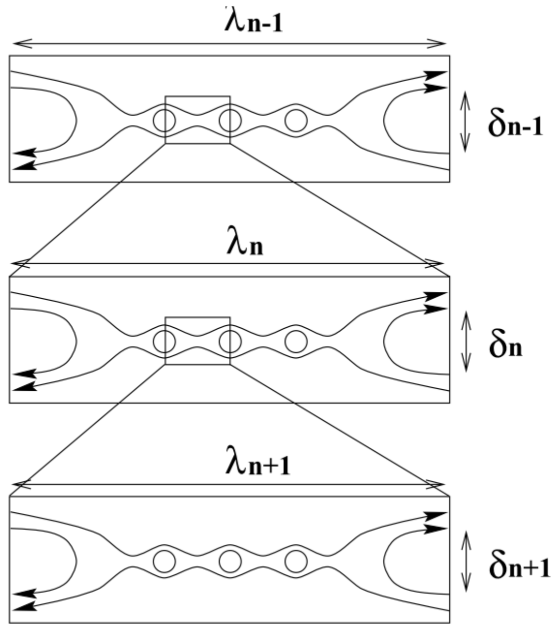

Figure 2.4 Schematic view of fractal reconnection. Reprinted from Shibata and Tanuma (2001) with permission of Springer.

current sheet and the current density scale like

$$\delta_c = \frac{L_c}{\sqrt{S_c}} = \eta c^2 \frac{\sqrt{S_c}}{4\pi v_A} = \delta_{SP}\sqrt{\frac{S_c}{S}}; \tag{2.40}$$

$$j = \frac{c}{4\pi}\frac{B}{\delta_c} = \frac{B v_A}{\eta c\sqrt{S_c}} = \frac{c}{4\pi}\frac{BS}{L\sqrt{S_c}}, \tag{2.41}$$

where δ_{SP} is the thickness of the Sweet-Parker current sheet. Then, the reconnection electric field is $\eta j = Bv_A/(c\sqrt{S_c})$, and the normalized reconnection rate

$$E_R = \eta j/(Bv_A/c) = S_c^{-1/2} \tag{2.42}$$

Both heuristic argument (Biskamp, 1986) and numerical simulations (Lee and Fu, 1986; Lapenta, 2008; Bhattacharjee et al., 2009; Cassak et al., 2009; Huang and Bhattacharjee, 2010; Loureiro et al., 2012) have shown that $S_c \sim 10^4$, so the reconnection rate at high-S regime is ~ 0.01, much faster than the Sweet-Parker reconnection.

The continuous formation of current sheet between the plasmoids will lead to the breakdown of the MHD approximation when the current sheet thickness approaches the ion kinetic scale (Daughton et al., 2009b; Ji and Daughton, 2011; Daughton and Roytershteyn, 2012). Since the current sheet thickness $\delta/\delta_{SP} \sim S^{-1/2} \sim N^{-1/2}$, δ can reach the ion kinetic scale much faster than would be expected for the original Sweet-Parker current sheet. Both two-fluid simulation (Ma and Bhattacharjee, 1996; Cassak et al., 2005) and kinetic simulation (Daughton et al., 2009a) have shown that the kinetic scale is the ion inertial length d_i for anti-parallel reconnection. The transition to kinetic scale leads to a dramatic enhancement in the reconnection rate (Daughton et al., 2009b), which is about 0.04–0.2 (Birn et al., 2001; Hesse et al., 2001; Pritchett, 2001; Shay et al., 2001, 2007), compared with 0.01 in the MHD regime. The breakdown of the MHD description at kinetic scales requires fully kinetic simulations (see Appendix E for an introduction) to capture the plasma dynamics.

2.2 Particle acceleration during reconnection

Charged particles are accelerated by the electric field, which can be supported by the reconnection outflow, the divergence of the electron pressure tensor, the electron inertia and the resistivity, according to the generalized Ohm's law in Equation 2.2. The acceleration mechanisms can be divided into parallel acceleration by $E_\parallel$ and perpendicular acceleration by $E_\perp$.

2.2.1 Parallel acceleration

Electrons can be accelerated by $E_\parallel$ in the electron diffusion region and the reconnection separatrix. In the electron diffusion region, $E_\parallel$ is supported by $\nabla \cdot \mathbf{P}_e$, in particular, the non-gyrotropic component of $\mathbf{P}_e$ (Hesse et al., 2011). $\mathbf{P}_e$ becomes non-gyrotropic because the electrons are demagnetized in the electron diffusion region where the particle gyroradius is large due to the weak magnetic field. However, the electron diffusion region is only on a scale of the electron Larmor radius (Hesse et al., 2011), so it can not accelerate a significant fraction of electrons in the whole reconnection region. Besides $\nabla \cdot \mathbf{P}_e$, the resistive term can support $E_\parallel$ if anomalous resistivity arises due to instabilities such as the low hybrid drift instability, the drift-kink instability and the Buneman instability (Hesse et al., 2011). Numerical simulations (Drake et al., 2003) have shown that the Buneman instability can form electron hole structures (low density regions) with strong localized parallel electric field. The electron hole structures tend to distribute along the reconnection separatrix and have been observed in the Earth's magnetotail reconnection (Cattell et al., 2005). The arising of the Buneman instability is due to electron beams when they are streaming into the diffusion region along the reconnection separatrix (Drake et al., 2003). The streaming electrons can be accelerated by the parallel electric field, which is due to a pseudo-electric potential[2] along the reconnection separatrix (Egedal et al., 2012).

2.2.2 Perpendicular acceleration associated with magnetic islands

The dominant perpendicular acceleration is due to the inductive electric field $-\boldsymbol{v}\times\boldsymbol{B}/c$ by the reconnection outflow (Hoshino et al., 2001; Fu et al., 2006; Pritchett, 2006; Oka et al., 2010), contracting magnetic island (or plasmoid) (Drake et al., 2006) or anti-reconnection outflow at the island coalescence region (Oka et al., 2010). A schematic illustration of these phases is shown in Figure 2.5. Magnetic island plays a unique role because it can trap particles, so they can interact with the reconnection outflow several times. The island contracting is widely referred as a *Fermi*-type acceleration mechanism (Fermi, 1949) for magnetic reconnection. Each time a particle crosses the two sides of a contracting magnetic island, it collides "head-on" with the Alfvénic outflow driven by the tension force release of the magnetic field lines. Since an elongated current sheet can generate multiple magnetic islands (Bhattacharjee et al., 2009; Daughton et al., 2009b), they tend to coalesce with each other through anti-reconnection processes. Through tracking energetic electron trajectories, kinetic simulations have suggested that the most energetic electrons are accelerated in the magnetic island merging region (Oka et al., 2010; Nalewajko et al., 2015).

[2] This potential is defined as $\Phi_{\parallel}(\boldsymbol{x}) = \int_{\boldsymbol{x}}^{\infty} \boldsymbol{E}\cdot d\boldsymbol{l}$, where the integration is carried from the location $\boldsymbol{x}$ along the magnetic field line to the ambient plasma. It measures the work done by $E_{\parallel}$ on a electron streaming along the magnetic field line. It is a pseudo-potential because the gradient of $\Phi_{\parallel}$ perpendicular to the magnetic field has no physical importance (Egedal et al., 2008, 2009).

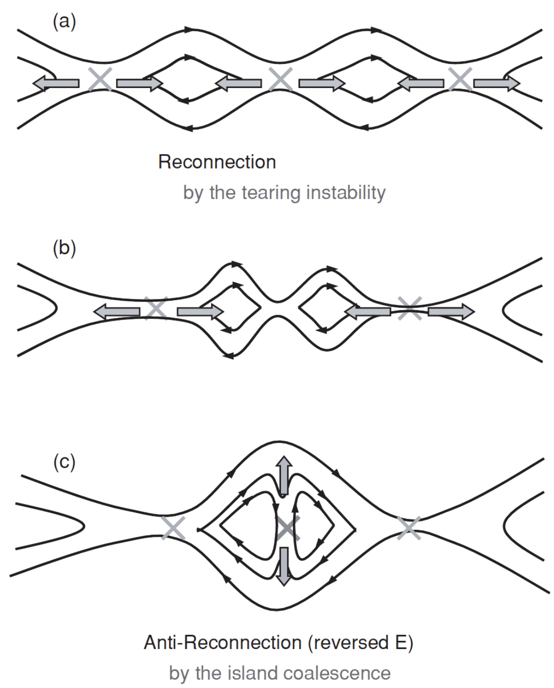

Figure 2.5 Schematic illustration of different phase of magnetic island. The lines with directions are the magnetic field lines. The arrows are indicate the flow direction. The thin cross marks are the X-points of the primary reconnection sites. The thick cross mark indicates the anti-reconnection X-point at the magnetic island coalescence site. (a) Three primary reconnection sites forms two magnetic islands. (b) The two islands are contracting due to magnetic tension force. (c) The two islands coalesce and generate an anti-reconnection site. Reprinted from Oka et al. (2010) with permission of AAS.

2.2.3 Problems to be solved

An emerging picture is that particles in a sea of magnetic islands can form power-law energy distribution (Drake et al., 2006, 2013; Zank et al., 2014). An illustration of such configuration is shown in Figure 2.6. Most previous simulations have

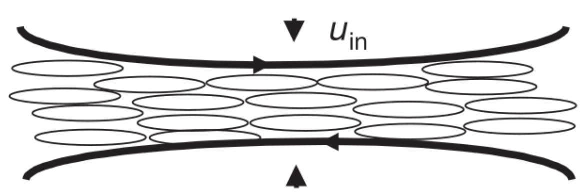

Figure 2.6 Diagram showing volume filling magnetic islands at a reconnection site. Reprinted from Drake et al. (2006) with permission of Nature Publishing Group.

focused on reconnection in a plasma with relatively high β ($\beta > 0.1$). They found energetic particles but no obvious power-law distributions is obtained (Hoshino et al., 2001; Drake et al., 2006, 2010; Oka et al., 2010). Meanwhile, simulations of relativistic reconnection did show nonthermal distribution but only within the localized X-region (Zenitani and Hoshino, 2001), which is on the kinetic scale and cannot account for the observed particle acceleration. In the past few years, kinetic simulations (Guo et al., 2014; Melzani et al., 2014; Sironi and Spitkovsky, 2014; Werner et al., 2016; Guo et al., 2015, 2016) have made significant progresses in the magnetically dominated regime (magnetic energy $\gg$ plasma kinetic energy). These works showed that particles over the entire reconnection region can develop a power-law energy distribution, when the magnetization parameter $\sigma = B^2/(4\pi n_e m_e c^2) \gg 1$. This suggests that particles are more efficiently accelerated in a magnetically dominated plasma. Recall that the plasma $\beta \ll 1$ in solar corona (Gary, 2001; Lin, 2011), so it is natural to anticipate that reconnection in a low-β plasma can lead to power-law energy distributions that could explain the solar flare observations.

Using kinetic simulation, one can identify different acceleration regions through tracking the trajectories of a small number of energetic electrons. The limitation of this method is that it cannot explain the bulk energization with over 50% of electrons being nonthermal. The bulk energization suggests that the energy conversion and particle acceleration are intrinsically related. We can use fluid quantities (e.g. current density $\boldsymbol{j}$) to describe the energization process by averaging the drift motions of a large number of particles. Using this description, we expect to identify the role of parallel acceleration and particle drift motions in different acceleration regions. The relative importance of different terms may vary with plasma β, mass ratio and guide-field strength. A parametric study of these acceleration mechanisms is required.

CHAPTER 3

PARTICLE ACCELERATION IN A WIRE-LOOP-CURRENT-SYSTEM

In this work we study particle acceleration in a time-dependent chaotic electric field that results from a time-dependent chaotic magnetic field. This model is based on the observations of electric currents in the solar corona (e.g. Spangler, 2007) and solar flare regions (Georgoulis et al., 2012; Sun et al., 2012). We construct a time-dependent chaotic magnetic field that is due to a simple configuration of electric currents as described in earlier works (Li et al., 2009; Ram and Dasgupta, 2010; Dasgupta et al., 2012). We then examine charged particle acceleration in such a field using a test-particle method. We emphasize here that we do not claim that this simple system can represent the realistic magnetic field in the solar corona or flare regions. Rather, we use it because it is computationally tractable.

In Section 3.1, I describe the model setup and relative parameters. In Section 3.2, I present the results of particle motion and transport in this system by tracking particles in a time-independent field. In Section 3.3, I present the results of particle energization in a time-dependent field. I will discuss our results and conclude in Section 3.4.

3.1 The wire-loop-current-system (WLCS)

3.1.1 A single WLCS

Section 1.5 shows that the electric currents in solar active regions peak in magnetic field loops and form complex patch structures. We build a model here to mimic the current loops and current filaments. A wire-loop-current-system consists of a circular loop and a straight wire with an infinite length (Figure 3.1). When the

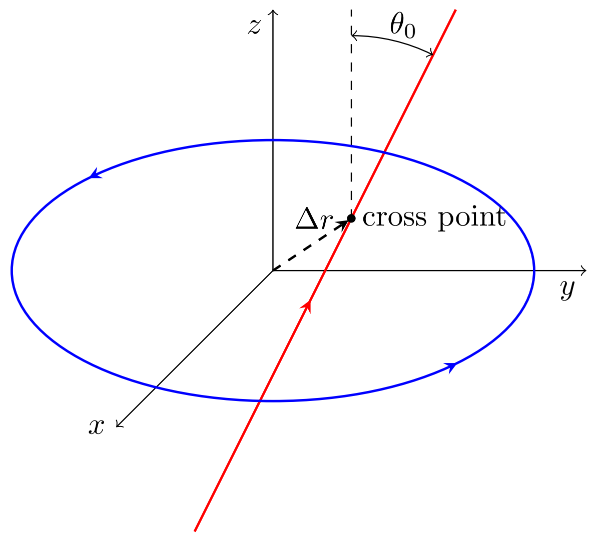

Figure 3.1 Illustration of the wire-loop-current-system (WLCS). The blue circle on the $x-y$ plane is the loop current with the origin point as its center. The red line is the wire current, which has an arbitrary inclination angle θ_0. Its cross point on the $x-y$ plane has a distance Δr to the origin.

wire passes through the center of the loop ($\Delta r = 0$) and is perpendicular to the plane of the loop ($\theta_0 = 0$), the system is symmetric, and the resulting magnetic field is non-chaotic. We plot in Figure 3.2 the Poincaré map of the magnetic field lines. A Poincaré map, named after Henri Poincaré, is often used in dynamical systems. For magnetic field lines, a Poincaré map is the intersection of field lines with a 2D surface ($y-z$ plane in Figure 3.2). For a symmetric WLCS, the Poincaré maps are closed loops. When the wire is tilted and/or shifted from the center of the loop, the system becomes asymmetric, and the resulting magnetic field becomes chaotic. Figure 3.2 (b) and (c) show that the Poincaré maps break into discrete points spreading over a broad space. The chaotic nature of the asymmetric current systems has been studied in various literatures (Li et al., 2009; Ram and Dasgupta, 2010; Hosoda et al., 2009; Aguirre and Peralta-Salas, 2007; Aguirre et al., 2010).

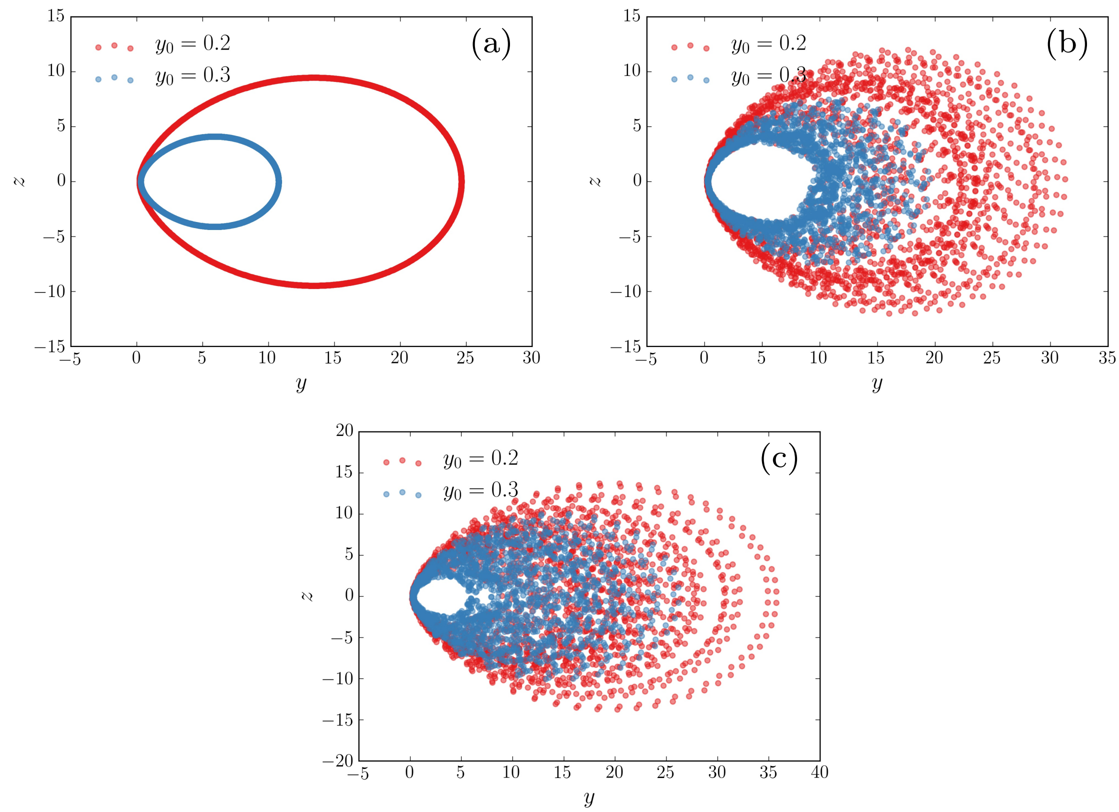

Figure 3.2 Poincaré map the magnetic field lines. The field lines all start from $x_0 = 0$, $z_0 = 0$, and $y_0 = 0.2$ or 0.3. (a) Symmetric system. (b) Asymmetric system with $\Delta y = 0.01$. $\theta_0 = 0$. (b) Asymmetric system with $\Delta y = 0$. $\theta_0 = 1°$.

The advantage of the WLCS is that it has analytic solutions for the magnetic and electric fields. See Section B.1 and Section B.2 for a derivation of these expressions. In a cylindrical coordinate system, the electromagnetic fields of an infinite straight wire along the z-direction with a time-varying current are

$$\frac{\boldsymbol{E}(\rho,t)}{\text{Gauss}} = -\hat{\boldsymbol{z}}\frac{1}{5}\frac{I/\text{Amp}}{\rho/\text{cm}}\frac{\pi x}{2}\left[Y_0(x)\sin(\omega t) + J_0(x)\cos(\omega t)\right] \tag{3.1}$$

$$\frac{\boldsymbol{B}(\rho,t)}{\text{Gauss}} = \hat{\phi}\frac{1}{5}\frac{I/\text{Amp}}{\rho/\text{cm}}\frac{\pi x}{2}\left[-Y_1(x)\cos\omega t + J_1(x)\sin\omega t\right] \tag{3.2}$$

where $\boldsymbol{E}$ and $\boldsymbol{B}$ are in Gaussian unit, ω is the current varying frequency, $x = \omega\rho/c$, $Y_0(x)$, $Y_1(x)$, $J_0(x)$ and $J_1(x)$ are Bessel functions. The expression uses current I in Ampere and ρ in cm. For static current ($\omega = 0$), $E_z = 0$ and $B_z = I/5\rho$. The fields are cylindrically symmetric with respect to the z-axis. The only nonzero components are B_ϕ and E_z. Figure 3.3 shows the spatial distribution and time evolution of B_ϕ and E_z. The fields vary along the ρ-direction and change with time. The amplitude of the field is proportional to the current I and time-varying frequency ω of the current. In a cylindrical coordinate system, the magnetic field of a loop current is

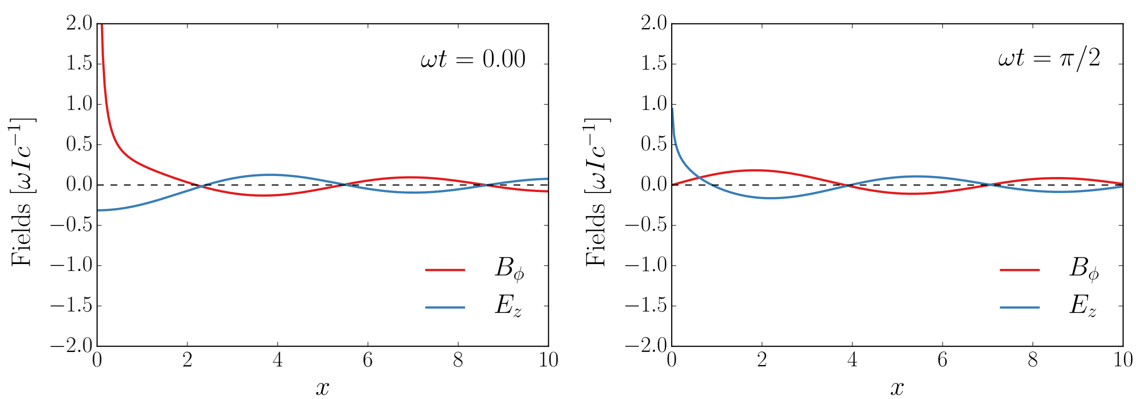

Figure 3.3 Electromagnetic fields of an infinite straight wire along the z-direction with a time-varying current at $\omega t = 0$ and $\pi/2$.

$$\frac{B_\rho}{\text{Gauss}} = \frac{1}{5}\frac{I/\text{Amp}}{c}\frac{\cos\theta}{\sin\theta}\frac{1}{\sqrt{a^2+r^2+2ar\sin\theta}}\left[-K(k)+\frac{a^2+r^2}{r^2+a^2-2ar\sin\theta}E(k)\right] \tag{3.3}$$

$$\frac{B_z}{\text{Gauss}} = \frac{1}{5}\frac{I/\text{Amp}}{c}\frac{1}{\sqrt{a^2+r^2+2ar\sin\theta}}\left[K(k)-\frac{r^2-a^2}{r^2+a^2-2ar\sin\theta}E(k)\right] \tag{3.4}$$

where $k^2 = 4ar\sin\theta/(a^2+r^2+2ar\sin\theta)$, $K(k)$ and $E(k)$ are the complete elliptical integral of the first kind and the second kind, $r = \sqrt{\rho^2+z^2}$ and $\theta = \arctan(z/\rho)$ are the spherical coordinates of the point. We can then use B_ρ to calculate $B_x = B_\rho\cos\phi$ and $B_y = B_\rho\sin\phi$. Figure 3.4 shows the contour plot of B_ρ and B_z. The field gets stronger close to the loop and the z-axis.

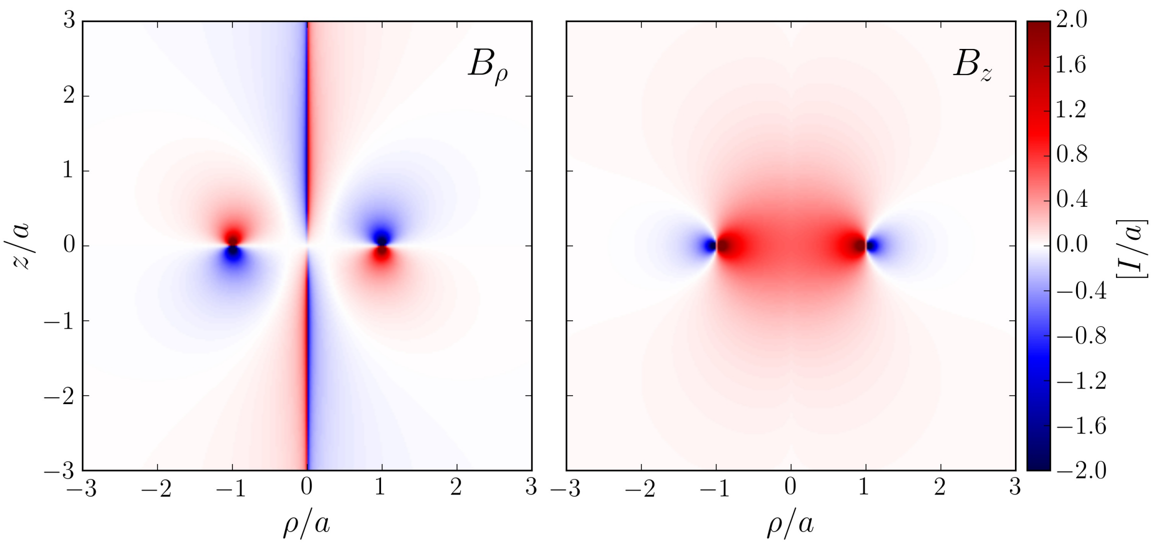

Figure 3.4 Magnetic field of a loop current in a cylindrical coordinate system. a is the radius of the loop in cm. I_0 is the normalized current in Ampere.

The electromagnetic field at one point depends on the current amplitude I, the time-varying frequency ω and the distance to the wire current and the loop current. We normalize the lengths with L_0 and the current with I_0. We set $L_0 = 0.01R_\odot \approx$ 6.96 Mm, based on the sizes of the solar active regions, which are typically $5-10^2$ Mm in diameter (van Driel-Gesztelyi and Green, 2015). We set $a = L_0$ to mimic the flare loops, which have lengths about the sizes of the solar active regions. We choose I_0 based on the measurements of electric current density in solar active regions. Spangler (2007) measured the electric currents in the solar corona using radio astronomical polarization measurements of a spatially extended radio source viewed through the solar corona. For two observed events, he found $I = 2.5 \times 10^9$ A and $I = 2.3 \times 10^8$ A in the solar corona. The current density can also be determined by calculating $\boldsymbol{J} = \nabla \times \boldsymbol{B}/\mu_0$ using extrapolated magnetic field based on the vector magnetic field measurements (Georgoulis et al., 2012; Sun et al., 2012). $\boldsymbol{J}$ on a cross section is $\sim 10 - 50$ mA m^{-2} in solar flare regions. In our model, $\pi a^2 J_z \approx 1.5 - 7.5 \times 10^{12}$ A, which is consistent with the results from Georgoulis et al. (2012) but much larger than that in Spangler (2007). This suggests that a large variation of electric currents exists in the solar corona and solar active regions. In our system, we consider the typical magnetic field $B \sim 0.2I/\rho < 50$ Gauss at $\rho = a/2$, so $I < 10^{11}$ Ampere. We will examine the particle energization in systems carrying different current $I = 10^8 - 10^{11}$ Ampere. We use the flare time scale $\sim 10^{2-3}$ s (Lin, 2011) as the time varying period of the current, noting that the currents rise with solar flares and peak during the impulsive phase of solar flares (Sun et al., 2012). So we set $\omega = 0.001 - 0.1$ Hz, corresponding to a period of $62.4 - 6240$ seconds.

3.1.2 An ensemble of WLCSs

A single WLCS is not enough to mimic the complexity of the current system in solar flare regions. Instead, we consider a system with 8 asymmetric WLCSs.

Figure 3.5 shows the configuration of 8 WLCSs, located at the eight corners of a box with length $2.5L_0$. The direction of the wire current and the normal direction of loop planes are arbitrary. Particles are initially injected randomly in the inner box. They are tracked until they reach the outer box with a side length $7.5L_0$.

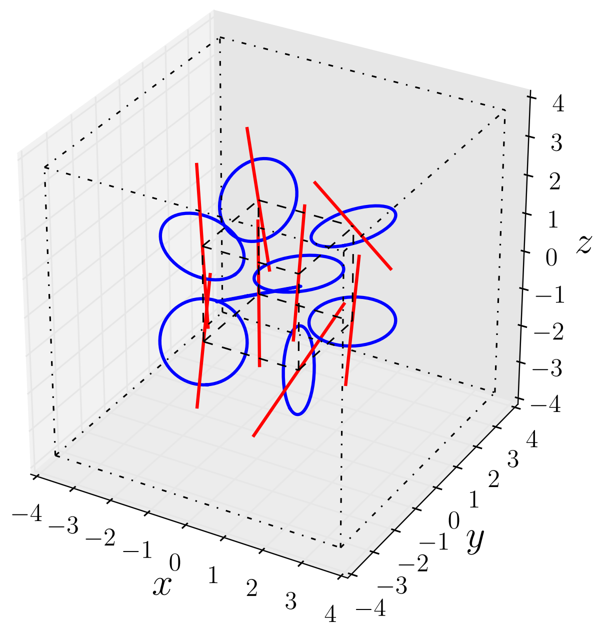

Figure 3.5 An ensemble of WLCSs, which are placed at the eight corners of the inner cube (black dashed line). The radius of the loops is L_0. The length of the inner box is $2.5L_0$. The orientation of the wire current and the normal directions of the loop current are arbitrary. The outer box (black dash-dotted line) is the simulation domain with side length $7.5L_0$.

3.2 Particle motion and transport in a time-independent field

To follow particle's motion, we numerically integrate the Lorentz equation.

$$\frac{d(\gamma\boldsymbol{\beta})}{dt} = \frac{Q}{A}\frac{e}{m_p c}(\boldsymbol{E} + \boldsymbol{\beta} \times \boldsymbol{B}) \tag{3.5}$$

where e is the electron charge; Q is the charge state, and A is the nucleon number; m_p is the proton mass; γ is the Lorentz factor; $\boldsymbol{\beta} = \boldsymbol{v}/c$. We employ three different tracking methods, including the 4^{th} order Runge-Kutta method (RK4), the Dormand-Prince method (Press, 2007) and the Wirz's Modified Boris method (WIRZ) (Mao and Wirz, 2011). The RK4 method is a general ordinary differential equation integrator. The Dormand-Prince method is a Runge-Kutta method with adaptive size control. It has higher order accuracy and runs faster than RK4 (Press, 2007). The WIRZ method is adapted from the Buneman-Boris particle tracker which is widely used in Particle-in-Cell (PIC) simulations (Birdsall and Langdon, 1991). It provides a better estimations of the magnetic field at each time step which is accomplished by using a corrected magnetic field values at the midpoint (Mao and Wirz, 2011). Comparisons between these three methods showed that the same particle trajectories are obtained in both the time-independent and time-dependent cases. This provides a consistency check to ensure, for example, that our numerical scheme does not introduce any artificial energy changes.

3.2.1 Particle trajectories

Figure 3.6 shows typical particle trajectories (proton here) for five systems, including a single wire current along the z-direction, a single loop current on the $x-y$ plane, a symmetric WLCS, an asymmetric WLCS with $\Delta r = 0.1a$ and a system with 8 WLCSs. For a single wire current, the particle gyrates around and streams along the magnetic field lines and also drifts along the z-direction due to the curvature and gradient of the magnetic field along the ρ-direction, yielding a helical trajectory.

For a loop current, the particle follows the field line and drifts along the ϕ direction at the same time, forming a drifting shell. The particle is essentially trapped on the drifting shell. For a symmetric WLCS, the particle is trapped on a torus. When the system becomes asymmetric, the particle can follow the chaotic magnetic field lines and access different regions, leading to a more complicated trajectory. But the particle cannot escape from the system due to the trapping by the magnetic field. Particles in a system with 8 WLCSs have more freedom because they can "jump" between different WLCSs. The trajectory will become chaotic as shown in Figure 3.6 (e).

3.2.2 Particle spatial diffusion coefficient

In many astrophysical problems, the motion of charged particles are assumed to be diffusive. For example, Parker's cosmic ray transport equation implicitly assumes that cosmic ray's motion in the solar system is diffusive (Parker, 1965). In a collisionless plasma such as the solar wind, this diffusion is due to the interaction between the charged particle and the irregular turbulent magnetic field δB of the solar wind (Jokipii, 1966, 1971). In the case of a slab turbulence (where the k vector of the turbulent field is along the B_0 direction), this interaction leads to a diffusion coefficient $\kappa_{\parallel}$ whose value is decided by the power density $\delta^2 B$ of the turbulent field. The corresponding motion of the charged particle is a diffusion along the background magnetic field. Charge particles can also diffuse in the direction perpendicular to the background field B_0. This is often described by $\kappa_{\perp}$.

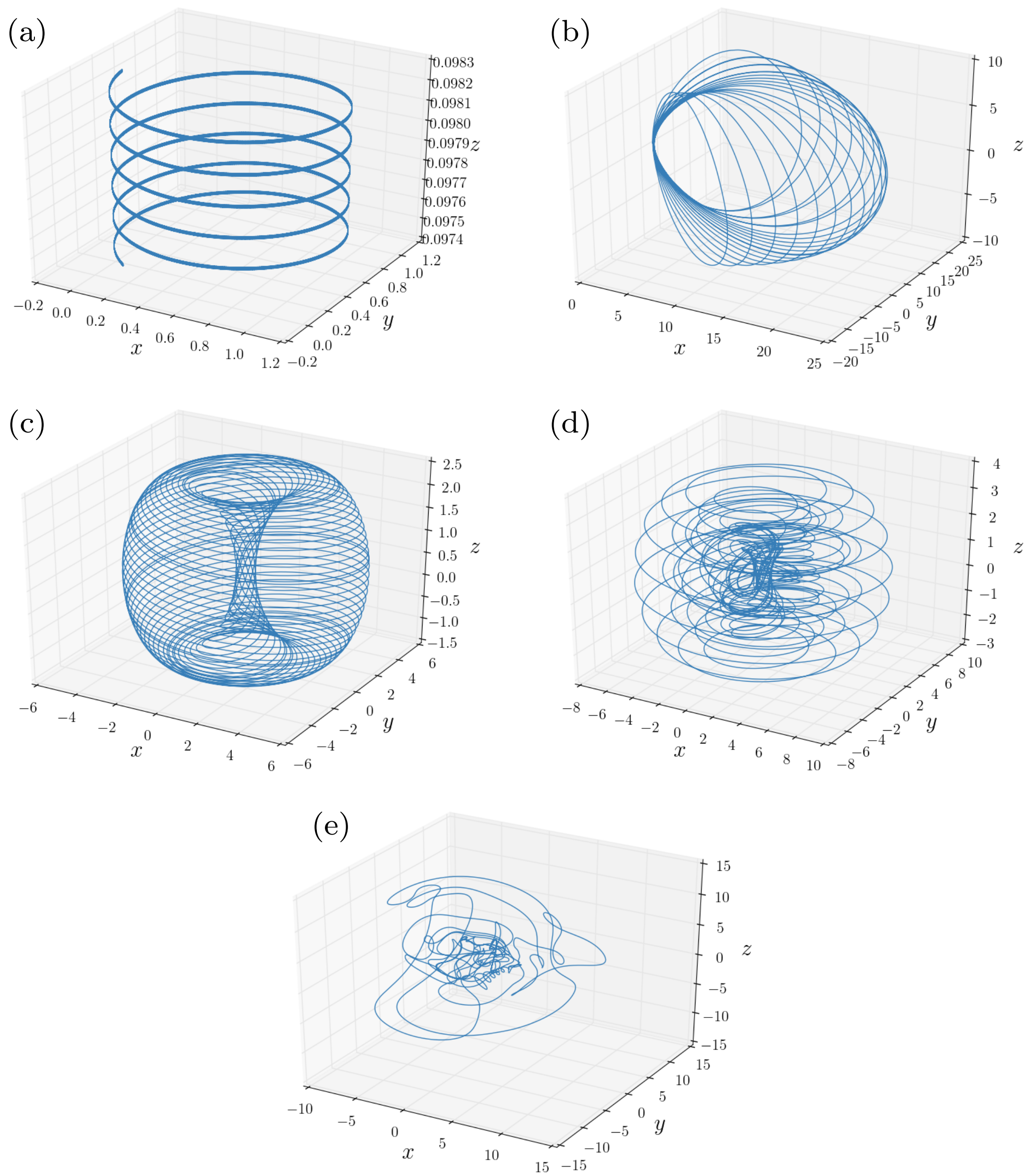

Figure 3.6 Particle trajectories in different system. (a) A single wire current along the z-direction. (b) A single loop current on the $x-y$ plane. (c) A symmetric WLCS. (d) An asymmetric WLCS with $\delta r = 0.1a$. (e) 8 WLCSs.

For a chaotic magnetic field, an ordered background field B_0 is hard to define. Furthermore there is no turbulent magnetic field δB. Therefore, we do not consider explicitly the parallel or the perpendicular diffusion. Instead, we calculate the running diffusion coefficient $D_{rr}(t)$ (Qin et al., 2002), which is defined as,

$$D_{rr}(t) = \frac{\langle (\boldsymbol{r} - \boldsymbol{r}_0)^2 \rangle}{2t} \tag{3.6}$$

where $\langle \cdots \rangle$ indicates ensemble average over all test particles; $\boldsymbol{r}$ is current position of a particle; $\boldsymbol{r}_0$ is particle's initial position; and t is the time differences between $\boldsymbol{r}$ and $\boldsymbol{r}_0$. Figure 3.7 shows D_{rr} for particles in a single WLCS and the system with 8 WLCSs.

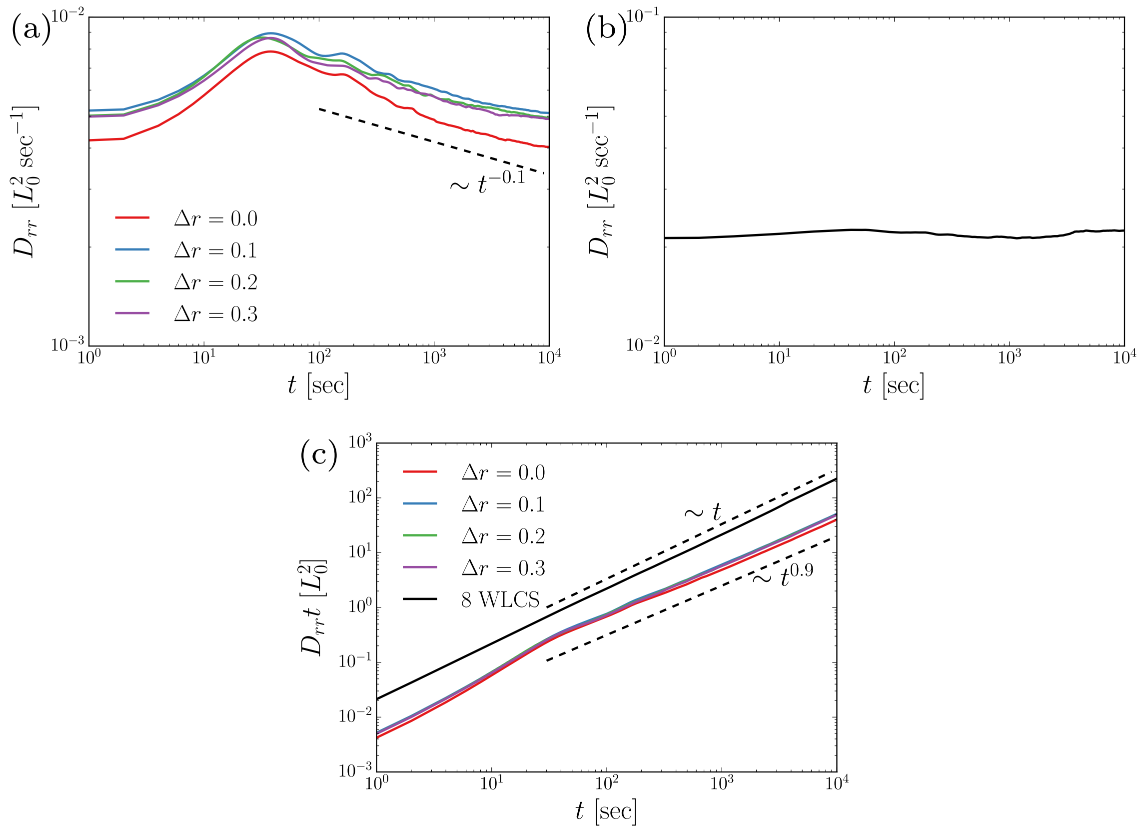

Figure 3.7 Particle running diffusion coefficient $D_{rr}(t)$ for (a) a single WLCS with different Δr and (b) 8 WLCSs. (c) $D_{rr}t$ for the same configurations.

Particles with the same energy 8.6 keV ($T = 100$ MK) are randomly injected in a box with a side length $2.5L_0$. The loop current of the single WLCS is at the center of the box, and the wire current has displacement Δr to the loop center. As seen in Figure 3.6, particles can access larger regions in an asymmetric WLCS ($\Delta r \neq 0$) due to chaotic magnetic field lines, so that D_{rr} is larger in an asymmetric WLCS than that in a symmetric WLCS, as shown in Figure 3.7 (a). The D_{rr}s have an initial increase with t when the particles are still in their first cycling around the system (motion along the ϕ-direction as shown in Figure 3.6 (d)). D_{rr} is similar for different asymmetric system. The trajectories in Figure 3.6 show that particles are trapped in the loop, so we expect D_{rr} to gradually decrease at long times. For the asymmetric WLCS, we find $D_{rr} \sim t^{-0.1}$, resembling a sub-diffusion process. In contrast, D_{rr} is near-constant for particles in a system with 8 WLCSs, resembling a diffusion process. D_{rr} is larger in this system than a single WLCS because particles can "jump" between different WLCS and therefore access a larger region. It is conceivable that this D_{rr} may eventually decrease since the region the particles can access is likely decided by the region in which the B field occupies. While the B field is more chaotic in 8 WLCSs, therefore the region it occupies can be considerable larger than the single WLCS, it may still be "confined". We also plot $D_{rr}t$ in Figure 3.7 (c) which shows clear difference of D_{rr} for these systems.

3.3 Particle energization in a time-dependent field

We implement a series of simulations to track protons and electrons in a time-dependent magnetic field when $\omega \neq 0$. We track 10^6 protons in each simulation but only 2.5×10^4 electrons due to the time limitation for electron tracking. The time step Δt depends on the particle gyro-period $\tau = 2\pi mc/qB$, which depends on m and B. So Δt for electrons is $m_p/m_e = 1836$ times smaller than that for protons. Electrons escape from the simulation domain faster than protons with the same thermal energy, as the thermal speed $v_{\rm th} \sim 1/\sqrt{m}$. So we set the total tracking time $t_{\rm max}$ for electrons 40 times smaller than that for protons. The initial particle distribution resembles a Maxwellian distribution with $T = 10^6$ K, a typical plasma temperature in quiet solar corona.

Figure 3.8 shows the time evolution of the proton energy spectra for systems with different I_0. We set $t_{\rm max} \sim 1/I_0$, then $t_{\rm max}/\tau$ is about the same for all simulations, as $\tau \sim B \sim I_0$. Protons are highly efficiently accelerated and develop power-law distribution $f(E) \sim E^{-p}$ at the end of the simulation. $p \sim 0.8$ when $I_0 = 10^8$ A and gets smaller when I_0 increases, suggesting that the spectrum gets harder when the electric field gets stronger. Figure 3.8 also shows the fraction $F_{\rm in}$ of particles remaining in the simulation box at the end of the simulation. $F_{\rm in} = 54.9\%$ when $I_0 = 10^8$ A and increases to 99.8% when $I_0 = 10^{11}$ A, suggesting stronger particle trapping when B is stronger. The spectra of escaped particles (black solid line) are even flatter than the spectra inside the simulation box, because most of the escaped particles are high energy particles that cannot be trapped by the magnetic field.

Figure 3.9 shows electron energy spectra for simulations with different I_0. Note that the statistics is poor because we only tracked 2.5×10^4 electrons for each simulation. But the spectra are similar to the proton energy spectra. $F_{\rm in}$ is smaller than that of protons, because electrons can get out the system faster as they have

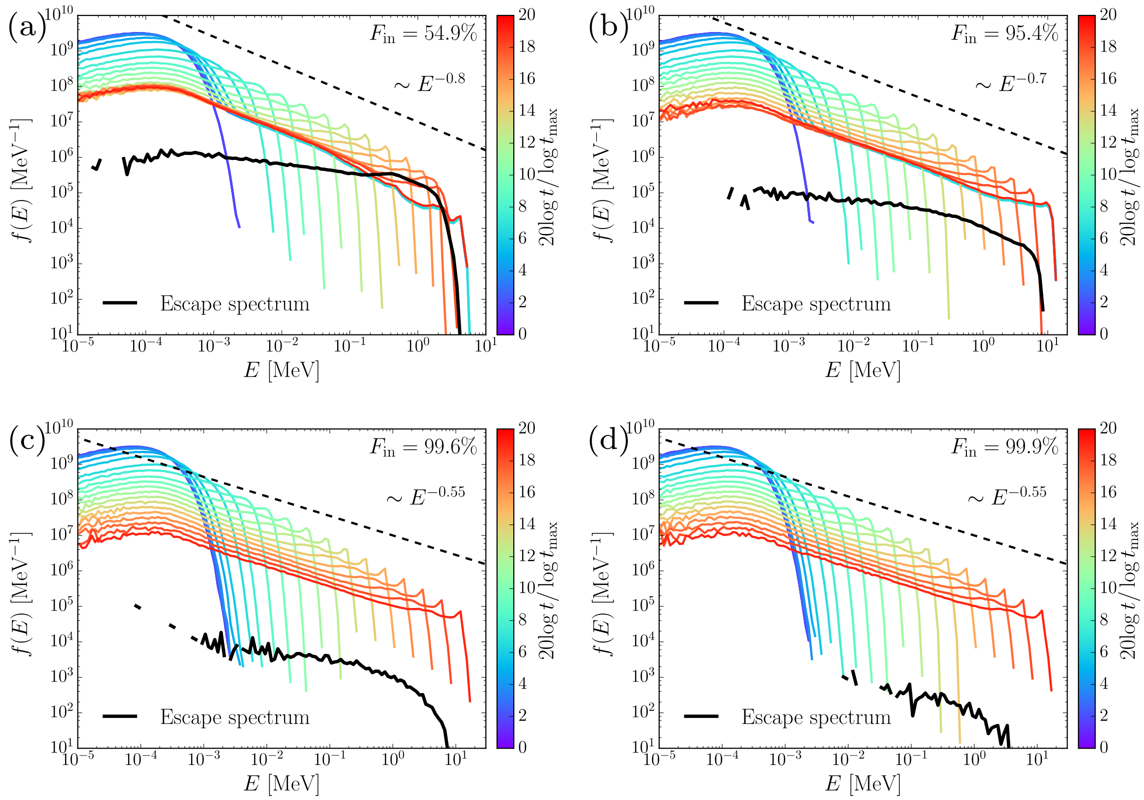

Figure 3.8 Time evolution of proton energy spectra for system with $\omega = 0.001$ Hz for all runs. (a) $I_0 = 10^8$ A and $t_{\rm max} = 4$ sec, (b) $I_0 = 10^9$ A and $t_{\rm max} = 0.4$ sec, (c) $I_0 = 10^{10}$ A and $t_{\rm max} = 0.04$ sec, (d) $I_0 = 10^{11}$ A and $t_{\rm max} = 0.004$ sec. The black thick solid line is the accumulated spectrum for escaped particles. The black dashed line the fitted power-law spectrum. The fraction of particles remaining in the simulations $F_{\rm in}$ is shown in top right corner of each plot.

larger speeds. The maximum energy is $\sim 2-3$ MeV, which is smaller than that of protons. Note that $t_{\rm max}$ is 40 times smaller than that for protons in a system with the same I_0, so the maximum electron energy may be comparable with the maximum energy of protons if the simulation time is the same.

Figure 3.10 shows the proton energy spectra for higher ω. Comparing with Figure 3.8 (a), the energy spectra are harder when ω is larger and the resulting electric field is stronger. This is consistent with previous results that the spectra are harder

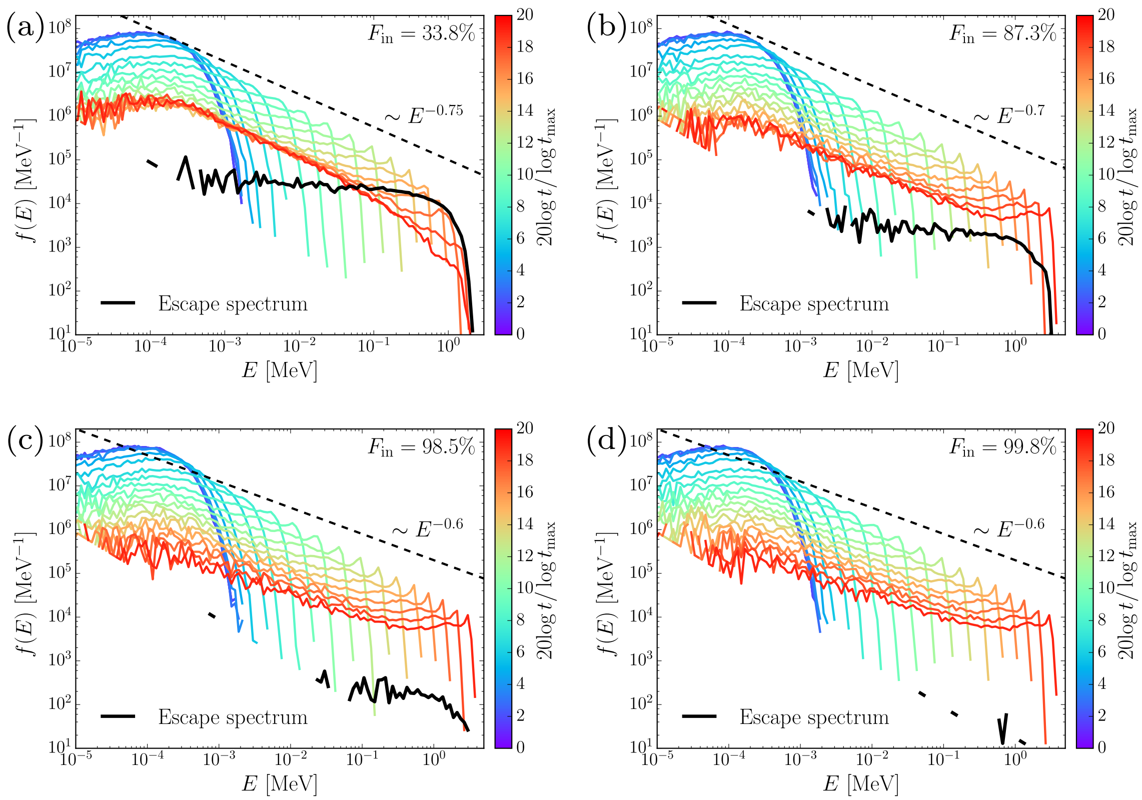

Figure 3.9 Time evolution of electron energy spectra for system with $\omega = 0.001$ Hz for all runs. (a) $I_0 = 10^8$ A and $t_{\max} = 0.1$ sec, (b) $I_0 = 10^9$ A and $t_{\max} = 0.01$ sec, (c) $I_0 = 10^{10}$ A and $t_{\max} = 10^{-3}$ sec, (d) $I_0 = 10^{11}$ A and $t_{\max} = 10^{-4}$ sec. The black thick solid line is the accumulated spectrum for escaped particles. The black dashed line the fitted power-law spectrum. The fraction of particles remaining in the simulations $F_{\rm in}$ is shown in top right corner of each plot.

when the electric field gets stronger with current I. The spectrum for the case with $\omega = 0.1$ Hz has a flat low-energy part and a break at $E \sim 100$ keV.

3.4 Discussion and conclusion

In this work, motivated by the observation of time-dependent electric currents in the solar corona and solar flare regions, we investigate charged particle transport and energization in a wire-loop-current-system (WLCS). We find the energy spectra are harder than E^{-1}. Such a hard spectrum is possible for particles that are acceler-

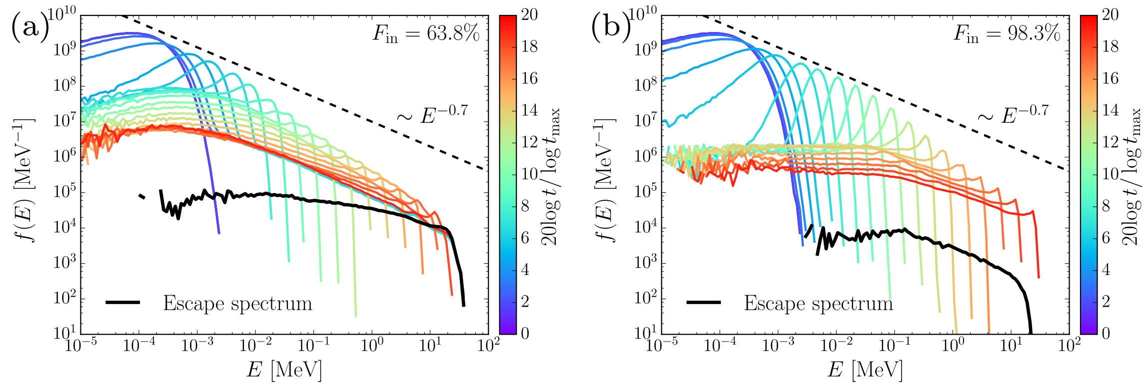

Figure 3.10 Proton energy spectrum for different ω. $I_0 = 10^8$ A for all runs. (a) $\omega = 0.01$ Hz and $t_{\rm max} = 0.4$ sec, (b) $\omega = 0.1$ Hz and $t_{\rm max} = 0.04$ sec, The black thick solid line is the accumulated spectrum for escaped particles. The black dashed line the fitted power-law spectrum. The fraction of particles remaining in the simulations $F_{\rm in}$ is shown in top right corner of each plot.

ated via the second order Fermi mechanism. In our case, the time-dependent current induces a time-dependent electric field. As particles move, they sample electric fields with different phases, therefore their acceleration is by nature of 2nd order Fermi. Similar hard spectra have been obtained by Dauphin et al. (2007). In their work, the authors examined the acceleration and radiation of electrons and ions interacting with multiple small-scale dissipation regions. These small scale energy release regions can be, for example, magnetic reconnection sites where reconnecting current sheets (RCSs) exist. At these current sheets particles are subject to be accelerated by direct electric field. In modeling an ensemble of such multiple energy release regions, Dauphin et al. (2007) used a cellular automaton (CA) model based on the concept of self-organized criticality. They showed that the spectra of accelerated ions and electrons are power-law-like. For certain values of the electric field, they obtained spectra that are considerably harder than E^{-1} for both electrons and protons. Comparing to the model of Dauphin et al. (2007), in our model, the electric field is not restricted to the current sheets. As the number of energy release sites increases, one expects that the model examined in Dauphin et al. (2007) and ours should have many similarities.

In calculating the spectra, we do not follow particles that reach the simulation box and assume that these particles will leave the system. In the case of the solar corona, if particles reach certain height, they likely encounter open interplanetary magnetic field lines and can propagate out and be observed in-situ. If a CME accompanies the flare, then the CME and the shock it drives can plow through these energetic particles. This makes our proposed mechanism interesting in that it may provide the pre-acceleration mechanism to generate the seed particles for a possible subsequent diffusive shock acceleration at a CME-driven shock (e.g. Desai et al., 2003). Our model shows that the energy spectrum gets harder with stronger electric current, which are most likely exist in solar flare regions (Sun et al., 2012; Georgoulis et al., 2012). If a correlation exists between the pre-event current and the flare size, then our mechanism would predict that there will be more energetic seed particles in large flares.

We emphasize that our system is by no means representative of the realistic solar magnetic fields. Instead, it provides a simple and tractable system from which we can learn some fundamental behaviors of the particles in a time-dependent chaotic magnetic field, which, we believe will shed lights on our understanding of particle acceleration in the solar corona.

To summarize, we investigate charged particle behavior in a chaotic magnetic field, which is generated from one or multiple asymmetric wire-loop-current-systems (WLCSs). We find that particle transport in one WLCS is a sub-diffusion process due to the trapping by the magnetic field. In contrast, particle transport in 8 WLCSs is a diffusion process as particles are not trapped by one WLCS but jump between different WLCSs. When including time-dependent electric current, both electrons and protons are accelerated to develop power-law energy distribution with power-law index < 1, which is consistent with the model of particle acceleration by multiple reconnection current sheet (Dauphin et al., 2007). The spectra get harder with stronger or faster varying electric current. The maximum energy reaches to $1 - 10$ MeV for both electrons and protons, which can provide a seed population for the CME-driven shock acceleration.

CHAPTER 4

NONTHERMAL ELECTRON ACCELERATION DURING MAGNETIC RECONNECTION IN A LOW-BETA PLASMA

4.1 Introduction

Particle acceleration associated with reconnection has been studied in reconnection driven turbulence (Miller et al., 1996; Liu et al., 2013a), at shocks in the outflow region (Tsuneta and Naito, 1998; Guo and Giacalone, 2012), and in the reconnection layer (Drake et al., 2006; Fu et al., 2006; Oka et al., 2010; Kowal et al., 2012; Guo et al., 2014; Zank et al., 2014; le Roux et al., 2015). Two-dimensional kinetic simulations have identified different acceleration regions in reconnection. Electrons get accelerated by parallel electric field when they enter the reconnection region along the reconnection separatrix (Drake et al., 2005; Egedal et al., 2012, 2015). They are then accelerated by the reconnection electric field in the X-type region close to the reconnection point (Hoshino et al., 2001; Fu et al., 2006; Pritchett, 2006; Oka et al., 2010). When these electrons get convected out with the reconnection outflow, they are further accelerated by the reconnection electric field through particle curvature drift and gradient drifts (Hoshino et al., 2001; Fu et al., 2006; Pritchett, 2006; Oka et al., 2010). Drake et al. (2006) proposed a mechanism by which particles gain energy when they reflect from the ends of contracting magnetic islands. Since recent numerical simulations (Shibata and Tanuma, 2001; Drake et al., 2006; Loureiro et al., 2007; Bhattacharjee et al., 2009; Daughton et al., 2009b) and observations (Sheeley et al., 2004; Savage et al., 2012) suggest that reconnection in solar flares involves many flux ropes, this mechanism could be efficient at accelerating a large number of electrons. Further simulations have shown that the magnetic island merging regions are also efficient at accelerating electrons by anti-reconnection electric field (Oka et al., 2010; Le et al., 2012; Drake et al., 2013). An important problem is to identify the main acceleration region and primary acceleration mechanism. Through tracking energetic electron trajectories, several works have suggested that the most energetic electrons are accelerated in the magnetic island merging region (Oka et al., 2010; Nalewajko et al., 2015). To identify the major acceleration regions for solar corona and accretion disk corona, simulations with more realistic conditions (nonrelativistic proton-electron plasma with $\beta \ll 1$) are necessary.

Most simulations focus on regimes with plasma $\beta \geq 0.1$, with no obvious power-law distributions emerged. Simulations of relativistic reconnection in a low-density pair plasma have shown the development of a power-law distribution in the X-region (Zenitani and Hoshino, 2001). It was argued that particle loss from the simulation domain is important for developing a power-law distribution (Drake et al., 2010). Recent kinetic simulations with a highly magnetized ($\sigma \equiv B^2/4\pi n_e m_e c^2 \gg 1$) relativistic pair plasma showed that a power-law distribution develops without particle loss, although loss mechanism may be important in determining the spectral index (Guo et al., 2014, 2015). It is unknown whether this is still valid for reconnection in a nonrelativistic proton-electron plasma, since the property of relativistic reconnection can be significantly different from the nonrelativistic case (Liu et al., 2015).

In this chapter, motivated by the results of relativistic reconnection, we consider fully kinetic simulations of magnetic reconnection in a nonrelativistic proton-electron plasma with a range of electron and ion betas: $\beta_e = \beta_i = 0.007 - 0.2$. The low-$\beta$ regime is relatively unexplored previously due to various numerical challenges. For example, the numerical heating can be larger than the kinetic energy when $\beta < 0.01$, since the initial kinetic energy is $< 1.5\%$ of the total energy. We find that reconnection in the low-β regime can drive efficient energy conversion and accelerate electrons into a power-law distribution $f(E) \sim E^{-1}$. By the end of the simulations, more than half of electrons in number and 90% in energy are in the nonthermal population of electrons in the system. This strong energy conversion and particle acceleration lead to a post-reconnection region where the kinetic energy of energetic particles is comparable to the magnetic energy. Since most electrons are magnetized in low-β plasma, we use a guiding-center drift description to demonstrate that the main acceleration process is a *Fermi*-type mechanism through the particle curvature drift motion along the electric field induced by fast plasma flows. The development of a power-law distribution is consistent with the analytical model (Guo et al., 2014). The nonthermally dominated energization process may help explain the efficient electron acceleration in the low-β plasma environments, such as solar flares and other astrophysical reconnection sites.

In Section 4.2, we describe the numerical simulations. In Section 4.3, we present results of the simulations and describe the conditions for the development of a power-law energy distribution. We discuss our results and conclude in Section 4.4.

4.2 Numerical simulations

The kinetic simulations are carried out using the VPIC code (Bowers et al., 2008), which solves the Maxwell's equations and follows particles in a fully relativistic manner. Appendix E contains an introduction of the PIC method and detailed steps to implement a 2D PIC code. We use 2D simulations because it is computationally tractable, while the 3D simulations with similar system size requires $\sim 10^3$ times more computational resources. And the results from 3D simulations with pair plasmas have shown no obvious difference in particle energization between 2D and 3D simulations (Guo et al., 2014; Sironi and Spitkovsky, 2014). Therefore, 2D simulations are still very useful in studying particle energization processes during reconnection.

In our simulations, the initial condition is a force-free current sheet with magnetic field

$$\boldsymbol{B} = B_0 \tanh(z/\lambda)\hat{x} + B_0 \,\mathrm{sech}(z/\lambda)\hat{y} \tag{4.1}$$

where $\lambda = d_i$ is the half thickness of the layer. Here, d_i is the ion inertial length. The magnetic field rotates 180° across this current sheet. Figure 4.1 shows the profile of B_x and B_y along the z-direction. The plasma consists of protons and electrons with a mass ratio $m_i/m_e = 25$, yielding a spatial scale separation $d_i/d_e = 5$. Although 25 is much smaller than the proton-electron mass ratio 1836, it has been argued that

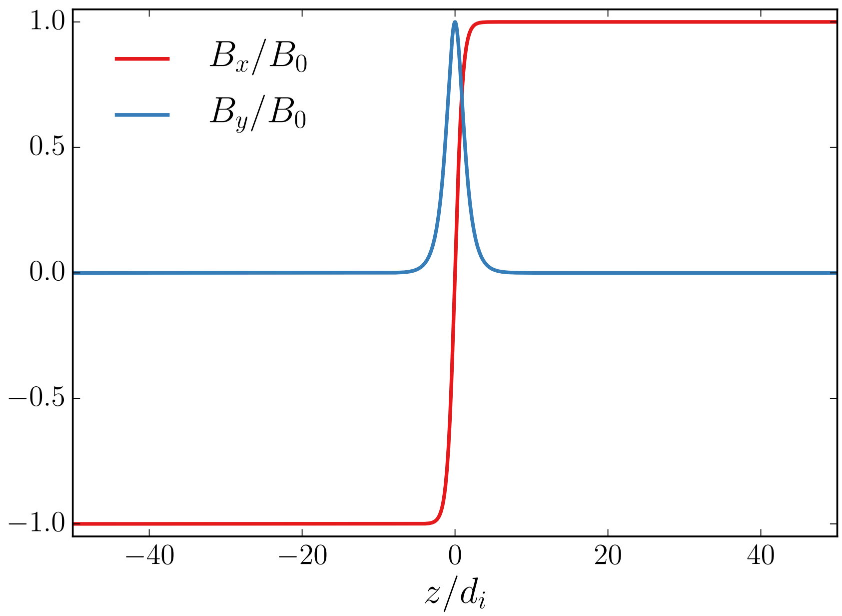

Figure 4.1 Magnetic field profile of a force-free current sheet. $\lambda = d_i$ in this plot. B_x and B_y are normalized by B_0.

the reconnection rate and the structure of the reconnection outflow does not depends on this ratio (Shay and Drake, 1998; Shay et al., 2007; Hesse et al., 1999). This artificial mass ratio makes the simulation tractable since the computational time scales as $\sim (m_i/m_e)^2$ for 2D simulations ($\sim (m_i/m_e)^{5/2}$ for 3D simulations). The initial distributions for both electrons and protons are Maxwellian with uniform density n_0 and temperature $kT_i = kT_e = 0.01 m_e c^2$. A drift velocity for electrons U_e is added to represent the current density that satisfies the Ampere's law initially. The initial electron and ion $\beta_e = \beta_i = 8\pi n_0 kT_e/B_0^2$ are varied by changing ω_{pe}/Ω_{ce}, where $\omega_{pe} = \sqrt{4\pi n_0 e^2/m_e}$ is the electron plasma frequency and $\Omega_{ce} = eB_0/(m_e c)$ is the electron gyrofrequency. Values of $\beta_e = 0.007$, 0.02, 0.06 and 0.2 correspond to $\omega_{pe}/\Omega_{ce} = 0.6$, 1, $\sqrt{3}$ and $\sqrt{10}$, respectively. The domain sizes are $L_x \times L_z = 200 d_i \times 100 d_i$. We use $N_x \times N_z = 4096 \times 2048$ cells with 200 particles per species per cell. The grid size is about the Debye length $\lambda_D = \sqrt{kT_e/4\pi n_0 e^2}$ to reduce numerical heating. The boundary conditions are periodic along the x direction, perfectly conducting boundaries for fields and reflecting boundaries for particles along the z direction. No escape of particles are considered in our simulations. A modified long wavelength perturbation is added to induce the reconnection (Birn et al., 2001).

$$\psi = \psi_0 \cos\left[2\pi\left(\frac{x}{L_x} - \frac{1}{2}\right)\right]\cos\left(\frac{\pi z}{L_z}\right); \tag{4.2}$$

$$\delta\boldsymbol{B} = \hat{\boldsymbol{y}} \times \nabla\psi, \tag{4.3}$$

where $\psi_0 = 0.03 B_0 L_z/2\pi$. Each simulation uses $\sim 2\times10^4$ CPU core hours and dumps $\sim$ 500 GiB of fields data, including the electromagnetic fields, the current densities, the charge densities, the momentum densities and the stress tensor. The fluid velocities for each species are obtained using their current densities. The four-velocities are calculated using the momentum densities. The pressure tensor are calculated using the stress tensor. Besides the fields data, about 2 TiB of particle data is dumped for the diagnostics of particle energy spectra and phase space distribution. As mentioned previously, the simulation time scales as $(m_i/m_e)^2$ for 2D simulations. The size of the dumped data scales as m_i/m_e[1].

[1]3D simulations are more expensive because the computational time will be $\sim 10^3$ more than that of the 2D simulations and the data size is $\sim 10^3$ times of the 2D simulations. Additionally, the computational time scales as $(m_i/m_e)^{5/2}$ and the data size scales as $(m_i/m_e)^{3/2}$ in 3D simulations, which grows faster with m_i/m_e than 2D simulations.

4.3 Simulation results

4.3.1 General energy evolution

Under the influence of the initial perturbation, the current sheet quickly thins down to a thickness of $\sim d_e$ (electron inertial length c/ω_{pe}). Figure 4.2 shows j_y at $t = 0$ and $t\Omega_{ci} = 40$. Note that the magnetic field lines in Figure 4.2 (a) are not exactly antiparallel to each other across the current sheet due to the initial perturbation. The instability starts growing at $t\Omega_{ci} = 40$. The current sheet is thinner than the initial current sheet seen from Figure 4.2 (c). The thin current sheet is unstable to the plasmoid instability (Daughton et al., 2009b; Liu et al., 2013b). Figure 4.3(a) and (b) show the evolution of the out-of-plane current density j_y at two latter times. The reconnection layer breaks and generates a chain of magnetic islands that interact and coalesce with each other. The largest island eventually grow comparable to the system size and the reconnection saturates at $t\Omega_{ci} \sim 800$.

Figure 4.4(a) shows time evolution of the magnetic energy (integrated over the system) in the x direction (the reconnecting component) ε_{bx}, the kinetic energy of electrons K_e and ions K_i for the case with $\beta_e = 0.02$, respectively. Throughout the simulation (until $t\Omega_{ci} = 800$), 40% of the initial ε_{bx} is converted into plasma kinetic energy, and 10% of ε_{bx} is transferred into ε_{by} and ε_{bz}. Of the converted energy, 38% goes into electrons and 62% goes into ions. We have carried out simulations with larger domains (not shown) to confirm that the energy conversion is still efficient and it only depends on system size weakly. Since the free magnetic energy overwhelms the initial plasma kinetic energy, particles in the reconnection region are strongly

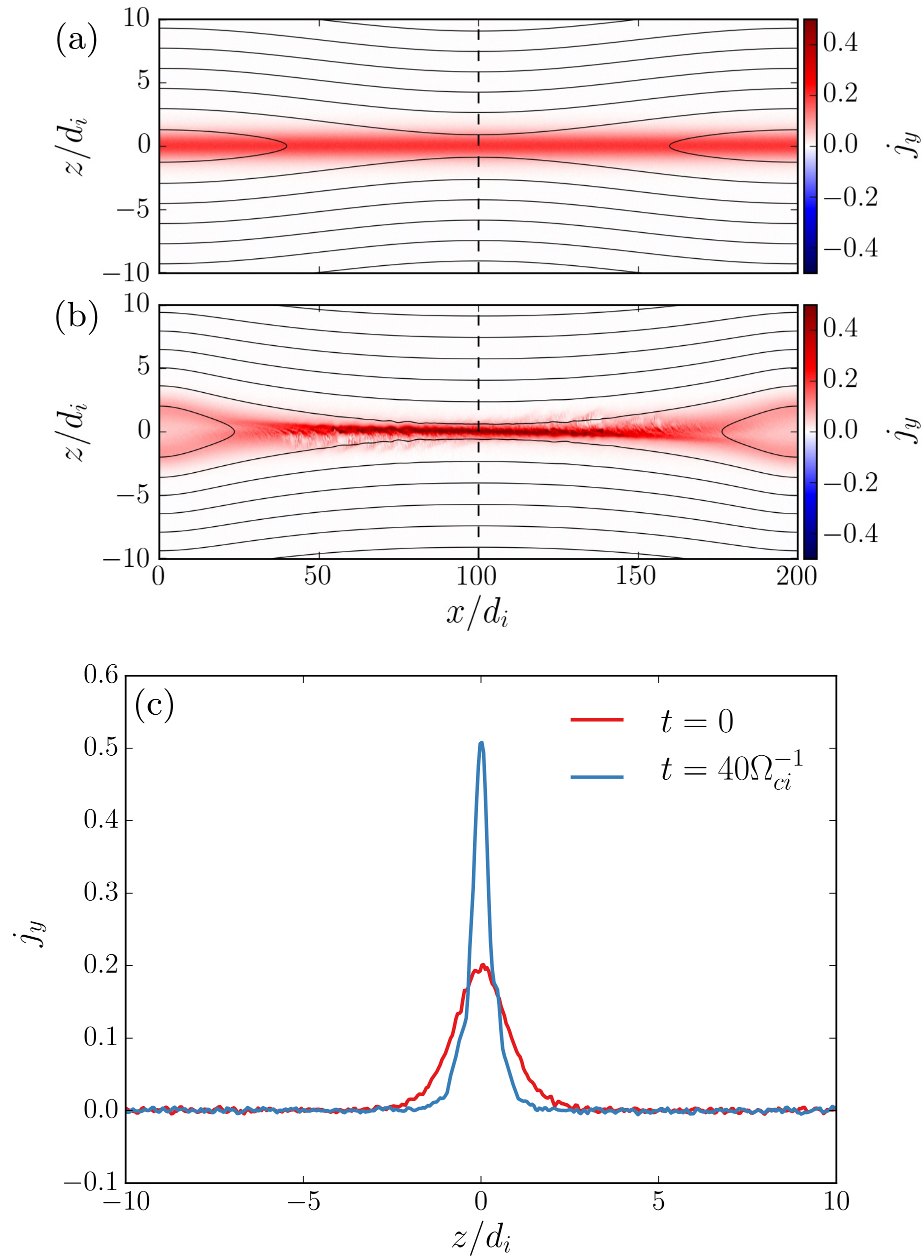

Figure 4.2 Out-of-plane current density for the case with $\beta_e = 0.02$ at (a) $t\Omega_{ci} = 0$, (b) $t\Omega_{ci} = 40$. The dashed lines indicate a cut along the z-direction. (c) j_y along the cut.

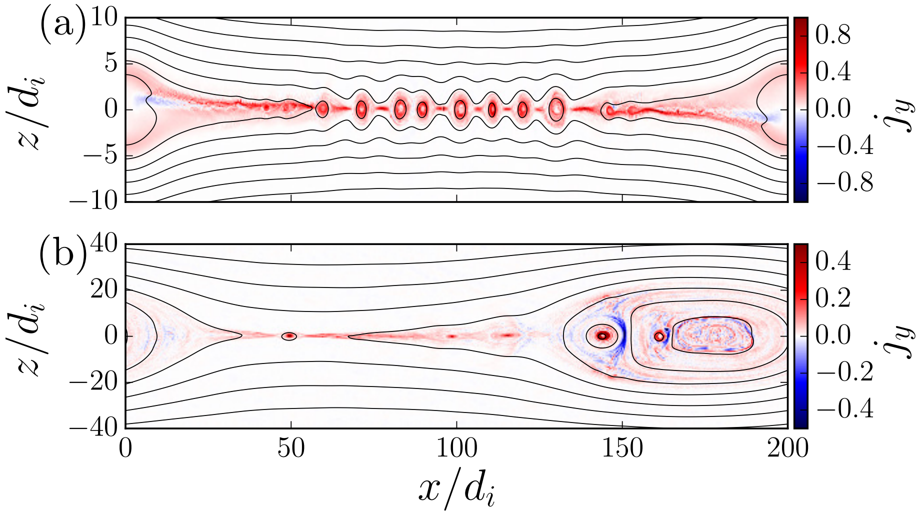

Figure 4.3 Out-of-plane current density j_y for the case with $\beta_e = 0.02$ at (a) $t\Omega_{ci} = 62.5$, (b) $t\Omega_{ci} = 400$.

energized. By the end of the simulation, K_e and K_i are 5.8 and 9.4 times of their initial values, respectively. Figure 4.4(b) shows the ratio of the energy gain ΔK_e of electrons to the initial electron energy $K_e(0)$ for different cases. While the $\beta_e = 0.2$ case shows only mild energization, cases with lower β_e give stronger energization as the free energy increases.

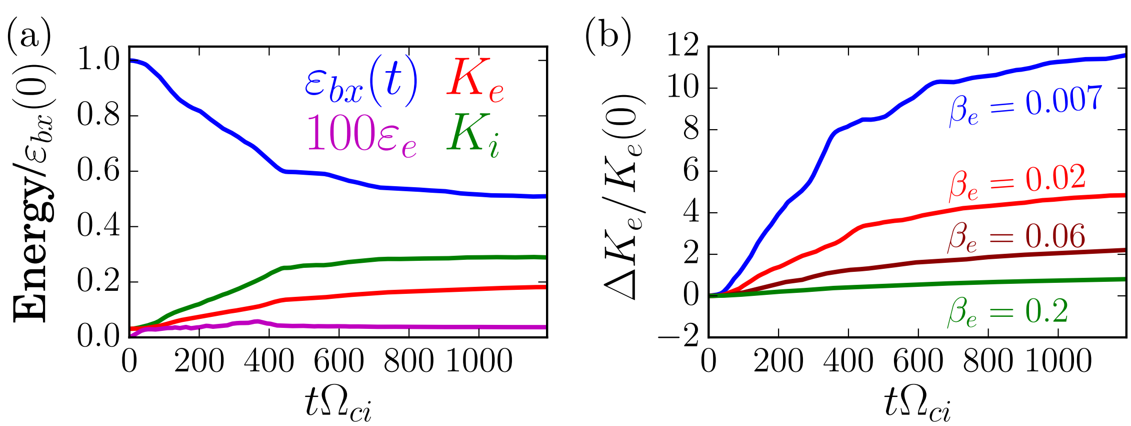

Figure 4.4 (a) The energy evolution for $\beta_e = 0.02$ case. $\varepsilon_{bx}(t)$ is the magnetic energy of the reconnecting component. ε_e is the electric energy. K_i and K_e are ion and electron kinetic energies respectively. They are normalized by $\varepsilon_{bx}(0)$. (b) The ratio of electron energy gain ΔK_e to the initial K_e for different initial β_e.

4.3.2 Particle energization

The energy conversion drives strong nonthermal electron acceleration. Figure 4.5(a) shows the final electron energy spectra over the whole simulation domain for the four cases. More electrons are accelerated to high energies for lower-β cases, consistent with the simulations in a low-density plasma (Bessho and Bhattacharjee, 2010). More interestingly, in the cases with $\beta_e = 0.02$ and 0.007, the energy spectra develop a power-law-like tail $f(E) \sim E^{-p}$ with the spectral index $p \sim 1$. This is similar to the results from kinetic simulations of relativistic magnetic reconnection (Guo et al., 2014, 2015). We have carried out one simulation with $m_i/m_e = 100$ and $\beta_e = 0.02$, and find similar electron spectrum. The results are presented in the next chapter. In contrast, the case with $\beta_e = 0.2$ does not show any obvious power-law tail, consistent with earlier simulations (Drake et al., 2010; Dahlin et al., 2014). The nonthermal population dominates the distribution function in the low-β cases. For example, at $t\Omega_{ci} = 1200$, when we subtract the thermal population by fitting the low-energy particle distribution as a Maxwellian distribution with thermal energy $\sim E_{th}$, the nonthermal tail in the $\beta_e = 0.02$ case contains 55% of electrons and 92% of the total electron energy. The power-law tail breaks at energy $E_b \sim 10E_{th}$ for $\beta_e = 0.02$, and extends to higher energy for $\beta_e = 0.007$. Figure 4.5(b) shows the fraction of nonthermal electrons n_{nth}/N_0 for different cases. It keeps increasing until reconnection saturates. For the lowest β_e in this study, the nonthermal fraction goes up to 66%, but it decreases to 17% for $\beta_e = 0.2$. Figure 4.5(c) and (d) show the ratio n_{acc}/n_e at $t\Omega_{ci} = 125$ and 400 for the case with $\beta_e = 0.02$, where n_{acc} is the number density of energetic electrons with energies larger than 3 times of their initial thermal energy, and n_e is the total electron number density. The fraction of energetic electrons is over 40% and up to 80% inside the magnetic islands and reconnection exhausts, indicating a bulk energization for most of electrons in the reconnection layer. Finally, Figure 4.5(d) shows the energetic electrons will eventually be trapped inside the largest magnetic island. No mechanism exists to split the magnetic island, so no "quench" of the nonthermal electrons. The nonthermally dominated distribution contains most of the converted magnetic energy, indicating that energy conversion and particle acceleration are intimately related.

4.3.3 Drift-current analysis of the energy conversion

To study the energy conversion process in detail, Figure 4.6(a) shows the energy conversion rate $d\varepsilon_c/dt$ from magnetic field to electrons through the parallel and perpendicular directions with respect to local magnetic fields. We define $d\varepsilon_c/dt = \int_{\mathcal{D}} \boldsymbol{j}' \cdot \boldsymbol{E} dV$, where $\mathcal{D}$ indicates the simulation domain, and $\boldsymbol{j}'$ is $\boldsymbol{j}_\parallel$ or $\boldsymbol{j}_\perp$ here. We find that the energy conversion from the perpendicular direction gives $\sim 90\%$ of the electron energy gain. By tracking the trajectories (shown in the next chapter) of a large number of accelerated electrons, we find that electrons can be accelerated in the diffusion region, contracting magnetic island, magnetic field pile-up region and by magnetic island coalescence. The acceleration mechanisms have been associated with particle drift motions along the motional electric field (Hoshino et al., 2001; Hoshino, 2005; Drake et al., 2006; Oka et al., 2010; Guo et al., 2014; Dahlin et al., 2014). To reveal the role of particle drift motions, we use a guiding-center drift description to

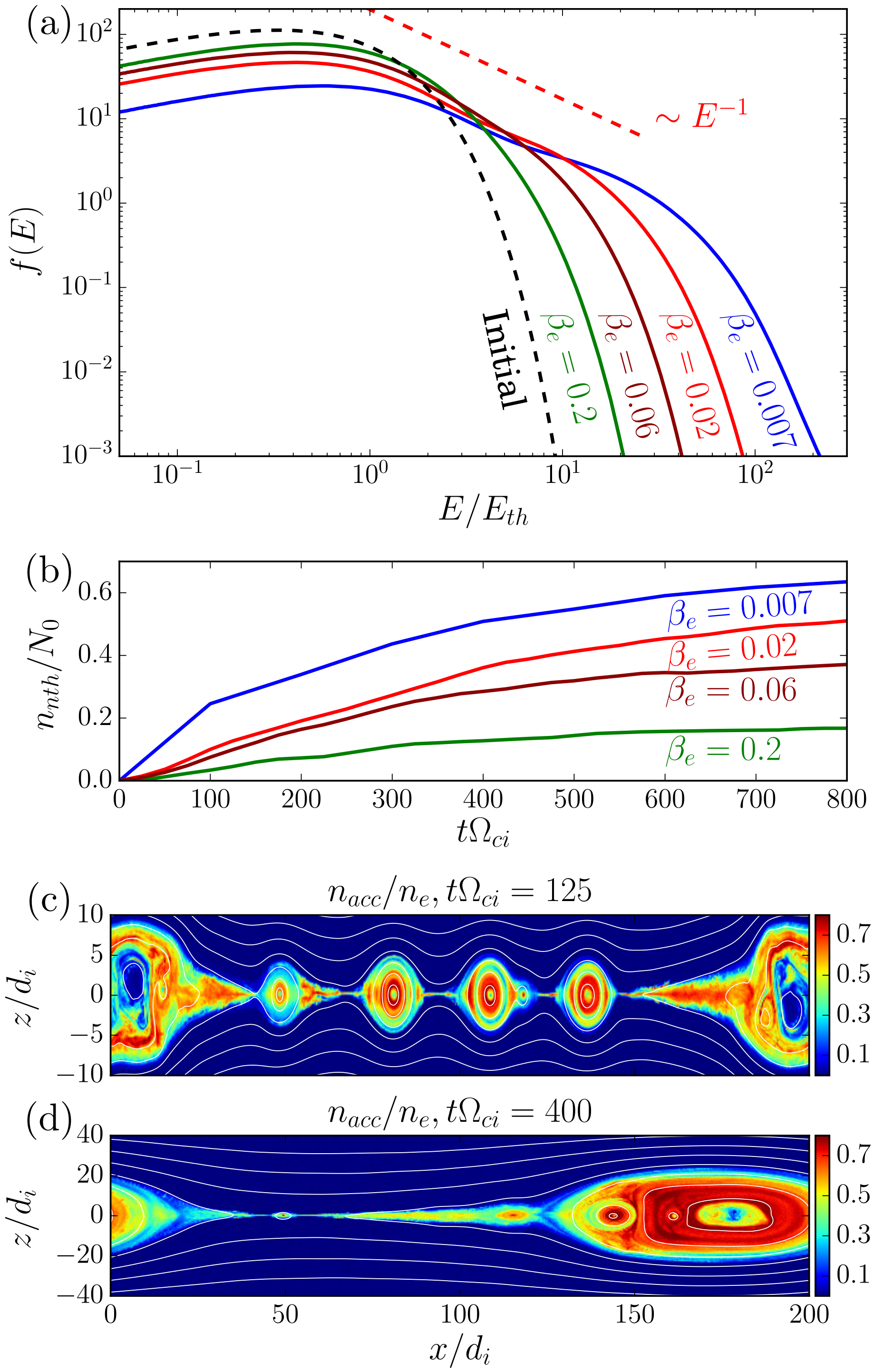

Figure 4.5 (a) Electron energy spectra $f(E)$ at $t\Omega_{ci} = 800$ for different β_e. The electron energy E is normalized to the initial thermal energy E_{th}. The black dashed line is the initial thermal distribution. (b) Time evolution of the fraction of nonthermal electrons for different initial β_e. n_{nth} is the number of nonthermal electrons, obtained by subtracting the fitted thermal population from whole particle distribution. The fraction of electrons with energies larger than 3 times of the initial thermal energy at (c) $t\Omega_{ci} = 125$, (d) $t\Omega_{ci} = 400$.

study in detail the electron energization process. Below we examine the $\beta_e = 0.02$ case as an example. The initial low β guarantees that guiding-center approximation is reasonable, since the typical electron gyroradius ρ_e is smaller than the spatial scale of the field variation ($\sim d_i$).

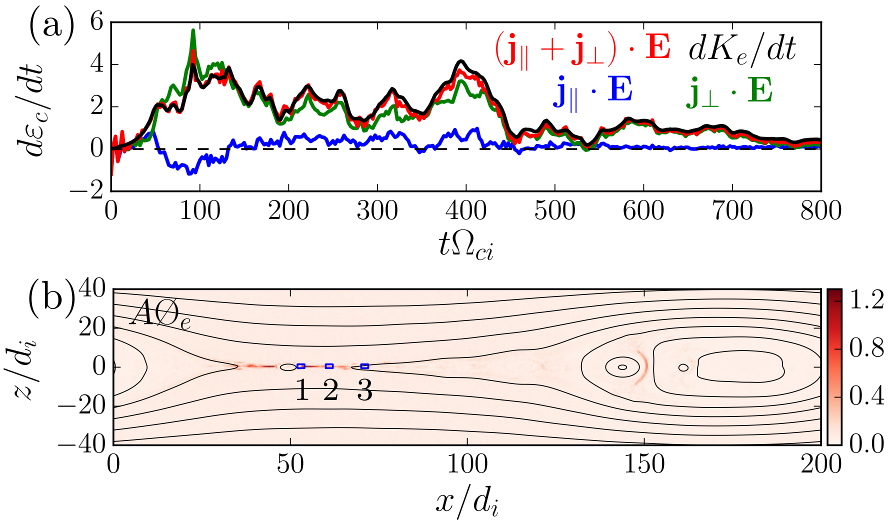

Figure 4.6 Verification of the guiding-center drift approximation for the case with $\beta_e = 0.02$. (a) Energy conversion rate $d\varepsilon_c/dt$ (integrated over the simulation domain)i for electrons in the parallel and perpendicular directions with respect to local magnetic fields, compared with the energy change rate of electrons dK_e/dt. They are normalized by $m_e c^2 \omega_{pe}$. (b) Electron pressure agyrotropy $A\O_e$ at $t\Omega_{ci} = 400$. See Equation 4.12 for the definition of $A\O_e$. The momentum space distributions in the three blue boxes ($x = 53$, 61 and $71 d_i$) are shown in Figure 4.7. Boxes 1 and 2 are close to the reconnection X-point. Box 3 is in the reconnection outflow.

The perpendicular current density can be obtained by ensemble averaging the particle gyromotion and drift motion (Parker, 1957a) or through the momentum equation of the two-fluid model (Blandford et al., 2014). We start from the momentum equation

$$n_s m_s \frac{d\boldsymbol{u}_s}{dt} = -\nabla \cdot \mathbf{P} + \rho \boldsymbol{E} + \boldsymbol{j}_s \times \boldsymbol{B} \tag{4.4}$$

where n_s is the particle number density, m_s is the particle mass, $\rho = n_s q_s$ is the charge density, $\boldsymbol{j}_s$ is the current density, P is the pressure tensor. We neglect the subscript s for simplicity. Taking cross product on both sides with $\boldsymbol{B}$

$$\boldsymbol{j}_\perp = -\frac{(\nabla \cdot \mathsf{P}) \times \boldsymbol{B}}{B^2} + \rho\frac{\boldsymbol{E} \times \boldsymbol{B}}{B^2} - nm\frac{d\boldsymbol{u}}{dt} \times \boldsymbol{B} \tag{4.5}$$

Assuming the pressure tensor is gyrotropic (particles are magnetized),

$$\mathsf{P} = p_\perp \mathsf{I} + (p_\parallel - p_\perp)\hat{\boldsymbol{b}}\hat{\boldsymbol{b}} \tag{4.6}$$

$$\nabla \cdot \mathsf{P} = \nabla p_\perp + \nabla \cdot \left(\frac{p_\parallel - p_\perp}{B^2}\boldsymbol{B}\right)\boldsymbol{B} + \frac{p_\parallel - p_\perp}{B^2}(\boldsymbol{B} \cdot \nabla)\boldsymbol{B} \tag{4.7}$$

where $p_\parallel$ and $p_\perp$ are parallel and perpendicular pressures with respect to the local magnetic field; I is the unit dyadic; $\hat{\boldsymbol{b}} = \boldsymbol{B}/B$ is the unit vector along the local magnetic field. We calculate $p_\parallel$ and $p_\perp$ using the particle distribution f in each cell. $p_\parallel \equiv m\int(v_\parallel - u_\parallel)^2 f d\boldsymbol{v}$ and $p_\perp \equiv 0.5m\int(v_\perp - u_\perp)^2 f d\boldsymbol{v}$. Insert into Equation 4.5.

$$\boldsymbol{j}_\perp = -\frac{\nabla p_\perp \times \boldsymbol{B}}{B^2} + (p_\parallel - p_\perp)\frac{\boldsymbol{B} \times (\boldsymbol{B} \cdot \nabla)\boldsymbol{B}}{B^4} + \rho\frac{\boldsymbol{E} \times \boldsymbol{B}}{B^2} - nm\frac{d\boldsymbol{u}}{dt} \times \frac{\boldsymbol{B}}{B^2} \tag{4.8}$$

The first term on the right is due to diamagnetic drift[2]. The second term is due to magnetic curvature. The third term is due to the $\boldsymbol{E} \times \boldsymbol{B}$ drift. The last term is due to the acceleration/deceleration of the bulk flow. The terms associated with $p_\perp$

[2] A diamagnetic drift is not a guiding-center drift but a fluid drift due to the presence of a pressure gradient.

in Equation 4.8 further reduces to

$$
\begin{aligned}
& -\frac{\nabla p_\perp \times \boldsymbol{B}}{B^2} + \frac{p_\perp}{B^4}\left[(\boldsymbol{B}\cdot\nabla)\boldsymbol{B}\right]\times\boldsymbol{B} \\
= & -\nabla \times \frac{p_\perp \boldsymbol{B}}{B^2} + p_\perp \nabla \times \frac{\boldsymbol{B}}{B^2} + \frac{p_\perp}{B^4}\left(\frac{1}{2}\nabla B^2 - \boldsymbol{B}\times(\nabla\times\boldsymbol{B})\right)\times\boldsymbol{B} \\
= & -\nabla \times \frac{p_\perp \boldsymbol{B}}{B^2} + p_\perp\left(\frac{\boldsymbol{B}}{B^3}\right)\times\nabla B + \frac{p_\perp}{B^4}\boldsymbol{B}\cdot(\nabla\times\boldsymbol{B})\boldsymbol{B}
\end{aligned}
\tag{4.9}
$$

where the last term can further reduce to

$$
\frac{\boldsymbol{B}}{B^2}\cdot\left(\nabla\times\frac{p_\perp\boldsymbol{B}}{B^2} - \nabla\frac{p_\perp}{B^2}\times\boldsymbol{B}\right)\boldsymbol{B} = \left[\nabla\times\frac{p_\perp\boldsymbol{B}}{B^2}\right]_\parallel \tag{4.10}
$$

So, $\boldsymbol{j}_\perp$ becomes

$$
\boldsymbol{j}_\perp = p_\parallel\frac{\boldsymbol{B}\times(\boldsymbol{B}\cdot\nabla)\boldsymbol{B}}{B^4} + p_\perp\frac{\boldsymbol{B}\times\nabla B}{B^3} - \left[\nabla\times\frac{p_\perp\boldsymbol{B}}{B^2}\right]_\perp + \rho\frac{\boldsymbol{E}\times\boldsymbol{B}}{B^2} - nm\frac{d\boldsymbol{u}}{dt}\times\frac{\boldsymbol{B}}{B^2} \tag{4.11}
$$

where the first term on the right is due to curvature drift, the second term is due to gradient drift, the third term is due to perpendicular magnetization, the fourth term is due to the $\boldsymbol{E}\times\boldsymbol{B}$ drift, and the last term is due to polarization drift. The expression is simplified as $\boldsymbol{j}_\perp = \boldsymbol{j}_c + \boldsymbol{j}_g + \boldsymbol{j}_m + \boldsymbol{j}_{\boldsymbol{E}\times\boldsymbol{B}} + \boldsymbol{j}_p$, in which $\boldsymbol{j}_{\boldsymbol{E}\times\boldsymbol{B}}$ has no direct contribution to the energy conversion. This gives an accurate description for $\boldsymbol{j}_\perp$ if the pressure tensor is gyrotropic. To confirm this, we calculate the electron pressure agyrotropy

$$
A\O_e \equiv 2\frac{|p_{\perp e1} - p_{\perp e2}|}{p_{\perp e1} + p_{\perp e2}}, \tag{4.12}
$$

where $p_{\perp e1}$ and $p_{\perp e2}$ are the two pressure eigenvalues associated with eigenvectors perpendicular to the mean magnetic field direction (Scudder and Daughton, 2008). $A\O_e$ measures the departure of the pressure tensor from cylindrical symmetry about the local magnetic field. It is zero when the local particle distribution is gyrotropic. Figure 4.6(b) shows that the regions with nonzero $A\O_e$ are localized to the X-points. The small $A\O_e$ indicates that the electron distributions are nearly gyrotropic in most regions, and most electrons are well-magnetized. Figure 4.7 shows the non-gyrotropic particle distributions only exist close to the reconnection X-line (top and middle rows). The particle distributions are nearly isotropic in the reconnection outflow, which is the major particle acceleration region. Therefore, a drift description is a good approximation for electrons in our simulations even when there is no external guide field. This is in contrast to high-β plasma, where a guide field is necessary to assume a gyrotropic distribution (e.g. Dahlin et al., 2014).

Figure 4.8(a) and (b) show time-dependent $d\varepsilon_c/dt$ and ε_c due to different current terms, where $\varepsilon_c = \int(d\varepsilon_c/dt)dt$. The contribution from polarization current and parallel current are small and not shown. The curvature drift term is the dominant term of $\boldsymbol{j}_\perp \cdot \boldsymbol{E}$, the ∇B term gives a net cooling effect, and the magnetization term is small compared to these two. Figure 4.8(c) shows the spatial distribution of $\boldsymbol{j}_c \cdot \boldsymbol{E}$. When the plasma flow velocity $\boldsymbol{u}$ is along the magnetic field curvature $\boldsymbol{\kappa}$ due to tension force, $\boldsymbol{j}_c \cdot \boldsymbol{E} \approx (p_\parallel \boldsymbol{B} \times \boldsymbol{\kappa}/B^2) \cdot (-\boldsymbol{u} \times \boldsymbol{B})$ is positive. These regions are a few d_i along the z direction, but over $50d_i$ along the x direction. $\boldsymbol{j}_c \cdot \boldsymbol{E}$ can be negative when $\boldsymbol{u}$ and $\boldsymbol{\kappa}$ are opposite in direction due to a background flow (Dahlin et al., 2014). The overall effect of $\boldsymbol{j}_c \cdot \boldsymbol{E}$ is a strong electron energization. Figure 4.8(d) shows that $\boldsymbol{j}_g \cdot \boldsymbol{E}$ is neg-

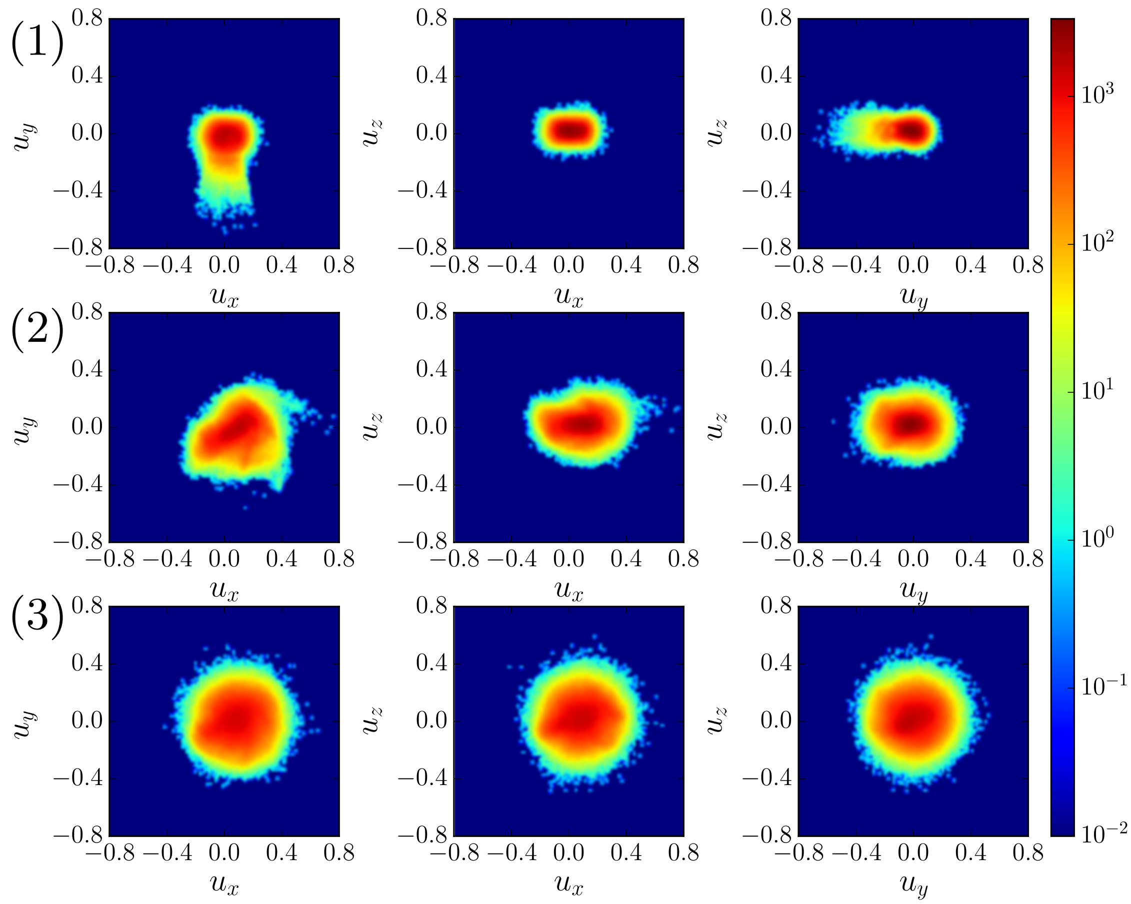

Figure 4.7 Electron momentum distributions in the 3 boxes shown in Figure 4.6 (b). $\boldsymbol{u} = \gamma \boldsymbol{v}/c$, and γ is the Lorentz factor.

ative in most regions. This is because the strong ∇B is along the direction out of the reconnection exhausts. Then, $\boldsymbol{j}_g \cdot \boldsymbol{E} \sim (\boldsymbol{B} \times \nabla B) \cdot (-\boldsymbol{u} \times \boldsymbol{B})$ is negative. Figure 4.8(e) shows the cumulative $\boldsymbol{j}_c \cdot \boldsymbol{E}$ and $\boldsymbol{j}_g \cdot \boldsymbol{E}$ along the x-direction, i.e. $\int_0^x \int_0^{L_z} \boldsymbol{j}_c \cdot \boldsymbol{E} dx'dz$ and $\int_0^x \int_0^{L_z} \boldsymbol{j}_g \cdot \boldsymbol{E} dx'dz$. In the reconnection exhaust region($x = 60 - 115 d_i$), $\boldsymbol{j}_c \cdot \boldsymbol{E}$ is stronger than $\boldsymbol{j}_g \cdot \boldsymbol{E}$, so the electrons can be efficiently accelerated when going through these regions. In the pile-up region($x = 120 - 140 d_i$), $\boldsymbol{\kappa}$, ∇B and $\boldsymbol{u}$ are along the same direction, so both terms give net electron heating. In the island coalescence region($x \sim 150 d_i$), $\boldsymbol{j}_c \cdot \boldsymbol{E}$ gives electron heating, while $\boldsymbol{j}_g \cdot \boldsymbol{E}$ gives strong electron cooling. Although the net effect is electron cooling, island coalescence can be efficient in accelerating electrons to the high energies in agreement with earlier simulation by Oka et al. (2010).

It has been shown that the curvature drift acceleration in the reconnection region corresponds to a *Fermi*-type mechanism (Guo et al., 2014; Dahlin et al., 2014; Guo et al., 2015). To develop a power-law energy distribution for the *Fermi* acceleration mechanism, the characteristic acceleration time $\tau_{\mathrm{acc}} = 1/\alpha$ needs to be smaller than the particle injection time τ_{inj} (Guo et al., 2014, 2015), where $\alpha = (1/\varepsilon)(\partial\varepsilon/\partial t)$, and $\partial\varepsilon/\partial t$ is the energy change rate of particles. To estimate the ordering of *Fermi* acceleration rate from the single-particle drift motion, consider the curvature drift velocity $\boldsymbol{v}_c = v_{\parallel}^2 \boldsymbol{B} \times \boldsymbol{\kappa}/(\Omega_{ce}B)$ in a curved field where $R_c = |\boldsymbol{\kappa}|^{-1}$, so the time for a particle to cross this region is $\sim R_c/v_{\parallel}$ and the electric field is mostly induced by the Alfvénic plasma flow $\boldsymbol{E} \sim -\boldsymbol{v}_A \times \boldsymbol{B}/c$. The energy gain in one cycle is $\delta\varepsilon \sim m v_A v_{\parallel}$. The time for a particle to cross the island is $L_{\mathrm{island}}/v_{\parallel}$. Then the acceleration rate $\partial\varepsilon/\partial t \sim \varepsilon v_A/L_{\mathrm{island}}$ for a nearly isotropic particle distribution. The characteristic acceleration time $\tau_{\mathrm{acc}} \sim L_{\mathrm{island}}/v_A$. Taking $L_{\mathrm{island}} \sim 50 d_i$ and $v_A \sim 0.2c$, the acceleration time $\tau_{\mathrm{acc}} \sim 250\Omega_{ci}^{-1}$. The actual acceleration time may be longer because the outflow speed will decrease from v_A away from the X-points, and the ∇B term gives a non-negligible cooling effect. Our analysis has also found that pre-acceleration and trapping effects at the X-line region can lead to more efficient electron acceleration by *Fermi* mechanism and are worthwhile to be investigated further (Hoshino, 2005; Egedal et al., 2015; Huang et al., 2015). Taking the main energy release phase as the injection time $\tau_{\mathrm{inj}} \sim 800\Omega_{ci}^{-1}$, the estimated value of $\tau_{\mathrm{inj}}/\tau_{\mathrm{acc}} \sim 3.2$, well above

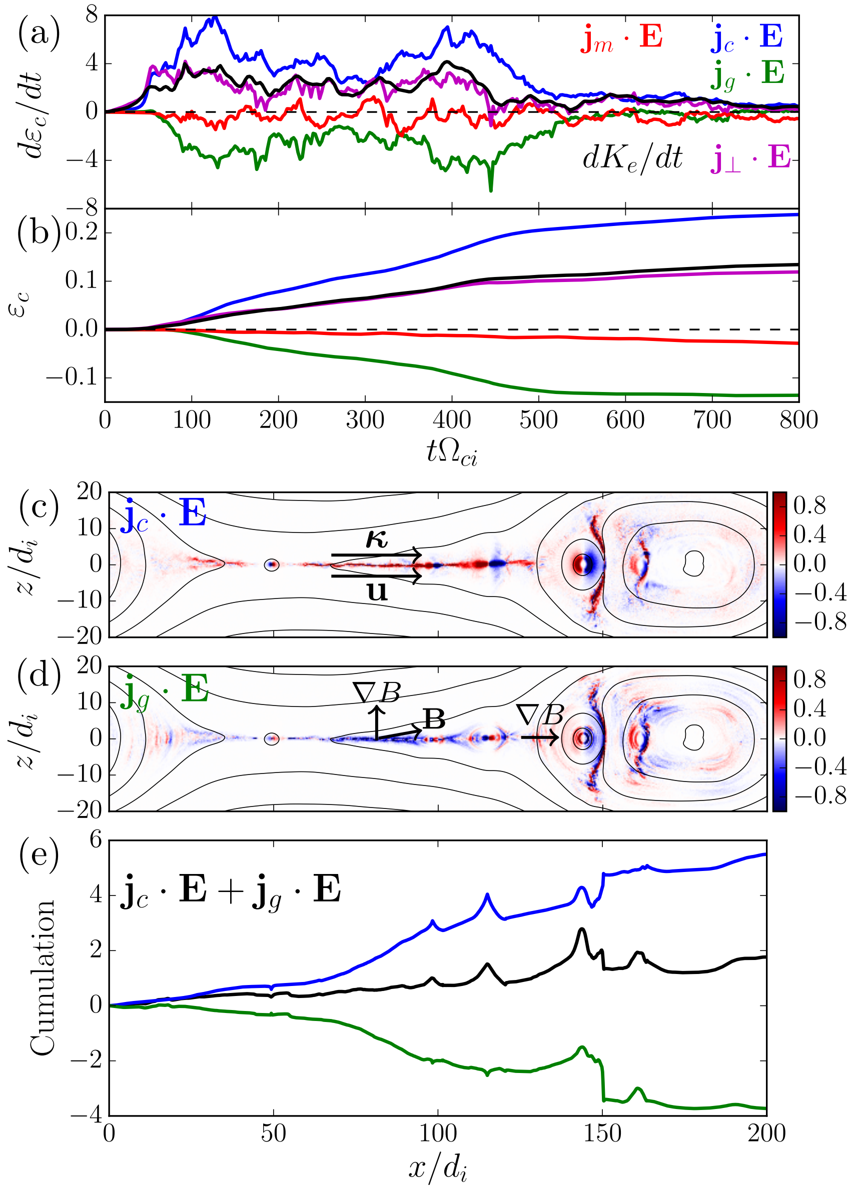

Figure 4.8 Various energization of electrons using a drift description for the case with $\beta_e = 0.02$. (a) the energy conversion rate due to different type of current terms, compared with the electron energy change rate dK_e/dt. $\boldsymbol{j}_c \cdot \boldsymbol{E}$, $\boldsymbol{j}_g \cdot \boldsymbol{E}$, and $\boldsymbol{j}_m \cdot \boldsymbol{E}$ represent energy conversion due to curvature drift, ∇B drift, and magnetization, respectively. (b) The converted magnetic energy due to various terms in (a), normalized to the initial magnetic energy of the reconnecting component $\varepsilon_{bx}(0)$. (c) Color-coded contours of energy conversion rate due to curvature drift at $t = 400\Omega_{ci}^{-1}$. $\boldsymbol{\kappa}$ and $\boldsymbol{u}$ indicate the directions of the magnetic field curvature and the bulk flow velocity. (d) Color-coded contours of energy conversion rate due to ∇B drift at $t = 400\Omega_{ci}^{-1}$. $\boldsymbol{B}$ and ∇B indicate the directions of the magnetic field and the gradient of $|\boldsymbol{B}|$. Both $\boldsymbol{j}_c \cdot \boldsymbol{E}$ and $\boldsymbol{j}_g \cdot \boldsymbol{E}$ are normalized to the $0.002 n_0 m_e c^2 \omega_{pe}$. (e) $\int_0^x \int_0^{L_z} \boldsymbol{j}_i \cdot \boldsymbol{E} dx' dz$ for $\boldsymbol{j}_i = \boldsymbol{j}_c$ and $\boldsymbol{j}_i = \boldsymbol{j}_g$. The black line is the sum of these two.

the threshold. For the case with $\beta_e = 0.2$, v_A is $\sim 10\%$ of the v_A of the case with $\beta_e = 0.02$. The ratio $\tau_{\rm inj}/\tau_{\rm acc} \sim 0.32 < 1$, so there is no power-law energy distribution in the case with $\beta_e = 0.2$.

4.4 Discussion and conclusion

Nonthermal power-law distributions of electrons or ions have rarely been found in previous kinetic simulations of nonrelativistic simulations of magnetic reconnection (e.g. Drake et al., 2010). We find that two conditions are essential for producing power-law electron energization. The first condition is that the domain should be large enough to sustain reconnection for a sufficient long duration. A power-law tail develops as the acceleration continues long enough ($\tau_{\rm inj}/\tau_{\rm acc} > 1$). The second condition is that plasma β must be low, and it is essential to form a nonthermally dominated power-law distribution by providing enough free energy ($\propto 1/\beta$) for nonthermal electrons. Assuming 10% of magnetic energy is converted into nonthermal electrons with spectral index $p = 1$, one can estimate that β_e is about 0.02 for half of electrons to be accelerated into a power-law that extends to $10E_{th}$. This agrees well with our simulation. We point out that a loss mechanism (Fermi, 1949; Guo et al., 2014) or radiation cooling due to gyrosynchrotron radiation can affect the final power-law index of nonthermal electrons. Consequently, including loss mechanisms in a large three-dimensional open system is important, for example, to explain the observed power-law index in solar flares and other astrophysical reconnection sites. Another factor that may influence our results is the presence of an external guide field B_g. Our analysis has shown that the *Fermi* acceleration dominates when $B_g \lesssim B_0$.

The full discussion for the cases including the guide field will be reported in a latter chapter. A potentially important issue is the three-dimensional instability such as kink instability that may strongly influence the results. Unfortunately, the corresponding three-dimensional simulation is beyond the computing resource that is available. We note that results from three-dimensional simulations with pair plasmas have shown development of strong kink instability but appear to have no strong influence on particle acceleration (Guo et al., 2014; Sironi and Spitkovsky, 2014). The growth rate of the kink instability can be much less than the tearing instability for a high mass ratio (Daughton, 1999), and therefore the kink instability may be even less important for electron acceleration in a proton-electron plasma.

In our simulations, we vary plasma β by varying the magnetic field strength, which is equivalent to varying the plasma density. It has been shown that both the reconnection rate and the electron acceleration efficiency can be enhanced for the cases with low plasma density (Bessho and Bhattacharjee, 2010; Wu et al., 2011). We have carried out simulations with fixed plasma density, but varying electron and ion temperature. The results still show that the power-law energy distribution develops in the low-β cases, but not in the high-β cases. This is discussed in the next chapter.

The energy partition between electrons and protons shows that more magnetic energy is converted into protons. For simulations with higher mass ratio $m_i/m_e = 100$, the energetic electrons still develop a power-law distribution and the fraction of electron energy to the total plasma energy is about 33%, indicating that the energy conversion and electron acceleration are still efficient for higher mass ratios. Our results show that ions also develop a power-law energy spectrum for low-β cases and the curvature drift acceleration is the leading mechanism. The results are reported in the next chapter.

The energetic electrons can generate observable X-ray emissions. As nonthermal electrons are mostly concentrated inside the magnetic islands, the generated hard X-ray flux can be strong enough to be observed during solar flares in the above-the-loop-top region (Masuda et al., 1994; Krucker et al., 2010) and the reconnection outflow region (Liu et al., 2013a). The nonthermal electrons may also account for the X-ray flares in accretion disk corona (Galeev et al., 1979; Haardt et al., 1994).

In summary, we find that in a nonrelativistic low-β proton-electron plasma, magnetic reconnection is highly efficient at converting the free energy stored in a magnetic shear into plasma kinetic energy, and accelerate electrons into nonthermal energies. The nonthermal electrons contain more than half of the total electrons, and their distribution resembles power-law energy spectra $f(E) \sim E^{-1}$ when particle loss is absent. This is in contrast to the high-β cases, where no obvious power-law spectrum is observed (e.g. Drake et al., 2010). It is important to emphasize that the particle acceleration discussed here is distinct from the acceleration by shocks, where the nonthermal population contains only about 1% of particles (Neergaard Parker and Zank, 2012).

CHAPTER 5

PARAMETRIC STUDY OF PARTICLE ACCELERATION DURING MAGNETIC RECONNECTION WITHOUT A GUIDE FIELD

5.1 Introduction

In the last chapter, we performed kinetic simulations in a nonrelativistic low-β ($\beta \sim 0.01$) proton-electron plasma. We found similar power-law energy distributions as in the relativistic reconnection. When calculating the energy distribution over the whole simulation domain, the nonthermal electrons can be over 50% of the total electrons in the low-β simulations. In the simulation, the low plasma β is achieved by increasing the magnetic field (or equivalently decreasing the particle density with constant plasma temperature), and the Alfvèn speed is also increased. In this chapter, we examine other ways to achieve a low-β plasma. In particular, we will adjust the plasma temperature but keep v_A constant or increase the magnetic field.

We perform 2D kinetic simulations of magnetic reconnection in a nonrelativistic proton-electron plasma with a range of plasma $\beta_e = \beta_i = 0.007 - 0.2$. As a continuation of Li et al. (2015) and the last chapter, we focus on understanding the dependence of the energy conversion and particle energization on plasma β. By tracking a large number of particles, we identify the particle acceleration regions.

By implementing a drift current analysis, we examine particle acceleration due to different mechanisms. Comparing with the last chapter, a new topic we discuss in this chapter is ion acceleration. We carry out similar analysis for both electrons and ions to show differences and similarities between their acceleration processes. In Section 5.2, we list the parameters for our simulations. In Section 5.3, we present simulation results. In Section 5.4, we present discussions and conclusions based on our simulations results.

5.2 Numerical simulations

The simulation setup is similar as the previous chapter. The plasma consists of protons and electrons with mass ratio $m_i/m_e = 25$ for most of cases. We have run a case with $m_i/m_e = 100$ to examine the effect of mass ratio. The plasma $\beta = 2\beta_e = 16\pi n_0 kT_0/B_0^2$, where β_e is the electron plasma. We vary β_e by using different T_0 and/or B_0 in different simulations. Note a change of B_0 will also result in a change of the Alfvén speed $v_A = B_0/\sqrt{4\pi n_0 m_i}$. The parameters for all runs are listed in Table 5.1, which gives the asymptotic values of the magnetic field strength B_0, the light speed in the unit of Alfvén speed c/v_A, v_{the}, ω_{pe}/Ω_{ce}, the magnetization parameter σ, β_e, the box sizes and the number of particles per cell per species `nppc`. The domain sizes were chosen to be $L_x \times L_z = 200d_i \times 100d_i$ for all simulations. As in the last chapter, we choose the domains size large enough so that the reconnection can be sustained for a long time, which is essential for the development of a power-law energy distribution (Guo et al., 2014, 2015; Li et al., 2015). For fields, we employ periodic boundaries along the x-direction and perfectly conducting boundaries along

Table 5.1. List of simulation runs

Run	m_i/m_e	B_0	c/v_A	$v_{\rm the}/c$	ω_{pe}/Ω_{ce}	σ	β_e	$N_x \times N_z$	`nppc`
R1	25	1.0	5.0	0.14	1.0	1.0	0.02	4096× 2048	400
R2	25	$1/\sqrt{3}$	8.7	0.08	$\sqrt{3}$	0.33	0.02	4096× 2048	200
R3	25	$1/\sqrt{10}$	15.8	0.045	$\sqrt{10}$	0.1	0.02	4096× 2048	200
R4	25	1.0	5.0	0.14	1.0	1.0	0.02	4096× 2048	200
R5	100	1.0	10.0	0.14	1.0	1.0	0.02	8000× 4000	350
R6	25	$\sqrt{3}$	2.9	0.14	$1/\sqrt{3}$	3.0	0.007	4096× 2048	200
R7	25	$1/\sqrt{3}$	8.7	0.14	$\sqrt{3}$	0.33	0.07	4096× 2048	200
R8	25	$1/\sqrt{10}$	15.8	0.14	$\sqrt{10}$	0.1	0.2	4096× 2048	400

Note. — B_0 is the asymptotic magnetic field strength. $v_A = B_0/\sqrt{4\pi n_0 m_i}$ is the Alfvén speed of the inflow region. $v_{\rm the} = \sqrt{2kT_e/m_e}$ is the electron thermal speed. $\omega_{pe} = \sqrt{4\pi n_0 e^2/m_e}$ is the electron plasma frequency. $\Omega_{ce} = eB/(m_e c)$ is the electron gyrofrequency. $\sigma = B_0^2/(4\pi n_0 m_e c^2)$ is the magnetization parameter. $\beta_e = 8\pi n_0 kT_e/B_0^2$ is the electron plasma β. N_x and N_z are the grid sizes along the x-direction and z-direction, respectively. `nppc` is the number of particles per cell for each species. R4 is similar as R1 except there is no initial long wavelength perturbation.

the z-direction. For particles, we employ periodic boundaries along the x-direction, and they reflect at the boundaries along the z-direction. We add a long wavelength perturbation with $B_z = 0.03B_0$ to induce reconnection (Birn et al., 2001) for all runs except run R4, which starts from numerical noises due to the random sampling of a finite number of particles.

5.3 Results

5.3.1 Evolution of magnetic field and plasma

As reconnection starts, the current layer breaks into a series of magnetic islands, which merge with each other into larger island. The largest island keeps grow-

Table 5.2. Energy conversion for different runs

Run	$\lvert\Delta\varepsilon_b\rvert/\varepsilon_{b0}$	$\Delta K_e/K_{e0}$	$\Delta K_i/K_{i0}$	F_{nte}	F_{nti}	K_{nte}/K_e	K_{nti}/K_i
R1	0.39	4.85	8.43	0.55	0.52	0.92	0.95
R2	0.38	5.11	7.43	0.52	0.49	0.91	0.95
R3	0.37	6.22	6.59	0.49	0.50	0.90	0.92
R4	0.38	5.16	7.93	0.53	0.49	0.90	0.95
R5	0.38	4.09	8.82	0.42	0.44	0.87	0.95
R6	0.42	13.29	28.05	0.66	0.60	0.97	0.99
R7	0.36	2.21	2.29	0.38	0.40	0.74	0.81
R8	0.29	0.57	0.54	0.17	0.19	0.39	0.47

Note. — ΔK_e and ΔK_i are the energy gain for electrons and ions, respectively. K_{e0} and K_{i0} are the initial energy of electrons and ions, respectively. N_{nth}/N_0 is the fraction of nonthermal particles. $\lvert\Delta\varepsilon_b\rvert/\varepsilon_{b0}$ is the fraction of dissipated magnetic energy. $F_{\text{nthe}} = N_{\text{nthe}}/N_0$ and $F_{\text{nthi}} = N_{\text{nthi}}/N_0$ are the fraction of nonthermal electrons and ions, respectively. K_{nthe}/K_e and K_{nthi}/K_i are the fraction energy that nonthermal electrons and ions contain, respectively.

ing until its size is comparable to the system size and at that time the reconnection ceased. Figure 5.1 (a) shows the evolution of the out-of-plane magnetic field B_y for run R1. About 10 small magnetic islands are generated from the initial current sheet and interact and coalesce with each other, with three islands remaining at $t\Omega_{ci} = 152.5$. One of them, located at $x \sim 120d_i$, consists of two smaller merging islands. The elongated current layer becomes unstable again after $t\Omega_{ci} = 152.5$ (Daughton et al., 2006) and breaks into secondary islands (e.g. $x \sim 90d_i$ in the middle panel). The out-of-plane component of the magnetic field B_y is initially in the center of the force-free current sheet. As the current layer breaks into multiple magnetic islands, the magnetic flux of B_y get trapped in the center of these islands. The current sheet then evolves like a Harris current sheet without a guide field (anti-parallel reconnection). As similar to the case of last chapter, B_y at late times shows quadrupole structures (bottom two panels of Figure 5.1), which are a signature of Hall physics in anti-parallel reconnection (Drake et al., 2008).

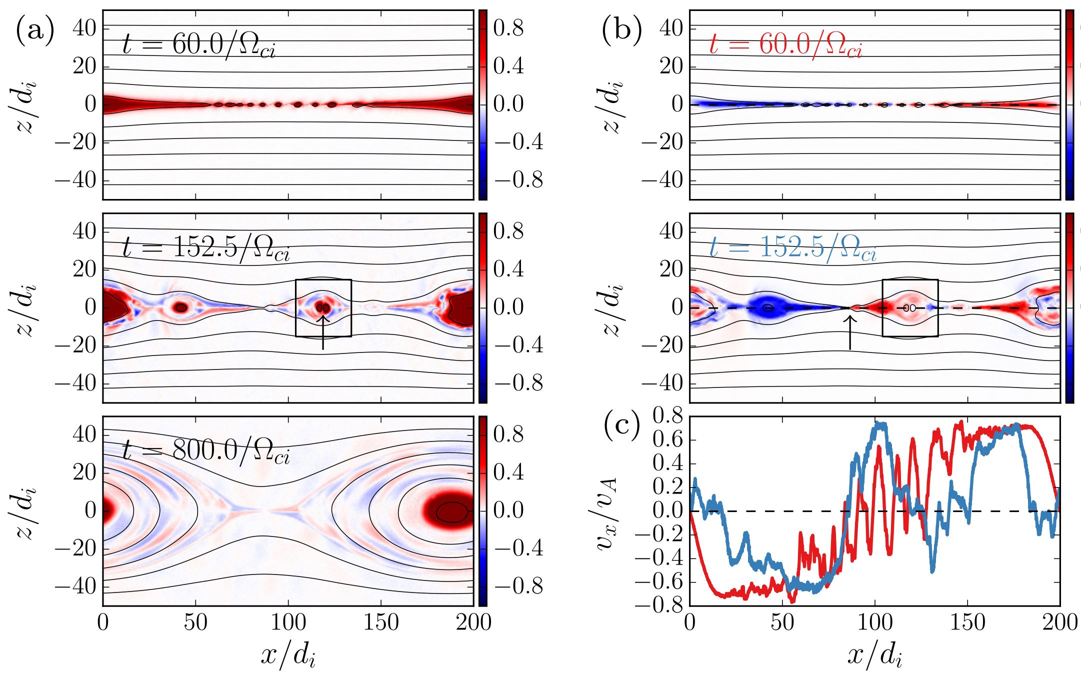

Figure 5.1 (a) Out-of-plane magnetic field B_y for run R1 at $t\Omega_{ci} = 60$, 152.5 and 800. The arrow in the middle panel indicates one island merging region. We study the energy conversion in the box in Figure 5.14. (b) The bulk flow velocity $v_x = \sum_s n_s m_s v_{sx} / \sum_s n_s m_s$ for run R1 at $t\Omega_{ci} = 60$ and 152.5. The dashed line in the upper two panels are a horizontal cut along $z = 0$. Plotted in (c) is v_x along the cut. The red line is the cut at $t\Omega_{ci} = 60$. The blue line is the cut at $t\Omega_{ci} = 152.5$. v_x is normalized to the reconnection inflow Alfvén speed v_A. The overplotted arrow indicates a reconnection X-point. The square indicates a contracting magnetic island with two smaller merging islands.

The reconnection process drives fast bulk flow in the x-direction. Figure 5.1 (b) shows the velocity v_x at $t\Omega_{ci} = 60$ and 152.5. v_x is the center-of-mass velocity by averaging over electrons and ions in a computing cell $v_x = \sum_s n_s m_s v_{sx} / \sum_s n_s m_s$. At $t\Omega_{ci} = 60$, the newly formed magnetic islands are strongly contracting. A cut along the x-direction shows v_x switches between $0.5 v_A$ and $-0.5 v_A$ in $10 d_i$. At $t\Omega_{ci} = 152.5$, the diverging flow (shown by the arrow) at $x \sim 85d_i$ indicates a reconnection X-point, and the converging flow at $x \sim 100 - 140d_i$ indicates a contracting magnetic island. Both regions can be efficient at accelerating particles. The reconnection generated bulk flow induces electric field $-\boldsymbol{u} \times \boldsymbol{B}$ mostly along the y-direction. Figure 5.2 shows E_y and the parallel electric field $E_\parallel$ for run R1 at $t\Omega_{ci} = 60$ and $t\Omega_{ci} = 152.5$. E_y broadly distributes in the reconnection region and peaks at the two sides of magnetic islands. The amplitude of $E_y \sim v_A B_0$, as expected. $E_\parallel$ peaks at the reconnection separatrix. It accelerates electrons when they are streaming into the reconnection region (Egedal et al., 2012), generating electron beams that drive instabilities to form the electron hole structures in $E_\parallel$ plots (Omura et al., 1996). But $E_\parallel$ is much smaller than E_y. The dominance of E_y suggests that particles are most accelerated along the perpendicular direction to the local magnetic field.

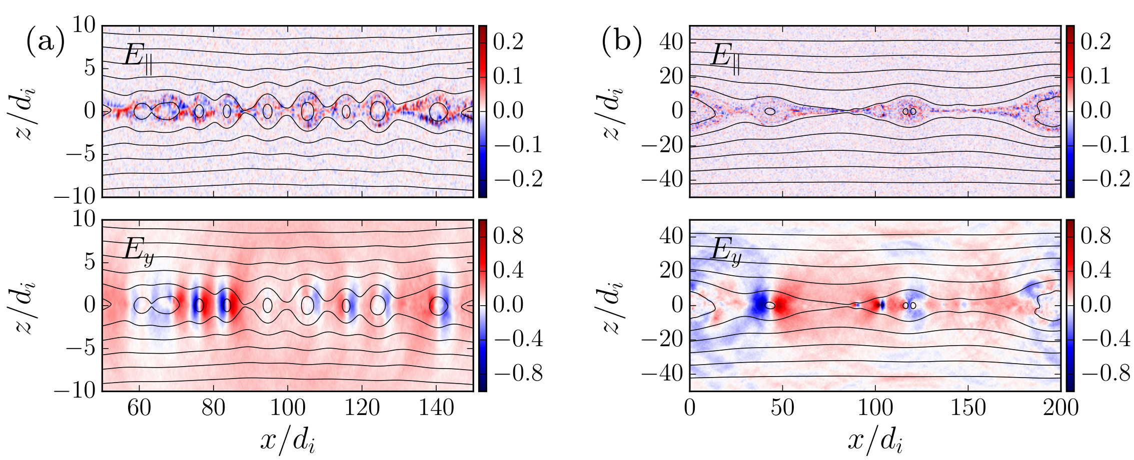

Figure 5.2 Parallel electric field $E_\parallel$ and out-of-plane electric field E_y for run R1 at (a) $t\Omega_{ci} = 60$ and (b) $t\Omega_{ci} = 152.5$. The parallel direction is respect to the local magnetic field direction. We normalize the electric field to $0.5v_A B_0$. Note that the color scales are different for $E_\parallel$ and E_y.

We also check whether the reconnection rate depends on the simulation plasma parameters. We calculate the reconnection rate as $E_R = \langle \partial\psi/\partial t \rangle / (Bv_A)$, in which $\psi = \max(A_y) - \min(A_y)$ along $z = 0$, where A_y is the y component of the vector potential (Daughton et al., 2009b). B is B_0, and v_A is the inflow Alfvén speed. Figure 5.3 gives the evolution of the reconnection rates E_R for 5 runs. The peak reconnection rate is ~ 0.1 for all runs. Runs R1 and R3 have different plasma temperature, but the evolution of their E_R is similar, suggesting that the plasma temperature does not change the reconnection rate when the initial plasma β is the same. The mass ratio does not change the reconnection rate either, as E_R for run R5 ($m_i/m_e = 100$) is close to that of R1 and R3 ($m_i/m_e = 25$). This agrees with earlier works (Hesse et al., 1999; Shay et al., 1999). The bottom panel of Figure 5.3 shows two runs with different plasma β. R6 and R8 have the same plasma temperature but different magnetic field strength (or equivalently different plasma density). The reconnection rate of R6 ($\beta_e = 0.007$)is larger than that of R8 ($\beta_e = 0.2$), but not by much. This difference is probably due to the fact that the current layer breaks into more islands initially in the low-β reconnection than in the high-β reconnection (Figure 5.4). More islands in the low-β reconnection will drive the current sheet thinner to d_e scale faster and therefore faster reconnection rate, as discussed in Chapter 2.

5.3.2 Energy evolution

We now consider how the energy conversion differs for different runs. Table 5.2 lists the fraction of dissipated magnetic energy $\Delta\varepsilon_b/\varepsilon_{b0}$, the ratio of electron energy gain ΔK_e and ion energy gain ΔK_i to their initial energies at the end of the simula-

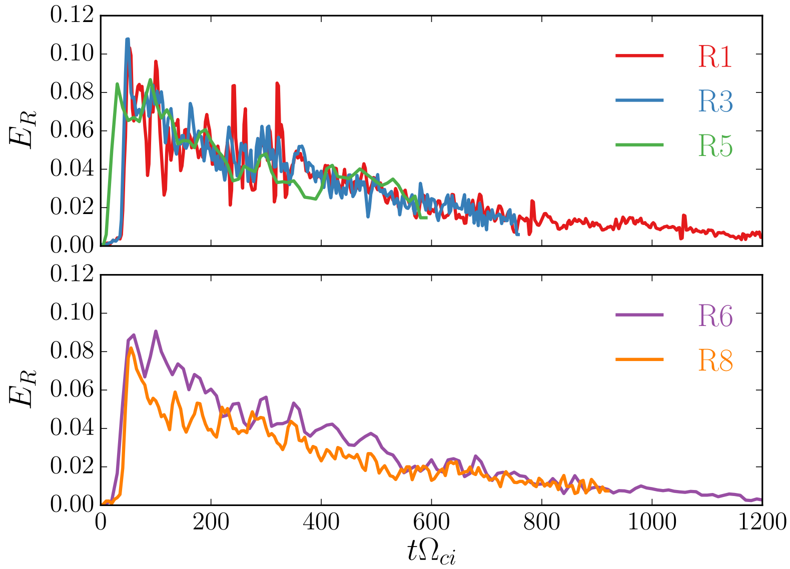

Figure 5.3 Reconnection rate for different runs. (a) 3 runs with the same $\beta_e = 0.02$. R1 and R3 have $m_i/m_e = 25$ but different plasma temperature. R5 has a mass ratio $m_i/m_e = 100$. (b) 2 runs with the same plasma temperature but different magnetic field strength. The corresponding β_e is 0.007 for R6 and 0.2 for R8.

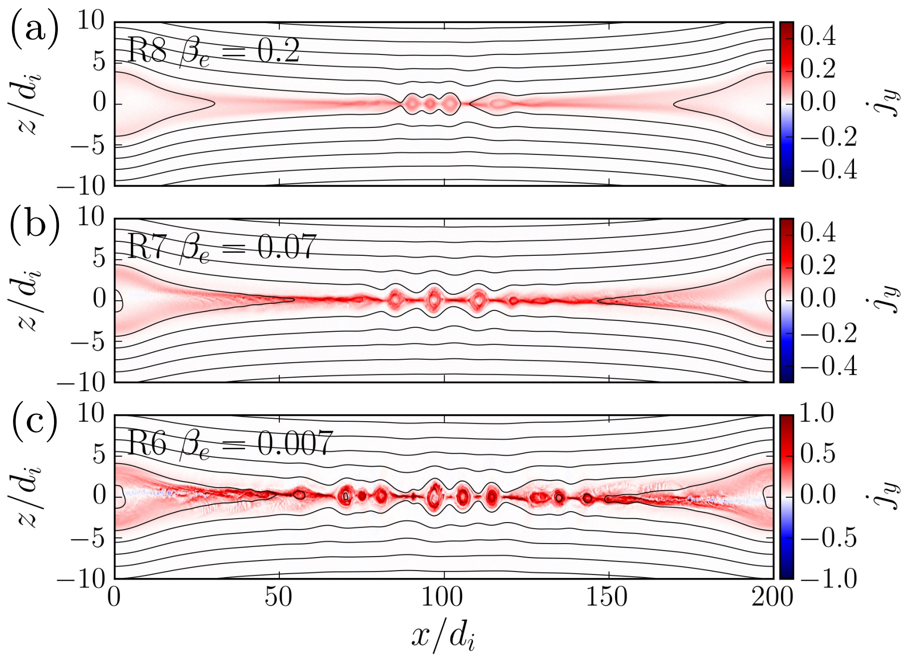

Figure 5.4 The out-of-plane current density j_y for (a) run R8, (b) run R7 (c) run R6 at $t\Omega_{ci} = 27.5$.

tions. Several trends can be seen from simulations. The magnetic energy conversion is more efficient in low-β reconnection. About 38% of magnetic energy get converted in R1-R5 which have the same plasma $\beta_e = 0.02$. The fraction increases to 42% in R6 with $\beta_e = 0.007$ but decreases to 29% in R8 with $\beta_e = 0.2$. One possible reason is that the reconnection rate is higher in lower-β reconnection, as discussed in the previous section. Another possible reason is that more magnetic islands in the low-β reconnection will convert more magnetic energy through magnetic island merging processes. The reconnection in low-β plasma is more powerful at energizing particles. K_e increases by 57%, and K_i increases by 54% in run R8 ($\beta_e = 0.2$). As the free energy increases with lower plasma β, K_e increases 13.29 times, and K_i increase 28.05 times in run R6 ($\beta_e = 0.007$). The low-β reconnection is more efficient at energizing ions. This can be seem from runs R8, R7, R1 and R6 which have different plasma β. We see that $\Delta K_e/\Delta K_i > 1$ for R8, while the ratio decreases to 0.47 for run R6. The possible reason is that the acceleration mechanism allows ions to gain energy faster than electrons. For example, the *Fermi* mechanism accelerates particles proportional to its energy. If ions can gain energy faster than electrons initially, they can get accelerated more efficiently latter. We will examine a pickup process in the next subsection by tracking particle trajectories. As the energization becomes more efficient in the low-β reconnection, the difference between ΔK_e and ΔK_i will get larger. Reconnection is more efficient at accelerating electrons than ions in a low temperature plasma. Comparing R1, R2 and R3 with different plasma temperature but the same β_e, $\Delta K_i/\Delta K_e$ decreases from 1.74 for R1 to 1.06 for R3. Finally, ions gain more energy than electrons for cases with higher mass ratio. We see that $\Delta K_i/\Delta K_e > 2$ when $m_i/m_e = 100$ (run R5), which is larger than that when $m_i/m_e = 25$ (run R1-R4).

5.3.3 Particle acceleration

Energy conversion during reconnection leads to efficient particle acceleration. Figure 5.5 shows the time evolution of particle energy spectra for run R1 with $\beta_e = 0.02$ and R8 with $\beta_e = 0.2$. Embedded plots are the time evolution of the maximum particle energy. The final energy spectrum (red) for run R1 develops prominent nonthermal tail. The maximum electron energy is 500 times larger than its initial thermal energy $\varepsilon_{\rm th}$, and the maximum ion energy is 1500 times of its thermal energy. For run R8 ($\beta_e = 0.2$), the nonthermal tail is not as obvious as case R1, and the final energy distribution is close to a thermal distribution. The maximum energy is about $40\varepsilon_{\rm th}$ for electrons and $80\varepsilon_{\rm th}$ for ions, an order of magnitude lower than that of run R1. More efficient energy conversion in low-β reconnection drives more efficient particle acceleration. This is not surprising since the particle acceleration and the energy conversion are intrinsically related.

To reveal the nonthermal nature of the spectrum tail, we plot the final energy spectra for all runs and for both electrons and ions in Figure 5.6. For electrons, we fit the power-law spectrum over the whole distribution since the thermal component and nonthermal component show no clear separation. For ions, we first subtract the lower-energy thermal core (a Maxwellian distribution) to obtain the nonthermal component, then fit the power-law spectrum over the nonthermal component. From Figure 5.6 (a) and (c), we see that the spectrum develops power-law tail $f(\varepsilon) \sim \varepsilon^{-p}$ with p close to

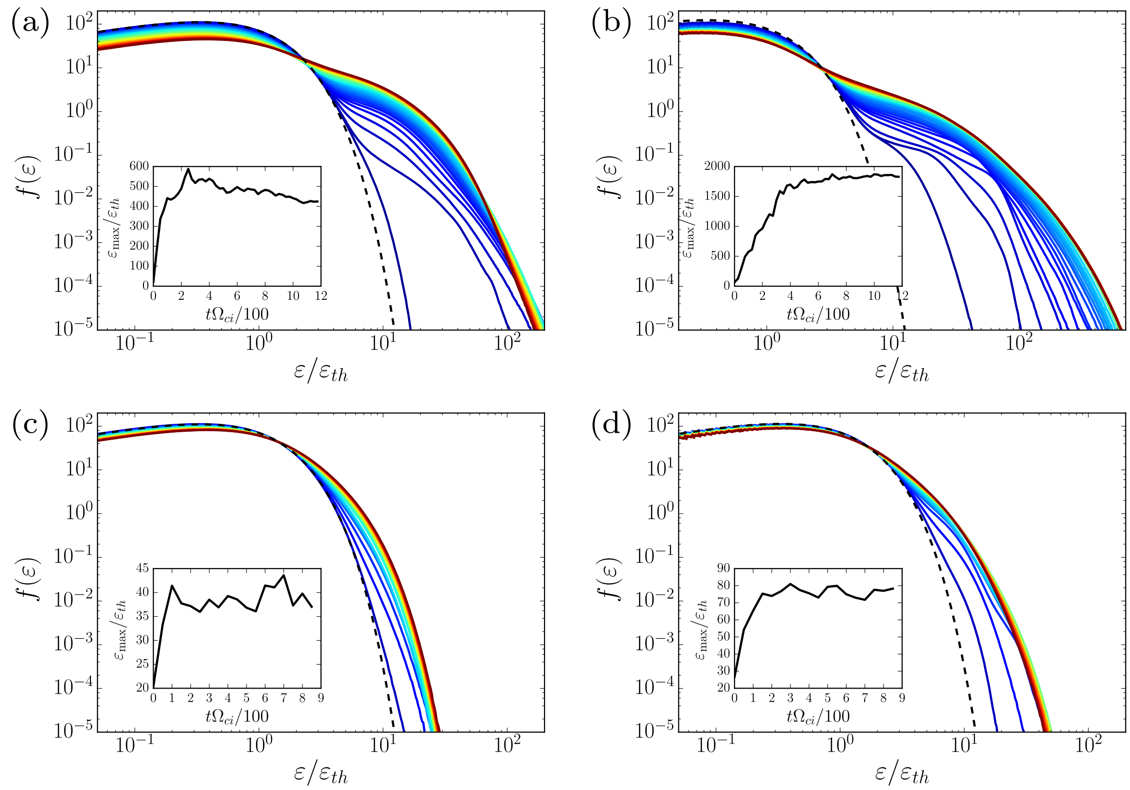

Figure 5.5 Time evolution of particle energy spectra for run R1 and R8. The lines with different colors are particle spectra at different times. Curves are evenly spaced in time interval of $\Delta t\Omega_{ci} = 25$ for R1 and $t\Omega_{ci} = 50$ for R8. The dashed line is the initial thermal distribution. The embedded plots give the time evolution of the maximum energy $\varepsilon_{\max}$ normalized to the initial thermal energy $\varepsilon_{\rm th}$. (a) Electron energy spectra for run R1. (b) Ion energy spectra for run R1. (c) Electron energy spectra for run R8. (d) Ion energy spectra for run R8.

1 for both electrons and ions for R1 ($\beta_e = 0.02$) and R6 ($\beta_e = 0.007$). The power-law spectrum extends about one decade in energy. For R7 ($\beta_e = 0.07$), the power-law index $p \sim 1.51$ for electrons and ~ 1.37 for ions, and the power-law extends a smaller range in energy than the low-β runs. For R8 ($\beta_e = 0.2$), the spectrum is close to a thermal distribution, and there is no power-law tail. Figure 5.6 (b) shows the energy spectra for R2, R3 and R4 with the same β_e but different plasma temperature. These runs have the same mass ratio $m_i/m_e = 25$. Also plotted is the spectrum for R5

with $m_i/m_e = 100$ and $\beta_e = 0.02$ as comparison. The spectra for all runs develop a power-law spectrum with a power-law index $p \sim 1$. When $m_i/m_e = 100$, the electrons have a spectrum $\sim \varepsilon^{-1.22}$, slightly steeper than the runs with $m_i/m_e = 25$. Panel (d) is similar to (b) but for ions. We see that ions have a spectrum $\sim \varepsilon^{-0.79}$, even flatter than the runs with $m_i/m_e = 25$. This is probably due to that reconnection with $m_i/m_e = 100$ is more efficient at accelerating ions than electrons, as given in Table 5.2.

The extended hard power-law spectrum contains a large fraction of nonthermal particles. We get the nonthermal component $f_{\rm nt}(\varepsilon)$ by subtracting a Maxwellian distribution fitting the lower-energy thermal distribution. Integrate it over ε, we obtain the number $N_{\rm nt}$ and kinetic energy $K_{\rm nt}$ of the nonthermal particles. Table 5.2 shows the nonthermal fraction $F_{\rm nte} = N_{\rm nte}/N_0$ for electrons and $F_{\rm nti} = N_{\rm nti}/N_0$ for ions. The nonthermal fractions are about 50% for the run R1-5 ($\beta_e = 0.02$). They increase to over 60% for R6 ($\beta_e = 0.007$) but decrease to $\sim 40\%$ for run R7 ($\beta_e = 0.07$) and $\sim 20\%$ for run R8 ($\beta_e = 0.2$). The nonthermal fractions for R5 ($m_i/m_e = 100$) are lower than that of R1-4 ($m_i/m_e = 25$) with the same β_e. This is probably due to that the run time $\sim 600\Omega_{ci}^{-1}$ for R5 is shorter than in the other runs with run time over $> 800\Omega_{ci}^{-1}$ for R1-4. Figure 5.3 shows that the reconnection rate for run R5 is still decreasing at $t\Omega_{ci} = 600$, suggesting that the reconnection is still ongoing. The nonthermal particles contain even larger fractions of total energy of the systems because their energies are higher than the low-energy part. The fraction is 39% for electrons and 47% for ions for R8 with the highest β_e. It can go over 90% in the

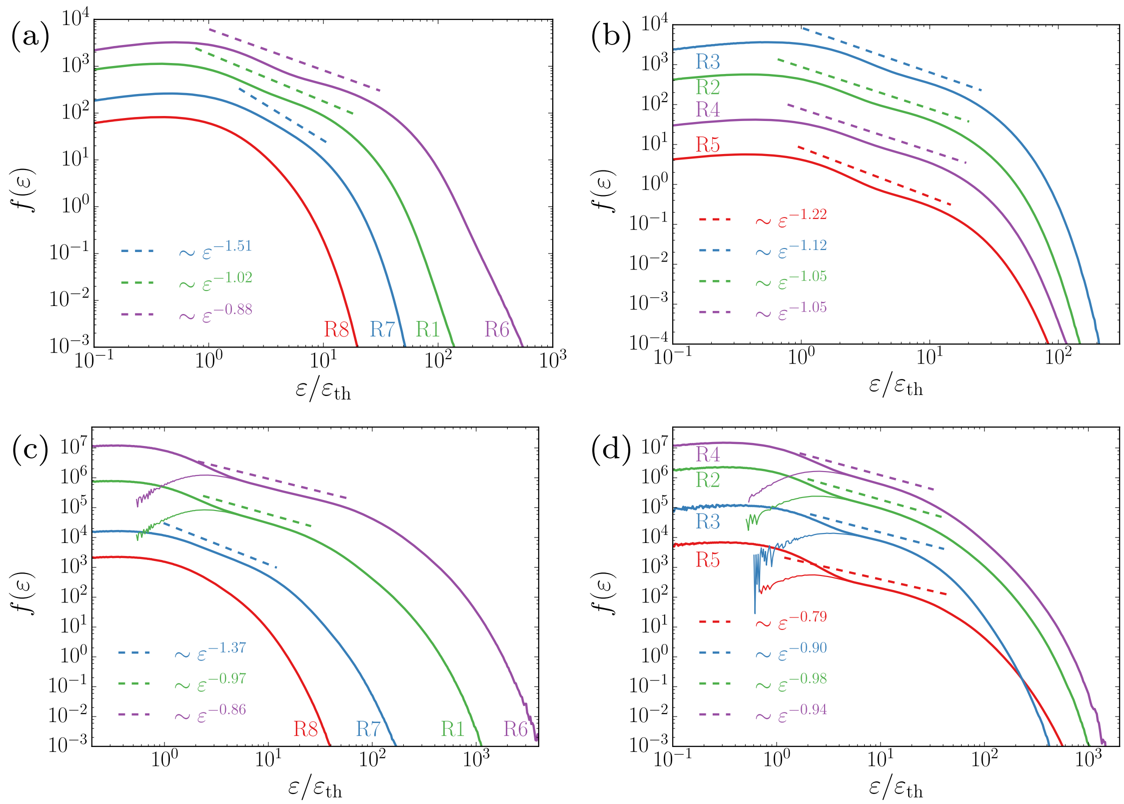

Figure 5.6 Particle energy spectra for different simulations. $f(\varepsilon) \equiv dN/d\varepsilon$. We normalize the kinetic energy ε to the initial thermal energy $\varepsilon_{\mathrm{th}}$, which is same for both electrons and ions in our simulations. (a) Electron spectra for 4 runs with different plasma β. R8 has a $\beta_e = 0.2$. R7 has $\beta_e = 0.07$. R1 has $\beta_e = 0.02$. R6 has the lowest $\beta_e = 0.007$. (b) Electron spectra for 4 runs with the same β, but different plasma temperature. Among them, R5 has a different mass ratio $m_i/m_e = 100$. (c) Ion spectra for the 4 runs with different plasma β. (d) Ion spectra for the 4 runs with the same plasma β but different plasma temperature. All the dashed lines are power-law spectrum through fitting. For electrons, we fit the power-law spectrum over the whole distribution. For ions, we subtract the lower-energy thermal core to get the nonthermal component (thin solid lines in (c) and (d)). We then fit the power-law spectrum over the nonthermal component.

lower-β cases. The large nonthermal fractions suggest that the nonthermal particles can dominate the reconnection process of low β plasma.

We track individual particles in run R1 to identify various particle acceleration regions. We choose electrons that are energetic by the end of the simulation. These electrons are accelerated either in X-type regions by the parallel electric field and reconnection electric field, in contracting magnetic islands through the *Fermi* mechanism or in island merging regions by the anti-reconnection electric field. Figure 5.7 shows three typical electron trajectories in this simulation. The electron in Figure 5.7 (a) enters the reconnection region when two islands are merging. It bounces twice and get energized at $x \sim 116 - 124d_i$ in the large island formed by the merging islands. It then enters the anti-reconnection region and get accelerated in $10\Omega_{ci}^{-1}$. We calculate the electron's y position by integrating v_y over time in this 2D simulation. During the fast energization, this electron moves along the y-direction to $-40d_i$. This electron is then circling around the large island as the whole island is moving towards the right direction. This rightward motion induces opposite $E_y \approx v_x B_z$ at the two sides of the island as B_z changes sign (frame $t\Omega_{ci} = 241.7$). As the electron is drifting along the positive y-direction ($x \sim 120 - 160d_i$), it gets accelerated at one side and decelerated at the other side. The net effect is an acceleration because this island is contracting, which is an efficient particle acceleration mechanism during reconnection (Drake et al., 2006). In the end, this island merges with the large island at the boundary, and the electron gets trapped at the left side by the mirror force. The top panel of (d) shows the energy evolution of this electron. Figure 5.7 (b) shows another electron getting accelerated through the island contracting mechanism. It gets accelerated at the X-type region ($x \sim 90d_i$) when it enters the reconnection region. Both its energy and y-position have a jump at $t\Omega_{ci} = 116$. The electron is then accelerated in three regions of contracting islands shown with different sizes at $t\Omega_{ci} = 116$, $t\Omega_{ci} = 222.4$ and $t\Omega_{ci} = 497.9$. The electron gets energized every time it passes the two sides of these islands. As the island gets larger, the electron has to travel longer around the island to get accelerated. As a result, the acceleration becomes slower, as shown in the middle panel of (d). The electron shown in Figure 5.7 (c) enters the same island merging region as the electron in (a), but it does not pass the anti-reconnection region. Instead, it gets efficiently accelerated in the compressed region when these two merging islands are getting close to each other. The electron is then trapped in the merged large island and is convected with the reconnection outflow to $x \sim 160d_i$. This electron is not circling around the island but shows meandering characteristics at $t\Omega_{ci} = 265.9$. The electron does not gain much energy or drift along the y-direction. After some meandering, the electron is then trapped at the left end of the largest island by the mirror force. The acceleration is more efficient than that of the electron in (b) as the electron does not have to travel around the whole island.

Figure 5.8 shows three typical ion trajectories in run R1. In general, ions also gain energy at the X-type region, the island contracting regions and the island merging regions similar to electrons. One difference between ion acceleration and electron acceleration is that ions can be "picked-up" by the reconnection outflow when they enter the reconnection region. The ions gain energy $\sim 0.5m_iv_A^2$ is much larger than the electron energy gain $\sim 0.5m_ev_A^2$ during this process. For example, the ion in (a) enters the reconnection region at $x \sim 90d_i$ and then moves to $x \sim 100d_i$

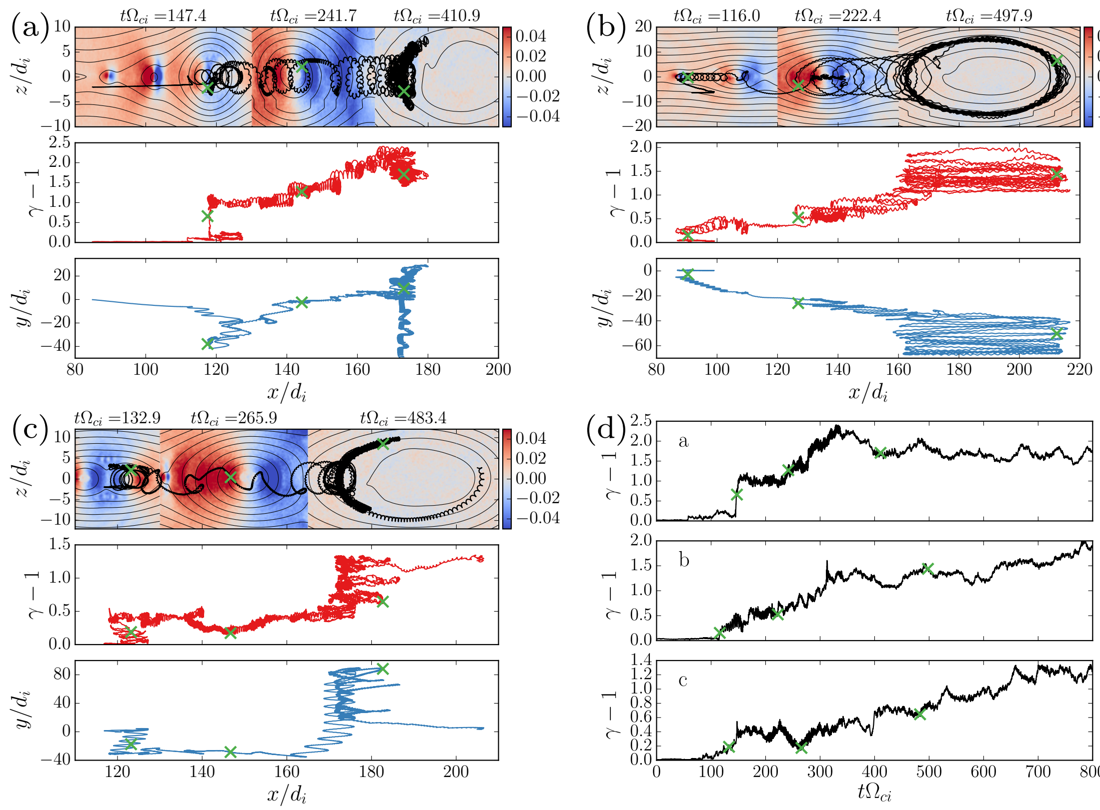

Figure 5.7 Three typical electron trajectories in run R1. The top panels of (a)–(c) show the trajectories in the simulation $x - z$ plane. The background is the out-of-plane electric field E_y. We plot E_y at three time frames, labeled at the top in (a)–(c). The green crosses are the particle position at that time step. The middle panels of (a)–(c) show the electron energy evolution with its x position. The bottom panels show the electron's y position versus its x position. We calculate the y position by integrating v_y over time. The green crosses correspond to 3 time frames indicated in the top panels. Note that the x can be larger than $200d_i$ in these two plots. As particles can cross the right boundary and come back from the left boundary due to the periodic boundary condition, we shift the leftmost trajectory points to the right. (d) The time evolution of the electron kinetic energies for the three electrons plotted in (a)-(c). Again, the green crosses corresponds to the three time steps for each electron.

without a whole gyromotion. Its energy gradually increases (top panel of (d)) and the ion drifts along the positive y-direction during this period. The ions in (b) and (c) also have similar phase at $200 - 250\Omega_{ci}^{-1}$ and $120 - 150\Omega_{ci}^{-1}$, respectively. The "pick-up" mechanism was originally proposed for heavy ions (e.g., α particles, Drake et al., 2009a,b), but it seems to work for protons too. The ion in (a) gets further accelerated by the contracting islands as shown in time frame $t\Omega_{ci} = 193.3$ and $t\Omega_{ci} = 531.7$. It drifts along the y-direction to $160d_i$ at the end of the simulation. The ion in (b) gets efficiently accelerated in an island merging region from $250\Omega_{ci}^{-1}$ to $300\Omega_{ci}^{-1}$. It gets efficiently energized because it drifts along the negative y-direction, same as E_y. Figure 5.8 (c) shows that one ion gets accelerated through the pickup process first and then through bouncing back and forth inside the contracting island.

5.3.4 Energy conversion in different regions

Examining particle trajectories can help identify various acceleration regions, but the fact that we can only trace a small number of them makes it hard to decide which sites are more important in leading to the bulk acceleration of $> 50\%$ of the particles. Besides, the trajectories show that particle acceleration is associated with particle drift motions, but we can not tell which drift motion is the dominate one. To answer these questions, instead of tracking individual particles, we can study macroscopic quantities that characterize the energy conversion processes.

The conversion between the kinetic energy and plasma kinetic energy is through the work done by the electric force on the particles $\int\int_0^{t_0} \boldsymbol{j}\cdot\boldsymbol{E}dtd\boldsymbol{r}$. For a single particle

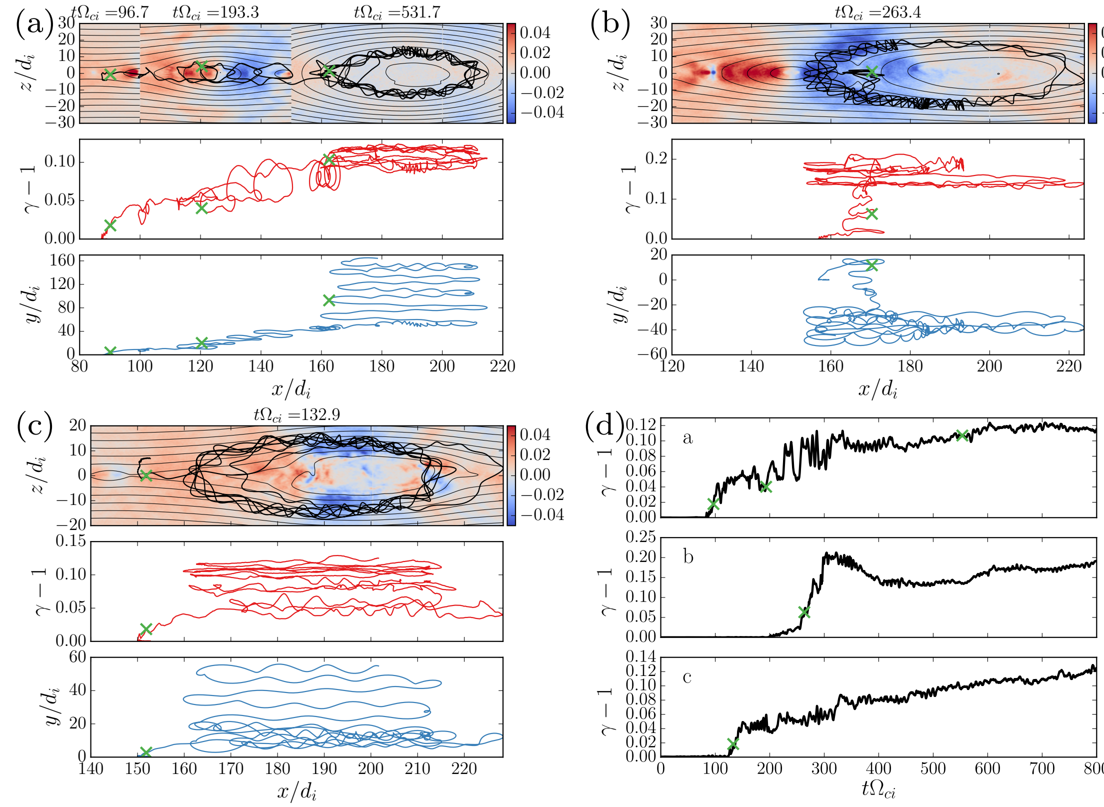

Figure 5.8 Typical ion trajectories in run R1. The plots are similar to electrons in Figure 5.7. (a) One ion has three phases of acceleration. The plot in (b) and (c) is similar except that we plot one frame of E_y. (d) Time evolution of ion energy $\gamma - 1$ for the three ions.

species, the parallel and perpendicular current densities are

$$\boldsymbol{j}_\parallel = qn\boldsymbol{v}_\parallel, \quad \boldsymbol{j}_\perp = qn\boldsymbol{v}_\perp \tag{5.1}$$

where q is the particle charge, n is the particle number density, $\boldsymbol{v}_\parallel$ and $\boldsymbol{v}_\perp$ are the parallel and perpendicular bulk velocities obtained by averaging over the particles. The parallel and perpendicular directions are with respect to the local magnetic field direction. $\dot{\varepsilon}_c \equiv \boldsymbol{j} \cdot \boldsymbol{E}$ is the energy conversion rate between the magnetic energy and the plasma kinetic energy, where $\boldsymbol{E}$ is the electric field. Figure 5.9 shows $\dot{\varepsilon}_c$ through

$\boldsymbol{j}_\parallel$ and $\boldsymbol{j}_\perp$ for run R1. At the beginning of the simulation, $\boldsymbol{j}_\parallel \cdot \boldsymbol{E}$ is comparable with $\boldsymbol{j}_\perp \cdot \boldsymbol{E}$ for electrons but negligible for ions. Electrons get energized by parallel electric field along the reconnection separatrix when they enter the reconnection region (Drake et al., 2005; Egedal et al., 2012). These electrons are further accelerated in the X-type region by the reconnection electric field (Fu et al., 2006). The parallel electric field is inefficient at accelerating ions because ions have smaller parallel velocity and larger mass than electrons. This leads to weaker acceleration as $d\gamma/dt = (q/m)\boldsymbol{v} \cdot \boldsymbol{E}_\parallel \sim v_\parallel/m$, where γ is the Lorentz factor. As the reconnection evolves, $\boldsymbol{j}_\perp \cdot \boldsymbol{E}$ becomes dominant for both electron and ions. Towards the end of the simulation, $\boldsymbol{j}_\perp \cdot \boldsymbol{E}$ accounts for over 80% of the energy conversion from the magnetic energy to the particle kinetic energies. Table 5.3 and Table 5.4 summarize the energy conversion ε_c through $\boldsymbol{j}_\parallel$ and $\boldsymbol{j}_\perp$ for electrons and ions, respectively. The parallel energy conversion is $\sim$ 10% for both electrons and ions. The perpendicular energy conversion is $\sim$ 80% for electrons and increases to over 90% for ions. This suggests that particles are preferentially accelerated along the perpendicular direction to the local magnetic field.

We use a drift-current approximation to separate $\boldsymbol{j}_\perp$ into different terms, as shown in Section 4.3.3, to reveal the effect of $\boldsymbol{j}_\perp$ and hence the particle perpendicular motions. Assuming a gyrotropic pressure tensor (particles are magnetized), we get

$$\boldsymbol{j}'_\perp = \boldsymbol{j}_c + \boldsymbol{j}_g + \boldsymbol{j}_m + \boldsymbol{j}_p + \rho_s \frac{\boldsymbol{E} \times \boldsymbol{B}}{B^2} \tag{5.2}$$

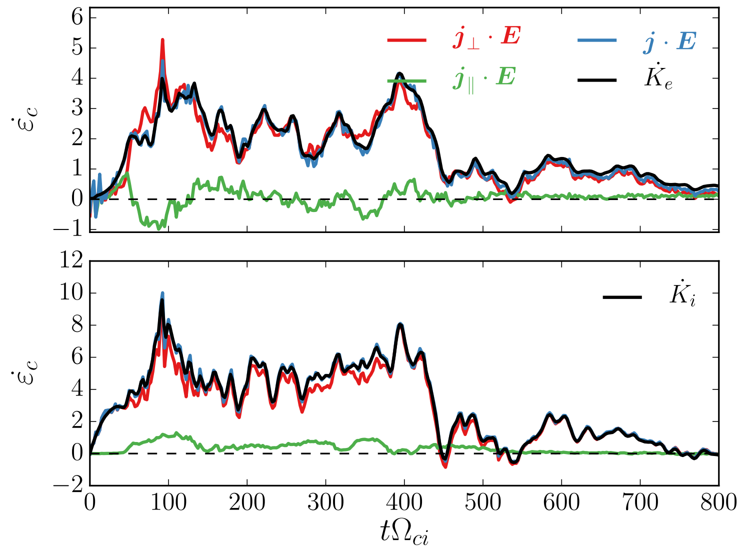

Figure 5.9 Energy conversion rate $\dot{\varepsilon}_c$ through parallel current $\boldsymbol{j}_\parallel \cdot \boldsymbol{E}$, perpendicular current $\boldsymbol{j}_\perp \cdot \boldsymbol{E}$ and total current $(\boldsymbol{j}_\parallel + \boldsymbol{j}_\perp) \cdot \boldsymbol{E}$ for electrons (top) and ions (bottom). The electric field $\boldsymbol{E}$ is from the PIC simulation. It includes both ideal and non-ideal electric fields. $\dot{K}_e$ and $\dot{K}_i$ are the energy change rate for electrons and ions. They are all normalized to $m_e c^2 \omega_{pe}$. The energy conversion for the other runs are summarized in Table 5.3 and Table 5.4.

Table 5.3. Energy conversion ε_c due to different currents for electrons. The results are the ratios of different terms to ΔK_e, e.g., $\int \boldsymbol{j}_c \cdot \boldsymbol{E} d\boldsymbol{x} dt / \Delta K_e$

Run	$\boldsymbol{j}_\parallel \cdot \boldsymbol{E}$	$\boldsymbol{j}_\perp \cdot \boldsymbol{E}$	$\boldsymbol{j}'_\perp \cdot \boldsymbol{E}$	$\boldsymbol{j}_c \cdot \boldsymbol{E}$	$\boldsymbol{j}_m \cdot \boldsymbol{E}$	$\boldsymbol{j}_g \cdot \boldsymbol{E}$	$\boldsymbol{j}_p \cdot \boldsymbol{E}$	$\boldsymbol{j}_a \cdot \boldsymbol{E}$
R1	0.10	0.81	0.77	1.51	-0.30	-0.58	0.04	0.10
R2	0.03	0.87	0.74	1.39	0.05	-0.80	0.03	0.07
R3	0.10	0.69	0.61	1.45	-0.20	-0.72	0.03	0.05
R4	0.11	0.85	0.82	1.28	-0.10	-0.53	0.04	0.13
R5	0.02	0.82	0.84	1.75	-0.03	-1.02	0.02	0.12
R6	0.04	0.87	0.98	1.34	-0.04	-0.52	0.06	0.14
R7	0.02	0.74	0.63	1.63	0.01	-1.12	0.02	0.09
R8	-0.08	0.73	0.43	2.43	-0.36	-1.70	0.03	0.03

Note. — $\boldsymbol{j}_\parallel$ is due to parallel electric field. $\boldsymbol{j}_\perp$ is due to perpendicular electric field. $\boldsymbol{j}_c$ is due to curvature drift. $\boldsymbol{j}_m$ is due to the magnetization. $\boldsymbol{j}_g$ is due to gradient B drift. $\boldsymbol{j}_p$ is due to polarization drift. $\boldsymbol{j}_a$ is due to the agyrotropic pressure tensor. $\boldsymbol{j}'_\perp = \boldsymbol{j}_c + \boldsymbol{j}_m + \boldsymbol{j}_g + \boldsymbol{j}_p + \boldsymbol{j}_a$

Table 5.4. Energy conversion ε_c due to different currents for ions. The results are the ratios of different terms to ΔK_i, e.g., $\int \boldsymbol{j}_c \cdot \boldsymbol{E} d\boldsymbol{x} dt / \Delta K_i$

Run	$\boldsymbol{j}_\parallel \cdot \boldsymbol{E}$	$\boldsymbol{j}_\perp \cdot \boldsymbol{E}$	$\boldsymbol{j}'_\perp \cdot \boldsymbol{E}$	$\boldsymbol{j}_c \cdot \boldsymbol{E}$	$\boldsymbol{j}_m \cdot \boldsymbol{E}$	$\boldsymbol{j}_g \cdot \boldsymbol{E}$	$\boldsymbol{j}_p \cdot \boldsymbol{E}$	$\boldsymbol{j}_a \cdot \boldsymbol{E}$
R1	0.10	0.91	0.88	1.78	-0.31	-0.70	0.17	-0.06
R2	0.10	0.92	0.99	1.74	0.15	-1.04	0.20	-0.06
R3	0.08	1.00	1.19	2.11	-0.15	-0.98	0.42	-0.21
R4	0.10	0.92	0.87	1.72	-0.08	-0.89	0.14	-0.02
R5	0.10	0.90	0.94	1.93	0.03	-1.14	0.24	-0.02
R6	0.12	0.91	0.99	1.47	-0.01	-0.60	0.16	-0.03
R7	0.10	0.94	0.97	2.30	0.13	-1.54	0.26	-0.18
R8	0.04	1.00	0.90	3.54	-0.28	-2.29	0.18	-0.25

Note. — $\boldsymbol{j}_c$ is due to curvature drift. $\boldsymbol{j}_m$ is due to the magnetization. $\boldsymbol{j}_g$ is due to gradient B drift. $\boldsymbol{j}_p$ is due to polarization drift. $\boldsymbol{j}_\parallel$ is due to parallel electric field. $\boldsymbol{j}_\perp$ is due to perpendicular electric field. $\boldsymbol{j}_a$ is due to the agyrotropic pressure tensor. $\boldsymbol{j}'_\perp = \boldsymbol{j}_c + \boldsymbol{j}_m + \boldsymbol{j}_g + \boldsymbol{j}_p + \boldsymbol{j}_a$

where $p_\parallel$ and $p_\perp$ are parallel and perpendicular pressure with respect to the local magnetic field; I is the unit dyadic; $\hat{\boldsymbol{b}} = \boldsymbol{B}/B$ is the unit vector along the magnetic field. We calculate $p_\parallel$ and $p_\perp$ using the particle distribution f in each cell. $\boldsymbol{j}_c$ is due to particle curvature drift, $\boldsymbol{j}_m$ is due to the magnetization (originated from particle gyro-motion), $\boldsymbol{j}_g$ is due to particle gradient B drift, $\boldsymbol{j}_p$ is due to particle polarization drift. The $\boldsymbol{E}\times\boldsymbol{B}$ drift does not contribute to the energy conversion since $\boldsymbol{j}_{\boldsymbol{E}\times\boldsymbol{B}}\cdot\boldsymbol{E} = 0$.

A gyrotropic pressure tensor assumes that particles are well-magnetized. In the low-β simulations, electrons are well-magnetized since the electron gyroradius is much smaller than the fields variation scale d_e as $\rho_e/d_e = \sqrt{\beta_e/2} \ll 1$. Note, $\rho_e = m_e v_e/eB$ can be comparable with d_e in the diffusion regions with weak magnetic field or for energetic electrons, and it can be larger than d_e in high-β simulations where $\sqrt{\beta_e/2} \sim 1$. The non-gyrotropic effect gets more important for ions as their gyroradii are much larger than that of electrons. To estimate the effect, we define an agyrotropic current density as

$$\boldsymbol{j}_a \equiv -\frac{c}{B^2}\left[\nabla\cdot\left(\mathbf{P} - p_\perp\mathbf{I} - (p_\parallel - p_\perp)\hat{\boldsymbol{b}}\hat{\boldsymbol{b}}\right)\right]\times\boldsymbol{B} \tag{5.3}$$

which measures the differences of using a full pressure tensor $\mathbf{P}$ and a gyrotropic pressure tensor.

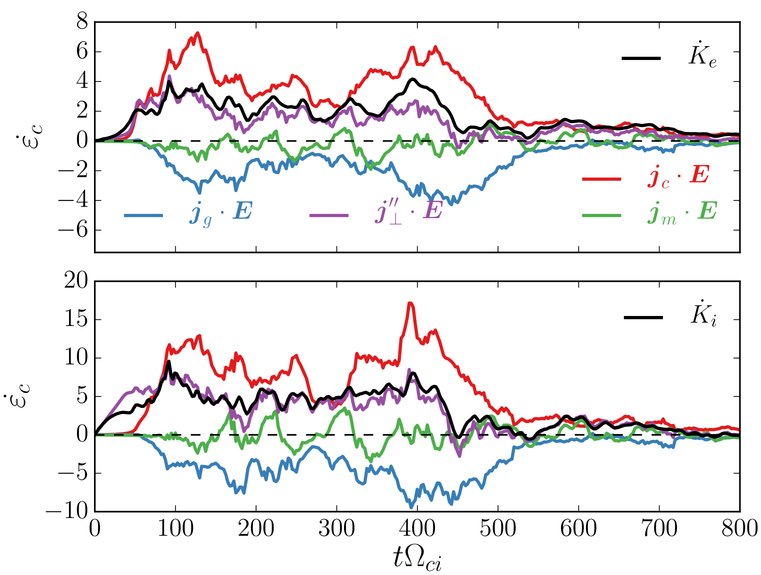

Figure 5.10 Energy conversion due to different drift currents for electrons (top) and ions (bottom) for run R1. $\boldsymbol{j}_c$ is due to particle curvature drift. $\boldsymbol{j}_g$ is due to particle ∇B drift. $\boldsymbol{j}_m$ is due to magnetization. $\boldsymbol{j}''_\perp \equiv \boldsymbol{j}_c + \boldsymbol{j}_g + \boldsymbol{j}_m$, which does not include the current densities due to particle polarization drift and agyrotropic pressure tensor. $\dot{K}_e$ and $\dot{K}_i$ are the energy change rate for electrons and ions, respectively. They are all normalized to $m_e c^2\omega_{pe}$.

Figure 5.10 shows the energy conversion rate $\dot{\varepsilon}_c$ due to curvature drift current $\boldsymbol{j}_c$, ∇B drift current $\boldsymbol{j}_g$ and magnetization $\boldsymbol{j}_m$ for run R1. The current due to curvature drift $\boldsymbol{j}_c$ gives most of the energy conversion, suggesting particles are preferentially accelerated when they are curvature drifting along the perpendicular electric field. The current due to ∇B drift gives non-negligible energy loss, although it gives net particle energy gain in the flux pileup region (Hoshino et al., 2001; Li et al., 2015). The energy conversion through magnetization current $\boldsymbol{j}_m$ varies between energy gain and energy loss, but the net effect is small compared to $\boldsymbol{j}_c$ and $\boldsymbol{j}_g$. We also plot $\boldsymbol{j}''_\perp = \boldsymbol{j}_c + \boldsymbol{j}_g + \boldsymbol{j}_m$ in Figure 5.10. In general, $\boldsymbol{j}''_\perp$ captures the time evolution of $\dot{\varepsilon}_c$ well, but it misses some features. For example, $\boldsymbol{j}''_\perp$ underestimates $\dot{\varepsilon}_c$ for ions at the beginning of the simulation. This might be due to the fact that $\boldsymbol{j}_p$ or $\boldsymbol{j}_a$ are not included in $\boldsymbol{j}''$. Thus, we include $\boldsymbol{j}_p$ and $\boldsymbol{j}_a$ in Figure 5.11 for run R1. For electrons,

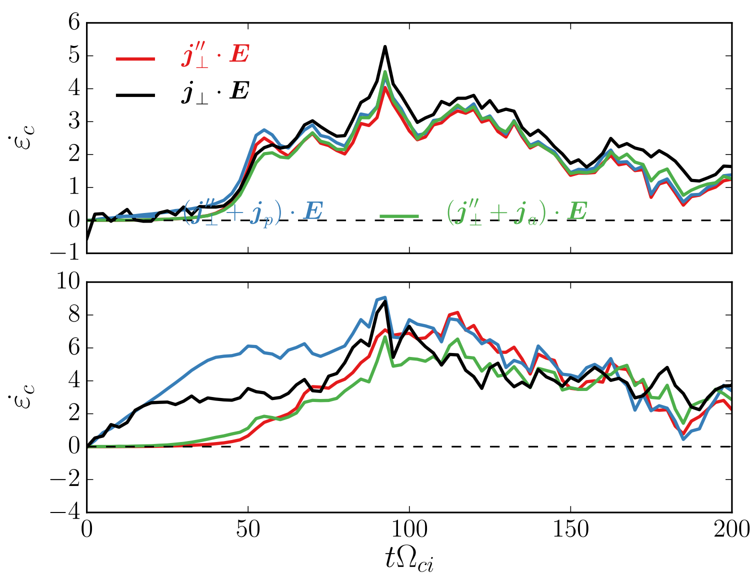

Figure 5.11 Energy conversion rate through perpendicular current densities for electrons (top) and ions (bottom) for run R1. $\boldsymbol{j}_\perp = nq\boldsymbol{u}_\perp$, and $\boldsymbol{j}''_\perp$ is the summation of the current densities due to particle curvature drift, ∇B drift and magnetization. $\boldsymbol{j}_p$ is due to particle polarization drift. $\boldsymbol{j}_a$ is due agyrotropic pressure tensor. The plotted quantities are normalized to $m_e c^2 \omega_{pe}$.

$\boldsymbol{j}_a$ yields negligible effect because electrons are well-magnetized at $\beta_e = 0.02$. $\boldsymbol{j}_p$ also gives a negligible effect because the polarization drift is proportional to the electron mass. Towards the end of the simulation, $\boldsymbol{j}_p$ yields 4% of the electron energy gain; $\boldsymbol{j}_a$ yields 10% of the electron energy gain. For ions, both $\boldsymbol{j}_a$ and $\boldsymbol{j}_p$ give noticeable effects. Comparing $\boldsymbol{j}_\perp''$ (red) and $(\boldsymbol{j}_\perp'' + \boldsymbol{j}_a) \cdot \boldsymbol{E}$ (green), $\boldsymbol{j}_a$ yields a cooling effect when ions are more energized later in the simulation ($> 75\Omega_{ci}^{-1}$). $\boldsymbol{j}_p$ is more important at the beginning of the simulation when the outflow accelerates along the x-direction. It overestimates the perpendicular current densities. This might be due to numerical uncertainties when calculating the time derivative $d\boldsymbol{u}/dt$ which requires a $\boldsymbol{u}$ field with high time resolution ($< \omega_{pi}^{-1}$), while the time resolution of $\boldsymbol{u}$ fields output in run R1 is $12.5\omega_{pi}^{-1}$. $\boldsymbol{j}_p$ gives 17% of the ion energy gain, while $\boldsymbol{j}_a$ contribute 6% of the ion energy loss in run R1. We summarize the contributions of all drift currents in Table 5.3 and Table 5.4. For all runs, $\boldsymbol{j}_c \cdot \boldsymbol{E}$ is dominant; $\boldsymbol{j}_p$ gives non-negligible particle cooling; $\boldsymbol{j}_m$ gives cooling effect for 6 of the 8 runs and can be over 30% for run R1 and R8. For electrons, $\boldsymbol{j}_p \cdot \boldsymbol{E}$ contributes $\leq 6\%$ of the energy conversion, and $\boldsymbol{j}_a$ contributes $\leq 15\%$ of the energy conversion. For ions, $\boldsymbol{j}_p \cdot \boldsymbol{E}$ gives $14\% - 42\%$ of the ion energy gain; $\boldsymbol{j}_a \cdot \boldsymbol{E}$ gives net ion cooling and it gets more important with higher β (run R7 and R8) because of increasing fraction of unmagnetized particles in high-β plasma.

Next, we use the drift-current analysis to study the energy conversion in different acceleration regions. Figure 5.12 gives the energy conversion in one reconnection exhaust ($145d_i < x < 185d_i$) for run R1 at $t\Omega_{ci} = 137.5$. For both electrons and ions, $\boldsymbol{j}_c \cdot \boldsymbol{E}$ is the dominant term, and $\boldsymbol{j}_g \cdot \boldsymbol{E}$ cools the particles. Both terms peak in the center of the exhaust where the curvature of the magnetic field and ∇B are the largest. $\boldsymbol{j}_c \cdot \boldsymbol{E} \approx (p_\parallel \boldsymbol{B} \times \boldsymbol{\kappa}/B^2) \cdot (-\boldsymbol{u} \times \boldsymbol{B})$ is positive as $\boldsymbol{u}$ and $\boldsymbol{\kappa}$ are along the same direction.

$\boldsymbol{j}_g \cdot \boldsymbol{E} \approx (p_\perp/B^3)(\boldsymbol{B} \times \nabla B) \cdot (-\boldsymbol{u} \times \boldsymbol{B})$ is negative as $\boldsymbol{B} \times \nabla B$ and $-\boldsymbol{u} \times \boldsymbol{B}$ are along the opposite directions. $\boldsymbol{j}_c \cdot \boldsymbol{E}$ is stronger than $\boldsymbol{j}_g \cdot \boldsymbol{E}$ in this region, so particles gain energy passing through the reconnection exhausts. The other terms are small compared to these two terms. $\boldsymbol{j}_\parallel \cdot \boldsymbol{E}$ is noisy as E_x shows electron holes (top-right panel of Figure 5.13 (a)), which has been associated with a pseudo electric potential that can accelerate electrons (Egedal et al., 2012), but the effect is small compared to the other terms in out simulations. When particles stream along the field line to the positive x-direction, electrons get decelerated while ions get accelerated. $\boldsymbol{j}_p \cdot \boldsymbol{E}$ is negligible for electrons compared to that for ions. It accelerates ions when the flow speed increases along the x-direction ($x \sim 150 - 175d_i$), as $\boldsymbol{j}_p \sim \boldsymbol{B} \times \dot{\boldsymbol{u}}_i$ is parallel to $-\boldsymbol{u} \times \boldsymbol{B}$. It decelerates ions when the flow slows down when it hits the magnetic structure at $x \sim 180d_i$. $\boldsymbol{j}_m \cdot \boldsymbol{E}$ strongly accelerates particles right outside the center of the reconnection exhaust. This is due to the enhanced $\boldsymbol{j}_p$ driven by the strong gradient of perpendicular pressure $p_\perp$. In the center of the exhaust, $\nabla \times (\boldsymbol{B}/B^2)$ becomes large due to a weaker B and a stronger $\nabla \times \boldsymbol{B}$ since the magnetic field must rotate 180° across a thin layer ($\sim d_e$). The strong acceleration and deceleration cancel each other, and the $\boldsymbol{j}_m \cdot \boldsymbol{E}$ gives negligible effect. The energy conversion due to the agyrotropic current $\boldsymbol{j}_a \cdot \boldsymbol{E}$ peaks at the center of the current sheet where particles can become unmagnetized due to the weak magnetic field. For electrons, this region is narrow, so $\boldsymbol{j}_m \cdot \boldsymbol{E}$ is negligible. For ions, the region is comparable with the whole reconnection exhaust, so the effect is noticeable.

Figure 5.14 shows the energy conversion in a region where two magnetic islands are merging ($x \sim 115 - 120d_i$). A secondary current sheet along the z-direction forms

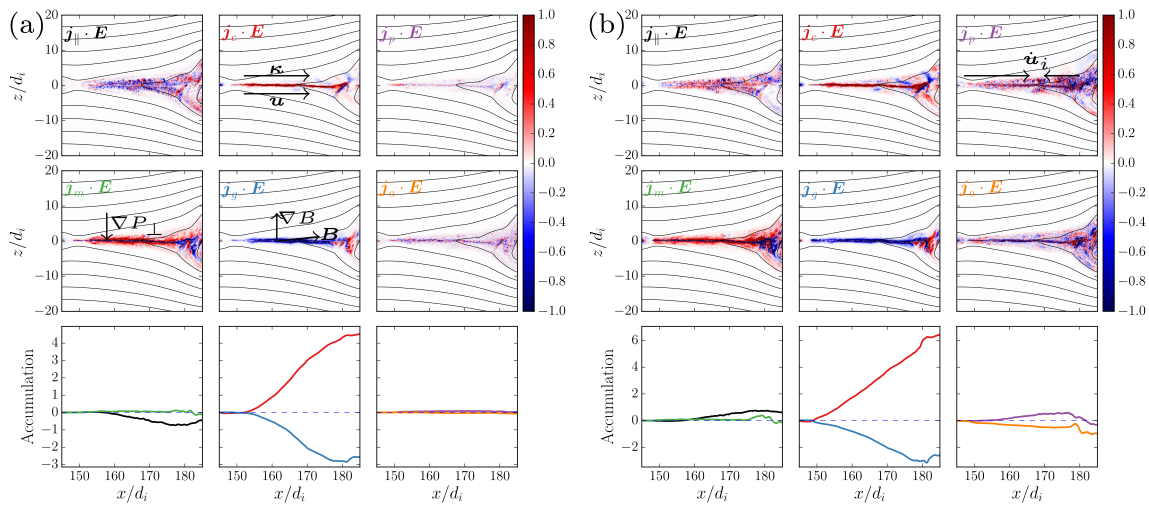

Figure 5.12 Energy conversion in the reconnection exhaust for run R1 at $t\Omega_{ci} = 137.5$ for (a) electrons, (b) ions. The top two rows plot the 2D contour of different terms. They are normalized to $0.1en_0 v_A^2 B_0$, where v_A is the Alfvén speed. The bottom panels are the accumulation of the top panels along the x-direction, e.g., $\int_{x0}^{x}\int_{z_{\min}}^{z_{\max}} \boldsymbol{j}_c \cdot \boldsymbol{E} dxdz$. Overplotted are the directions of magnetic curvature $\boldsymbol{\kappa}$, bulk flow velocity $\boldsymbol{u}$, ∇B, the magnetic field $\boldsymbol{B}$, the acceleration of the ion bulk flow velocity $\dot{\boldsymbol{u}}_i = d\boldsymbol{u}_i/dt$ and the gradient of the perpendicular pressure $\nabla p_\perp$.

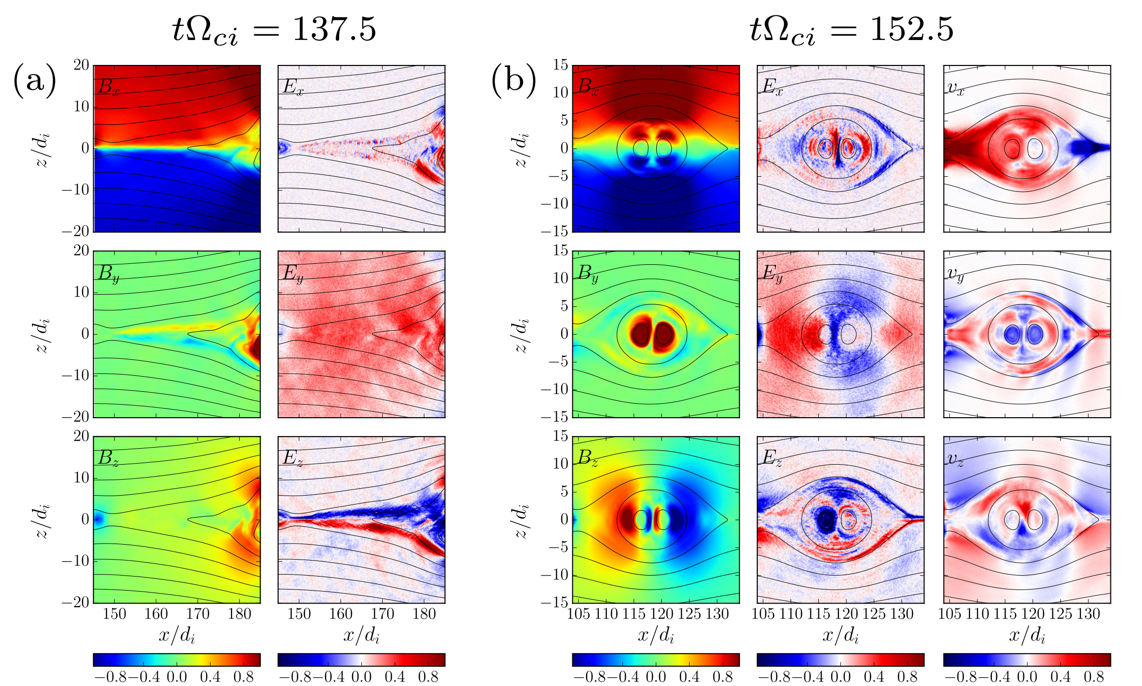

Figure 5.13 (a) Electric field and mangetic field at $t\Omega_{ci} = 137.5$, corresponding to Figure 5.12. (b) Electric field, magnetic field and flow velocity at $t\Omega_{ci} = 152.5$, corresponding to Figure 5.14. The magnetic field is normalized to B_0. The electric field is normalized to $v_A B_0$. The velocity is normalized to $v_A/2$.

in this process at $x \sim 117d_i$ by antiparallel B_z as shown in the bottom left panel of Figure 5.13 (b). This current sheet has a guide field along y-direction. This guide field originates from the initial force-free setup. Figure 5.14 shows efficient electron acceleration by parallel electric field, consistent with previous results where efficient parallel acceleration occurs in a guide-field reconnection (Dahlin et al., 2014) (see also next chapter). $E_\parallel$ is, however, inefficient at accelerating ions. This is because $d\gamma/dt = (q/m)\boldsymbol{v} \cdot \boldsymbol{E}_\parallel \sim v_\parallel/m$ is much smaller for ions as ions have much smaller $\boldsymbol{v}_\parallel$ and larger m than that of electrons. Both $\boldsymbol{j}_c \cdot \boldsymbol{E}$ and $\boldsymbol{j}_g \cdot \boldsymbol{E}$ give strong energy conversion in the island merging region. Similar as the main reconnection site (B_x reconnects), $\boldsymbol{j}_c \cdot \boldsymbol{E}$ strongly accelerates particles, while $\boldsymbol{j}_g \cdot \boldsymbol{E}$ strongly decelerates particles. $\boldsymbol{j}_p \cdot \boldsymbol{E}$ is negligible for electrons but important for ions. It decelerates ions at $x \sim 117 - 120d_i$ and $z \sim -5 - 5d_i$ due to the decelerated v_z. The closed field lines containing the two small islands block the bulk flow v_z at $z \sim -5d_i$ and $5d_i$, as shown in the bottom right panel of Figure 5.13 (b). $\boldsymbol{j}_a \cdot \boldsymbol{E}$ is comparable with $\boldsymbol{j}_c \cdot \boldsymbol{E}$, suggesting that the gyrotropic pressure tensor is not a good assumption in the island merging region. This is because particle gyroradii are large as the magnetic field is weak in islands merging region (Figure 5.13 (b) left panels) and the particles are pre-accelerated to higher energies. Note that $\boldsymbol{j}_a \cdot \boldsymbol{E}$ accelerates both electrons and ions in the island merging region.

Besides the island merging region, contracting islands are also efficient at accelerating particles. The large island formed by the merging islands in Figure 5.14 is contracting as indicated by the opposite v_x at the two opposite sides of this island (top right panel of Figure 5.13). The dominant positive v_x indicates this island is

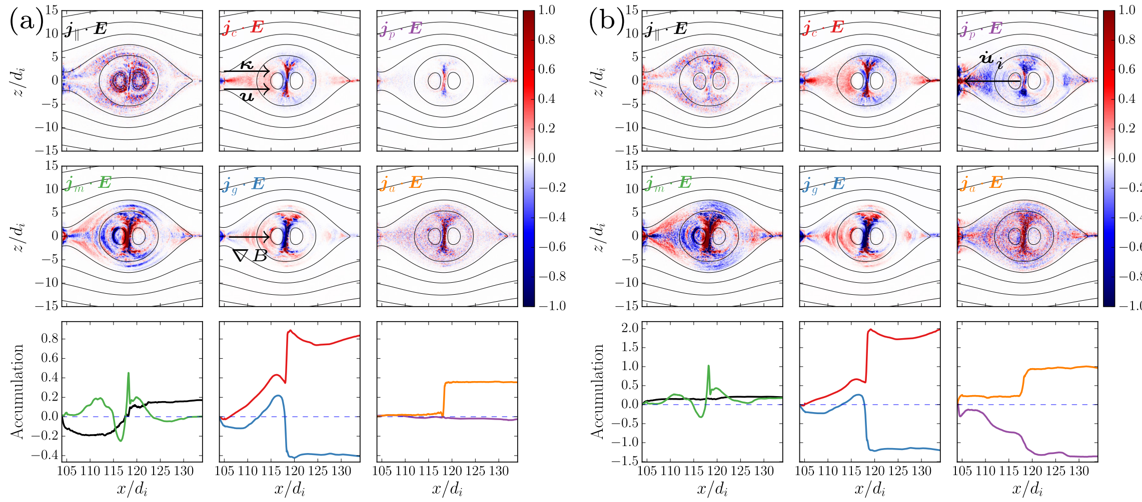

Figure 5.14 Energy conversion in an island merging region for run R1 at $t\Omega_{ci} = 152.5$ for (a) electrons and (b) ions. Overplotted arrows are the direction of magnetic field curvature $\boldsymbol{\kappa}$, the bulk flow $\boldsymbol{u}$, the gradient of magnetic field ∇B and the acceleration of the ion flow.

moving rightward, opposite to the contracting direction of the right side of this island. This leads to a region ($x \sim 120 - 127 d_i$) with small v_x hence weak $E_y \approx v_x B_z$. We limit the following discussion in the left side ($x \sim 105 - 115 d_i$) of this contracting island. Both $\boldsymbol{j}_c \cdot \boldsymbol{E}$ and $\boldsymbol{j}_g \cdot \boldsymbol{E}$ accelerates particles as $\boldsymbol{\kappa}$, ∇B and $\boldsymbol{u}$ are along the same direction. $\boldsymbol{j}_p \cdot \boldsymbol{E}$ is efficient at decelerating ions as the bulk flow is slowing down along the x-direction (top right panel of Figure 5.13), so $\boldsymbol{j}_p \sim \boldsymbol{B} \times \dot{\boldsymbol{u}}_i$ is along the same direction as $-\boldsymbol{u} \times \boldsymbol{B}$. The other terms are negligible compared to these three terms. Notice that $\boldsymbol{j}_m \cdot \boldsymbol{E}$ is efficient at local regions, but its total effect is negligible when integrated over the entire simulation box.

5.4 Discussion and Conclusion

Nonthermal particle acceleration is a central topic of space physics and astrophysics. In this chapter, we perform a series of 2D kinetic simulations to examine the particle acceleration during magnetic reconnection in a nonrelativistic plasma with electron β_e ranging from 0.007 to 0.2. We achieve the low-β of a thin current sheet by increasing the magnetic field strength or decreasing the plasma temperature. We study both electrons and ions.

The initial current sheet breaks into a chain of magnetic islands, which interact and coalesce with each other. Magnetic energy gets converted into plasma energy during this process. Although the reconnection rate only weakly increase when plasma β decreases, the energy conversion is much more efficient in a low-β reconnection than in a high-β reconnection. We find that the reconnection in a low-temperature plasma is more efficient at accelerating electrons than in a high-temperature plasma. We also find that the low-β reconnection is more efficient at accelerating ions than electrons. The highly efficient energy conversion in the low-β reconnection drives efficient nonthermal particle acceleration yielding over 50% of particles being nonthermal in the low-β reconnection. Both nonthermal electrons and ions develop power-law energy distributions with power-law index $p \sim 1$ in the low-β regime ($\beta_e \leq 0.02$). The highly efficient electron acceleration could explain the highly efficient nonthermal electron acceleration during solar flares. However, the power-law spectrum is much harder than the observed electron spectrum ($p > 2$). In addition, the maximum particle energy is limited by the hard spectrum and the total dissipated magnetic energy. One possible reason for the hard spectrum may be the periodic boundary conditions we use. Such a boundary condition leads to confinement of particles. For a system such as the reconnection region of solar flares, open boundary conditions for particles may be more appropriate. Analytically, this could lead to a steeper power-law spectrum (Guo et al., 2014, 2015). Our preliminary results show that the power-law index p can be larger than 2 in simulations with open boundaries.

We identify various particle acceleration regions through particle tracking in our simulation. Both electrons and ions get efficiently accelerated when they are drifting along the electric field induced by the bulk flow in the X-type region, contracting magnetic islands, anti-reconnection region where two islands are merging. Furthermore, protons (ions) gain energy when they are "picked-up" by the reconnection outflow. This initial fast energy gain makes ions more energetic than electrons, so that they can be accelerated more efficiently through the *Fermi* mechanism later in the simulation. This provides a good explanation on why ions gain more energy than electron in our simulations.

By studying $\boldsymbol{j} \cdot \boldsymbol{E}$, we find that over 80% of the energy conversion is in the perpendicular direction to the local magnetic field. We construct $\boldsymbol{j}_\perp$ by averaging the particle drift motions and studying the energy conversion through the perpendicular direction. The major energy conversion mechanism is through particle curvature drift along the electric field induced by the reconnection outflow in the reconnection exhausts, at the two sides of contracting magnetic islands and in the islands merging regions. The ∇B gives non-negligible deceleration in the reconnection exhausts and island merging regions but significant acceleration at the two sides of contracting magnetic islands. The current due to particle polarization drift is negligible for electrons. Polarization drift accelerates ions in the reconnection exhausts where the flow is accelerating, but decelerates ions at the two sides of contracting islands and island merging regions where the flow is decelerating. The parallel electric field accelerates ions but decelerates electrons in the reconnection exhausts; it accelerates electrons but not ions in the island merging regions. The current due to magnetization gives both acceleration and deceleration in the reconnection exhausts and the island merging regions but the net effect is negligible. By considering the current density due to non-gyrotropic pressure tensor, we find that it gives particle acceleration in the island merging regions. This suggests that meandering particles can subject to acceleration due to non-gyrotropic pressure tensor.

In summary, we find that magnetic reconnection in nonrelativistic low-β proton-electron plasam is highly efficient at accelerating both electrons and ions into non-thermal energies. The plasma β is the controlling factor of particle acceleration. Either decreasing T or increasing B_0 have similar effects on the energy conversion and particle acceleration processes.

CHAPTER 6

PARTICLE ACCELERATION DURING MAGNETIC RECONNECTION WITH A GUIDE FIELD

6.1 Introduction

A guide field is the magnetic field component that is normal to the reconnecting component. Presence of guide field is expected to be natural in solar corona. Observations have shown that the guide field strength is correlated with the HXR emission, hence the nonthermal electron acceleration (Qiu et al., 2010). The guide field can vary throughout one solar flare (about 0.4–1.2 times of the reconnecting component in Qiu et al. (2010)).

A guide field changes the reconnection process through modifying the reconnection layer. Without a guide field, the transition from the collisional regime to the collisionless regime occurs when the current sheet thickness δ_{CS} approaches ion inertial length d_i. With a guide field, the transition occurs when $\delta_{CS} \sim \rho_s$ (Rogers et al., 2001), where $\rho_s = c_s/\Omega_{ci}$ is the ion sound radius, $c_s = \sqrt{\Gamma k_B(T_i + T_e)/m_i}$ is the ion sound speed, Γ is the adiabatic index.

$$\frac{d_i}{\rho_s} = \frac{c}{c_s}\frac{\Omega_{ci}}{\omega_{pi}} = \frac{c}{c_s}\frac{v_A}{c} = \frac{v_A}{c_s} \tag{6.1}$$

In coronal plasma, $v_A > c_s$ (see Appendix A), so that $d_i > \rho_s$. Depending on the guide field strength, the structure of the reconnection diffusion region is different due to the presence of pressure anisotropy (Le et al., 2013; Egedal et al., 2013). A guide field can lead to multiple resonance layers in 3D reconnection (Daughton et al., 2011; Baalrud et al., 2012; Liu et al., 2013b; Huang and Bhattacharjee, 2016) rather than only one resonance layer at the middle plane in 2D reconnection (see Section 2.1.4). The multiple resonance layer can interact with each other, leading to complex current layers (Liu et al., 2013b; Guo et al., 2014).

The effects of different acceleration mechanisms vary with the guide field strength. As the guide field strength increases, the parallel acceleration becomes more important for electrons (Dahlin et al., 2014), in contrast to the negligible parallel acceleration in reconnection without a guide field as discussed in the previous chapters. In addition, reconnection with a guide field preferentially accelerates heavy ions through a pickup process (Drake et al., 2009a,b; Drake and Swisdak, 2014; Knizhnik et al., 2011), in which unmagnetized heavy ions get "picked-up" by the reconnection outflow. The energy gain is proportional to the ion mass, so that heavy ions gain more energy.

However, these simulations have focused on high-β ($\beta > 0.1$) reconnection and find no power-law distribution of particles. As shown in the previous chapters, low-β reconnection without a guide field can efficiently accelerate both electrons and ions to develop power-law distributions, it is therefore natural to ask how a guide field can change the particle acceleration process in a low-β reconnection.

In this chapter, we perform 2D kinetic simulations of magnetic reconnection in a nonrelativistic low-β plasma ($\beta_e = 0.02$ using the reconnecting component of the magnetic field B_0) with a series of guide field $B_g/B_0 = 0$, 0.2, 0.5, 1.0 and 4.0. We examine how the energy spectra for both electrons and ions vary as function of B_g/B_0.

In Section 6.2, we describe the numerical methods and parameters. In Section 6.3 we present simulation results. In Section 6.4, we conclude on our simulations results.

6.2 Numerical simulations

We carry out two-dimensional kinetic simulations using the VPIC code (Bowers et al., 2008). The initial configuration is a force-free current sheet with an external guide field B_g.

$$\boldsymbol{B} = B_0 \tanh\left(\frac{z}{\lambda}\right)\hat{x} + B_0\sqrt{\mathrm{sech}^2\left(\frac{z}{\lambda}\right) + \frac{B_g^2}{B_0^2}}\hat{y} \tag{6.2}$$

corresponding to a magnetic field with uniform strength $\sqrt{B_0^2 + B_g^2}$ rotating by $2\arctan(B_0/B_g)$ across a layer with a half-thickness λ. We choose $\lambda = d_i$ in all simulations. $d_i = c/\omega_{pi} = c/\sqrt{4\pi n_i e^2/m_i}$ is the ion inertial length. The plasma consists of protons and electrons with mass ratio $m_i/m_e = 25$. The initial distributions for both electrons and protons are Maxwellian with uniform density n_0 and temperature $T_i = T_e = T_0$. We use the reconnection component B_0 to define the plasma β instead of the total magnetic field. $\beta \equiv 2\beta_e = 16\pi n_0 k T_0/B_0^2$, where β_e is the electron plasma. We set $\beta_e = 0.02$ for all simulations. The ratio of electron plasma frequency and gyrofrequency $\omega_{pe}/\Omega_{ce} = 1$. The Alfvèn speed using the reconnecting component of the magnetic field is $v_A = B_0/\sqrt{4\pi n_0 m_i} = 0.2c$. The domain sizes are $L_x \times L_z = 200d_i \times 100d_i$ for all simulations. The number of particle per species per cell is 200. We employ periodic boundaries along the x-direction and perfectly conducting boundaries along the z-direction for fields. We employ periodic boundaries along the x-direction and reflective boundaries along the z-direction for particles. We add a long wavelength perturbation to induce reconnection (Birn et al., 2001).

6.3 Simulation results

A guide field changes the field structures. Figure 6.1 shows the in-plane electric field E_z and the out-of-plane current density j_y for all five cases of B_g/B_0. In the case without a guide field, E_z is dominated by the Hall electric field $v_y B_x$, forming bipolar structures (e.g. $x \sim 95d_i$ in the top panel of (a)). When the guide field becomes large (e.g. $B_g = 4.0$), $E_z \sim E_y B_y / B_z$ due to the constraint that the force $\boldsymbol{E} \cdot \boldsymbol{B} \sim E_y B_y + E_z B_z$ is approximately zero (Drake et al., 2009a,b). E_z will be much larger than the reconnection electric field E_y, since $B_z \sim 0.1 B_x \ll B_y$. Figure 6.1 (a) shows the transition from a case without a guide field to a case with a strong guide field. The structure of j_y also varies with B_g. In the cases which have no guide field ($B_g = 0$) or weak guide field ($B_g = 0.2$), j_y is located in the center of the reconnection exhaust and close the reconnection X-line. As the guide field increases, j_y becomes centered along one pair of the reconnection separatrix. For example, in the case with $B_g = 0.5$, j_y is along the diagonal direction at $x \sim 105d_i$. The different structures of j_y form due to the pressure anisotropy (Le et al., 2013), which can be generated in collisionless plasma due to the conservation of magnetic moment and the longitudinal adiabatic invariant, and also by a fluid shear (e.g. Kunz et al., 2014) and a parallel electric field (e.g. Egedal et al., 2013). Appendix C shows one derivation of the generation of pressure anisotropy starting from the focused transport equation.

Table 6.1 lists the fraction of dissipated magnetic energy $\Delta\varepsilon_b/\varepsilon_{bx}$, the ratio of electron energy gain ΔK_e and ion energy gain ΔK_i to their initial energies at the end of the simulations. As B_g increases, $\Delta\varepsilon_b/\varepsilon_{bx}$ decreases from 49% to 14%, so that less magnetic energy is converted into plasma kinetic energy in reconnection with a stronger guide field. Particles gain less energy in the cases with a stronger guide field. The electron energy gain decreases slower with B_g than the ion energy gain. As a result, electrons gain more energy than ions in the cases when $B_g \geq 1$. In contrast, ions gain more energy than electrons when $B_g < 1$. This is consistent with previous chapters. When $B_g = 0$, we find ion acceleration dominates electron acceleration.

Figure 6.2 and Figure 6.3 show the time evolution of the electron and ion spectra. Both electron and ion spectra develop prominent nonthermal tails. The electron spectra (Figure 6.2) appear to be power-law in the energy range ($\varepsilon_{\text{th}} - 10\varepsilon_{\text{th}}$) in the cases with a moderate guide field ($B_g \leq 1$). The power-law spectrum extends to a higher energyrange in the case with a strong guide field.

Comparing to electrons, it is not obvious if the ion energy spectra are power-law. We do a power-law fitting below to check confirm they are power-laws. In the cases with a moderate guide field, the maximum particle energy saturate at $t\Omega_{ci} \sim 200 - 400$. In the case with $B_g = 4$, the maximum energies keeps increasing until $t\Omega_{ci} \sim 600$. The electron maximum energy does not vary much with B_g, but the

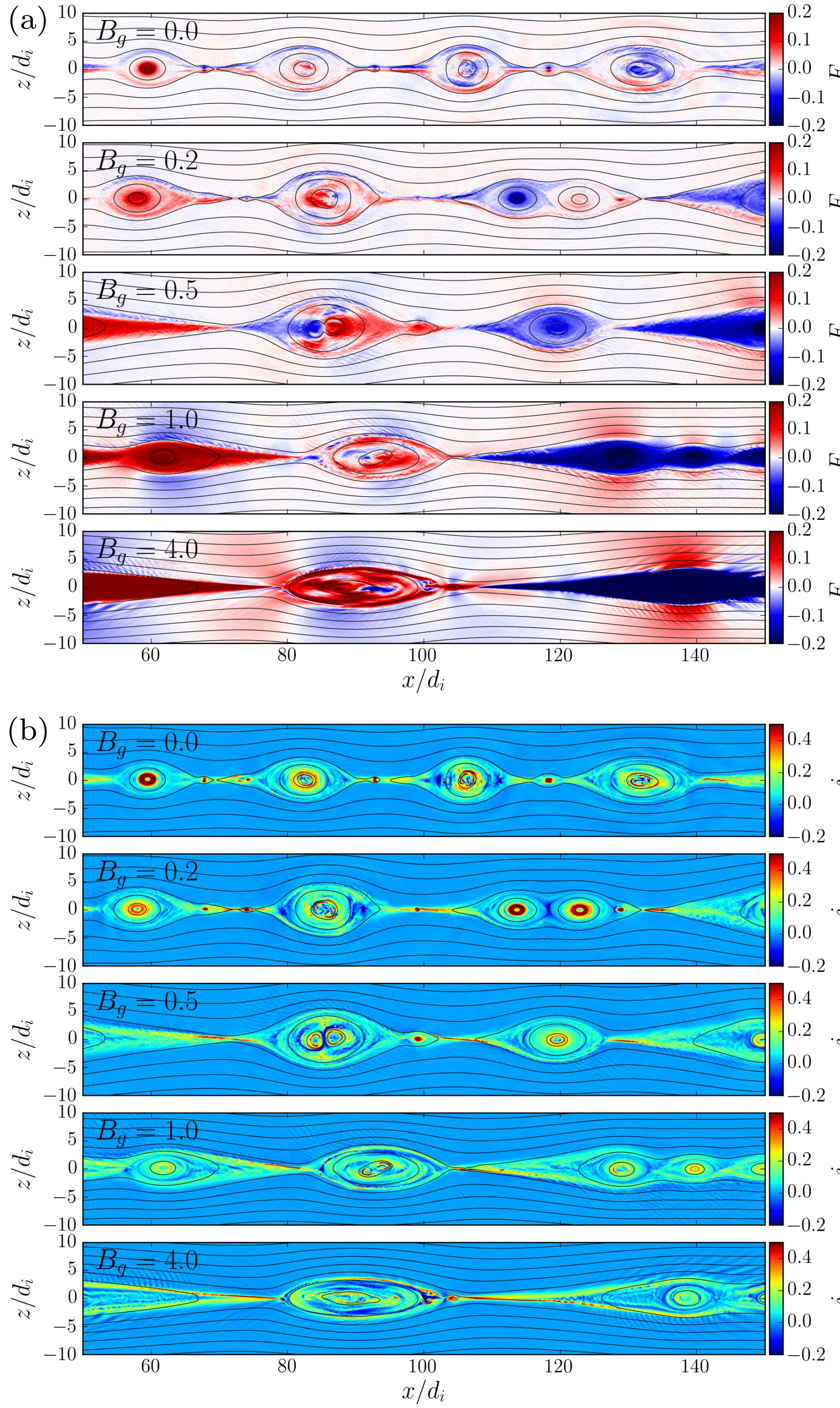

Figure 6.1 In-plane electric field E_z and out-of-plane current density j_y at $t\Omega_{ci} = 100$ except that the case with $B_g = 4.0$ is at $t\Omega_{ci} = 150$. E_z is normalized by cB_0. j_y is normalized by n_0ce.

Table 6.1. Energy conversion for different runs

B_g/B_0	$\lvert\Delta\varepsilon_b\rvert/\varepsilon_{bx}$	$\Delta K_e/K_{e0}$	$\Delta K_i/K_{i0}$	$F_{\rm nte}$	$F_{\rm nti}$	$K_{\rm nte}/K_e$	$K_{\rm nti}/K_i$
0.0	0.49	4.85	8.43	0.55	0.52	0.92	0.95
0.2	0.47	5.30	7.23	0.54	0.52	0.90	0.94
0.5	0.40	4.32	5.25	0.50	0.45	0.87	0.90
1.0	0.28	3.03	2.92	0.41	0.35	0.80	0.80
4.0	0.14	2.16	0.97	0.19	0.19	0.70	0.52

Note. — ΔK_e and ΔK_i are the energy gain for electrons and ions, respectively. K_{e0} and K_{i0} are the initial energy of electrons and ions, respectively. $N_{\rm nth}/N_0$ is the fraction of nonthermal particles. $\lvert\Delta\varepsilon_b\rvert/\varepsilon_{bx}$ is the fraction of dissipated magnetic energy. $F_{\rm nthe} = N_{\rm nthe}/N_0$ and $F_{\rm nthi} = N_{\rm nthi}/N_0$ are the fraction of nonthermal electrons and ions, respectively. $K_{\rm nthe}/K_e$ and $K_{\rm nthi}/K_i$ are the fraction energy that nonthermal electrons and ions contain, respectively.

ion maximum energy decreases sharply from $\sim 1400\varepsilon_{\rm th}$ in the case where $B_g = 0$ to $\sim 200\varepsilon_{\rm th}$ in the case where $B_g = 4$.

Figure 6.4 shows the final energy spectra for all the cases for electrons in panel (a) and ions in panel (b). For cases from $B_g = 0$ to $B_g = 1.0$, electrons develop into power-law distribution $f(\varepsilon) \sim \varepsilon^{-1}$ for $\varepsilon \in (\varepsilon_{\rm th}, 10\varepsilon_{\rm th})$. The electron spectra become steeper (power-law index ~ 1.3) in the cases with $B_g = 1$, and the power-law energy range is similar as the cases with a weaker guide field. The power-law energy range shift to a higher energy range in the case with $B_g = 4$, but the power-law index still remains ~ 1.3. Note that there is spectral hardening at $\varepsilon \sim 100\varepsilon_{\rm th}$ in the cases with $B_g = 0.5$ and 1.0, which might provide an alternative explanation for the electron spectral hardening at ~ 300 keV in solar flare observations (Li et al., 2013).

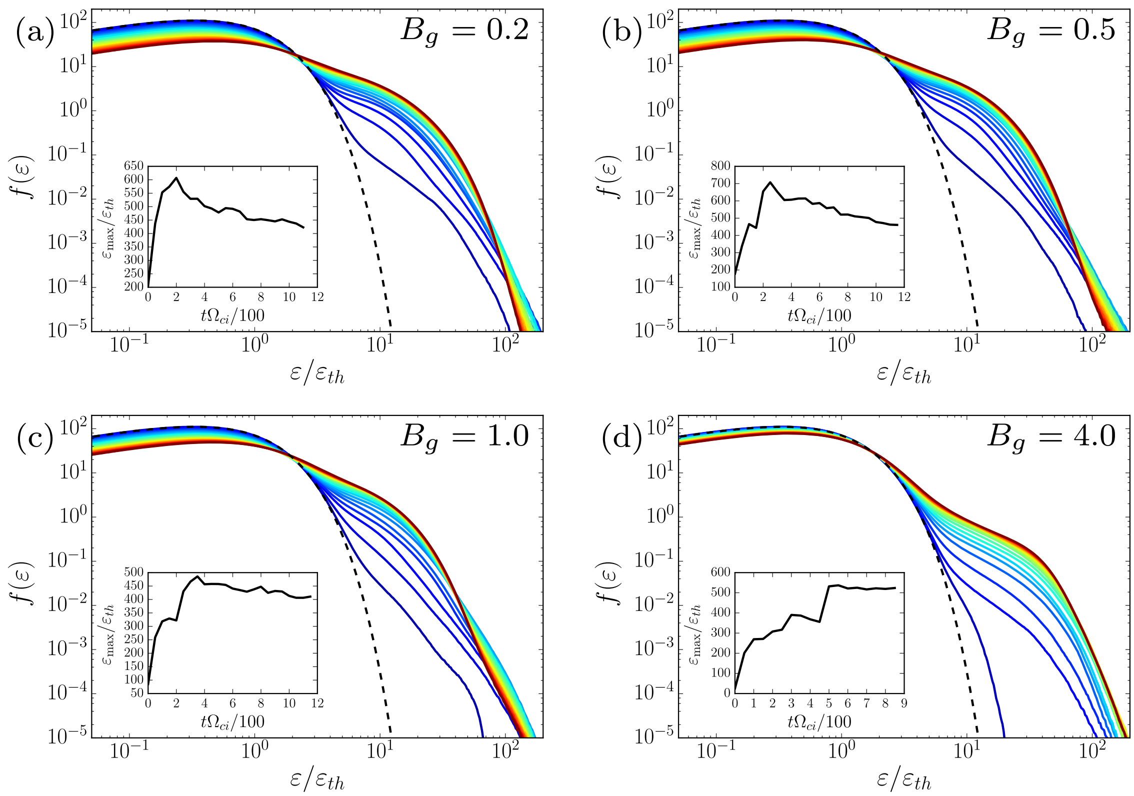

Figure 6.2 Time evolution of particle energy spectra for cases which have different guide field. The lines with different colors are particle spectra at different times. Curves are evenly spaced in a time interval of $t\Omega_{ci} = 50$. The dashed line is the initial thermal distribution. The embedded plots give the time evolution of the maximum energy $\varepsilon_{\max}$ normalized by the initial thermal energy ε_{th}.

The ion energy spectra varies significantly with B_g. The power-law index is ~ 1 in the cases with $B_g = 0$ and 0.2 and increases to 1.35 in the case with $B_g = 0.5$ and 1.74 in the case with $B_g = 1$. For $B_g = 4$, if we fit the nonthermal tail as a power-law, we obtain a steep power-law distribution which has a power-law index ~ 4.4. Such a steep power-law may explain the observed ion spectra which usually have a power-law index ~ 4 during solar flares (Lin et al., 2003).

As in previous chapters, we also did the drift-current analysis. Table 6.2 lists the energy conversion due to different currents. Perpendicular acceleration dominates

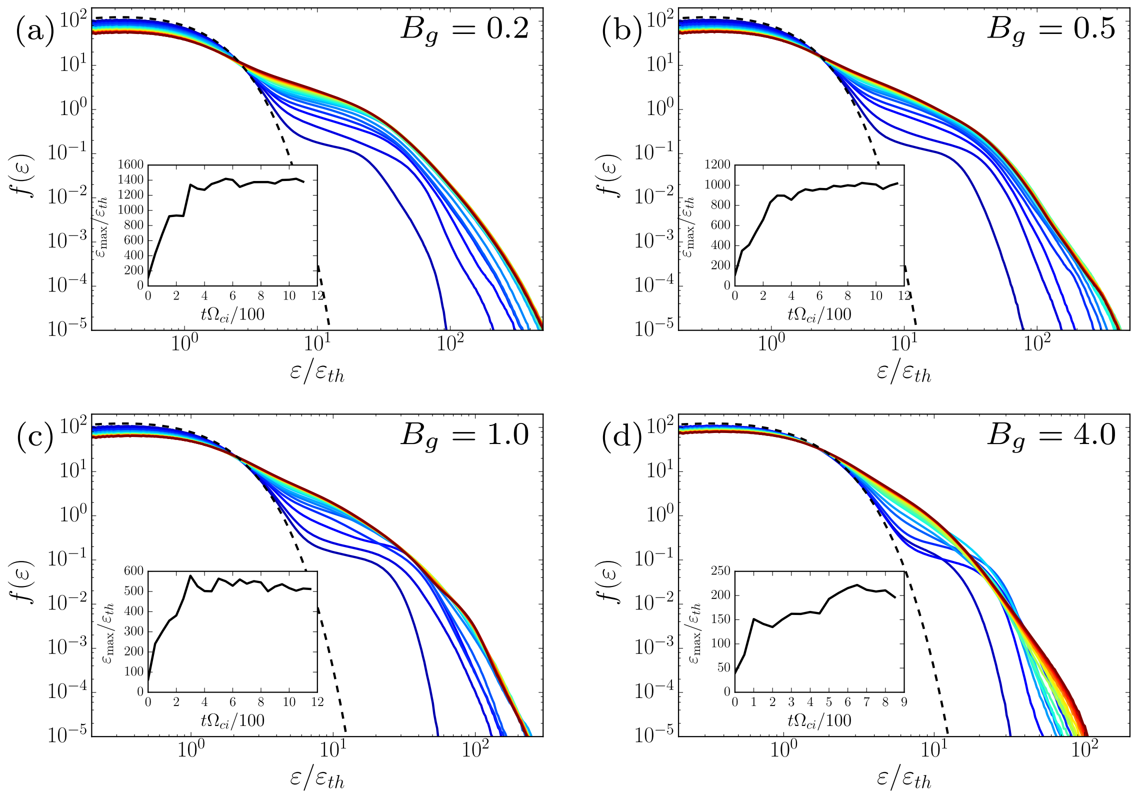

Figure 6.3 Similar as Figure 6.2 but for ions.

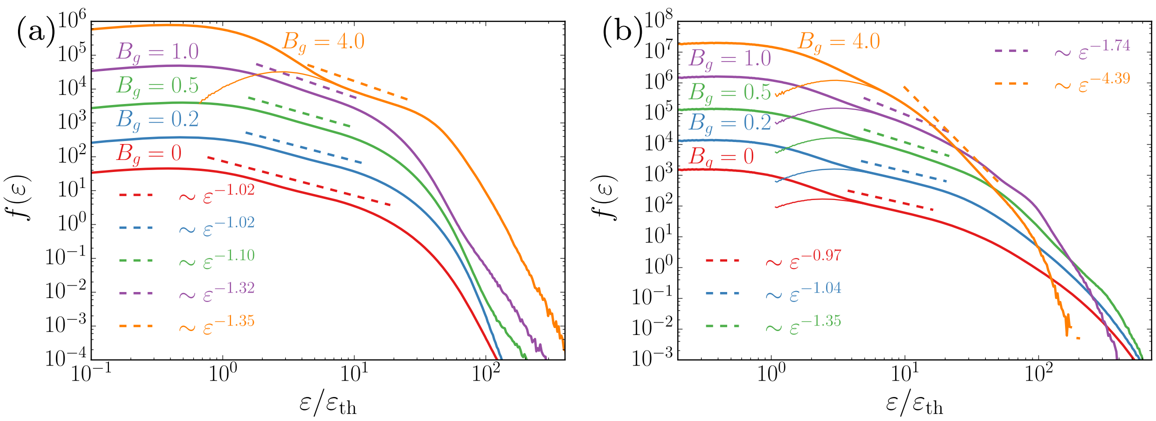

Figure 6.4 Final energy spectra for cases with different B_g for (a) electrons, and (b) ions. ε_{th} is the initial particle thermal energy. The thick solid lines are the energy spectra. We shift it along the y-axis to clearly separate different cases. The thin solid lines are the nonthermal part of the spectra by subtracting a low-energy Maxwellian distribution. The dashed lines are the power-law fitting.

Table 6.2. Energy conversion ε_c due to different currents for electrons. The results are the ratios of different terms to ΔK_e, e.g., $\int \boldsymbol{j}_c \cdot \boldsymbol{E} d\boldsymbol{x} dt / \Delta K_e$

B_g/B_0	$\boldsymbol{j}_\parallel \cdot \boldsymbol{E}$	$\boldsymbol{j}_\perp \cdot \boldsymbol{E}$	$\boldsymbol{j}_c \cdot \boldsymbol{E}$	$\boldsymbol{j}_m \cdot \boldsymbol{E}$	$\boldsymbol{j}_g \cdot \boldsymbol{E}$	$\boldsymbol{j}_p \cdot \boldsymbol{E}$	$\boldsymbol{j}_a \cdot \boldsymbol{E}$
0.0	0.05	0.88	1.46	-0.08	-0.75	0.04	0.08
0.2	0.12	0.76	0.68	-0.04	-0.06	0.04	0.13
0.5	0.23	0.68	0.41	-0.02	0.05	0.04	0.11
1.0	0.54	0.37	0.13	-0.005	0.02	0.05	0.05
4.0	0.91	0.05	0.015	-0.001	0.0004	0.014	-0.01

Note. — $\boldsymbol{j}_\parallel$ is due to parallel electric field. $\boldsymbol{j}_\perp$ is due to perpendicular electric field. $\boldsymbol{j}_c$ is due to curvature drift. $\boldsymbol{j}_m$ is due to the magnetization. $\boldsymbol{j}_g$ is due to gradient B drift. $\boldsymbol{j}_p$ is due to polarization drift. $\boldsymbol{j}_a$ is due to the agyrotropic pressure tensor.

parallel acceleration for electrons in the cases with $B_g \leq 0.5$. Parallel acceleration becomes comparable with perpendicular acceleration in the case with $B_g = 1$ and dominates in the cases with $B_g = 4$. Among all these perpendicular currents, $\boldsymbol{j}_c$ due to the curvature drift is always dominant, and it gradually decreases with B_g. The energy conversion due to the gradient drift only yields significant cooling in the case with no guide field. The other terms are all small compared to $\boldsymbol{j}_c \cdot \boldsymbol{E}$. We show in Appendix D that $\boldsymbol{j}_\perp \cdot \boldsymbol{E}$ excluding the $\boldsymbol{j}_p$ term yields compressional effect during the energy conversion. This indicates that the decrease of the energy conversion and particle acceleration with B_g is due to that the plasma is less compressible if there is guide field. This result is consistent with previous resistive MHD simulations (Birn et al., 2012).

Ions are different in that the perpendicular acceleration is always dominant. The competing terms are $\boldsymbol{j}_c \cdot \boldsymbol{E}$ and $\boldsymbol{j}_p \cdot \boldsymbol{E}$. The term due to the curvature drift

Table 6.3. Energy conversion ε_c due to different currents for ions. The results are the ratios of different terms to ΔK_i, e.g., $\int \boldsymbol{j}_c \cdot \boldsymbol{E} d\boldsymbol{x} dt/\Delta K_i$

B_g/B_0	$\boldsymbol{j}_\parallel \cdot \boldsymbol{E}$	$\boldsymbol{j}_\perp \cdot \boldsymbol{E}$	$\boldsymbol{j}_c \cdot \boldsymbol{E}$	$\boldsymbol{j}_m \cdot \boldsymbol{E}$	$\boldsymbol{j}_g \cdot \boldsymbol{E}$	$\boldsymbol{j}_p \cdot \boldsymbol{E}$	$\boldsymbol{j}_a \cdot \boldsymbol{E}$
0.0	0.10	0.92	1.73	0.0087	-0.96	0.16	-0.06
0.2	0.13	0.89	0.86	0.0040	-0.14	0.13	0.19
0.5	0.24	0.77	0.35	0.0014	0.06	0.46	0.19
1.0	0.18	0.79	0.08	0.0036	0.04	0.87	0.17
4.0	0.14	0.78	0.002	0.0132	0.0007	0.27	0.23

Note. — $\boldsymbol{j}_\parallel$ is due to parallel electric field. $\boldsymbol{j}_\perp$ is due to perpendicular electric field. $\boldsymbol{j}_c$ is due to curvature drift. $\boldsymbol{j}_m$ is due to the magnetization. $\boldsymbol{j}_g$ is due to gradient B drift. $\boldsymbol{j}_p$ is due to polarization drift. $\boldsymbol{j}_a$ is due to the agyrotropic pressure tensor.

decreases with B_g as the plasma becomes less compressible. The relative contribution from $\boldsymbol{j}_p \cdot \boldsymbol{E}$ increases B_g. Since ΔK_i decreases with B_g as well (Table 6.1), the absolute energy conversion due to $\boldsymbol{j}_p \cdot \boldsymbol{E}$ does not change much. Note that for the case with $B_g = 4$, the smaller contribution from $\boldsymbol{j}_p \cdot \boldsymbol{E}$, compared to that when $B_g = 1$, is due to the integration error since $\boldsymbol{j}_p \cdot \boldsymbol{E}$ oscillates strongly between negative values and positive values throughout the simulation. Thus, we can regard that $\boldsymbol{j}_p \cdot \boldsymbol{E}$ is a term that does not change with B_g.

6.4 Conclusion

In this chapter, we performed a series of kinetic simulations with different guide-field strength. We find that the energy conversion becomes less efficient as the guide field increases. This is due to the fact that the plasma becomes less compressible when there is a guide field. Comparing to previous chapters, we find that reconnection with no guide field preferentially accelerate ions, and reconnection with a strong guide field preferentially accelerate electrons. Both electrons and ions develop into power-law energy distributions, which become steeper as the guide field gets stronger. For electrons, perpendicular acceleration is dominant in the cases with a weak guide field, and the parallel acceleration becomes more important as the guide field increases. For ions, the perpendicular acceleration is always dominant. The drift-current analysis shows that the dominant acceleration mechanism for ions is the polarization drift along the motional electric field.

CHAPTER 7

CONCLUSION

Solar flares are the most explosive energy release in the solar system and the main driver of space weather. They are driven by magnetic reconnection, a fundamental plasma process that rearranges the magnetic topology and converts the stored magnetic energy into plasma kinetic energy. Numerous observations exist and support the central role of the reconnection process in the energy conversion at solar flares. One major unsolved problem in solar flare research is the acceleration of nonthermal particles. The observations of above-the-loop-top hard X-ray sources strongly indicate that the acceleration processes are associated with magnetic reconnection (Masuda et al., 1994; Krucker et al., 2010; Krucker and Battaglia, 2014). Both modeling and observations have suggested that during reconnection, current sheets break into a large number of magnetic islands, which are efficient at accelerating particles either through island contraction or island merging processes.

Particle acceleration during solar flares is a multi-scale problem. This thesis focuses on addressing the particle acceleration mechanisms in kinetic scales and particle acceleration in global scales as well. In particular, we address the formation of power-law energy distributions for both electrons and ions in a reconnection site with and without a guide-field. We show in Chapter 2 that the plasmoid instability drives the reconnection current sheet to kinetic scales where MHD descriptions break down. That's why we use fully kinetic particle-in-cell simulations in this thesis to study the particle acceleration processes self-consistently. Besides studying particle acceleration at reconnection, we also examine particles in a time-dependent chaotic magnetic field. Observationally, solar flares are usually accompanied by coronal mass ejections (CMEs), which drive shocks that are efficient in accelerating particle to high energies through a diffusive shock acceleration (DSA) mechanism. The DSA requires "seed" particles, which are superathermal particles capable of crossing the shock front repeatedly and getting efficiently accelerated. This "seed" population is most likely originated at solar active regions and is accelerated before the eruption of CMEs. The acceleration mechanism of this "seed" population has not been well addressed. Inspired by the observations of large scale time-dependent electric current in solar corona and solar flare regions, we have built a model consisting of time-dependent electric currents that generate time-dependent electric field, which accelerates the charged particles.

We start this dissertation by presenting our work on particle acceleration in a time-dependent chaotic magnetic field. We proceed to discuss particle acceleration during magnetic reconnection without and with a guide field.

In Chapter 3 and Li et al. (2014), we investigate charged particle behavior in a chaotic magnetic field, which is generated from one or multiple asymmetric wire-loop-current-systems (WLCSs). We find that particle transport in one WLCS is a sub-diffusion process due to the trapping by the magnetic field. In contrast, particle transport in 8 WLCSs is a diffusion process as particles are not trapped by one WLCS but jump between different WLCSs. When including time-dependent electric currents, both electrons and protons are accelerated to develop power-law energy distribution with power-law index < 1, which is consistent with the model of particle acceleration by multiple reconnection current sheet (Dauphin et al., 2007). The spectra get harder with stronger electric current and faster varying electric current. The maximum energy reaches to $1 - 10$ MeV for both electrons and protons, which can provide a seed population for the CME-driven shock acceleration.

In Chapter 4 and Li et al. (2015), we carried out kinetic simulations in a nonrelativistic plasma with low plasma β. The initial current sheet breaks into a chain of magnetic islands, which interact and merge with each other. Magnetic energy is converted into plasma kinetic energy during this process. The results show that accelerated nonthermal electrons contain more than half of the total electrons, and their distribution resembles a power-law energy distribution $f(E) \sim E^{-1}$ when particle loss is absent. By ensemble averaging the electron guiding center drift motions, we reveal the main acceleration mechanism as a *Fermi*-type acceleration accomplished by the particle curvature drift along the electric field induced by the reconnection outflows. This is in contrast to the high-β cases, where no obvious power-law spectrum is obtained (e.g. Drake et al., 2010).

In Chapter 5 and Li et al. (2016), we perform 2D kinetic simulations of reconnection without a guide field in a nonrelativistic proton-electron plasma with a range of plasma $\beta_e = \beta_i = 0.007 - 0.2$. This work is an extension of the earlier work of Li et al. (2015). We achieve lower plasma β condition by either increasing the magnetic field strength (or equivalently decreasing the particle density), or by decreasing the plasma temperature. We compare the energy conversion and particle acceleration for simulations with different plasma βs. We find that both nonthermal electrons and ions develop power-law energy distributions with power-law index $p \sim 1$ in the low-β regime ($\beta_e \leq 0.02$). Through tracking a large number of particles we find that both electrons and ions get efficiently accelerated when they are drifting along the electric field induced by the bulk flow in the X-type region, anti-reconnection region where two islands are merging, and contracting magnetic islands. Furthermore, ions gain energy when they are "picked-up" by the reconnection outflow. This initial fast energy gain makes ions more energetic than electrons, so they can be accelerated more efficiently through the *Fermi* mechanism later in the simulation. This provides a good explanation on why ions gain more energy than electron in our simulations. By studying $\boldsymbol{j} \cdot \boldsymbol{E}$, we find the major acceleration mechanism is through particle curvature drift along the motional electric field. Particle ∇B drift, polarization drift, parallel electric field and non-gyrotropic pressure tensor all play important roles in different acceleration regions at different times.

In Chapter 6, we performed a series of kinetic simulations with different guide-field strength. We find that the energy conversion becomes less efficient as the guide field increases. This is due to the fact that the plasma becomes less compressible when there is a guide field. An interesting finding is that reconnection with no guide field preferentially accelerate ions, but reconnection with a strong guide field preferentially accelerate electrons. Both electrons and ions develop into power-law energy distributions, which become steeper as the guide field gets stronger. Perpendicular acceleration is dominant for electrons in the cases with a weak guide field, and the parallel acceleration gets more important as the guide field increases. However, the perpendicular acceleration is always dominant for ions. The drift-current analysis shows that the dominant acceleration mechanism for ions is the polarization drift along the motional electric field.

APPENDICES

APPENDIX A

SOLAR CORONA PLASMA PARAMETERS

Some of the plasma parameters in solar corona are listed here. All quantities are in Gaussian cgs except the quantities with $\sim$ on head, which are normalized values using typical solar corona plasma conditions. T_i and T_e are normalized to 86.25 eV (1 MK). B is normalized to 10 Gauss. n_i and n_e are normalized to 10^9 cm^{-3}. Ion mass is normalized to the proton mass $\mu = m_i/m_p$. Z is the charge state. k is Boltzmann constant. Others are specified in calculation.

- Frequencies
  - Electron gyrofrequency $\omega_{ce} = eB/m_e c = 1.76 \times 10^8 \tilde{B}$ rad/sec
  - Ion gyrofrequency $\omega_{ci} = ZeB/m_i c = 9.58 \times 10^4 \tilde{B} Z \mu^{-1}$ rad/sec
  - Electron plasma frequency $\omega_{pe} = \sqrt{4\pi n_e e^2/m_e} = 1.78 \times 10^9 \tilde{n}_e^{1/2}$ rad/sec
  - Ion plasma frequency $\omega_{pi} = \sqrt{4\pi n_i Z^2 e^2/m_i} = 4.17 \times 10^7 \tilde{n}_i^{1/2} \mu^{-1/2} Z$ rad/sec
- Length scales
  - Electron gyroradius $r_e = V_{Te}/\omega_{ce} = 2.21 \tilde{T}_e^{1/2} \tilde{B}^{-1}$ cm
  - Ion gyroradius $r_i = V_{Ti}/\omega_{ci} = 94.68 \tilde{T}_i^{1/2} \tilde{B}^{-1} \mu^{1/2} Z^{-1}$ cm

- Electron inertial length $d_e = c/\omega_{pe} = 16.8\tilde{n}_e^{-1/2}$ cm
- Ion inertial length $d_i = c/\omega_{pi} = 7.21 \times 10^2 \tilde{n}_i^{-1/2} \mu^{1/2} Z^{-1}$ cm
- Debye length $\lambda_D = (kT/4\pi ne^2)^{1/2} = 0.22\tilde{T}^{1/2}\tilde{n}^{-1/2}$ cm

- Velocities
  - Electron thermal speed $V_{Te} = (kT_e/m_e)^{1/2} = 3.88 \times 10^3 \tilde{T}_e^{1/2}$ km/sec
  - Ion thermal speed $V_{Ti} = (kT_i/m_i)^{1/2} = 90.57\tilde{T}_i^{1/2}$ km/sec
  - Alfvén speed $V_A = B/\sqrt{4\pi n_i m_i} = 6.89 \times 10^2 \tilde{n}_i^{-1/2}\tilde{B}$ km/sec
  - Ion sound speed $C_s = (\gamma Z k T_e/m_i)^{1/2} = 90.92(\gamma Z\tilde{T}_e/\mu)^{1/2}$ km/sec, where γ is the adiabatic index.

- Associated with collisions
  - Electron collision frequency $\nu_e = 3.63\tilde{n}_e \ln\Lambda \tilde{T}_e^{-3/2}$ sec^{-1}, where $\Lambda = n_e\lambda_D^3 = 1.04 \times 10^7 \tilde{T}^{3/2}\tilde{n}_e^{-1/2}$; $\ln\Lambda = 16.16 + \ln(\tilde{T}^{3/2}\tilde{n}_e^{-1/2})$.
  - Electron mean free path $\lambda_{mfp} = V_{Te}/\nu_e = 1.07 \times 10^8 \tilde{n}_e^{-1}\tilde{T}_e^2(\ln\Lambda)^{-1}$ cm, which is much larger than all of the kinetic scales.
  - Classical conductivity: $\sigma = n_e e^2/m_e\nu_c = 6.97 \times 10^{16}(\ln\Lambda)^{-1}\tilde{T}_e^{3/2}$ sec^{-1}, where $\nu_c = \nu_e$.
  - Magnetic diffusivity $\eta = c^2/4\pi\sigma = 1.03 \times 10^3 \ln\Lambda \tilde{T}_e^{-3/2}$.
  - Lundquist number: $S = LV_A/\eta = 6.69 \times 10^{13}(\ln\Lambda)^{-1}\tilde{L}\tilde{T}_e^{3/2}\tilde{n}_i^{-1/2}\tilde{B}$, where L is normalized to $L_0 = 10^9$ cm (10 Mm).

– The resistive scale $\delta = LS^{-1/2} = 122.2(\ln\Lambda)^{1/2}\tilde{L}^{1/2}\tilde{T}_e^{-3/4}\tilde{n}_i^{1/4}\tilde{B}^{-1/2}$ cm, where L is normalized to $L_0 = 10^9$ cm (10 Mm).

APPENDIX B

ELECTROMAGNETIC FIELD IN A WIRE-LOOP-CURRENT-SYSTEM

B.1 Electromagnetic field of a straight wire current

The magnetic vector potential $\boldsymbol{A}(\boldsymbol{x}, t)$ for a time-varying current density $\boldsymbol{J}(\boldsymbol{x}, t)$ can be shown to satisfy the following equation,

$$\nabla^2 \boldsymbol{A} - \frac{1}{c^2}\frac{\partial^2 \boldsymbol{A}}{\partial t^2} = -\frac{4\pi}{c}\boldsymbol{J} \tag{B.1}$$

It can be solved in terms of the Green's function $G(\boldsymbol{x}, t; \boldsymbol{x'}, t')$ (Jackson, 1998). The solution is

$$\boldsymbol{A}(\boldsymbol{x}, t) = \frac{1}{c}\int \frac{[\boldsymbol{J}(\boldsymbol{x'}, t')]_{ret}}{R} d^3x \tag{B.2}$$

where the suffix ret indicates the retarded time $t' = t - R/c$; $R = |\boldsymbol{x} - \boldsymbol{x'}|$. We assume that the current of the wire has a simple sinusoidal time variation at all points, i.e., $\boldsymbol{J}(\boldsymbol{x'}, t') = \hat{\boldsymbol{z}} I \cos(\omega t')$, then

$$[\boldsymbol{J}(\boldsymbol{x'}, t')]_{ret} = \hat{\boldsymbol{z}} I \cos[\omega(t - R/c)] \tag{B.3}$$

The resulting vector potential is

$$
\begin{aligned}
\boldsymbol{A}(\boldsymbol{x}, t) = & \lim_{L\to\infty} \hat{\boldsymbol{z}} \frac{I}{c} \int_{-L}^{L} \frac{\cos[\omega(t - R/c)]}{R} \; dz' \\
= & \hat{\boldsymbol{z}} \frac{2I}{c} \left[\cos(\omega t) \lim_{L\to\infty} \int_{\rho}^{\rho_1} \frac{\cos[\omega R/c]}{\sqrt{R^2 - \rho^2}} dR + \sin(\omega t) \lim_{L\to\infty} \int_{\rho}^{\rho_1} \frac{\sin[\omega R/c]}{\sqrt{R^2 - \rho^2}} dR \right] \\
= & \hat{\boldsymbol{z}} \frac{2I}{c} \left[-\frac{\pi}{2} Y_0(\omega\rho/c)\cos(\omega t) + \frac{\pi}{2} J_0(\omega\rho/c)\sin(\omega t) \right] \qquad \text{(B.4)}
\end{aligned}
$$

where $R = \sqrt{\rho^2 + z'^2}$, $\rho_1 = \sqrt{\rho^2 + L^2}$, and we have used the integral representations of Bessel functions of first and second kind (Abramowitz and Stegun, 1964). The resulting electric field $\boldsymbol{E}$ is

$$
\boldsymbol{E} = -\nabla\phi - \frac{1}{c}\frac{\partial \boldsymbol{A}}{\partial t} = -\frac{1}{c}\frac{\partial \boldsymbol{A}}{\partial t} = -\hat{\boldsymbol{z}} \frac{\pi I \omega}{c^2} \left[Y_0(\omega\rho/c)\sin(\omega t) + J_0(\omega\rho/c)\cos(\omega t) \right] \quad \text{(B.5)}
$$

where we have let $\phi = 0$ by a suitable choice of gauge (in absence of any electric charge). For $\omega \to 0$, $\boldsymbol{E} \to 0$. The time dependent magnetic field $\boldsymbol{B}(\rho, t)$ can be evaluated from $\boldsymbol{B}(\rho, t) = \nabla \times \boldsymbol{A}(\rho, t)$. In cylindrical coordinates, the only non-vanishing component of $\boldsymbol{B}(\rho, t)$ is $B_\phi(\rho, t)$, which is given by

$$
\begin{aligned}
\boldsymbol{B}_\phi(\rho, t) &= -\frac{\partial A_z(\rho, t)}{\partial \rho} \\
&= \frac{\pi I}{c} \left[\frac{\partial Y_0(\omega\rho/c)}{\partial \rho} \cos\omega t - \frac{\partial J_0(\omega\rho/c)}{\partial \rho} \sin\omega t \right] \\
&= \frac{\pi I \omega}{c^2} \left[-Y_1(\omega\rho/c)\cos\omega t + J_1(\omega\rho/c)\sin\omega t \right] \qquad \text{(B.6)}
\end{aligned}
$$

The magnetic field of a straight wire $B = 2I/c\rho$ in cgs

$$\frac{B}{\text{Gauss}} = \frac{1}{5}\frac{I/\text{Ampere}}{\rho/\text{cm}} \tag{B.7}$$

Defining a dimensionless variable $x = \omega\rho/c$, we obtain

$$\frac{\boldsymbol{E}(\rho,t)}{\text{Gauss}} = -\hat{\boldsymbol{z}}\frac{1}{5}\frac{I/\text{Amp}}{\rho/\text{cm}}\frac{\pi x}{2}\left[Y_0(x)\sin(\omega t) + J_0(x)\cos(\omega t)\right] \tag{B.8}$$

$$\frac{\boldsymbol{B}(\rho,t)}{\text{Gauss}} = \hat{\phi}\frac{1}{5}\frac{I/\text{Amp}}{\rho/\text{cm}}\frac{\pi x}{2}\left[-Y_1(x)\cos\omega t + J_1(x)\sin\omega t\right] \tag{B.9}$$

B.2 Magnetic field of a loop current

For a current loop with its center located at the origin of the Cartesian coordinate system as shown below. The current density $\boldsymbol{J}$ has only a component in the ϕ direction.

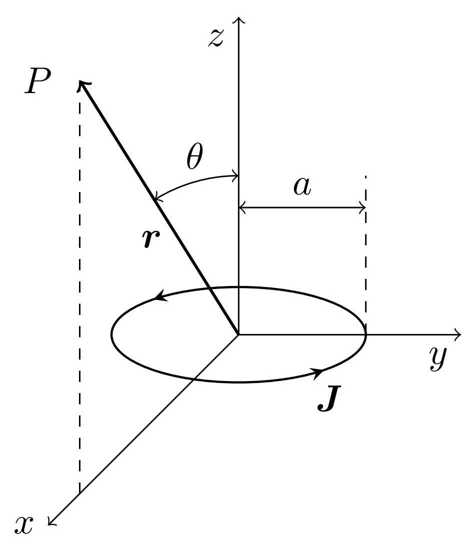

Figure B.1 Illustration of a loop current with a radius a located in the $x-y$ plane. $\boldsymbol{J}$ is the current density.

$$J_\phi = I \sin\theta' \delta(\cos\theta') \frac{\delta(r'-a)}{a} \tag{B.10}$$

The only non-zero component of the vector potential $\boldsymbol{A}$ is (Jackson, 1998)

$$A_\phi(r,\theta) = \frac{\mu_0}{4\pi} \frac{4Ia}{\sqrt{a^2+r^2+2ar\sin\theta}} \left[\frac{(2-k^2)K(k)-2E(k)}{k^2}\right] \tag{B.11}$$

where $K(k)$ and $E(k)$ are the complete elliptical integral of the first kind and the second kind.

$$k^2 = \frac{4ar\sin\theta}{a^2+r^2+2ar\sin\theta} \tag{B.12}$$

$$K(k) = \int_0^{\pi/2} \frac{d\theta'}{\sqrt{1-k^2\sin^2\theta'}} \tag{B.13}$$

$$E(k) = \int_0^{\pi/2} \sqrt{1-k^2\sin^2\theta'}d\theta' \tag{B.14}$$

The magnetic field is

$$B_r = \frac{1}{r\sin\theta}\frac{\partial}{\partial\theta}(\sin\theta A_\phi) \tag{B.15}$$

$$B_\theta = -\frac{1}{r}\frac{\partial}{\partial r}(rA_\phi) \tag{B.16}$$

$$B_\phi = 0 \tag{B.17}$$

Then, the ρ component of the magnetic field in the cylindrical coordinate is

$$B_\rho = B_r\sin\theta + B_\theta\cos\theta = \frac{\sin\theta}{r}\frac{\partial A_\phi}{\partial\theta} - \cos\theta\frac{\partial A_\phi}{\partial r} \tag{B.18}$$

Using temporary variables $C(k) = ((2-k^2)K(k)-2E(k))/k^2$ and $\rho' = \sqrt{a^2 + r^2 + 2ar\sin\theta}$,

$$\frac{\partial A_\phi}{\partial \theta} = \frac{\mu_0}{4\pi}\frac{-4Ia^2 r\cos\theta}{\rho'^3}C(k) + \frac{\mu_0}{4\pi}\frac{4Ia}{\rho'}\frac{\partial C(k)}{\partial k}\frac{\partial k}{\partial \theta} \tag{B.19}$$

$$\frac{\partial A_\phi}{\partial r} = \frac{\mu_0}{4\pi}\frac{-4Ia(r + a\sin\theta)}{\rho'^3}C(k) + \frac{\mu_0}{4\pi}\frac{4Ia}{\rho'}\frac{\partial C(k)}{\partial k}\frac{\partial k}{\partial r} \tag{B.20}$$

$$\frac{\partial k}{\partial \theta} = \frac{1}{2k}\left[\frac{4ar\cos\theta}{\rho'^2} - \frac{8a^2r^2\sin\theta\cos\theta}{\rho'^4}\right] \tag{B.21}$$

$$\frac{\partial k}{\partial r} = \frac{1}{2k}\left[\frac{4a\sin\theta}{\rho'^2} - \frac{4ar\sin\theta(2r + 2a\sin\theta)}{\rho'^4}\right] \tag{B.22}$$

$$\frac{\partial C(k)}{\partial k} = \frac{4 - 3k^2}{k^3(1-k^2)}E(k) + \frac{k^2 - 4}{k^3}K(k) \tag{B.23}$$

where we have used (Abramowitz and Stegun, 1964)

$$\frac{\partial K(k)}{\partial k} = \frac{E(k)}{k(1-k^2)} - \frac{K(k)}{k} \tag{B.24}$$

$$\frac{\partial E(k)}{\partial k} = \frac{E(k) - K(k)}{k} \tag{B.25}$$

Then,

$$\begin{aligned} B_\rho &= \frac{\mu_0}{2\pi}\frac{4Iar\cos\theta}{(a^2 + r^2 + 2ar\sin\theta)^{2/3}}\left[C(k) + \frac{\partial C(k)}{\partial k}\right] \\ &= \frac{\mu_0 I}{2\pi}\frac{\cos\theta}{\sin\theta}\frac{1}{\sqrt{a^2 + r^2 + 2ar\sin\theta}}\left[-K(k) + \frac{a^2 + r^2}{r^2 + a^2 - 2ar\sin\theta}E(k)\right] \end{aligned}$$

We can use B_ρ to calculate $B_x = B_\rho\cos\phi$ and $B_y = B_\rho\sin\phi$. The z-component is

$$B_z = B_r\cos\theta - B_\theta\sin\theta \tag{B.26}$$

$$= \frac{\mu_0 I}{2\pi}\frac{1}{\sqrt{a^2 + r^2 + 2ar\sin\theta}}\left[K(k) - \frac{r^2 - a^2}{r^2 + a^2 - 2ar\sin\theta}E(k)\right] \tag{B.27}$$

We use Taylor expansion of $K(k)$ and $K(k)$ for fast calculation (Fukushima, 2009).

$$K(m) \approx \sum_{j=0}^{J_K} K_j(m - m_0)^j, \quad E(m) \approx \sum_{j=0}^{J_E} E_j(m - m_0)^j \tag{B.28}$$

where the changing variable is changed to $m = k^2$. To guarantee accurate calculation, J_K and J_E, m_0, K_j and E_j change with m. The values are given in Fukushima (2009).

APPENDIX C

GENERATION OF PRESSURE ANISOTROPY

In Chapter 4.1 of Zank (2014), we get the focussed transport equation.

$$\frac{\partial f}{\partial t} + (U_i + c\mu b_i)\frac{\partial f}{\partial x_i} + \frac{1-\mu^2}{2}\left[c\nabla\cdot\boldsymbol{b} + \mu\nabla\cdot\boldsymbol{U} - 3\mu b_i b_j\frac{\partial U_i}{\partial x_j} - \frac{2b_i}{c}\left(\frac{\partial U_i}{\partial t} + U_j\frac{\partial U_i}{\partial x_j}\right)\right]\frac{\partial f}{\partial \mu}$$
$$- \left[\frac{\mu b_i}{c}\left(\frac{\partial U_i}{\partial t} + U_j\frac{\partial U_i}{\partial x_j}\right) + \frac{1-\mu^2}{2}\nabla\cdot\boldsymbol{U} - \frac{1-3\mu^2}{2}b_i b_j\frac{\partial U_i}{\partial x_j}\right]c\frac{\partial f}{\partial c} = \left\langle \frac{\delta f}{\delta t}\bigg|_s\right\rangle \tag{C.1}$$

where $\boldsymbol{b} \equiv \boldsymbol{B}/B$ is the unit vector along the large scale magnetic field; c is particle speed in the flow frame; $\boldsymbol{U}$ is the flow velocity; μ is the cosine of particle pitch angle; the right term is the scattering term by small scale magnetic field, which tends to isotropize the particles. The above equation is gyro-averaged over ϕ. The operator looks like $\langle Q\rangle = 1/2\pi\int_0^{2\pi} Q d\phi$. The gradient of flow velocity can be written in to three terms.

$$\frac{\partial U_i}{\partial x_j} = \frac{1}{3}\nabla\cdot\boldsymbol{U}\delta_{ij} + \frac{1}{2}\left(\frac{\partial U_i}{\partial x_j} + \frac{\partial U_j}{\partial x_i} - \frac{2}{3}\nabla\cdot\boldsymbol{U}\delta_{ij}\right) + \frac{1}{2}\left(\frac{\partial U_i}{\partial U_j} - \frac{\partial U_j}{\partial U_i}\right) \tag{C.2}$$

$$= \frac{1}{3}\nabla\cdot\boldsymbol{U}\delta_{ij} + \sigma_{ij} + \omega_{ij} \tag{C.3}$$

where σ_{ij} is shear tensor; ω_{ij} is rotation tensor. Using the method of characteristics,

$$\frac{1}{c}\left\langle\frac{\partial c}{\partial t}\right\rangle = -\frac{1}{3}\frac{\partial U_i}{\partial x_i} + \frac{1-3\mu^2}{2}b_ib_j\sigma_{ij} - \frac{\mu b_i}{c}\frac{dU_i}{dt} \tag{C.4}$$

$$\left\langle\frac{\partial \mu}{\partial t}\right\rangle = \frac{1-\mu^2}{2}\left(c\frac{\partial b_i}{\partial x_i} - 3\mu b_ib_j\sigma_{ij} - \frac{2b_i}{c}\frac{dU_i}{dt}\right) \tag{C.5}$$

Since it is in the flow frame, the inductive electric field $-\boldsymbol{U}\times\boldsymbol{B}$ is cancelled out. But the parallel electric field may still play a roll. The modified equations are

$$\frac{1}{c}\left\langle\frac{\partial c}{\partial t}\right\rangle = -\frac{1}{3}\frac{\partial U_i}{\partial x_i} + \frac{1-3\mu^2}{2}b_ib_j\sigma_{ij} - \frac{\mu b_i}{c}\frac{dU_i}{dt} + \frac{q}{m}\frac{E_\parallel}{c}\mu \tag{C.6}$$

$$\left\langle\frac{\partial \mu}{\partial t}\right\rangle = \frac{1-\mu^2}{2}\left(c\frac{\partial b_i}{\partial x_i} - 3\mu b_ib_j\sigma_{ij} - \frac{2b_i}{c}\frac{dU_i}{dt}\right) + \frac{q}{m}\frac{E_\parallel}{c}(1-\mu^2) \tag{C.7}$$

The focussed transport equation can be written as

$$\frac{\partial f}{\partial t} + (U_i + c\mu b_i)\frac{\partial f}{\partial x_i} + \frac{\partial \mu}{\partial t}\frac{\partial f}{\partial \mu} + \frac{\partial c}{\partial t}\frac{\partial f}{\partial c} = \left.\frac{\delta f}{\delta t}\right|_s \tag{C.8}$$

where <> is neglected for simplicity. We multiply $c^2\mu^2$ to the equation and integrate over the distribution function. We get

$$\begin{aligned}\frac{\partial P_\parallel}{\partial t} + \boldsymbol{U}\cdot\nabla P_\parallel + \boldsymbol{b}\cdot\nabla q_\parallel + \int c^2\mu^2\frac{\partial \mu}{\partial t}\frac{\partial f}{\partial \mu}(-c^2dcd\mu) + \\ \int c^2\mu^2\frac{\partial c}{\partial t}\frac{\partial f}{\partial c}(-c^2dcd\mu) = \int c^2\mu^2\left.\frac{\delta f}{\delta t}\right|_s(-c^2dcd\mu)\end{aligned} \tag{C.9}$$

where $q_\parallel$ is one component of the pressure-transport tensor, and $q_\parallel = \int c_\parallel^3 f(-c^2dcd\mu)$; $P_\parallel$ is the parallel pressure. We assume the scattering term is represented in pitch-angle.

$$\left\langle \frac{\delta f}{\delta t}\bigg|_s \right\rangle = \frac{\partial}{\partial \mu}\left(\nu(1-\mu^2)\frac{\partial f}{\partial \mu}\right) \tag{C.10}$$

The fourth and fifth term on the left and right term can integrated by parts.

$$\int c^2\mu^2 \frac{\partial \mu}{\partial t}\frac{\partial f}{\partial \mu}(-c^2 dc d\mu) \tag{C.11}$$

$$= -\int \frac{\partial}{\partial \mu}\left(c^2\mu^2\frac{\partial \mu}{\partial t}\right) f(-c^2 dc d\mu) \tag{C.12}$$

$$= -\int \frac{\partial}{\partial \mu}\left[\frac{\mu^2-\mu^4}{2}c^2\left(c\frac{\partial b_i}{\partial x_i} - 3\mu b_i b_j \sigma_{ij} - \frac{2b_i}{c}\frac{dU_i}{dt} + 2\frac{q}{m}\frac{E_\parallel}{c}\right)\right] f(-c^2 dc d\mu) \tag{C.13}$$

$$= -\int (\mu - 2\mu^3)c^2\left(c\frac{\partial b_i}{\partial x_i} - \frac{2b_i}{c}\frac{dU_i}{dt} + 2\frac{q}{m}\frac{E_\parallel}{c}\right) f(-c^2 dc d\mu)$$

$$+ \int \frac{3}{2}(3\mu^2 - 5\mu^4)c^2 b_i b_j \sigma_{ij} f(-c^2 dc d\mu) \tag{C.14}$$

And

$$\int c^2\mu^2 \frac{\partial c}{\partial t}\frac{\partial f}{\partial c}(-c^2 dc d\mu) \tag{C.15}$$

$$= -\int \frac{\partial}{\partial c}\left(c^2\mu^2\frac{\partial c}{\partial t}\right) f(-c^2 dc d\mu) \tag{C.16}$$

$$= -\int \frac{\partial}{\partial c}\left[c^5\mu^2\left(-\frac{1}{3}\frac{\partial U_i}{\partial x_i} + \frac{1-3\mu^2}{2}b_i b_j \sigma_{ij} - \frac{\mu b_i}{c}\frac{dU_i}{dt} + \frac{q}{m}\frac{E_\parallel}{c}\mu\right)\right] f(-dc d\mu) \tag{C.17}$$

$$= -\int 5c^2\mu^2\left(-\frac{1}{3}\frac{\partial U_i}{\partial x_i} + \frac{1-3\mu^2}{2}b_i b_j \sigma_{ij}\right)(-c^2 dc d\mu)$$

$$- \int 4c\mu^2\left(-\mu b_i\frac{dU_i}{dt} + \frac{qE_\parallel}{m}\mu\right)(-c^2 dc d\mu) \tag{C.18}$$

Equation Equation C.14 and Equation C.18 are combined to get

$$\frac{5}{3}P_{\|}\frac{\partial U_i}{\partial x_i} + 2P_{\|}b_ib_j\sigma_{ij} + \int 2\mu c\left(b_i\frac{dU_i}{dt} - \frac{qE_{\|}}{m}\right)f(-c^2dcd\mu) - \int(\mu - 2\mu^3)c^3\frac{\partial b_i}{\partial x_i}f(-c^2dcd\mu) \tag{C.19}$$

where the last term is going to be $-2q_{\perp}\nabla\cdot\boldsymbol{b}+q_{\|}\nabla\cdot\boldsymbol{b}$, where $q_{\perp} = \frac{1}{2}\int c_{\perp}^2 c_{\|} f(-c^2dcd\mu)$; $q_{\|}$ is as mentioned before. The scattering term is going to be

$$\begin{aligned}\int c^2\mu^2\frac{\partial}{\partial\mu}\left(\nu(1-\mu^2)\frac{\partial f}{\partial\mu}\right)(-c^2dcd\mu) &= -\int 2c^2\mu\nu(1-\mu^2)\frac{\partial f}{\partial\mu}(-c^2dcd\mu)\\ &= \int 2c^2\nu(1-3\mu^2)f(-c^2dcd\mu)\\ &= 4\nu(P_{\perp} - P_{\|})\end{aligned} \tag{C.20}$$

Then we have

$$\begin{aligned}\frac{dP_{\|}}{dt} =& -\frac{5}{3}P_{\|}\frac{\partial U_i}{\partial x_i} - 2P_{\|}b_ib_j\sigma_{ij} - \int 2\mu c\left(b_i\frac{dU_i}{dt} - \frac{qE_{\|}}{m}\right)f(-c^2dcd\mu)\\ &+ 2q_{\perp}\nabla\cdot\boldsymbol{b} - \nabla\cdot(q_{\|}\boldsymbol{b}) + 4\nu(P_{\perp} - P_{\|})\end{aligned} \tag{C.21}$$

which is the same with the results in the original paper of the CGL closure (Chew et al., 1956). Similarly, for perpendicular pressure, we get

$$\frac{dP_{\perp}}{dt} = -\frac{5}{3}P_{\perp}\frac{\partial U_i}{\partial x_i} + P_{\perp}b_ib_j\sigma_{ij} - q_{\perp}\nabla\cdot\boldsymbol{b} - \nabla\cdot(q_{\perp}\boldsymbol{b}) - 2\nu(P_{\perp} - P_{\|}) \tag{C.22}$$

which is exactly the same with the results in the original paper of the CGL closure (Chew et al., 1956) except for the pitch angle scattering term. We need to find out the reason. When the particle distribution is not symmetric with respect to μ, $q_\parallel$, $q_\perp$, the terms related the flow acceleration/deceleration and parallel electric field will play a role in the evolution pressure anisotropy.

$$
\begin{aligned}
\frac{d(P_\parallel/P_\perp)}{dt} =& -3\frac{P_\parallel}{P_\perp} b_i b_j \sigma_{ij} + \frac{1}{P_\perp}\left[-\int 2\mu c\left(b_i\frac{dU_i}{dt} - \frac{qE_\parallel}{m}\right) f(-c^2 dc d\mu)\right. \\
&\left. + 2q_\perp \nabla\cdot\boldsymbol{b} - \nabla\cdot(q_\parallel \boldsymbol{b}) + 4\nu(P_\perp - P_\parallel)\right] \\
&+ \frac{P_\parallel}{P_\perp^2}\left[q_\perp \nabla\cdot\boldsymbol{b} + \nabla\cdot(q_\perp\boldsymbol{b}) + 2\nu(P_\perp - P_\parallel)\right]
\end{aligned}
\tag{C.23}
$$

The pressure anisotropy due to parallel electric field has been considered in a series of papers (see Egedal et al. (2013) for a recent review). The pressure anisotropy and the resulting firehose and mirror instabilities have been studied by Kunz et al. (2014) (see its citations for more reference).

APPENDIX D

COMPRESSIONAL EFFECT IN RECONNECTION

We derived the expression of $\boldsymbol{j}_\perp$ in the previous chapter (Equation 4.8). Here, we will show that the energy conversion is associated with fluid compression and shear. Neglecting the $\boldsymbol{E} \times \boldsymbol{B}$ drift term (no energy conversion) and the fluid acceleration term (small compared with the other terms),

$$\boldsymbol{j}_\perp = -\frac{\nabla P_\perp \times \boldsymbol{B}}{B^2} + (P_\parallel - P_\perp)\frac{\boldsymbol{B} \times (\boldsymbol{B} \cdot \nabla)\boldsymbol{B}}{B^4} \tag{D.1}$$

Assuming $\boldsymbol{E} \approx -\boldsymbol{v} \times \boldsymbol{B} = -\boldsymbol{v}_\perp \times \boldsymbol{B}$ for anti-parallel reconnection,

$$\boldsymbol{j}_\perp \cdot \boldsymbol{E} = \frac{\nabla P_\perp \times \boldsymbol{B}}{B^2} \cdot (\boldsymbol{v}_\perp \times \boldsymbol{B}) - (P_\parallel - P_\perp)\frac{\boldsymbol{B} \times (\boldsymbol{B} \cdot \nabla)\boldsymbol{B}}{B^4} \cdot (\boldsymbol{v}_\perp \times \boldsymbol{B}) \tag{D.2}$$

$$= \nabla P_\perp \cdot \boldsymbol{v}_\perp + (P_\parallel - P_\perp)\frac{(\boldsymbol{B} \cdot \nabla)\boldsymbol{B}}{B^2} \cdot \boldsymbol{v}_\perp \tag{D.3}$$

$$= \nabla P_\perp \cdot \boldsymbol{v}_\perp + (P_\parallel - P_\perp)\frac{B\nabla B - \boldsymbol{B} \times (\nabla \times \boldsymbol{B})}{B^2} \cdot \boldsymbol{v}_\perp \tag{D.4}$$

where

$$
\begin{aligned}
\boldsymbol{B} \times (\nabla \times \boldsymbol{B}) \cdot \boldsymbol{v}_\perp &= [(\nabla \times \boldsymbol{B}) \times \boldsymbol{v}_\perp] \cdot \boldsymbol{B} \\
&= -\nabla(\cancel{\boldsymbol{v}_\perp \cdot \boldsymbol{B}}) \cdot \boldsymbol{B} + B\boldsymbol{v}_\perp \cdot \nabla B + \boldsymbol{B} \cdot [(\boldsymbol{B} \cdot \nabla)\boldsymbol{v}_\perp] \qquad \text{(D.5)}
\end{aligned}
$$

Then,

$$
\begin{aligned}
\boldsymbol{j}_\perp \cdot \boldsymbol{E} &= \nabla P_\perp \cdot \boldsymbol{v}_\perp + (P_\parallel - P_\perp)\boldsymbol{b} \cdot [(\boldsymbol{b} \cdot \nabla)\boldsymbol{v}_\perp] \qquad \text{(D.6)} \\
&= \nabla \cdot (P_\perp \boldsymbol{v}_\perp) - P_\perp \nabla \cdot \boldsymbol{v}_\perp - (P_\parallel - P_\perp) b_i b_j \frac{\partial v_{i\perp}}{\partial x_j} \qquad \text{(D.7)} \\
&= \nabla \cdot (P_\perp \boldsymbol{v}_\perp) - p \nabla \cdot \boldsymbol{v}_\perp - (P_\parallel - P_\perp) b_i b_j \sigma_{ij} \qquad \text{(D.8)}
\end{aligned}
$$

where $p = (P_\parallel + 2P_\perp)/3$ is effective scaler pressure, where $\sigma_{ij} = \frac{1}{2}\left(\frac{\partial u_{\perp j}}{\partial x_i} + \frac{\partial u_{\perp i}}{\partial x_j} - \frac{2}{3}\nabla \cdot \boldsymbol{u}_\perp \delta_{ij}\right)$ is the shear tensor of the perpendicular bulk flow $\boldsymbol{u}_\perp$.

APPENDIX E

PARTICLE-IN-CELL METHOD

In plasma physics, particle-in-cell (PIC) method refers to a computational method to solve the Maxwell-Boltzmann system of equations (Birdsall and Langdon, 1991; Hockney and Eastwood, 1988; Bowers et al., 2008).

$$\partial_t f_s + \boldsymbol{v} \cdot \nabla f_s + \frac{q_s}{m_s}\left(\boldsymbol{E} + \frac{1}{c}\boldsymbol{v} \times \boldsymbol{B}\right) \cdot \nabla_{\boldsymbol{v}} f_s = \sum_{s'} \mathcal{C}\{f_s, f_{s'}\} \tag{E.1}$$

$$\rho = \sum_s q_s \int d^3 v f_s(\boldsymbol{r}, \boldsymbol{v}, t), \quad \boldsymbol{j} = \sum_s q_s \int d^3 v \boldsymbol{v} f_s(\boldsymbol{r}, \boldsymbol{v}, t) \tag{E.2}$$

$$\nabla \times \boldsymbol{E} = -\frac{1}{c}\frac{\partial \boldsymbol{B}}{\partial t}, \quad \nabla \cdot \boldsymbol{E} = 4\pi\rho \tag{E.3}$$

$$\nabla \times \boldsymbol{B} = \frac{4\pi}{c}\boldsymbol{j} + \frac{1}{c}\frac{\partial \boldsymbol{E}}{\partial t}, \quad \nabla \cdot \boldsymbol{B} = 0 \tag{E.4}$$

where $f_s(\boldsymbol{r}, \boldsymbol{v}, t)$ is the phase-space distribution of a particle species s with charge q_s and mass m_s. c is the speed of light in vacuum. $\boldsymbol{v}$ is the particle momentum normalized by c. $\boldsymbol{E}$ and $\boldsymbol{B}$ are the electric and magnetic field. ρ is the particle number density. $\boldsymbol{j}$ is the current density. $\sum_{s'} \mathcal{C}\{f_s, f_{s'}\}$ represents Coulomb collisions and is zero for space and astrophysical collisionless plasma. The direct discretization of the 6-dimensional f_s is usually prohibitive, so PIC simulations sample it with a collections of computational particles—each computational particle typically represents many physical particles (or chunks of phase space). The left panel of Figure E.1 shows one computing cell with charged particles overplotted. Particles with different positions and velocities sample $f_s(\boldsymbol{r}, \boldsymbol{v}, t)$. The electric and magnetic field is defined on the grid. Maxwell's equations are solved using the charge and current deposited on the grids from the particles. To move a particle, the E/M fields is interpolated from the grid to the particle position. The right panel of Figure E.1 shows one computing time step of PIC simulation.

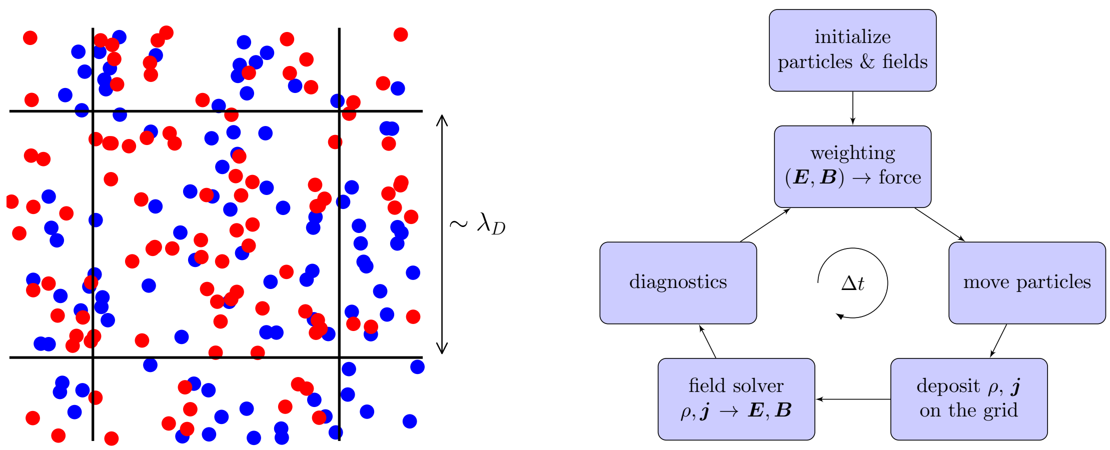

Figure E.1 Left: one cell in PIC simulation. λ_D is the Debye length. Electric and magnetic fields are sampled on the grids (black lines). The red and blue dots are computational particles. Right: one computing time step of PIC simulation.

The Gauss's law for $\boldsymbol{E}$ and $\boldsymbol{B}$ are satisfied as initial conditions, so they are not solved. Divergence clean procedures are applied to $\boldsymbol{E}$ and $\boldsymbol{B}$ to make sure they satisfy the Gauss's law. The steps to build a 2D PIC code are listed below.

E.1 Units and normalization

The Faraday's equation, Ampère's law, Lorentz's equation and Newton's law in Gaussian units,

$$\frac{\partial \boldsymbol{B}}{\partial t} = -c\nabla \times \boldsymbol{E}, \quad \frac{\partial \boldsymbol{E}}{\partial t} = c\nabla \times \boldsymbol{B} - 4\pi \boldsymbol{J} \tag{E.5}$$

$$\frac{d\boldsymbol{u}_s}{dt} = \frac{q_s}{m_s c}(\boldsymbol{E} + \gamma^{-1}\boldsymbol{u}_s \times \boldsymbol{B}), \quad \frac{d\boldsymbol{r}_s}{dt} = c\gamma^{-1}\boldsymbol{u}_s \tag{E.6}$$

where $\boldsymbol{u}_s = \gamma \boldsymbol{v}_s / c$; $\gamma = \sqrt{1 + u_s^2} = 1/\sqrt{1 - v_s^2}$.

$$m_s = m_s^* m_0, \quad n_s = n_s^* n_0, \quad q_s = q_s^* q_0 \tag{E.7}$$

$$\boldsymbol{v}_s = \boldsymbol{v}_s^* v_0, \quad t = t^* t_0, \quad l = l^* l_0 \tag{E.8}$$

$$\nabla = \nabla^* / l_0, \quad \boldsymbol{E} = \boldsymbol{E}^* E_0, \quad \boldsymbol{B} = \boldsymbol{B}^* B_0 \tag{E.9}$$

where quantities with * are the normalized ones; $m_0, n_0, \cdots$ are normalization of corresponding physical quantities. Then we have

$$\frac{\partial \boldsymbol{B}}{\partial t} = -\frac{cE_0 t_0}{l_0 B_0}\nabla \times \boldsymbol{E}, \quad \frac{\partial \boldsymbol{E}}{\partial t} = \frac{cB_0 t_0}{l_0 E_0}\nabla \times \boldsymbol{B} - \frac{4\pi n_0 q_0 v_0 t_0}{E_0}\boldsymbol{J} \tag{E.10}$$

$$\frac{d\boldsymbol{u}_s}{dt} = \frac{q_s}{m_s c}\left(\frac{q_0 E_0 t_0}{m_0}\boldsymbol{E} + \gamma^{-1}\frac{q_0 B_0 t_0}{m_0}\boldsymbol{u}_s \times \boldsymbol{B}\right), \quad \frac{d\boldsymbol{r}_s}{dt} = \frac{ct_0}{l_0}\gamma^{-1}\boldsymbol{u}_s \tag{E.11}$$

where * has been neglected for simplification. We choose

$$l_0 = d_i = \frac{c}{\omega_{pi}} = \frac{c\sqrt{m_i}}{\sqrt{4\pi n_i q_i^2}} \tag{E.12}$$

$$t_0 = \frac{1}{\Omega_{ci}} = \frac{m_i c}{q_i B_0} \tag{E.13}$$

where ω_{pi} is ion plasma frequency; Ω_{ci} is ion gyrofrequency. $v_0 = l_0/t_0 = v_A$. For electron-proton plasma, we choose $q_i = q_0$, $n_i = n_0$, $m_e = m_0$. If we choose $E_0 c = v_A B_0$,

$$\frac{\partial \boldsymbol{B}}{\partial t} = -\nabla \times \boldsymbol{E}, \quad \frac{\partial \boldsymbol{E}}{\partial t} = \frac{c^2}{v_A^2}(\nabla \times \boldsymbol{B} - \boldsymbol{J}) \tag{E.14}$$

$$\frac{d\boldsymbol{u}_s}{dt} = \frac{q_s}{m_s}\frac{m_i}{m_0}\left(\frac{v_A}{c}\boldsymbol{E} + \gamma^{-1}\boldsymbol{u}_s \times \boldsymbol{B}\right), \quad \frac{d\boldsymbol{r}_s}{dt} = \frac{c}{v_A}\gamma^{-1}\boldsymbol{u}_s \tag{E.15}$$

E.2 Time and space discretization (grids)

Two and half dimensional simulation usually means 2D3V. The particle information for particle include x, y, u_x, u_y, u_z, q. The positions are given by the containing cell index and the offset from the cell center, normalized to the cell dimensions. This can guarantee identical numerical properties for each cell (Bowers et al., 2008). A particle structure is defined to contain `dx, dy, grid, test, ux, uy, uz, q`. `dx` and `dy` are normalized shifts from the cell center; `grid` is the containing cell index; `test` is a flag for particle information diagnostics; `ux`, `uy` and `uz` are three components of particle velocity; `q` is the carrying charge for this particle. `q=1` for ions; `q=-1` for electrons. We choose a 2D Yee lattice shown in Figure E.2

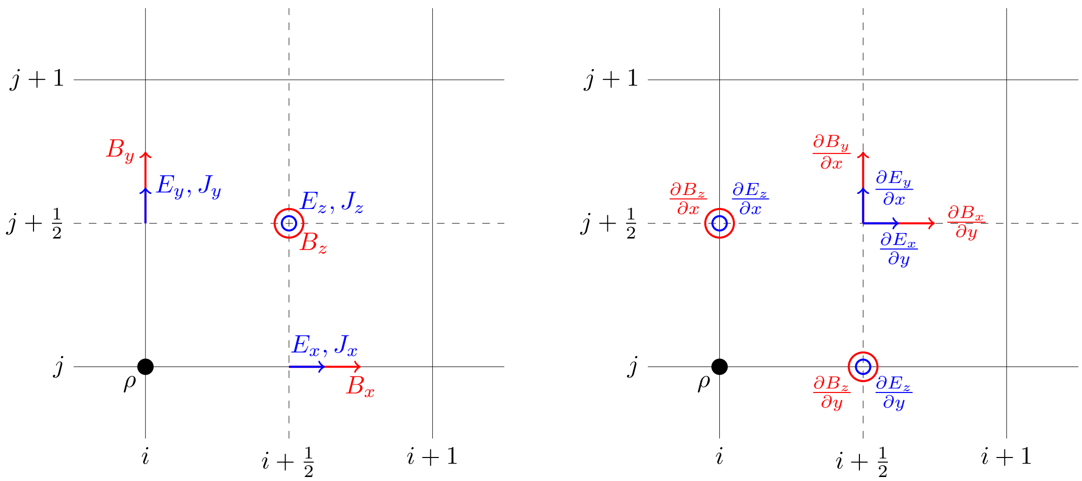

Figure E.2 2D Yee lattice for PIC simulation.

for the field solver. $\boldsymbol{E}$ and $\boldsymbol{B}$ are staggered. The following quantities are put into a single structure in the code: $E_x(i+\frac{1}{2},j)$, $E_y(i,j+\frac{1}{2})$, $E_z(i+\frac{1}{2},j+\frac{1}{2})$, $B_x(i+\frac{1}{2},j)$, $B_y(i,j+\frac{1}{2})$, $B_z(i+\frac{1}{2},j+\frac{1}{2})$, $\frac{\partial E_x}{\partial y}(i+\frac{1}{2},j+\frac{1}{2})$, $\frac{\partial E_y}{\partial x}(i+\frac{1}{2},j+\frac{1}{2})$, $\frac{\partial E_z}{\partial x}(i,j+\frac{1}{2})$, $\frac{\partial E_z}{\partial y}(i+\frac{1}{2},j)$, $\frac{\partial B_x}{\partial y}(i+\frac{1}{2},j+\frac{1}{2})$, $\frac{\partial B_y}{\partial x}(i+\frac{1}{2},j+\frac{1}{2})$, $\frac{\partial B_z}{\partial x}(i,j+\frac{1}{2})$, $\frac{\partial B_z}{\partial y}(i+\frac{1}{2},j)$. This makes it easy to move the whole structure when exchanging ghost cells. In actual code, $i+\frac{1}{2}\to i$, $i-\frac{1}{2}\to i-1$, $j+\frac{1}{2}\to j$, $j-\frac{1}{2}\to j-1$.

E.3 Field solver

We need to solve Faraday's equation and Ampère's law. In the following discussion, we neglect the constant term c^2/v_A^2 first. In 2D, the field components can be decomposed into 2 independent modes.

- TE mode ($\boldsymbol{k}\cdot\boldsymbol{E}=0$): E_z, B_x, B_y
- TM mode ($\boldsymbol{k}\cdot\boldsymbol{B}=0$): B_z, E_x, E_y

Then we have

$$\partial_t B_x = -\partial_y E_z, \quad \partial_t B_y = \partial_x E_z, \quad \partial_t E_z = \partial_x B_y - \partial_y B_x - J_z \tag{E.16}$$

$$\partial_t E_x = \partial_y B_z - J_x, \quad \partial_t E_y = -\partial_x B_z - J_y, \quad \partial_t B_z = -\partial_x E_y + \partial_y E_x \tag{E.17}$$

The field solve uses leapfrog integration method shown in Figure E.3. $\boldsymbol{E}$ is sampled

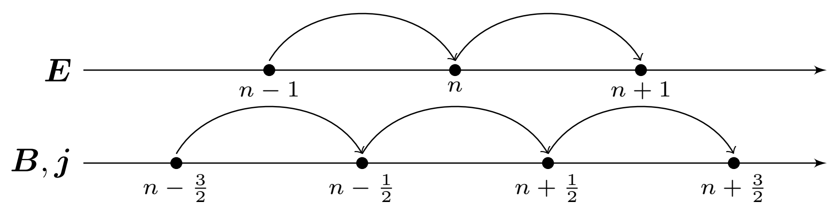

Figure E.3 Leapfrog integration for the E/M field.

on the integer time points. $\boldsymbol{B}$ and $\boldsymbol{j}$ are sampled on the half time points.

$$\frac{B_x^{n+\frac{1}{2}}(i,j) - B_x^{n-\frac{1}{2}}(i,j)}{\Delta t} = -\partial_y E_z^n(i,j) \tag{E.18}$$
$$\frac{B_y^{n+\frac{1}{2}}(i,j) - B_y^{n-\frac{1}{2}}(i,j)}{\Delta t} = \partial_x E_z^n(i,j) \tag{E.19}$$
$$\frac{E_z^{n+1}(i,j) - E_z^{n}(i,j)}{\Delta t} = \partial_x B_y^{n+\frac{1}{2}}(i,j) - \partial_y B_x^{n+\frac{1}{2}}(i,j) - J_z^{n+\frac{1}{2}}(i,j) \tag{E.20}$$
$$\frac{B_z^{n+\frac{1}{2}}(i,j) - B_z^{n-\frac{1}{2}}(i,j)}{\Delta t} = -\partial_x E_y^n(i,j) + \partial_y E_x^n(i,j) \tag{E.21}$$
$$\frac{E_x^{n+1}(i,j) - E_x^{n}(i,j)}{\Delta t} = \partial_y B_z^{n+\frac{1}{2}}(i,j) - J_x^{n+\frac{1}{2}}(i,j) \tag{E.22}$$
$$\frac{E_y^{n+1}(i,j) - E_y^{n}(i,j)}{\Delta t} = -\partial_x B_z^{n+\frac{1}{2}}(i,j) - J_y^{n+\frac{1}{2}}(i,j) \tag{E.23}$$

So we need to update fields components B_x, B_y, B_z, E_x, E_y, E_z first using the curl of fields. Then we need to update the curl of fields using updated fields.

A variety of boundary conditions can be used in PIC codes include Periodic Boundary Condition (PBC), Perfect Electric Conductor (PEC), Perfect Magnetic Conductor (PMC), field emitting, field absorbing (Higdon, 1986) and open boundary condition (Birdsall and Langdon, 1991; Daughton et al., 2006). A PEC is characterized by vanishing tangential electric field at the conducting surface, and zero total electric field inside. While a PMC is characterized by a vanishing tangential magnetic field at the surface.

$$\text{(PEC)}\ \hat{n} \times \bar{E} = 0, \quad \hat{n} \times \bar{H} = \bar{J}_s \tag{E.24}$$

$$\text{(PMC)}\ \hat{n} \times \bar{E} = -\bar{M}_s, \quad \hat{n} \times \bar{H} = 0 \tag{E.25}$$

where $\bar{J}_s$ is electric current density; $\bar{M}_s$ is magnetic current density. The simplest open boundary condition is to have a resistive layer surrounding the simulation domain. Alternatively, one can impose outgoing wave boundary conditions (Birdsall and Langdon, 1991). A more complicated and physical open boundary condition is to open the boundary for both particles and fields (Daughton et al., 2006). Particle reaching the boundary are removed, and new particles satisfying specific distribution are injected at the same time.

The time step is determined by the Courant condition. Assuming the fields of the form $(\boldsymbol{E}, \boldsymbol{B}) \sim \exp(i\boldsymbol{k} \cdot \boldsymbol{x} - i\omega t)$, then the Maxwell's equations are

$$\Omega \boldsymbol{B} = c\boldsymbol{\kappa} \times \boldsymbol{E}, \quad \Omega \boldsymbol{E} = -c\boldsymbol{\kappa} \times \boldsymbol{B} \tag{E.26}$$

where $\Omega = \sin(\omega\Delta t/2)/(\Delta t/2)$, $\kappa_x = \sin(k_x\Delta x/2)/(\Delta x/2)$. When $\Delta t \to 0$ and $\Delta x \to 0$, Ω and $\boldsymbol{\kappa}$ reduces to ω and $\boldsymbol{k}$. Eliminating $\boldsymbol{E}$ and $\boldsymbol{B}$ yields $\Omega^2 = c^2\kappa^2$, which is expanded as

$$\left(\frac{\sin(\omega\Delta t/2)}{c\Delta t}\right)^2 = \left(\frac{\sin(k_x\Delta x/2)}{\Delta x}\right)^2 + \left(\frac{\sin(k_y\Delta y/2)}{\Delta y}\right)^2 \tag{E.27}$$

ω is real (no damping or growth) if

$$1 > (c\Delta t)^2\left(\frac{1}{\Delta x^2} + \frac{1}{\Delta y^2}\right) \tag{E.28}$$

which is the Courant condition. Considering a 1D case, Equation E.27 changes to

$$\cos(\omega\Delta t) = \left(\frac{c\Delta t}{\Delta x}\right)^2(\cos(k\Delta x) - 1) + 1 \tag{E.29}$$

$$\cos\left(\frac{\omega\Delta x}{c}\frac{c\Delta t}{\Delta x}\right) - 1 = \left(\frac{c\Delta t}{\Delta x}\right)^2(\cos(k\Delta x) - 1) \tag{E.30}$$

$$\cos(Cy') - 1 = C^2(\cos(x') - 1) \tag{E.31}$$

where $y' = \omega\Delta x/c$, $x' = k\Delta x$, Courant number $C = c\Delta t/\Delta x$. Figure E.4 shows the dispersion relation for different Courant number. For wavelengths comparable to the cell dimensions ($k\Delta x \sim \pi$), the discretized speed of light can deviate significantly from c. Then, relativistic particles might have speed larger than c, which can generate nonphysical Cerenkov radiation at these wavelength (Bowers et al., 2008). To reduce this numerical Cerenkov radiation, we need a transverse current (Bowers et al., 2008). Effectively, a current that obeys $\boldsymbol{J}_T = \tau\partial_t(\boldsymbol{J}_T - \nabla \times \mu^{-1}\boldsymbol{B})$ is included that damps

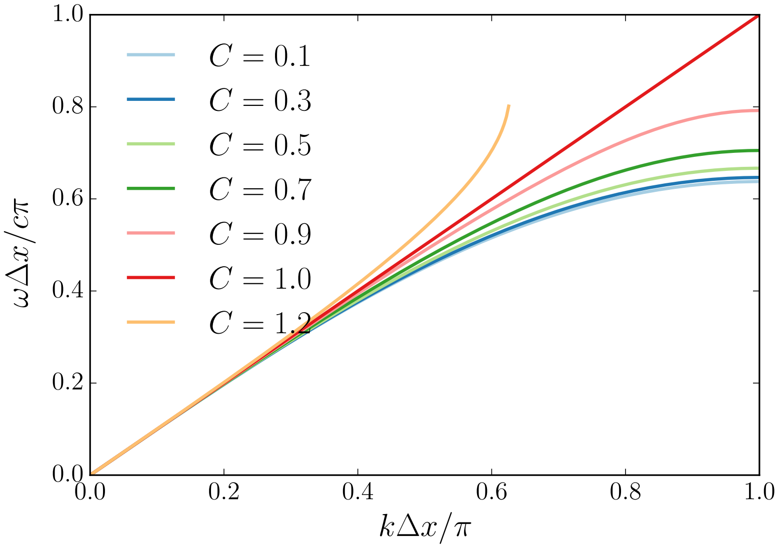

Figure E.4 Vacuum dispersion solution of Maxwell's equations for finite Δx, Δt. In one dimension, no dispersion error occurs for $C = 1.0$, which is marginally stable.

the short wavelength radiation on a time scale τ while leaving the discredited charge conservation properties unchanged (Bowers et al., 2008). This method needs an implicit field solver. An alternative explicit method uses $\boldsymbol{J}_T = \tau\partial_t(-\nabla\times\mu^{-1}\boldsymbol{B}) = \tau\mu^{-1}\nabla\times\nabla\times\boldsymbol{E}$, which can be written in normalized form as $\boldsymbol{J}_T = \tau\nabla\times\nabla\times\boldsymbol{E}$. The Ampère's law is modified to

$$\frac{\partial \boldsymbol{E}}{\partial t} = \frac{c^2}{v_A^2}(\nabla\times\boldsymbol{B} - \boldsymbol{J} - \tau\nabla\times\nabla\times\boldsymbol{E}) \tag{E.32}$$

Eastwood (1991) suggested that $\tau = 0.01$ would be enough, but the time step that he used is unknown. Zagorodnov and Weiland (2005); Bowers (2001) suggested that $\tau = 1/8$ or $1/4$ of the time step.

E.4 Divergence clean for electric field

We follow the method Marder passes (Marder, 1987). The Gauss's law for electric field is normalized as

$$\nabla \cdot \boldsymbol{E} = \frac{4\pi e n_0 d_i}{E_0}\rho = \left(\frac{c}{v_A}\right)^2 \rho \tag{E.33}$$

The charge density can be defined as

$$\rho(\boldsymbol{x}_p) = \frac{1}{n_0}\frac{1}{\Delta x \Delta y}\sum_{i=1}^{N_p} q_i W(\boldsymbol{x}_i - \boldsymbol{x}_p) \tag{E.34}$$

where $W(\boldsymbol{x}_i - \boldsymbol{x}_p)$ is the assignment function. Define

$$F = \nabla \cdot \boldsymbol{E} - \rho \tag{E.35}$$

Then, Gauss's law becomes $F = 0$. Ampère's law is changed as

$$\partial_t \boldsymbol{E} = \nabla \times \boldsymbol{B} - \boldsymbol{J} + d\nabla F \tag{E.36}$$

$d\nabla F$ will be referred as a "pseudo-current". d is numerical parameter chosen small enough not to affect adversely the stability but large enough to perform the desired function. Take the divergence of Equation E.36, F satisfies the inhomogeneous diffusion equation

$$\frac{\partial F}{\partial t} - d\nabla^2 F = -\left(\frac{\partial \rho}{\partial t} + \nabla \cdot \boldsymbol{J}\right) \tag{E.37}$$

The stability restriction introduced by this addition is the well-known heat equation constraint

$$2d\Delta t/\Delta x^2 < 1 \tag{E.38}$$

where δx and δt are the numerical space and time steps. Adding too much diffusion, however, can suppress the very physics the code is attempting to model. Adding to little, or none at all, allows the density obtained from the particles to differ from that obtained from the divergence of $\boldsymbol{E}$ to what may be an unacceptable degree. The discretized form of the modified Ampère's law can expressed as

$$\boldsymbol{E}^{n+1} - \boldsymbol{E}^{n} = \Delta t \left[\nabla \cdot \boldsymbol{B}^{n+\frac{1}{2}} - \boldsymbol{J}^{n+\frac{1}{2}} + d\nabla F^{n}\right] \tag{E.39}$$

It is shown in the original paper of Marder (1987) that $d = 0.001$ is good enough.

E.5 Particle advance

The Lorentz equation and Newton's equation are solved using a Buneman-Boris method (Birdsall and Langdon, 1991). In relativistic form,

$$\frac{\boldsymbol{u}^{n+1/2} - \boldsymbol{u}^{n-1/2}}{\Delta t} = \frac{q}{m}\left(\boldsymbol{E}^{n} + \frac{1}{c}\frac{\boldsymbol{u}^{n+1/2} + \boldsymbol{u}^{n-1/2}}{2\gamma^{n}} \times \boldsymbol{B}^{n}\right) \tag{E.40}$$

$$\boldsymbol{u}^{n-1/2} = \boldsymbol{u}^{-} - \frac{q\boldsymbol{E}^{n}\Delta t}{2m}, \quad \boldsymbol{u}^{n+1/2} = \boldsymbol{u}^{+} + \frac{q\boldsymbol{E}^{n}\Delta t}{2m} \tag{E.41}$$

$$\frac{\boldsymbol{u}^{+} - \boldsymbol{u}^{-}}{\Delta t} = \frac{q}{2\gamma^{n} mc}(\boldsymbol{u}^{+} + \boldsymbol{u}^{-}) \times \boldsymbol{B}^{n} \tag{E.42}$$

where $\boldsymbol{u} = \gamma \boldsymbol{v}$. Equation E.42 results a rotation of $\boldsymbol{u}$ about an axis parallel to $\boldsymbol{B}$ through and angle $\theta = -2\arctan(qB^n \Delta t/2\gamma mc)$. If we define $\boldsymbol{T} = q\boldsymbol{B}^n \Delta t/2\gamma^n mc$, with $(\gamma^n)^2 = 1 + (u^-/c)^2$. This method is implicit at first look, but it actually can be separated into several explicit steps.

$$\boldsymbol{u}^- = \boldsymbol{u}^{n-1/2} + \frac{q\boldsymbol{E}^n \Delta t}{2m} \tag{E.43}$$

$$\boldsymbol{u}' = \boldsymbol{u}^- + \boldsymbol{u}^- \times \boldsymbol{T}, \quad \boldsymbol{u}^+ = \boldsymbol{u}^- + \boldsymbol{u}' \times \boldsymbol{S} \tag{E.44}$$

$$\boldsymbol{u}^{n+1/2} = \boldsymbol{u}^+ + \frac{q\boldsymbol{E}^n \Delta t}{2m}, \quad \boldsymbol{r}^{n+1} = \boldsymbol{r}^n + \frac{\boldsymbol{u}^{n+1/2}\Delta t}{\gamma^{n+1/2}} \tag{E.45}$$

where $\boldsymbol{S} = 2\boldsymbol{T}/(1 + T^2)$, $(\gamma^{n+1/2})^2 = 1 + (u^{n+1/2}/c)^2$. Figure E.5 illustrates this process.

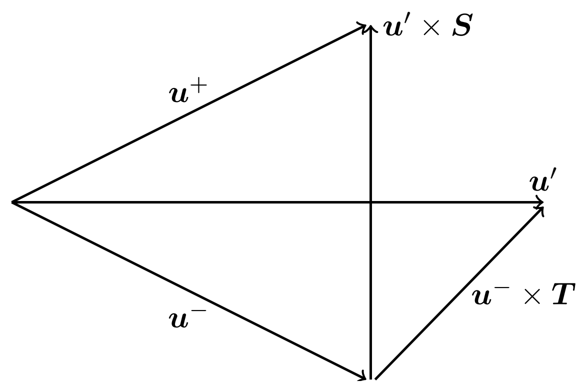

Figure E.5 Illustration of Borris rotation.

Change the equations to normalized form that can be used in the simulation.

$\boldsymbol{u} \rightarrow \boldsymbol{u}/c$

$$\boldsymbol{T} = \frac{q_s \boldsymbol{B}^n \Delta t}{2\gamma_s^n m_s} \frac{m_i}{m_0}, \quad \boldsymbol{u}^- = \boldsymbol{u}^{n-1/2} + \frac{q_s \boldsymbol{E}^n \Delta t}{2m_s} \frac{m_i}{m_0} \frac{v_A}{c} \tag{E.46}$$

$$\boldsymbol{u}' = \boldsymbol{u}^- + \boldsymbol{u}^- \times \boldsymbol{T}, \quad \boldsymbol{u}^+ = \boldsymbol{u}^- + \boldsymbol{u}' \times \boldsymbol{S} \tag{E.47}$$

$$\boldsymbol{u}^{n+1/2} = \boldsymbol{u}^+ + \frac{q_s \boldsymbol{E}^n \Delta t}{2m_s} \frac{m_i}{m_0} \frac{v_A}{c}, \quad \boldsymbol{r}^{n+1} = \boldsymbol{r}^n + \frac{c}{v_A} \frac{\boldsymbol{u}^{n+1/2} \Delta t}{\gamma^{n+1/2}} \tag{E.48}$$

Particle boundary conditions include periodic boundary condition, particle absorbing, particle reflecting and particle refluxing (Daughton et al., 2006). Particle collisions can be included in PIC code to collisional plasma (Takizuka and Abe, 1977; Daughton et al., 2009a; Lemons et al., 2009).

E.6 Particle sorting

Particles are initially assigned to each computing cell and continuously aligned in the memory. After several time steps, particles move into different cells, and the memory accessing is not continuous anymore. This will slow down the simulation. We have to sort the particles by cell every few steps to restore the spatial locality of the particles. A counting sort is an algorithm for sorting a length N list of values where only M different values are possible (Bowers, 2001). N corresponds the number of particles; M corresponds to the number of cells. In this algorithm, the particles are sorted by mesh location simultaneously with the push and accumulate. The implementation requires a minimal number of extra computations as the push and accumulate already generate most of the information necessary to do a counting sort.

A pseudo code for and out-of-place counting sort is copied here from (Bowers, 2001).

$j = P_i$ is changed to be $j = P_i + 1$ at the 3rd step.

Algorithm 1: Particle Counting Sort

Input : I is the particle array to sort containing N particles; M is the number of mesh cells

Output: O is the sorted particle array, P is a particle allocation such that $O_{P_{i-1}+1}$ to O_p are all the particles in cell i

```
begin
    allocate N particles for O
    allocate and set to zero M integers for P

    Step 1: Count the number of particles in each cell
    for n := 1 to N do
        i := compute the cell for particle I_n
        P_i := P_i + 1
    end for

    Step 2: Convert P to an allocation
    k := 0
    for i := 1 to M do
        j := P_i
        P_i := k
        k := k + j
    end for

    Step 3: Sort I into O
    for n := 1 to N do
        i := compute the cell for particle I_n
        j := P_i + 1
        P_i := j
        O_j := I_n
    end for

    return O, P
end
```

E.7 Charge conservation current deposition

The perfect particle shape is a Gaussian distribution. Depositing current using this particle shape is expensive because it covers infinite number of cells. In practice, particles have finite sizes so they only affect a finite number of cells. Figure E.6 shows three shapes of particle clouds. The lowest order is Nearest Grid Point (NGP) particle shape. The most commonly used shape is the linear Cloud in Cell (CIC) shape. The quadratic shape is called Triangular Shaped Cloud (TSC).

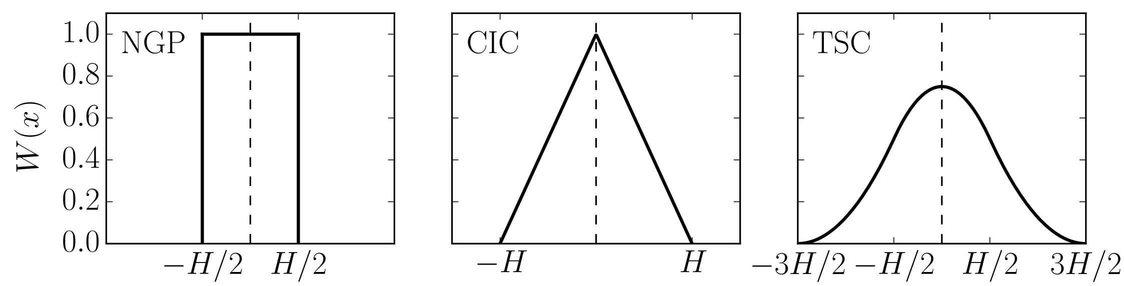

Figure E.6 Common particle shapes. H is the cell width. $W(x)$ is the assignment function. For NGP, $W(x) = 1$, when $|x| < H/2$ or $x = H/2$. For CIC, $W(x) = 1 - |x|/H$, when $|x| \leq H$. For TSC, $W(x) = 3/4 - (x/H)^2$, when $|x| \leq \frac{H}{2}$; $W(x) = (3/2 - |x|/H)^2 /2$, when $H/2 \leq |x| \leq 3H/2$.

The current deposition has to guarantee the charge is conserved as the Gauss's law is not solved. Three most commonly used charge conservation scheme (CCS) are from (Villasenor and Buneman, 1992; Esirkepov, 2001; Umeda et al., 2003). Villasenor and Buneman (1992)'s CCS assumes the particle trajectory over one time step is a straight line. When particles cross the cell boundary, the scheme has to decide the cross points. This may slow down the computation (Umeda et al., 2003). Esirkepov (2001); Umeda et al. (2003) avoid this problem and improves current deposition performance by separating the particle trajectory over one time step into different segments. Esirkepov (2001)'s CCS can be applied to high-order particle shape. Umeda et al. (2003)'s Zigzag scheme is only available in CIC particle shape. Please refer the original paper of Esirkepov (2001); Umeda et al. (2003) for detailed implementation of the schemes.

One effect of the finite-size particles on a grid is the aliasing effect. Without grid, and in one dimension,

$$\rho_c(x) = qn_c(x) = q\int_0^L dx' W(x-x')n(x') \tag{E.49}$$

where L is the length of the periodic system. Doing Fourier transform,

$$\begin{aligned}
\rho_c(k) &= \int_0^L \rho_c(x)e^{-ikx}dx \\
&= q\int_0^L n(x')dx' \int_0^L W(x-x')e^{-ikx}dx \\
&= q\int_0^L n(x')e^{-ikx'}dx' \int_0^L W(x)e^{-ikx}dx \\
&= qW(k)n(k)
\end{aligned} \tag{E.50}$$

With a grid, ρ_c will be sampled on the grid points.

$$\rho_j = \rho_c(X_j) = \int_{-\infty}^{\infty} \frac{dk}{2\pi}\rho_c(k)e^{ikX_j} = \int_{-\pi/H}^{\pi/H} \frac{dk}{2\pi}e^{ikX_j}\left[\sum_{p=-\infty}^{\infty} \rho_c(k_p)\right] \tag{E.51}$$

where X_j is the coordinate of a grid point, H is the grid size, $k_p = k - pk_g$ and $k_g = 2\pi/H$ is the grid wave number. Then,

$$\rho(k) = \sum_p \rho_c(k_p) = q\sum_p W(k_p)n(k_p) \tag{E.52}$$

suggesting that the aliases with a separation of integral multiples of k_g are coupled through the grid. In PIC simulations, we only have finite number of particles, so the density and other grid-based quantities always have high-k component, which are going to be folded into low-k components by aliasing. This introduces nosies to PIC simulations. To reduce the noise, higher-order/smoother particle shape $W(x)$ and more particles per cell are preferred.

E.8 Diagnostics

The typical diagnostics include

- Energies of the E/M field, particles. Particle energy distribution and phase space distribution.
- $\boldsymbol{E}$, $\boldsymbol{B}$, $\boldsymbol{j}$, ρ one the grid. Calculating $\nabla \cdot \boldsymbol{E}$ and $\nabla \cdot \boldsymbol{B}$ makes sure that the divergence clean procedures works.
- The fluid moments besides $\boldsymbol{j}$ and ρ, such as velocity $\boldsymbol{v}$ or momentum $\boldsymbol{u}$, stress tensor T.
- Power spectra $E(k)$ of the fluctuating field.
- Particle trajectories of energetic particles.

We show below how to calculate particle drift in a Yee Lattice. It is tricky to calculate the field and its derivatives at the particle position in Yee lattice shown in Figure E.7. As the fields are sampled at different positions, the field indices and weights will be different for different field when doing trilinear interpolation shown in Figure E.8. We assume the cell numbers in each MPI process are n_x, n_y, n_z in the PIC simulation. All of the fields have dimensions $n_x + 2$, $n_y + 2$, $n_z + 2$. $\boldsymbol{E}$ and $\boldsymbol{B}$

are staggered; E_x is sampled at the middle of x-directed cell edges, B_x is sampled at the middle of yz-oriented cell faces and similarly for the y and z components (Bowers et al., 2008). The hydro fields are sampled in the center of the cells. The position of

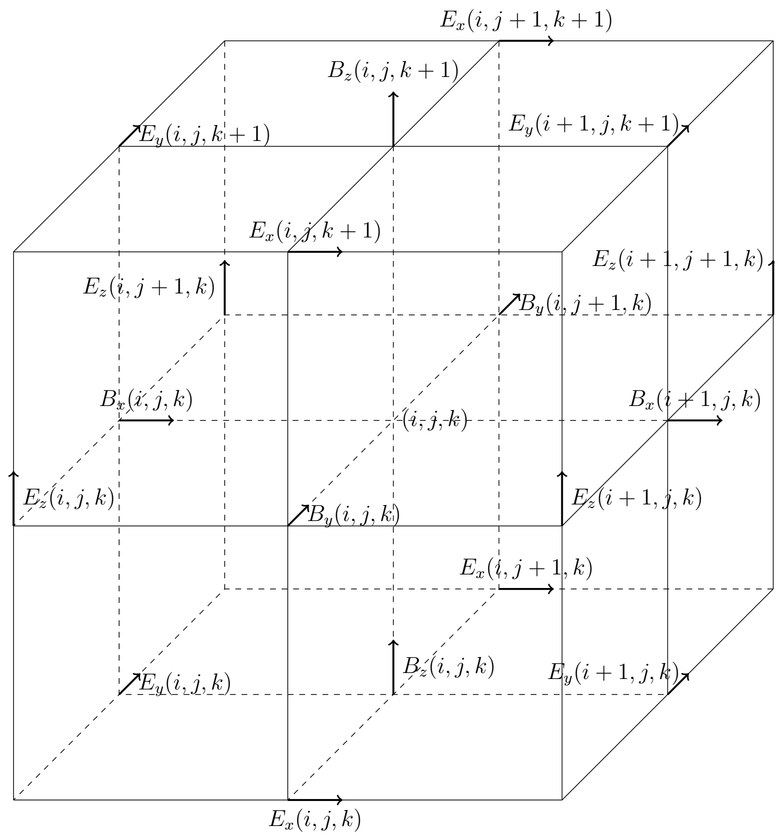

Figure E.7 Yee lattice. $i \in [1, n_x]$, $j \in [1, n_y]$, $k \in [1, n_z]$. The fields indices are in $[0, n_x + 1]$, $[0, n_y + 1]$, $[0, n_z + 1]$.

one particle in this grid is $\delta x \in [-1, 1]$, $\delta y \in [-1, 1]$, $\delta z \in [-1, 1]$, and the origin is the center of the cell.

We assume the origin of Figure E.8 is (i_1, j_1, k_1). For E_x and its derivatives, $j_1 = j$, $k_1 = k$, $\Delta y = 0.5(\delta y + 1)$, $\Delta z = 0.5(\delta z + 1)$. When $\delta x < 0$, $\Delta x = 0.5\delta x + 1$ and $i_1 = i - 1$. When $\delta x \geq 0$, $\Delta x = 0.5\delta x$ and $i_1 = i$. This is similar for E_y, E_z and their derivatives.

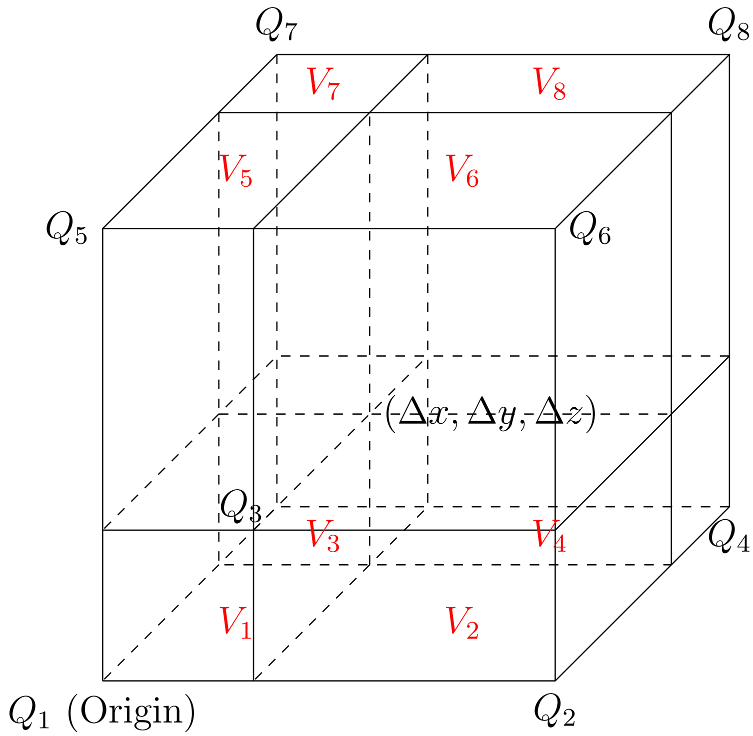

Figure E.8 Trilinear interpolation. $\Delta x, \Delta y, \Delta z \in [0, 1]$. Q can be any component of $\boldsymbol{E}$, $\boldsymbol{B}$ and their derivatives. $V_1 \cdots V_8$ are the weights for the trilinear interpolation. $V_1 = (1-\Delta x)(1-\Delta y)(1-\Delta z)$, $V_2 = \Delta x(1-\Delta y)(1-\Delta z)$, $V_3 = (1-\Delta x)\Delta y(1-\Delta z)$, $V_4 = \Delta x \Delta y(1-\Delta z)$, $V_5 = (1-\Delta x)(1-\Delta y)\Delta z$, $V_6 = \Delta x(1-\Delta y)\Delta z$, $V_7 = (1-\Delta x)\Delta y \Delta z$, $V_8 = \Delta x \Delta y \Delta z$.

For B_x and its derivatives, $i_1 = i$, $\Delta x = 0.5(1+\delta x)$. When $\delta y < 0$, $\Delta y = 0.5\delta y + 1$, $j_1 = j - 1$. When $\delta y \geq 0$, $\Delta y = 0.5\delta y$, $j_1 = j$. When $\delta z < 0$, $\Delta z = 0.5\delta z + 1$, $k_1 = k - 1$. When $\delta z \geq 0$, $\Delta z = 0.5\delta z$, $k_1 = k$. This is similar for the other two components.

Using these fields, particle curvature drift and gradient drift are calculated as

$$\boldsymbol{v}_g = \frac{v_\perp^2 \boldsymbol{b}}{2\Omega_{ce}} \times \frac{\nabla B}{B}, \quad \nabla B = \boldsymbol{b} \cdot \frac{\partial \boldsymbol{B}}{\partial x}\hat{x} + \boldsymbol{b} \cdot \frac{\partial \boldsymbol{B}}{\partial y}\hat{y} + \boldsymbol{b} \cdot \frac{\partial \boldsymbol{B}}{\partial z}\hat{z} \tag{E.53}$$

$$\boldsymbol{v}_c = \frac{v_\parallel^2 \boldsymbol{b}}{\Omega_{ce}} \times \boldsymbol{\kappa} \tag{E.54}$$

where $\Omega_{ce} = eB/(\gamma m_e c)$.

$$\begin{aligned}
\boldsymbol{\kappa} = (\boldsymbol{b}\cdot\nabla)\boldsymbol{b} &= \frac{1}{B}(\boldsymbol{b}\cdot\nabla\boldsymbol{B}) - \frac{\boldsymbol{B}}{B^2}(\boldsymbol{b}\cdot\nabla B) \\
&= \frac{1}{B}(\boldsymbol{b}\cdot\nabla B_x\hat{x} + \boldsymbol{b}\cdot\nabla B_y\hat{y} + \boldsymbol{b}\cdot\nabla B_z\hat{z}) - \frac{\boldsymbol{B}}{B^2}(\boldsymbol{b}\cdot\nabla B) \qquad \text{(E.55)}
\end{aligned}$$

REFERENCES

Milton Abramowitz and Irene A Stegun. *Handbook of mathematical functions: with formulas, graphs, and mathematical tables*, volume 55. Courier Corporation, 1964.

M. Ackermann, M. Ajello, and et al. Albert. High-energy Gamma-Ray Emission from Solar Flares: Summary of Fermi Large Area Telescope Detections and Analysis of Two M-class Flares. *The Astrophysical Journal*, 787:15, May 2014. doi: 10.1088/0004-637X/787/1/15.

Jacobo Aguirre and D Peralta-Salas. Realistic examples of chaotic magnetic fields created by wires. *EPL (Europhysics Letters)*, 80(6):60007, 2007.

Jacobo Aguirre, Alejandro Luque, and Daniel Peralta-Salas. Motion of charged particles in magnetic fields created by symmetric configurations of wires. *Physica D: Nonlinear Phenomena*, 239(10):654–674, 2010.

M. Ajello, A. Albert, and et al. Allafort. Impulsive and Long Duration High-energy Gamma-Ray Emission from the Very Bright 2012 March 7 Solar Flares. *The Astrophysical Journal*, 789:20, July 2014. doi: 10.1088/0004-637X/789/1/20.

H. Alfvén. Existence of Electromagnetic-Hydrodynamic Waves. *Nature*, 150:405–406, October 1942. doi: 10.1038/150405d0.

J. Arons. Pulsar Wind Nebulae as Cosmic Pevatrons: A Current Sheet's Tale. *Space Science Reviews*, 173:341–367, November 2012. doi: 10.1007/s11214-012-9885-1.

S. D. Baalrud, A. Bhattacharjee, and Y.-M. Huang. Reduced magnetohydrodynamic theory of oblique plasmoid instabilities. *Physics of Plasmas*, 19(2):022101, February 2012. doi: 10.1063/1.3678211.

S. G. Benka and G. D. Holman. A thermal/nonthermal model for solar hard X-ray bursts. *The Astrophysical Journal*, 435:469–481, November 1994. doi: 10.1086/174829.

Naoki Bessho and A Bhattacharjee. Fast magnetic reconnection in low-density electron-positron plasmas. *Physics of Plasmas*, 17(10):102104, 2010.

A. Bhattacharjee, Y.-M. Huang, H. Yang, and B. Rogers. Fast reconnection in high-Lundquist-number plasmas due to the plasmoid Instability. *Physics of Plasmas*, 16 (11):112102, November 2009. doi: 10.1063/1.3264103.

C. K. Birdsall and A. B. Langdon. *Plasma Physics via Computer Simulation*. CRC Press, 1991.

J. Birn and E. R. Priest. *Reconnection of magnetic fields : magnetohydrodynamics and collisionless theory and observations*. 2007.

J. Birn, J. F. Drake, M. A. Shay, B. N. Rogers, R. E. Denton, M. Hesse, M. Kuznetsova, Z. W. Ma, A. Bhattacharjee, A. Otto, and P. L. Pritchett. Geospace Environmental Modeling (GEM) magnetic reconnection challenge. *Journal of Geophysical Research*, 106:3715–3720, March 2001. doi: 10.1029/1999JA900449.

J. Birn, J. E. Borovsky, and M. Hesse. The role of compressibility in energy release by magnetic reconnection. *Physics of Plasmas*, 19(8):082109, August 2012. doi: 10.1063/1.4742314.

D. Biskamp. Magnetic reconnection via current sheets. *Physics of Fluids*, 29:1520–1531, May 1986. doi: 10.1063/1.865670.

D Biskamp and E Schwarz. Localization, the clue to fast magnetic reconnection. *Physics of Plasmas (1994-present)*, 8(11):4729–4731, 2001.

R. Blandford, P. Simeon, and Y. Yuan. Cosmic Ray Origins: An Introduction. *Nuclear Physics B Proceedings Supplements*, 256:9–22, 2014. doi: 10.1016/j.nuclphysbps.2014.10.002.

K. J. Bowers. *High-frequency electron resonances and surface waves in unmagnetized bounded plasmas*. PhD thesis, UNIVERSITY OF CALIFORNIA, BERKELEY, 2001.

K. J. Bowers, B. J. Albright, L. Yin, B. Bergen, and T. J. T. Kwan. Ultrahigh performance three-dimensional electromagnetic relativistic kinetic plasma simulationa). *Physics of Plasmas*, 15(5):055703, May 2008. doi: 10.1063/1.2840133.

J. Büchner and N. Elkina. Vlasov Code Simulation of Anomalous Resistivity. *Space Science Reviews*, 121:237–252, November 2005. doi: 10.1007/s11214-006-6542-6.

J. Büchner and N. Elkina. Anomalous resistivity of current-driven isothermal plasmas due to phase space structuring. *Physics of Plasmas*, 13(8):082304, August 2006. doi: 10.1063/1.2209611.

SV Bulanov, J Sakai, and SI Syrovatskii. Tearing-mode instability in approximately steady mhd configurations. *Sov. J. Plasma Phys.(Engl. Transl.);(United States)*, 5 (2), 1979.

H. Carmichael. A Process for Flares. *NASA Special Publication*, 50:451, 1964.

R. C. Carrington. Description of a Singular Appearance seen in the Sun on September 1, 1859. *Monthly Notices of the Royal Astronomical Society*, 20:13–15, November 1859. doi: 10.1093/mnras/20.1.13.

P. A. Cassak, M. A. Shay, and J. F. Drake. Catastrophe Model for Fast Magnetic Reconnection Onset. *Physical Review Letters*, 95(23):235002, December 2005. doi: 10.1103/PhysRevLett.95.235002.

P. A. Cassak, M. A. Shay, and J. F. Drake. Scaling of Sweet-Parker reconnection with secondary islands. *Physics of Plasmas*, 16(12):120702, December 2009. doi: 10.1063/1.3274462.

C. Cattell, J. Dombeck, J. Wygant, J. F. Drake, M. Swisdak, M. L. Goldstein, W. Keith, A. Fazakerley, M. André, E. Lucek, and A. Balogh. Cluster observations of electron holes in association with magnetotail reconnection and comparison to simulations. *Journal of Geophysical Research (Space Physics)*, 110:A01211, January 2005. doi: 10.1029/2004JA010519.

B. D. G. Chandran. Particle Acceleration by Slow Modes in Strong Compressible Magnetohydrodynamic Turbulence, with Application to Solar Flares. *The Astrophysical Journal*, 599:1426–1433, December 2003. doi: 10.1086/379317.

B. Chen, T. S. Bastian, C. Shen, D. E. Gary, S. Krucker, and L. Glesener. Particle acceleration by a solar flare termination shock. *Science*, 350:1238–1242, December 2015. doi: 10.1126/science.aac8467.

Q. Chen and V. Petrosian. Impulsive Phase Coronal Hard X-Ray Sources in an X3.9 Class Solar Flare. *The Astrophysical Journal*, 748:33, March 2012. doi: 10.1088/0004-637X/748/1/33.

G. F. Chew, M. L. Goldberger, and F. E. Low. The Boltzmann Equation and the One-Fluid Hydromagnetic Equations in the Absence of Particle Collisions. *Royal Society of London Proceedings Series A*, 236:112–118, July 1956. doi: 10.1098/rspa.1956.0116.

S. A. Colgate, H. Li, and V. Pariev. The origin of the magnetic fields of the universe: The plasma astrophysics of the free energy of the universe. *Physics of Plasmas*, 8: 2425–2431, May 2001. doi: 10.1063/1.1351827.

Luca Comisso and Daniela Grasso. Visco-resistive plasmoid instability. *Physics of Plasmas (1994-present)*, 23(3):032111, 2016.

B. Coppi, R. Galvao, R. Pellat, M. Rosenbluth, and P. Rutherford. Resistive internal kink modes. *Sov. J. Plasma Phys.*, 2:533–535, November 1976.

J. T. Dahlin, J. F. Drake, and M. Swisdak. The mechanisms of electron heating and acceleration during magnetic reconnection. *Physics of Plasmas*, 21(9):092304, September 2014. doi: 10.1063/1.4894484.

Joel Timothy Dahlin. *Electron acceleration in magnetic reconnection*. PhD thesis, University of Maryland, College Park, 2015.

B Dasgupta, Gang Li, Xiaocan Li, Abhay Ram, Qiang Hu, Gang Li, Gary P Zank, Xianzhi Ao, Olga Verkhoglyadova, and James H Adams. Particle transport and acceleration in a chaotic magnetic field: Implications for seed population to solar flare and cme. In *AIP Conference Proceedings-American Institute of Physics*, volume 1500, page 56, 2012.

W. Daughton. The unstable eigenmodes of a neutral sheet. *Physics of Plasmas*, 6: 1329–1343, April 1999. doi: 10.1063/1.873374.

W. Daughton and V. Roytershteyn. Emerging Parameter Space Map of Magnetic Reconnection in Collisional and Kinetic Regimes. *Space Science Reviews*, 172:271–282, November 2012. doi: 10.1007/s11214-011-9766-z.

W. Daughton, J. Scudder, and H. Karimabadi. Fully kinetic simulations of undriven magnetic reconnection with open boundary conditions. *Physics of Plasmas*, 13(7): 072101, July 2006. doi: 10.1063/1.2218817.

W. Daughton, V. Roytershteyn, B. J. Albright, H. Karimabadi, L. Yin, and K. J. Bowers. Influence of Coulomb collisions on the structure of reconnection layers. *Physics of Plasmas*, 16(7):072117, July 2009a. doi: 10.1063/1.3191718.

W. Daughton, V. Roytershteyn, B. J. Albright, H. Karimabadi, L. Yin, and K. J. Bowers. Transition from collisional to kinetic regimes in large-scale reconnection layers. *Physical Review Letters*, 103(6):065004, August 2009b. doi: 10.1103/PhysRevLett.103.065004.

W. Daughton, V. Roytershteyn, H. Karimabadi, L. Yin, B. J. Albright, B. Bergen, and K. J. Bowers. Role of electron physics in the development of turbulent magnetic reconnection in collisionless plasmas. *Nature Physics*, 7:539–542, July 2011. doi: 10.1038/nphys1965.

C. Dauphin, N. Vilmer, and A. Anastasiadis. Particle acceleration and radiation in flaring complex solar active regions modeled by cellular automata. *Astronomy & Astrophysics*, 468:273–288, June 2007. doi: 10.1051/0004-6361:20065131.

M. I. Desai, G. M. Mason, J. R. Dwyer, J. E. Mazur, R. E. Gold, S. M. Krimigis, C. W. Smith, and R. M. Skoug. Evidence for a Suprathermal Seed Population of Heavy Ions Accelerated by Interplanetary Shocks near 1 AU. *The Astrophysical Journal*, 588:1149–1162, May 2003. doi: 10.1086/374310.

J. F. Drake and M. Swisdak. The onset of ion heating during magnetic reconnection with a strong guide field. *Physics of Plasmas*, 21(7):072903, July 2014. doi: 10.1063/1.4889871.

J. F. Drake, M. Swisdak, C. Cattell, M. A. Shay, B. N. Rogers, and A. Zeiler. Formation of Electron Holes and Particle Energization During Magnetic Reconnection. *Science*, 299:873–877, February 2003. doi: 10.1126/science.1080333.

J. F. Drake, M. A. Shay, W. Thongthai, and M. Swisdak. Production of Energetic Electrons during Magnetic Reconnection. *Physical Review Letters*, 94(9):095001, March 2005. doi: 10.1103/PhysRevLett.94.095001.

J. F. Drake, M. Swisdak, H. Che, and M. A. Shay. Electron acceleration from contracting magnetic islands during reconnection. *Nature*, 443:553–556, October 2006. doi: 10.1038/nature05116.

J. F. Drake, M. A. Shay, and M. Swisdak. The Hall fields and fast magnetic reconnection. *Physics of Plasmas*, 15(4):042306, April 2008. doi: 10.1063/1.2901194.

J. F. Drake, P. A. Cassak, M. A. Shay, M. Swisdak, and E. Quataert. A Magnetic Reconnection Mechanism for Ion Acceleration and Abundance Enhancements in Impulsive Flares. *The Astrophysical Journal Letters*, 700:L16–L20, July 2009a. doi: 10.1088/0004-637X/700/1/L16.

J. F. Drake, M. Swisdak, T. D. Phan, P. A. Cassak, M. A. Shay, S. T. Lepri, R. P. Lin, E. Quataert, and T. H. Zurbuchen. Ion heating resulting from pickup in magnetic reconnection exhausts. *Journal of Geophysical Research (Space Physics)*, 114:A05111, May 2009b. doi: 10.1029/2008JA013701.

J. F. Drake, M. Opher, M. Swisdak, and J. N. Chamoun. A Magnetic Reconnection Mechanism for the Generation of Anomalous Cosmic Rays. *The Astrophysical Journal*, 709:963–974, February 2010. doi: 10.1088/0004-637X/709/2/963.

J. F. Drake, M. Swisdak, and R. Fermo. The Power-law Spectra of Energetic Particles during Multi-island Magnetic Reconnection. *The Astrophysical Journal Letters*, 763: L5, January 2013. doi: 10.1088/2041-8205/763/1/L5.

L. O. Drury. An introduction to the theory of diffusive shock acceleration of energetic particles in tenuous plasmas. *Reports on Progress in Physics*, 46:973–1027, August 1983. doi: 10.1088/0034-4885/46/8/002.

James W Eastwood. The virtual particle electromagnetic particle-mesh method. *Computer Physics Communications*, 64(2):252–266, 1991.

J. Egedal, W. Fox, N. Katz, M. Porkolab, M. ØIeroset, R. P. Lin, W. Daughton, and J. F. Drake. Evidence and theory for trapped electrons in guide field magnetotail reconnection. *Journal of Geophysical Research (Space Physics)*, 113:A12207, December 2008. doi: 10.1029/2008JA013520.

J. Egedal, W. Daughton, J. F. Drake, N. Katz, and A. Lê. Formation of a localized acceleration potential during magnetic reconnection with a guide field. *Physics of Plasmas*, 16(5):050701, May 2009. doi: 10.1063/1.3130732.

J. Egedal, W. Daughton, and A. Le. Large-scale electron acceleration by parallel electric fields during magnetic reconnection. *Nature Physics*, 8:321–324, April 2012. doi: 10.1038/nphys2249.

J. Egedal, A. Le, and W. Daughton. A review of pressure anisotropy caused by electron trapping in collisionless plasma, and its implications for magnetic reconnection. *Physics of Plasmas*, 20(6):061201, June 2013. doi: 10.1063/1.4811092.

J. Egedal, W. Daughton, A. Le, and A. L. Borg. Double layer electric fields aiding the production of energetic flat-top distributions and superthermal electrons within magnetic reconnection exhausts. *Physics of Plasmas*, 22(10):101208, October 2015. doi: 10.1063/1.4933055.

Nikolai V Erkaev, Vladimir S Semenov, and Ferdinand Jamitzky. Reconnection rate for the inhomogeneous resistivity petschek model. *Physical Review Letters*, 84(7): 1455, 2000.

T Zh Esirkepov. Exact charge conservation scheme for particle-in-cell simulation with an arbitrary form-factor. *Computer Physics Communications*, 135(2):144–153, 2001.

E. Fermi. On the Origin of the Cosmic Radiation. *Physical Review*, 75:1169–1174, April 1949. doi: 10.1103/PhysRev.75.1169.

H. S. Fu, Y. V. Khotyaintsev, M. André, and A. Vaivads. Fermi and betatron acceleration of suprathermal electrons behind dipolarization fronts. *Geophysical Research Letters*, 38:L16104, August 2011. doi: 10.1029/2011GL048528.

X. R. Fu, Q. M. Lu, and S. Wang. The process of electron acceleration during collisionless magnetic reconnection. *Physics of Plasmas*, 13(1):012309, January 2006. doi: 10.1063/1.2164808.

T. Fukushima. Fast computation of complete elliptic integrals and Jacobian elliptic functions. *Celestial Mechanics and Dynamical Astronomy*, 105:305–328, December 2009. doi: 10.1007/s10569-009-9228-z.

H. P. Furth, J. Killeen, and M. N. Rosenbluth. Finite-Resistivity Instabilities of a Sheet Pinch. *Physics of Fluids*, 6:459–484, April 1963. doi: 10.1063/1.1706761.

A. A. Galeev, R. Rosner, and G. S. Vaiana. Structured coronae of accretion disks. *The Astrophysical Journal*, 229:318–326, April 1979. doi: 10.1086/156957.

G. A. Gary. Plasma Beta above a Solar Active Region: Rethinking the Paradigm. *Solar Physics*, 203:71–86, October 2001. doi: 10.1023/A:1012722021820.

Manolis K Georgoulis, Viacheslav S Titov, et al. Non-neutralized electric current patterns in solar active regions: Origin of the shear-generating lorentz force. *The Astrophysical Journal*, 761(1):61, 2012.

R. G. Giovanelli. Magnetic and Electric Phenomena in the Sun's Atmosphere associated with Sunspots. *Monthly Notices of the Royal Astronomical Society*, 107:338, 1947. doi: 10.1093/mnras/107.4.338.

F. Guo and J. Giacalone. Particle Acceleration at a Flare Termination Shock: Effect of Large-scale Magnetic Turbulence. *The Astrophysical Journal*, 753:28, July 2012. doi: 10.1088/0004-637X/753/1/28.

F. Guo, H. Li, W. Daughton, and Y.-H. Liu. Formation of Hard Power-laws in the Energetic Particle Spectra Resulting from Relativistic Magnetic Reconnection. *Physical Review Letters*, 113(15):155005, May 2014.

F. Guo, Y.-H. Liu, W. Daughton, and H. Li. Particle Acceleration and Plasma Dynamics during Magnetic Reconnection in the Magnetically Dominated Regime. *The Astrophysical Journal*, 806:167, June 2015. doi: 10.1088/0004-637X/806/2/167.

F. Guo, X. Li, H. Li, W. Daughton, B. Zhang, N. Lloyd-Ronning, Y.-H. Liu, H. Zhang, and W. Deng. Efficient Production of High-energy Nonthermal Particles during Magnetic Reconnection in a Magnetically Dominated Ion-Electron Plasma. *The Astrophysical Journal Letters*, 818:L9, February 2016. doi: 10.3847/2041-8205/818/1/L9.

F. Haardt, L. Maraschi, and G. Ghisellini. A model for the X-ray and ultraviolet emission from Seyfert galaxies and galactic black holes. *The Astrophysical Journal*, 432:L95–L99, September 1994. doi: 10.1086/187520.

G. E. Hale. On the Probable Existence of a Magnetic Field in Sun-Spots. *The Astrophysical Journal*, 28:315, November 1908. doi: 10.1086/141602.

R. J. Hamilton and V. Petrosian. Stochastic acceleration of electrons. I - Effects of collisions in solar flares. *The Astrophysical Journal*, 398:350–358, October 1992. doi: 10.1086/171860.

M. Hesse, K. Schindler, J. Birn, and M. Kuznetsova. The diffusion region in collisionless magnetic reconnection. *Physics of Plasmas*, 6:1781–1795, May 1999. doi: 10.1063/1.873436.

M. Hesse, J. Birn, and M. Kuznetsova. Collisionless magnetic reconnection: Electron processes and transport modeling. *Journal of Geophysical Research*, 106:3721–3736, March 2001. doi: 10.1029/1999JA001002.

M. Hesse, T. Neukirch, K. Schindler, M. Kuznetsova, and S. Zenitani. The Diffusion Region in Collisionless Magnetic Reconnection. *Space Science Reviews*, 160:3–23, October 2011. doi: 10.1007/s11214-010-9740-1.

Robert L Higdon. Absorbing boundary conditions for difference approximations to the multidimensional wave equation. *Mathematics of computation*, 47(176):437–459, 1986.

T. Hirayama. Theoretical Model of Flares and Prominences. I: Evaporating Flare Model. *Solar Physics*, 34:323–338, February 1974. doi: 10.1007/BF00153671.

Roger W Hockney and James W Eastwood. *Computer simulation using particles*. CRC Press, 1988.

R. Hodgson. On a curious Appearance seen in the Sun. *Monthly Notices of the Royal Astronomical Society*, 20:15–16, November 1859. doi: 10.1093/mnras/20.1.15.

M. Hoshino. Electron surfing acceleration in magnetic reconnection. *Journal of Geophysical Research (Space Physics)*, 110:A10215, October 2005. doi: 10.1029/2005JA011229.

M. Hoshino, T. Mukai, T. Terasawa, and I. Shinohara. Suprathermal electron acceleration in magnetic reconnection. *Journal of Geophysical Research*, 106:25979–25998, November 2001. doi: 10.1029/2001JA900052.

M Hosoda, T Miyaguchi, K Imagawa, and K Nakamura. Ubiquity of chaotic magnetic-field lines generated by three-dimensionally crossed wires in modern electric circuits. *Physical Review E*, 80(6):067202, 2009.

Can Huang, Mingyu Wu, Quanming Lu, Rongsheng Wang, and Shui Wang. Electron acceleration in the dipolarization front driven by magnetic reconnection. *Journal of Geophysical Research (Space Physics)*, 120(3):1759–1765, 2015.

S. Y. Huang, A. Vaivads, Y. V. Khotyaintsev, M. Zhou, H. S. Fu, A. Retinò, X. H. Deng, M. André, C. M. Cully, J. S. He, F. Sahraoui, Z. G. Yuan, and Y. Pang. Electron acceleration in the reconnection diffusion region: Cluster observations. *Geophysical Research Letters*, 39:L11103, June 2012. doi: 10.1029/2012GL051946.

Y.-M. Huang and A. Bhattacharjee. Scaling laws of resistive magnetohydrodynamic reconnection in the high-Lundquist-number, plasmoid-unstable regime. *Physics of Plasmas*, 17(6):062104, June 2010. doi: 10.1063/1.3420208.

Y.-M. Huang and A. Bhattacharjee. Turbulent Magnetohydrodynamic Reconnection Mediated by the Plasmoid Instability. *The Astrophysical Journal*, 818:20, February 2016. doi: 10.3847/0004-637X/818/1/20.

D. E. Innes, D. E. McKenzie, and T. Wang. SUMER spectral observations of post-flare supra-arcade inflows. *Solar Physics*, 217:247–265, November 2003. doi: 10.1023/B:SOLA.0000006899.12788.22.

J. D. Jackson. *Classical Electrodynamics, 3rd Edition*. July 1998.

H. Ji and W. Daughton. Phase diagram for magnetic reconnection in heliophysical, astrophysical, and laboratory plasmas. *Physics of Plasmas*, 18(11):111207–111207, November 2011. doi: 10.1063/1.3647505.

J. R. Jokipii. Cosmic-Ray Propagation. I. Charged Particles in a Random Magnetic Field. *The Astrophysical Journal*, 146:480, November 1966. doi: 10.1086/148912.

J. R. Jokipii. Propagation of cosmic rays in the solar wind. *Reviews of Geophysics and Space Physics*, 9:27–87, 1971. doi: 10.1029/RG009i001p00027.

K. Knizhnik, M. Swisdak, and J. F. Drake. The Acceleration of Ions in Solar Flares during Magnetic Reconnection. *The Astrophysical Journal Letters*, 743:L35, December 2011. doi: 10.1088/2041-8205/743/2/L35.

X. Kong, Y. Chen, F. Guo, S. Feng, B. Wang, G. Du, and G. Li. The Possible Role of Coronal Streamers as Magnetically Closed Structures in Shock-induced Energetic Electrons and Metric Type II Radio Bursts. *The Astrophysical Journal*, 798:81, January 2015. doi: 10.1088/0004-637X/798/2/81.

E. P. Kontar, E. Dickson, and J. Kašparová. Low-Energy Cutoffs in Electron Spectra of Solar Flares: Statistical Survey. *Solar Physics*, 252:139–147, October 2008. doi: 10.1007/s11207-008-9249-x.

E. P. Kontar, J. C. Brown, A. G. Emslie, W. Hajdas, G. D. Holman, G. J. Hurford, J. Kašparová, P. C. V. Mallik, A. M. Massone, M. L. McConnell, M. Piana, M. Prato, E. J. Schmahl, and E. Suarez-Garcia. Deducing Electron Properties from Hard X-ray Observations. *Space Science Reviews*, 159:301–355, September 2011. doi: 10.1007/s11214-011-9804-x.

R. A. Kopp and G. W. Pneuman. Magnetic reconnection in the corona and the loop prominence phenomenon. *Solar Physics*, 50:85–98, October 1976. doi: 10.1007/BF00206193.

G. Kowal, E. M. de Gouveia Dal Pino, and A. Lazarian. Particle Acceleration in Turbulence and Weakly Stochastic Reconnection. *Physical Review Letters*, 108(24): 241102, June 2012. doi: 10.1103/PhysRevLett.108.241102.

S. Krucker and M. Battaglia. Particle Densities within the Acceleration Region of a Solar Flare. *The Astrophysical Journal*, 780:107, January 2014. doi: 10.1088/0004-637X/780/1/107.

S. Krucker, H. S. Hudson, L. Glesener, S. M. White, S. Masuda, J.-P. Wuelser, and R. P. Lin. Measurements of the Coronal Acceleration Region of a Solar Flare. *The Astrophysical Journal*, 714:1108–1119, May 2010. doi: 10.1088/0004-637X/714/2/1108.

M. W. Kunz, A. A. Schekochihin, and J. M. Stone. Firehose and Mirror Instabilities in a Collisionless Shearing Plasma. *Physical Review Letters*, 112(20):205003, May 2014. doi: 10.1103/PhysRevLett.112.205003.

G. Lapenta. Self-Feeding Turbulent Magnetic Reconnection on Macroscopic Scales. *Physical Review Letters*, 100(23):235001, June 2008. doi: 10.1103/PhysRevLett.100.235001.

A. Le, H. Karimabadi, J. Egedal, V. Roytershteyn, and W. Daughton. Electron energization during magnetic island coalescence. *Physics of Plasmas*, 19(7):072120, July 2012. doi: 10.1063/1.4739244.

A. Le, J. Egedal, O. Ohia, W. Daughton, H. Karimabadi, and V. S. Lukin. Regimes of the Electron Diffusion Region in Magnetic Reconnection. *Physical Review Letters*, 110(13):135004, March 2013. doi: 10.1103/PhysRevLett.110.135004.

J. A. le Roux, G. P. Zank, G. M. Webb, and O. Khabarova. A Kinetic Transport Theory for Particle Acceleration and Transport in Regions of Multiple Contracting and Reconnecting Inertial-scale Flux Ropes. *The Astrophysical Journal*, 801:112, March 2015. doi: 10.1088/0004-637X/801/2/112.

L. C. Lee and Z. F. Fu. Multiple X line reconnection. I - A criterion for the transition from a single X line to a multiple X line reconnection. *Journal of Geophysical Research*, 91:6807–6815, June 1986. doi: 10.1029/JA091iA06p06807.

Don S Lemons, Dan Winske, William Daughton, and Brian Albright. Small-angle coulomb collision model for particle-in-cell simulations. *Journal of Computational Physics*, 228(5):1391–1403, 2009.

G Li, B Dasgupta, G Webb, and AK Ram. Particle motion and energization in a chaotic magnetic field. In *SHOCK WAVES IN SPACE AND ASTROPHYSICAL ENVIRONMENTS: 18th Annual International Astrophysics Conference*, volume 1183, pages 201–211. AIP Publishing, 2009.

G. Li, X. Kong, G. Zank, and Y. Chen. On the Spectral Hardening at gsim300 keV in Solar Flares. *The Astrophysical Journal*, 769:22, May 2013. doi: 10.1088/0004-637X/769/1/22.

X. Li, B. Dasgupta, and G. Li. Energization of charged particle in a time-dependent chaotic magnetic field with an implication of the production of seed particles in solar energetic particle events. *Advances in Space Research*, 53:1153–1161, April 2014. doi: 10.1016/j.asr.2014.01.008.

X. Li, F. Guo, H. Li, and G. Li. Nonthermally Dominated Electron Acceleration during Magnetic Reconnection in a Low-β Plasma. *The Astrophysical Journal Letters*, 811:L24, October 2015. doi: 10.1088/2041-8205/811/2/L24.

X. Li, F. Guo, H. Li, and G. Li. Particle acceleration during magnetic reconnection in a low-beta plasma. *to be submitted to The Astrophysical Journal*, May 2016.

R. P. Lin. Energy Release and Particle Acceleration in Flares: Summary and Future Prospects. *Space Science Reviews*, 159:421–445, September 2011. doi: 10.1007/s11214-011-9801-0.

R. P. Lin, S. Krucker, G. J. Hurford, D. M. Smith, H. S. Hudson, G. D. Holman, R. A. Schwartz, B. R. Dennis, G. H. Share, R. J. Murphy, A. G. Emslie, C. Johns-Krull, and N. Vilmer. RHESSI Observations of Particle Acceleration and Energy Release in an Intense Solar Gamma-Ray Line Flare. *The Astrophysical Journal Letters*, 595:L69–L76, October 2003. doi: 10.1086/378932.

W. Liu, V. Petrosian, B. R. Dennis, and Y. W. Jiang. Double Coronal Hard and Soft X-Ray Source Observed by RHESSI: Evidence for Magnetic Reconnection and Particle Acceleration in Solar Flares. *The Astrophysical Journal*, 676:704–716, March 2008. doi: 10.1086/527538.

W. Liu, Q. Chen, and V. Petrosian. Plasmoid Ejections and Loop Contractions in an Eruptive M7.7 Solar Flare: Evidence of Particle Acceleration and Heating in Magnetic Reconnection Outflows. *The Astrophysical Journal*, 767:168, April 2013a. doi: 10.1088/0004-637X/767/2/168.

Y.-H. Liu, W. Daughton, H. Karimabadi, H. Li, and V. Roytershteyn. Bifurcated Structure of the Electron Diffusion Region in Three-Dimensional Magnetic Reconnection. *Physical Review Letters*, 110(26):265004, June 2013b. doi: 10.1103/PhysRevLett.110.265004.

Y.-H. Liu, F. Guo, W. Daughton, H. Li, and M. Hesse. Scaling of Magnetic Reconnection in Relativistic Collisionless Pair Plasmas. *Physical Review Letters*, 114(9): 095002, March 2015. doi: 10.1103/PhysRevLett.114.095002.

N. F. Loureiro and D. A. Uzdensky. Magnetic reconnection: from the Sweet–Parker model to stochastic plasmoid chains. *Plasma Physics and Controlled Fusion*, 58(1): 014021, January 2016. doi: 10.1088/0741-3335/58/1/014021.

N. F. Loureiro, A. A. Schekochihin, and S. C. Cowley. Instability of current sheets and formation of plasmoid chains. *Physics of Plasmas*, 14(10):100703, October 2007. doi: 10.1063/1.2783986.

N. F. Loureiro, R. Samtaney, A. A. Schekochihin, and D. A. Uzdensky. Magnetic reconnection and stochastic plasmoid chains in high-Lundquist-number plasmas. *Physics of Plasmas*, 19(4):042303–042303, April 2012. doi: 10.1063/1.3703318.

N. F. Loureiro, A. A. Schekochihin, and D. A. Uzdensky. Plasmoid and Kelvin-Helmholtz instabilities in Sweet-Parker current sheets. *Physical Review E*, 87(1): 013102, January 2013. doi: 10.1103/PhysRevE.87.013102.

Z. W. Ma and A. Bhattacharjee. Fast impulsive reconnection and current sheet intensification due to electron pressure gradients in semi-collisional plasmas. *Geophysical Research Letters*, 23:1673–1676, 1996. doi: 10.1029/96GL01600.

L. M. Malyshkin, T. Linde, and R. M. Kulsrud. Magnetic reconnection with anomalous resistivity in two-and-a-half dimensions. I. Quasistationary case. *Physics of Plasmas*, 12(10):102902–102902, October 2005. doi: 10.1063/1.2084847.

Hann-Shin Mao and Richard Wirz. Comparison of charged particle tracking methods for non-uniform magnetic fields. In *42nd AIAA Plasmadynamics and Lasers Conference*, 2011.

Barry Marder. A method for incorporating gauss' law into electromagnetic pic codes. *Journal of Computational Physics*, 68(1):48–55, 1987.

S. Masuda, T. Kosugi, H. Hara, S. Tsuneta, and Y. Ogawara. A loop-top hard X-ray source in a compact solar flare as evidence for magnetic reconnection. *Nature*, 371: 495–497, October 1994. doi: 10.1038/371495a0.

D. E. McKenzie and R. C. Canfield. Hinode XRT observations of a long-lasting coronal sigmoid. *Astronomy & Astrophysics*, 481:L65–L68, April 2008. doi: 10.1051/0004-6361:20079035.

M. Melzani, R. Walder, D. Folini, C. Winisdoerffer, and J. M. Favre. The energetics of relativistic magnetic reconnection: ion-electron repartition and particle distribution hardness. *Astronomy & Astrophysics*, 570:A112, October 2014. doi: 10.1051/0004-6361/201424193.

J. A. Miller, T. N. Larosa, and R. L. Moore. Stochastic Electron Acceleration by Cascading Fast Mode Waves in Impulsive Solar Flares. *The Astrophysical Journal*, 461:445, April 1996. doi: 10.1086/177072.

J. A. Miller, P. J. Cargill, A. G. Emslie, G. D. Holman, B. R. Dennis, T. N. LaRosa, R. M. Winglee, S. G. Benka, and S. Tsuneta. Critical issues for understanding particle acceleration in impulsive solar flares. *Journal of Geophysical Research*, 102: 14631–14660, July 1997. doi: 10.1029/97JA00976.

K. Nalewajko, D. A. Uzdensky, B. Cerutti, G. R. Werner, and M. C. Begelman. On the Distribution of Particle Acceleration Sites in Plasmoid-dominated Relativistic Magnetic Reconnection. *The Astrophysical Journal*, 815:101, December 2015. doi: 10.1088/0004-637X/815/2/101.

L. Neergaard Parker and G. P. Zank. Particle Acceleration at Quasi-parallel Shock Waves: Theory and Observations at 1 AU. *The Astrophysical Journal*, 757:97, September 2012. doi: 10.1088/0004-637X/757/1/97.

L. Ni, K. Germaschewski, Y.-M. Huang, B. P. Sullivan, H. Yang, and A. Bhattacharjee. Linear plasmoid instability of thin current sheets with shear flow. *Physics of Plasmas*, 17(5):052109, May 2010. doi: 10.1063/1.3428553.

M. Øieroset, R. P. Lin, T. D. Phan, D. E. Larson, and S. D. Bale. Evidence for Electron Acceleration up to ˜300 keV in the Magnetic Reconnection Diffusion Region of Earth's Magnetotail. *Physical Review Letters*, 89(19):195001, October 2002. doi: 10.1103/PhysRevLett.89.195001.

M. Oka, T.-D. Phan, S. Krucker, M. Fujimoto, and I. Shinohara. Electron Acceleration by Multi-Island Coalescence. *The Astrophysical Journal*, 714:915–926, May 2010. doi: 10.1088/0004-637X/714/1/915.

M. Oka, S. Krucker, H. S. Hudson, and P. Saint-Hilaire. Electron Energy Partition in the Above-the-looptop Solar Hard X-Ray Sources. *The Astrophysical Journal*, 799:129, February 2015. doi: 10.1088/0004-637X/799/2/129.

Y. Omura, H. Matsumoto, T. Miyake, and H. Kojima. Electron beam instabilities as generation mechanism of electrostatic solitary waves in the magnetotail. *Journal of Geophysical Research*, 101:2685–2698, February 1996. doi: 10.1029/95JA03145.

E. N. Parker. Newtonian Development of the Dynamical Properties of Ionized Gases of Low Density. *Physical Review*, 107:924–933, August 1957a. doi: 10.1103/PhysRev.107.924.

E. N. Parker. Sweet's Mechanism for Merging Magnetic Fields in Conducting Fluids. *Journal of Geophysical Research*, 62:509–520, December 1957b. doi: 10.1029/JZ062i004p00509.

E. N. Parker. The passage of energetic charged particles through interplanetary space. *Planetary and Space Science*, 13:9–49, January 1965. doi: 10.1016/0032-0633(65)90131-5.

V. Petrosian. Stochastic Acceleration by Turbulence. *Space Science Reviews*, 173: 535–556, November 2012. doi: 10.1007/s11214-012-9900-6.

V. Petrosian and S. Liu. Stochastic Acceleration of Electrons and Protons. I. Acceleration by Parallel-Propagating Waves. *The Astrophysical Journal*, 610:550–571, July 2004. doi: 10.1086/421486.

V. Petrosian, H. Yan, and A. Lazarian. Damping of Magnetohydrodynamic Turbulence in Solar Flares. *The Astrophysical Journal*, 644:603–612, June 2006. doi: 10.1086/503378.

H. E. Petschek. Magnetic Field Annihilation. *NASA Special Publication*, 50:425, 1964.

M. Piana, A. M. Massone, E. P. Kontar, A. G. Emslie, J. C. Brown, and R. A. Schwartz. Regularized Electron Flux Spectra in the 2002 July 23 Solar Flare. *The Astrophysical Journal Letters*, 595:L127–L130, October 2003. doi: 10.1086/378171.

William H Press. *Numerical recipes 3rd edition: The art of scientific computing.* Cambridge university press, 2007.

E. Priest and T. Forbes. *Magnetic Reconnection.* Cambridge University Press, June 2000.

P. L. Pritchett. Geospace Environment Modeling magnetic reconnection challenge: Simulations with a full particle electromagnetic code. *Journal of Geophysical Research*, 106:3783–3798, March 2001. doi: 10.1029/1999JA001006.

P. L. Pritchett. Relativistic electron production during guide field magnetic reconnection. *Journal of Geophysical Research (Space Physics)*, 111(A10):A10212, October 2006. doi: 10.1029/2006JA011793.

G. Qin, W. H. Matthaeus, and J. W. Bieber. Subdiffusive transport of charged particles perpendicular to the large scale magnetic field. *Geophysical Research Letters*, 29:1048, February 2002. doi: 10.1029/2001GL014035.

J. Qiu, W. Liu, N. Hill, and M. Kazachenko. Reconnection and Energetics in Two-ribbon Flares: A Revisit of the Bastille-day Flare. *The Astrophysical Journal*, 725: 319–330, December 2010. doi: 10.1088/0004-637X/725/1/319.

A. K. Ram and B. Dasgupta. Dynamics of charged particles in spatially chaotic magnetic fields. *Physics of Plasmas*, 17(12):122104, December 2010. doi: 10.1063/1.3529366.

R. Ramaty, N. Mandzhavidze, B. Kozlovsky, and R. J. Murphy. Solar Atmospheric Abundances and Energy Content in Flare Accelerated Ions from Gamma-Ray Spectroscopy. *The Astrophysical Journal Letters*, 455:L193, December 1995. doi: 10.1086/309841.

J. C. Raymond, S. Krucker, R. P. Lin, and V. Petrosian. Observational Aspects of Particle Acceleration in Large Solar Flares. *Space Science Reviews*, 173:197–221, November 2012. doi: 10.1007/s11214-012-9897-x.

B. N. Rogers, R. E. Denton, J. F. Drake, and M. A. Shay. Role of Dispersive Waves in Collisionless Magnetic Reconnection. *Physical Review Letters*, 87(19):195004, November 2001. doi: 10.1103/PhysRevLett.87.195004.

V. Roytershteyn, H. Karimabadi, and A. Roberts. Generation of magnetic holes in fully kinetic simulations of collisionless turbulence. *Philosophical Transactions of the Royal Society of London Series A*, 373:20140151–20140151, April 2015. doi: 10.1098/rsta.2014.0151.

R. Samtaney, N. F. Loureiro, D. A. Uzdensky, A. A. Schekochihin, and S. C. Cowley. Formation of Plasmoid Chains in Magnetic Reconnection. *Physical Review Letters*, 103(10):105004, September 2009. doi: 10.1103/PhysRevLett.103.105004.

Tetsuya Sato and Takaya Hayashi. Externally driven magnetic reconnection and a powerful magnetic energy converter. *Physics of Fluids (1958-1988)*, 22(6):1189–1202, 1979.

S. L. Savage, G. Holman, K. K. Reeves, D. B. Seaton, D. E. McKenzie, and Y. Su. Low-altitude Reconnection Inflow-Outflow Observations during a 2010 November 3 Solar Eruption. *The Astrophysical Journal*, 754:13, July 2012. doi: 10.1088/0004-637X/754/1/13.

P. V. Savrukhin. Generation of Suprathermal Electrons during Magnetic Reconnection at the Sawtooth Crash and Disruption Instability in the T-10 Tokamak. *Physical Review Letters*, 86:3036, April 2001. doi: 10.1103/PhysRevLett.86.3036.

M. Scholer. Undriven magnetic reconnection in an isolated current sheet. *Journal of Geophysical Research*, 94:8805–8812, July 1989. doi: 10.1029/JA094iA07p08805.

C. J. Schrijver and G. L. Siscoe. *Heliophysics: Plasma Physics of the Local Cosmos*. Cambridge University Press, July 2009.

J. Scudder and W. Daughton. "Illuminating" electron diffusion regions of collisionless magnetic reconnection using electron agyrotropy. *Journal of Geophysical Research (Space Physics)*, 113:A06222, June 2008. doi: 10.1029/2008JA013035.

M. A. Shay and J. F. Drake. The role of electron dissipation on the rate of collisionless magnetic reconnection. *Geophysical Research Letters*, 25:3759–3762, 1998. doi: 10.1029/1998GL900036.

M. A. Shay, J. F. Drake, B. N. Rogers, and R. E. Denton. The scaling of collisionless, magnetic reconnection for large systems. *Geophysical Research Letters*, 26:2163–2166, 1999. doi: 10.1029/1999GL900481.

M. A. Shay, J. F. Drake, B. N. Rogers, and R. E. Denton. Alfvénic collisionless magnetic reconnection and the Hall term. *Journal of Geophysical Research*, 106: 3759–3772, March 2001. doi: 10.1029/1999JA001007.

M. A. Shay, J. F. Drake, and M. Swisdak. Two-Scale Structure of the Electron Dissipation Region during Collisionless Magnetic Reconnection. *Physical Review Letters*, 99(15):155002, October 2007. doi: 10.1103/PhysRevLett.99.155002.

N. R. Sheeley, Jr., H. P. Warren, and Y.-M. Wang. The Origin of Postflare Loops. *The Astrophysical Journal*, 616:1224–1231, December 2004. doi: 10.1086/425126.

K. Shibata and T. Magara. Solar Flares: Magnetohydrodynamic Processes. *Living Reviews in Solar Physics*, 8, December 2011. doi: 10.12942/lrsp-2011-6.

K. Shibata and S. Tanuma. Plasmoid-induced-reconnection and fractal reconnection. *Earth, Planets, and Space*, 53:473–482, June 2001. doi: 10.1186/BF03353258.

K. Shibata, S. Masuda, M. Shimojo, H. Hara, T. Yokoyama, S. Tsuneta, T. Kosugi, and Y. Ogawara. Hot-Plasma Ejections Associated with Compact-Loop Solar Flares. *The Astrophysical Journal Letters*, 451:L83, October 1995. doi: 10.1086/309688.

A. Y. Shih, R. P. Lin, and D. M. Smith. RHESSI Observations of the Proportional Acceleration of Relativistic >0.3 MeV Electrons and >30 MeV Protons in Solar Flares. *The Astrophysical Journal Letters*, 698:L152–L157, June 2009. doi: 10.1088/0004-637X/698/2/L152.

L. Sironi and A. Spitkovsky. Relativistic Reconnection: An Efficient Source of Non-thermal Particles. *The Astrophysical Journal Letters*, 783:L21, March 2014. doi: 10.1088/2041-8205/783/1/L21.

B. V. Somov and T. Kosugi. Collisionless Reconnection and High-Energy Particle Acceleration in Solar Flares. *The Astrophysical Journal*, 485:859–868, August 1997.

Steven R Spangler. A technique for measuring electrical currents in the solar corona. *The Astrophysical Journal*, 670(1):841, 2007.

J. O. Stenflo. History of Solar Magnetic Fields Since George Ellery Hale. *Space Science Reviews*, September 2015. doi: 10.1007/s11214-015-0198-z.

P. A. Sturrock. Model of the High-Energy Phase of Solar Flares. *Nature*, 211: 695–697, August 1966. doi: 10.1038/211695a0.

L. Sui and G. D. Holman. Evidence for the Formation of a Large-Scale Current Sheet in a Solar Flare. *The Astrophysical Journal Letters*, 596:L251–L254, October 2003. doi: 10.1086/379343.

X. Sun, J. T. Hoeksema, Y. Liu, T. Wiegelmann, K. Hayashi, Q. Chen, and J. Thalmann. Evolution of Magnetic Field and Energy in a Major Eruptive Active Region Based on SDO/HMI Observation. *The Astrophysical Journal*, 748:77, April 2012. doi: 10.1088/0004-637X/748/2/77.

P. A. Sweet. The Neutral Point Theory of Solar Flares. In B. Lehnert, editor, *Electromagnetic Phenomena in Cosmical Physics*, volume 6 of *IAU Symposium*, page 123, 1958.

S. Takasao, A. Asai, H. Isobe, and K. Shibata. Simultaneous Observation of Reconnection Inflow and Outflow Associated with the 2010 August 18 Solar Flare. *The Astrophysical Journal Letters*, 745:L6, January 2012. doi: 10.1088/2041-8205/745/1/L6.

Tomonor Takizuka and Hirotada Abe. A binary collision model for plasma simulation with a particle code. *Journal of Computational Physics*, 25(3):205–219, 1977.

S. Tsuneta and T. Naito. Fermi Acceleration at the Fast Shock in a Solar Flare and the Impulsive Loop-Top Hard X-Ray Source. *The Astrophysical Journal Letters*, 495:L67–L70, March 1998. doi: 10.1086/311207.

M Ugai. Computer studies on powerful magnetic energy conversion by the spontaneous fast reconnection mechanism. *Physics of Plasmas (1994-present)*, 2(2):388–397, 1995.

Takayuki Umeda, Yoshiharu Omura, T Tominaga, and Hiroshi Matsumoto. A new charge conservation method in electromagnetic particle-in-cell simulations. *Computer Physics Communications*, 156(1):73–85, 2003.

D. A. Uzdensky and R. M. Kulsrud. Two-dimensional numerical simulation of the resistive reconnection layer. *Physics of Plasmas*, 7:4018–4030, October 2000. doi: 10.1063/1.1308081.

L. van Driel-Gesztelyi and L. M. Green. Evolution of Active Regions. *Living Reviews in Solar Physics*, 12, September 2015. doi: 10.1007/lrsp-2015-1.

John Villasenor and Oscar Buneman. Rigorous charge conservation for local electromagnetic field solvers. *Computer Physics Communications*, 69(2-3):306–316, 1992.

N. Vilmer, A. L. MacKinnon, and G. J. Hurford. Properties of Energetic Ions in the Solar Atmosphere from γ-Ray and Neutron Observations. *Space Science Reviews*, 159:167–224, September 2011. doi: 10.1007/s11214-010-9728-x.

M. Wan, W. H. Matthaeus, V. Roytershteyn, H. Karimabadi, T. Parashar, P. Wu, and M. Shay. Intermittent Dissipation and Heating in 3D Kinetic Plasma Turbulence. *Physical Review Letters*, 114(17):175002, May 2015. doi: 10.1103/PhysRevLett.114.175002.

G. R. Werner, D. A. Uzdensky, B. Cerutti, K. Nalewajko, and M. C. Begelman. The Extent of Power-law Energy Spectra in Collisionless Relativistic Magnetic Reconnection in Pair Plasmas. *The Astrophysical Journal Letters*, 816:L8, January 2016. doi: 10.3847/2041-8205/816/1/L8.

S. M. White, A. O. Benz, S. Christe, F. Fárník, M. R. Kundu, G. Mann, Z. Ning, J.-P. Raulin, A. V. R. Silva-Válio, P. Saint-Hilaire, N. Vilmer, and A. Warmuth. The Relationship Between Solar Radio and Hard X-ray Emission. *Space Science Reviews*, 159:225–261, September 2011. doi: 10.1007/s11214-010-9708-1.

T. Wiegelmann and T. Sakurai. Solar Force-free Magnetic Fields. *Living Reviews in Solar Physics*, 9, September 2012. doi: 10.12942/lrsp-2012-5.

T. Wiegelmann, G. J. D. Petrie, and P. Riley. Coronal Magnetic Field Models. *Space Science Reviews*, July 2015. doi: 10.1007/s11214-015-0178-3.

P Wu, MA Shay, TD Phan, M Oieroset, and M Oka. Effect of inflow density on ion diffusion region of magnetic reconnection: Particle-in-cell simulations. *Physics of Plasmas (1994-present)*, 18(11):111204, 2011.

M. Yamada, R. Kulsrud, and H. Ji. Magnetic reconnection. *Reviews of Modern Physics*, 82:603–664, January 2010. doi: 10.1103/RevModPhys.82.603.

M. Yan, L. C. Lee, and E. R. Priest. Fast magnetic reconnection with small shock angles. *Journal of Geophysical Research*, 97:8277–8293, June 1992. doi: 10.1029/92JA00170.

T. Yokoyama, K. Akita, T. Morimoto, K. Inoue, and J. Newmark. Clear Evidence of Reconnection Inflow of a Solar Flare. *The Astrophysical Journal Letters*, 546: L69–L72, January 2001. doi: 10.1086/318053.

Igor Zagorodnov and Thomas Weiland. Te/tm field solver for particle beam simulations without numerical cherenkov radiation. *Physical Review Special Topics-Accelerators and Beams*, 8(4):042001, 2005.

G. P. Zank, editor. *Transport Processes in Space Physics and Astrophysics*, volume 877 of *Lecture Notes in Physics, Berlin Springer Verlag*. Springer, 2014. doi: 10.1007/978-1-4614-8480-6.

G. P. Zank, J. A. le Roux, G. M. Webb, A. Dosch, and O. Khabarova. Particle Acceleration via Reconnection Processes in the Supersonic Solar Wind. *The Astrophysical Journal*, 797:28, December 2014. doi: 10.1088/0004-637X/797/1/28.

S. Zenitani and M. Hoshino. The Generation of Nonthermal Particles in the Relativistic Magnetic Reconnection of Pair Plasmas. *The Astrophysical Journal Letters*, 562:L63–L66, November 2001. doi: 10.1086/337972.

B. Zhang and H. Yan. The Internal-collision-induced Magnetic Reconnection and Turbulence (ICMART) Model of Gamma-ray Bursts. *The Astrophysical Journal*, 726:90, January 2011. doi: 10.1088/0004-637X/726/2/90.

V. V. Zharkova, K. Arzner, A. O. Benz, P. Browning, C. Dauphin, A. G. Emslie, L. Fletcher, E. P. Kontar, G. Mann, M. Onofri, V. Petrosian, R. Turkmani, N. Vilmer, and L. Vlahos. Recent Advances in Understanding Particle Acceleration Processes in Solar Flares. *Space Science Reviews*, 159:357–420, September 2011. doi: 10.1007/s11214-011-9803-y.

E. G. Zweibel and M. Yamada. Magnetic Reconnection in Astrophysical and Laboratory Plasmas. *Annual Review of Astronomy and Astrophysics*, 47:291–332, September 2009. doi: 10.1146/annurev-astro-082708-101726.